Biological Transport Networks

Luke Latham Moorhouse Heaton

New College
University of Oxford

A thesis submitted for the degree of
Doctor of Philosophy

Trinity 2012

Abstract

Cord-forming fungi form extensive networks that continuously adapt to maintain an efficient transport system, and we can photograph their growth, digitize the network structure, and measure the movement of radio-tracers. Mycelial networks are more accessible than the transport networks of other multicellular organisms, but there are many open questions concerning the coordination of growth and transport within fungal networks. As osmotically driven water uptake is often distal from the growing margin, and aqueous fluids are effectively incompressible, we propose that growth induces mass flows across the mycelium, towards the growing regions. We imaged the temporal evolution of networks formed by *Phanerochaete velutina*, and at each stage calculated the unique set of currents that account for the observed changes in cord volume, while minimizing the work required to overcome viscous drag. Predicted speeds were in reasonable agreement with experimental data, and cords that were predicted to carry large currents were significantly more likely to increase in size than cords with small currents.

We have also developed an efficient method for calculating the exact quantity of resource in each part of an arbitrary network, where the resource is lost or delivered out of the network at a given rate, while being subject to advection and diffusion. This method enabled us to model the spatial distribution of resource that emerges as a fungal network grows over time, and we found good empirical agreement between our model and experimental data gathered using radio-labeled tracers. Our results suggest that in well insulated fungal networks, growth-induced mass flow is sufficient to account for long distance transport. We conclude that active transport mechanisms may only be required at the very end of the transport pathway, near the growing tips. We also developed a simple model of glucose delivery through vascular networks, which indicates that increasing the number of blood vessels in a region can actually decrease the total rate of glucose delivery.

Biological Transport Networks

Luke Latham Moorhouse Heaton

New College

University of Oxford

A thesis submitted for the degree of

Doctor of Philosophy

Trinity 2012

Acknowledgements

First and foremost I would like to thank my supervisors, Nick S. Jones, Mark D. Fricker, Philip K. Maini and Eduardo López. It has been a pleasure working with all of them. I would also like to thank my friends and family for keeping me sane whilst completing my thesis, the EPSRC for providing funding, and the many people at the DTC who helped to provide a stimulating and sociable environment. I would also like to thank M. T. Gastner for giving me permission to reproduce Figure 3 of his paper Shape and efficiency in spatial distribution networks, J. Stat. Mech, 2006, and finally, I would like to thank D. Eamus and J. W. G. Cairney for giving me permission to reproduce Figure 1 of their paper Internal structure and hydraulic conductivity of basidiomycete translocating organs, J. Exp. Botany, 1985.

Models are partial representations. Their aim is explanation: to show which features of a system are necessary and sufficient to understand it. So, although we could try to understand cardiac rhythm as the interaction of the few thousand protein types that are in any cell, we can in fact understand most of what we wish to know about pace-maker activity from the interaction of around a dozen protein types. The power of a model lies in identifying what is essential, whereas a complete representation would leave us just as wise, or as ignorant, as before.

Denis Noble, *The Rise of Computational Biology*.

Abstract

Cord-forming fungi form extensive networks that continuously adapt to maintain an efficient transport system, and we can photograph their growth, digitize the network structure, and measure the movement of radio-tracers. Mycelial networks are more accessible than the transport networks of other multicellular organisms, but there are many open questions concerning the coordination of growth and transport within fungal networks. As osmotically driven water uptake is often distal from the growing margin, and aqueous fluids are effectively incompressible, we propose that growth induces mass flows across the mycelium, towards the growing regions. We imaged the temporal evolution of networks formed by *Phanerochaete velutina*, and at each stage calculated the unique set of currents that account for the observed changes in cord volume, while minimizing the work required to overcome viscous drag. Predicted speeds were in reasonable agreement with experimental data, and cords that were predicted to carry large currents were significantly more likely to increase in size than cords with small currents.

We have also developed an efficient method for calculating the exact quantity of resource in each part of an arbitrary network, where the resource is lost or delivered out of the network at a given rate, while being subject to advection and diffusion. This method enabled us to model the spatial distribution of resource that emerges as a fungal network grows over time, and we found good empirical agreement between our model and experimental data gathered using radio-labeled tracers. Our results suggest that in well insulated fungal networks, growth-induced mass flow is sufficient to account for long distance transport. We conclude that active transport mechanisms may only be required at the very end of the transport pathway, near the growing tips. We also developed a simple model of glucose delivery through vascular networks, which indicates that increasing the number of blood vessels in a region can actually decrease the total rate of glucose delivery.

Contents

Chapter 1

The Structure and Function of Biological Transport Networks

1.1 Transport in Biology

Living things are composed of cells, and to maintain their metabolic activity, cells require a supply of energy and molecules of various kinds. It follows from these very basic facts that any multicellular organism will have to tackle the fundamental challenge of supplying all of their component cells with the resources needed for survival. Multi-cellular organisms have evolved many sophisticated systems to tackle the transport problem, and many biomedical problems can be understood from the perspective of transport processes. For example, strokes and vascular dementia can be understood as failures of the transport system, and the growth of tumours is limited by the supply of resource reaching the cancerous cells.

The flow of fluid through a network is a common feature of biological transport systems, though the mechanisms driving the flow vary considerably across the different kingdoms of life. Plants circulate nutrients through the xylem and phloem, driving mass flows in the xylem by transpiration from the leaves. They also actively maintain osmotic gradients along the phloem, inducing a flow of sap from sources, where water is drawn from the surrounding tissue (companion cells) into the sieve-tubes of the phloem, and the fluid then flows towards the sinks, where water leaves the phloem [140, 141]. Animals utilize hearts or contractile regions to circulate blood through hierarchical, fractal-like vascular systems [24, 170, 173, 203, 205].

The translocation of resource within fungal networks is much less well studied than transport in the other major multi-cellular kingdoms of life, despite the fact that the translocation of carbon, phosphate and nitrogen by fungal colonies is an absolutely critical feature of many ecosystems [66, 86, 130].

Many organs, including lungs, livers and kidneys, are structured to enable the rapid exchange of molecules [194]. The need to transport resources efficiently places a significant constraint on the physical form of these organs of transport, and we might even go so far as to claim that the evolution of biological transport systems was not strongly constrained by the choice of morphogenetic mechanism. For example, independent of the complex molecular mechanisms involved in lung formation, it is quite obvious why lungs have such a large surface area (approximately two tennis courts in an adult human), given that the rate at which oxygen will diffuse from the air into the blood is proportional to the area of the surface through which the oxygen is diffusing [194]. As with any natural system, we do not know *a priori* what (if any) is the functional being optimized by any given structure. Nevertheless, many levels of biological organization, from the density of capillaries to the size and structure of cells, can be partially explained by the rates of transport of molecules from their sources to their sites of delivery. For example, the spacing of capillaries reflects the rate at which oxygen is consumed by respiration, and the rate at which oxygen can diffuse through the tissue [25, 26, 87, 90, 91, 97, 172, 194].

Understanding and exploiting transport processes in humans and other mammals is of obvious importance, not least because alterations in such processes are critical factors in many diseases, and natural transport processes are essential to understanding the removal of toxins and the delivery of drugs. Improving our understanding of biological transport networks in general and fungal networks in particular is of interest for numerous reasons. Fungi function as pathogens, mutualists, and decomposers, and play key roles in biogeochemical cycles and agriculture [86]. Crucially, such organisms forage through substrates for scarce and heterogeneously distributed resources, including phosphate and nitrogen, and individuals must both transport scavenged resources across the mycelium, and coordinate their use. Fungi are a

crucial component of soil, yet our understanding of these organisms is remarkably incomplete. The movement of soluble, radio-labelled tracers under various conditions have been analyzed by a number of research groups, using geiger counters [42, 49, 57, 130, 147, 188, 198] and scintillation screens [83, 189]. It has also been shown that in the apical compartment of fungal hyphae, the average rate of movement of the cytoplasm ($\sim 0.5\mu\text{ms}^{-1}$) matches the rate of tip extension [126]. Despite this experimental work, the relative roles of mass-flows (advection), diffusion and active transport are poorly understood [32, 48, 93, 115, 127], and there are many open questions concerning the mechanism(s) that drive and regulate transport in fungal networks.

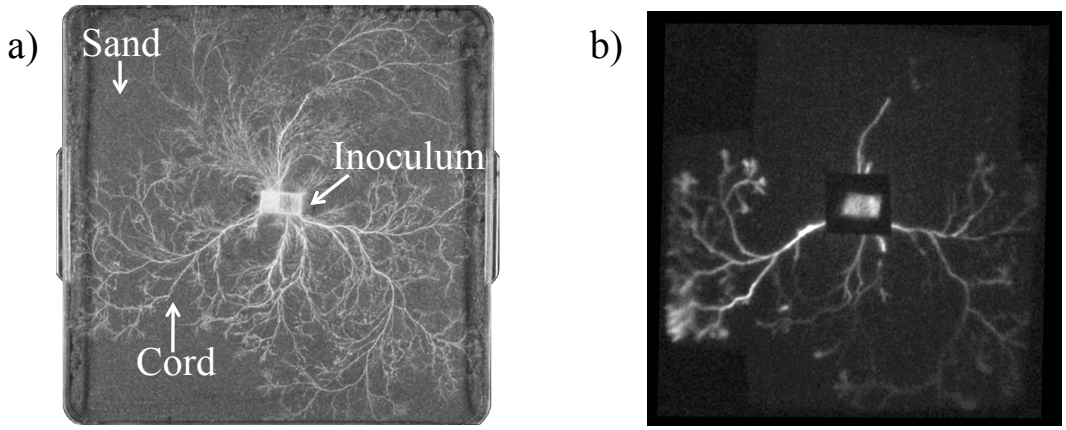

Figure 1.1: **Fungal network containing a radio-labelled tracer.**
(a) *Phanerochaete velutina* in a 24 cm $\times$ 24 cm microcosm, photographed just before radio-labeled AIB was dripped onto the inoculum.
(b) Image gathered by a photon counting camera. The brightness of the image reflects the total number of photons emitted from each region over the period of time starting 5.6 hours after the radio-labeled AIB was added, and finishing 37.6 hours after it was added. The principle aim of this thesis is to understand the mechanism(s) that are responsible for producing the observed spatio-temporal distribution of radio-labeled tracer.

This thesis aims to improve our understanding of transport in fungal networks (see Fig. 1.1). I believe that a combination of experimental work and mathematical modelling can help us gain insights as to the relative importance of advective mass flows, diffusion, and active transport, while well established biophysical principles can help to explain the mechanisms that drive fluxes through the mycelium. In par-

ticular, we investigate the extent to which the observed patterns of translocation be explained in terms of growth, mass flows and diffusion. As fungi explore their environment, parts of the mycelium thicken, while other parts are recycled through the process of autophagy. The developmental logic of fungal networks is not well understood [93, 157], but we propose that certain morphological features of fungal networks can be understood in terms of transport efficiency. In the future works section, we also suggest that the observed patterns of growth might be explicable in terms of optimal foraging strategies, given the heterogeneous distribution of resource, and the necessity of forming robust networks that can survive grazing by insects or other forms of damage.

Many fungi form remarkably large networks, with some individuals reaching across multiple hectares of habitat [177]. There are many species of network-forming fungi, and it is likely that they have evolved a range of solutions to the problems of exploration, transport efficiency and robustness. Because fungi are ecologically critical, fungal networks are important objects of study in their own right. Furthermore, the detailed characterization and modelling of such systems could be a first step in understanding how to construct efficient, robust transport networks based on local rules rather than global information, in the newly emerging field of biologistics [101]. Although it is far from certain that a biologistic approach to network design will be successful, it is worth noting that in comparison to other biological transport networks, fungal systems have the benefit that the network is accessible, and development can be readily followed through a sequence of images.

1.2 Networks in Space

Biological transport networks are physical objects, embedded in three-dimensional space. This fact is a massive constraint on the possible network structure. For example, the shortest path between any two points in such a network cannot be less than the Euclidean distance between those points. Network properties are even more restricted in the case of planar networks (that is, in the case of graphs that can be

drawn in the plane in such a way that the edges do not intersect). In a planar graph each face is bounded by at least three edges, and every edge separates at most two faces, so $E \leq \frac{3F}{2}$ where E denotes the number of edges and F denotes the number of faces. Where N denotes the number of nodes, it follows from Euler's polyhedral formula $N - E + F = 2$ [18] that

$$E \leq 3N - 6. \tag{1.1}$$

This puts a strong constraint on the possible degree distribution of planar graphs, which means that many network measures that are based on degree distribution may not be appropriate. For example, if we randomly reconnect the edges in a planar graph, we should expect to see certain changes in the summary statistics of the graph precisely because randomization is likely to mean that the graph is no longer planar. Whether or not a planar graph represents an efficient transport network, the network must be sparse, and the inequality 1.1 implies that all planar graphs have an average degree less than or equal to 6 [18].

Embedding a graph in a metric space such that there is a well defined distance between the nodes independent of the network (e.g. the Euclidean distance between the nodes) affects the statistical properties of the network in other, more subtle ways. For example, in the case of biological networks, it is clearly the case that nodes that are close to one another are much more likely to be connected by an edge than nodes which are far apart, and this fact has consequences for various network measures. The diameter of a network is defined as being the longest shortest path (where the path length between i and j is usually defined to be the smallest number of edges that need to be crossed to get from i to j), and the clustering coefficient of a network is defined to be the probability that nodes a and c are connected, given that a and b are connected, and b and c are connected [18]. The "small world" phenomenon of large networks with very small diameters cannot arise in spatially embedded networks, as if the maximum length of an edge is n and nodes i and j are a distance m apart, we cannot travel from i to j without crossing at least m/n edges. Also note that if node a is close to node b and node b is close to node c, it follows that a will be close to

c. As nodes that are close to one another are more likely to be connected, we should expect that spatially embedded networks will have a much higher number of cycles of length three, and a much higher clustering coefficient, than we would expect to find in a randomized network.

Spatial embedding also affects the betweenness centrality of edges in the network. By definition the betweenness centrality of an edge e is

$$g(e) = \sum_{s \neq t} \frac{\sigma_{s,t}(e)}{\sigma_{s,t}}, \tag{1.2}$$

where $\sigma_{s,t}$ is the number of shortest paths going from s to t and $\sigma_{s,t}(e)$ is the number of shortest paths going from s to t that pass through edge e. The betweenness centrality of an edge reflects its ability to provide a path between separated regions of the network, and in that sense it reflects the importance of the edge for flows across the network. In the case where we are interested in flows to or from a particular node i, it may also be useful to consider the local edge betweenness of each edge e, which is defined to be

$$g_i(e) = \sum_{s \neq i} \frac{\sigma_{s,i}(e)}{\sigma_{s,i}}, \tag{1.3}$$

In the case of a road network, a fungal network, or other spatially embedded networks, the spatial barycentre (centre of gravity) and its neighbours are likely to have a large betweenness centrality [17]. This is the case because if two points are far away from each other, the probability that the path between them passes near the barycentre of the network will be very large. By analogy, if we pick two random points in a circle, a straight line connecting those points is much more likely to pass close to the centre of the circle than any given point on the circumference. This consideration does not apply in the case of networks that are not embedded in a metric space, and as we randomize the links in a spatially embedded network, betweeness centrality becomes de-correlated with spatial centrality, while the correlation between node degree and betweeness increases [17].

The existence of two metrics of distance enables us to characterize the efficiency of networks in a manner that is not possible when the nodes of the network are not

embedded in a metric space. In particular, for each pair of nodes i and j we can define the 'route factor'

$$q(i,j) = \frac{d_R(i,j)}{d_E(i,j)}, \tag{1.4}$$

where $d_R(i,j)$ is the length of the shortest path through the network between nodes i to j, and $d_E(i,j)$ is the Euclidean distance between nodes i and j [88]. Now, many organisms and many man made systems need to transport materials from one source (the 'root' node), out to many different sinks. For example, the vascular network transports blood from the heart out to all the capillaries, and we can imagine wanting to find an efficient arrangement of electrical cables to connect a large number of houses to a single power station. In his book from 1974 "Patterns in Nature" [182], Stevens suggests that 'good' distribution networks of this kind have two definitive properties. First, the network should be efficient in the sense that the paths from each node to the root ought to be relatively short, as in all manner of systems short paths are more efficient than long ones. In other words, the route factor should not be much larger than one. Second, the sum of the lengths of all edges in the network should be low, so that the network is economical to build and maintain. These two criteria are often at odds with each other, as we may need to add an extra edge in order to reduce the route factor for some given node. Nevertheless, Gastner and Newman [88] have shown that there are actual solutions to the distribution problem that come remarkably close to being optimal in both senses (see Fig. 1.2).

In the case of road networks, electrical networks or vascular networks, some edges are easier to pass through than others, and the cost of transiting a given edge reflects more than just its length. In general, wide edges are more expensive to construct, but they are relatively easy to cross. For example, building and maintaining a mile of motorway is more expensive than building a mile of minor road, but there is a payoff because traffic travels faster on a motorway. In the case where our network description of a system includes weights for each of the edges, our metric for the 'distance' or shortest path between nodes should reflect the weight of the edges. In that case the diameter of a network can be kept small regard-

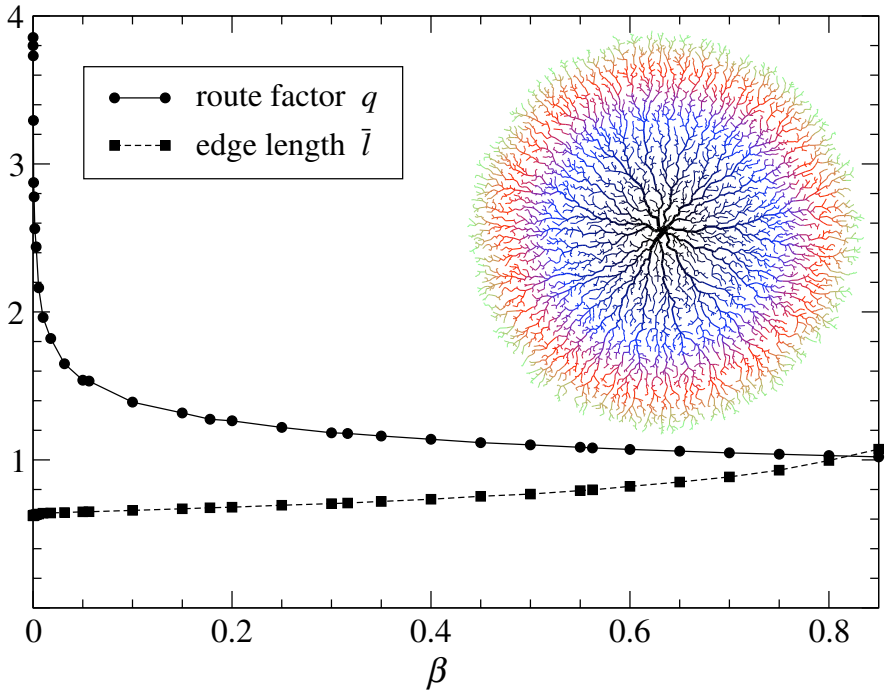

Figure 1.2: **Networks can be close to optimal in terms of both route factor and total length.** In Gastner and Newman's model [88], nodes are randomly distributed in two-dimensional space with unit mean density, and node 0 is designated as the root or source for the network. The network grows over time, and at each time step a new edge is added, connecting a previously unconnected node i to some node j that was already part of the network. The nodes i and j are chosen such that at each time step we minimize the cost $d_{ij} + \beta l_{j0}$, where d_{ij} is the Euclidean distance between i and j, l_{j0} is length through the network from node j to the source node 0, and β is a tunable parameter. When $\beta = 0$, we simply add the shortest possible edge at every time step. The resulting network will have the smallest possible mean length of edge $\bar{l}$, but it is likely that the mean route factor q will be large. By increasing β we no longer grow the network by adding the shortest possible edge, but the resulting networks have route factors which are remarkably close to 1 (the minimum possible). Each data point on the graph represents an example with 10,000 nodes, and the inset shows an example network with $\beta = 0.4$.

less of the number of nodes that need to be connected, or the Euclidean distance between them, as we can always increase the weight of some transport backbone to provide a 'short' route from one side of the network to the other [17, 18]. In general, it is important to consider the weights of edges when considering transport efficiency. Indeed, much of the literature on optimal transport networks is concerned with the optimal distribution of weights for a given network topology [30, 35, 58, 68, 73, 74, 119, 132, 137, 160, 161, 173, 203]. The merits of using

shortest path based summary statistics is more open to debate. On the one hand, metrics such as diameter, or betweenness centrality, are relatively easy to compute, and in each case there is a unique solution. However, such measures may be misleading, as in actual transport networks material moves along parallel flow paths, and not all of the material follows the very shortest path. In particular, comparable parallel pathways that are only marginally longer do not feature in the analysis, but might be expected to participate in transport in a real system. In this thesis we make minimal use of shortest path based metrics, preferring to model our networks as hydraulic circuits, with pressure drive flows.

An efficient transport network ought to minimize the distances that the resource needs to travel, but that does not mean that organisms will manage to form the structure with the shortest possible total length, or the smallest possible route factor. This illustrates a more general point that although biological transport networks need to be efficient in a range of different senses, there is evolutionary pressure to be close to optimal, not precisely optimal. For example, it is important that vascular networks are such that the energy required to pump blood through them is relatively small, but it is also important that blocking a few capillaries does not irreparably destroy an organism's ability to distribute blood through the system, and the network needs to be such that dilating parts of the vasculature will effectively shift where the blood will flow, without completely starving any part of the organism. Any cost function that incorporates all of these desirable features of a network is bound to be somewhat arbitrary, and identifying the optimal network for a given cost function does not necessarily provide biologically meaningful insights.

Rather than looking for an optimality condition that a given topology is likely to satisfy, we take a more elementary approach. We suggest that it is first necessary to establish the dynamics on and of the network, and so we model the relevant processes which occur over a given set of empirically determined networks. Given a clearly established form of dynamics one is then free to speculate about the optimality condition that the combination of dynamics (and time evolving network structure)

satisfies. We believe that this approach can help to illuminate the significance of particular features of biological networks, and we also believe that the models we have developed can help to explain the process of translocation over fungal networks. Despite our reservations about the biological relevance of many cost functions and the networks associated with them, we would not deny that an abstract, network theoretic approach can help to elucidate the value of certain features of actual transport networks, and various natural systems such as river networks and vascular systems have been fruitfully interpreted in light of such results [14, 30, 125, 161]. Such an approach can help to elucidate the value of hierarchically structured networks, as (for example) blood travels as far as possible in large vessels, which then branch to smaller vessels, and so on down to the capillaries. The actual, fractal like scaling of mammalian vascular networks is quite well predicted by various kinds of theoretical analysis [44, 87, 107, 108, 118, 125, 133, 137, 170, 173, 174, 204], and before moving onto my own research, we shall briefly review of some important classes of cost function, and the optimal networks associated with them.

1.3 Transport Costs and Optimal Transport Networks

The design of optimal distribution networks for water, electricity, telephone signals, etc is of great practical import in urban planning, and consequently aspects of this family of problems have been studied since antiquity. Over the last 15 years, a string of papers have explored the topic of transport networks that are optimal in some given sense. Some authors have pursued highly abstract models which assess the cost of different ways of connecting source nodes to sinks (with a variety ways of assessing the cost of any given pattern of flow) [7, 11, 12, 13, 14, 15, 30, 35, 58, 68, 71, 72, 113, 132, 160, 161], others have focussed on the general properties of networks with flows driven by potential differences [73, 74, 119, 173], while West et. al. consider the optimum network given a number of biologically inspired assumptions [170, 203, 204, 205, 206]. The papers by Banavar et. al. and West et. al. are particularly notable, as they played a key role in the development of

the theory of allometric scaling, which attempts to explain the relationship between body size and metabolic rate.

Different studies use different definitions of a network, and the authors optimize different cost functions. For example, Durand [73, 74] considers hydraulic networks that carry volumetric flows, quantified in terms of $\mathrm{mm}^3\mathrm{s}^{-1}$. These flows or currents are driven by pressure gradients, and the mathematics of currents in a hydraulic network are precisely analogous to the mathematics of electrical currents in network of resistors. The hydraulic networks that Durand considers are embedded in an ambient space, and he analyses both the optimal geometry for such networks and the relationship between the local geometry and the local topology. In contrast, Banavar et. al. [11, 12, 14, 15] propose a more abstract model where the graph is not assumed to be embedded in a target space, and the currents through the nodes are not explicitly constrained to derive from a potential difference. Instead, a "current" of size n is injected into node 1, and a unit current is removed from each of the other n nodes. The network is connected, and contains every one of the nodes, because, by assumption, a route must exist from any site X to the source node 1. The scalar quantity $|i_e|$ represents the magnitude of the current along edge e, and it is assumed that current is conserved, so at each node, the current flowing in must be one greater than the the current flowing out (because at each node, a unit current is removed from the network). In Banavar et. al's model, the total cost of transportation is defined to be

$$E = \sum_e k_e |i_e|^\gamma, \tag{1.5}$$

where k_e is a possibly link-dependent positive amplitude, and γ is a given real number. For example, standard circuit theory tells us that in the case of an electrical network, if E is the total amount of power dissipated overcoming the network's resistance, then k_e is the resistance of edge e, and $\gamma = 2$ [70].

A very general observation at the heart of Banavar et. al's analysis is that any efficient flow pattern must be such that at every point, the flow moves materials away from the source. In other words, although there may be loops in the networks they

consider, optimally efficient flows always transport materials in a directed manner. This feature of 'efficient' material flows is common to many definitions of 'efficient' [13, 30, 35, 68, 71, 73, 132, 203], and it is inevitable when the flows are driven by differences in potential. That is because at every point in any given network, material flows from high potential to low potential, and never the other way around. The other key result is that when we identify the optimal network for a range of values for γ, there is a transition from branching trees to structures containing loops, depending on whether the presence of current in an edge makes the marginal cost of transporting an additional current greater or smaller than otherwise it would have been. Indeed, it can be shown that for $\gamma > 1$, the pattern of flow that minimizes E is uniquely determined, and it contains nonzero currents along all of the edges [11, 12, 70]. For $0 < \gamma < 1$ there are multiple solutions, each of which has the topology of a spanning tree. Finally, the case where $\gamma = 1$ is rich, as all directed flow patterns are solutions when γ approaches 1 from above, while all directed spanning trees form degenerate solutions when γ approaches 1 from below [11].

Banavar et. al's highly abstract approach enables the construction of formal proofs concerning optimal networks, but the proper physical interpretation of those results is somewhat elusive [35]. A different approach, taken by West et. al, builds on the legacy of Cecil D. Murray, and the principle of minimum work [136, 137, 138, 139, 170, 173, 203, 204, 205, 206]. Fluid flow is essential to most biological transport networks, and so cost functions that reflect the energy required to overcome viscous drag are of particular biological significance. Indeed, as we shall see in Chapter 2, our modelling approach is to consider fungal networks as hydraulic systems with pressure driven flows, and so the physics of fluid flow and viscous drag are fundamental to this thesis.

Murray observed that vascular networks represent an optimal or near optimal compromise between conflicting costs, as it requires less energy to pump fluid through a large tube compared to a small one, but the metabolic cost of building and maintaing a large tube is greater than the cost of building a small one. More specifically, if gravitational and kinetic energy terms can be neglected, a Newtonian fluid inside a

vessel exhibits a volumetric flow rate $f = c\Delta P$, where c is the hydraulic conductance of the vessel and ΔP is the pressure drop between its ends. In the case of a laminar flow in a cylindrical tube, the Hagen-Poiseuille equation states that the conductance is

$$c = \frac{\pi r^4}{8\eta l}, \tag{1.6}$$

where r is the radius of the tube, l is the length of the tube and η is the dynamic viscosity of the fluid [141, 173, 194]. It follows that the power required to maintain a flow f along a vessel of length l and radius r is af^2lr^{-4}, where $a = 8\eta/\pi$. The work required to overcome viscous drag is much smaller in large vessels, but this benefit of thickening is offset by a cost, and as a simplifying assumption it is reasonable to assume that the metabolic cost of building and maintaining a vessel is proportional to its volume. It follows that the total cost of carrying a current f in a vessel of length l and radius r is

$$E = af^2lr^{-4} + blr^2, \tag{1.7}$$

where b is some constant of proportionality reflecting the metabolic rate per unit volume.

The terms a, b and f are all positive, so Equation (1.7) is at a minimum when

$$r^3 = f\left(\frac{2a}{b}\right)^{1/2}. \tag{1.8}$$

In branching networks such as mammalian circulatory or respiratory systems, current is preserved, which is to say that at each branch point the current in the parent vessel is equal to the total current in the daughter vessels. In the parts of these systems where the Reynold's number is small, Equation (1.8) implies that the optimal arrangement is when the cube of the radius of the parent vessel equals the sum of the cubes of the radii of the daughters (Murray's law). Actual vascular systems approximately follow Murray's law [44, 87, 107, 108, 118, 125, 133, 170, 173, 174], but it is worth noting that significant deviations from Murray's law can result in only modest increase in the amount of energy required to overcome viscous drag [174, 194]. For example, junctions in the transverse arteriolar trees of cat sartorius

muscle were found to have a broad range, with a median value greater than the Murray optimum of 3. The exponents were restricted, however, to values requiring, at individual junctions, little increase in energy. Indeed, the majority of junctions had energy costs less than 1% above the Murray minimum, and for entire trees involving many junctions the departures from optimality averaged less than 10% [174].

Murray's law can also be derived by considering the case where a given network carries a given current in each edge, and the total volume of the network is fixed. If we are free to choose the thickness of each edge subject to this constraint, the optimal thickness for each edge is in accordance with Murray's law [173]. The principle of minimizing energy loss can also be used to make predictions for the branching angles of vascular networks, and there is evidence that actual vascular networks branch in a manner that approximately follows Murray's prinicple of energy minimization [136, 194, 214]. It is also interesting to note that when we have laminar flow through a branching network that follows Murray's law, the velocity in each vessel is proportional to its radius r, and the shear wall stress is constant throughout [173, 194]. Endothelial cells are known to be sensitive to shear wall stress [55, 193, 194], and there is good evidence that this sensitivity is central to the mechanism(s) by which vessels mature to a near optimal cross-sectional area [117, 125, 153, 184].

Another critical factor determining the geometry and topology of vascular networks is the fact that they must be space filling, which is to say the network must reach every part of the organism. If blood supply for a volume V is carried through a parent vessel with two daughters, it is most efficient if each of those daughters supply non-overlapping regions, and so we can suppose that each of the daughter vessels supplies a volume $V/2$. If we are minimizing the work required to overcome viscous drag, the optimal arrangement is for the current to travel as far as possible along the largest available vessel, and so the length of each vessel ought to be proportional to the cube root of the volume it supplies [203, 204, 205, 206]. This implies that where l_1 is the length of the parent and l_2 is the length of each of the daughters, the optimal arrangement is such that $l_1/l_2 = 2^{1/3}$. Murray's law implies that $r_1/r_2 = 2^{1/3}$ (where r_1 is the radius of the parent and r_2 is the radius of the

two daughters), and so we expect to see that in each generation, the aspect ratio of the blood vessels is approximately constant. West et. al. conclude that the optimal form for a branching network carrying fluid at low Reynolds number is self-similar and fractal like: a statement which is approximately true of actual vascular networks [24, 194, 203, 204, 205, 206].

In the parts of the circulatory system where the flow is pulsatile, energy loss is minimized when the total cross-sectional area of the daughters is equal to the cross-sectional area of the parent, as that geometry ensures that energy-carrying waves are not reflected back up the tubes at branch points [194, 203, 204, 205, 206]. As we shall see in Section 2.9, in the case of fungal networks, there may be a completely unrelated reason why it is beneficial for the total cross sectional area of the daughter vessels to be greater than the cross sectional area of the parent vessel. If the total cross-sectional area of the growing front is much larger than the cross-sectional area of the supporting mycelium, our analysis suggests that because of the incompressibility of aqueous fluids, growth itself can drive mass flows which translocate resources towards the growing front at velocities that are much greater than the velocity of tip growth.

1.4 Fluctuating Demand, Robustness and Loops

Although vascular networks are frequently depicted as branching trees [24, 30, 152, 161, 173, 203, 204, 205, 206], many natural and almost all man made networks contain loops. Street plans are full of loops [19], most fungal networks contain loops [33, 34, 81, 82], as do retinal vasculatures [84], and the veins of many leaves contain recursively nested sets of loops [58, 59, 73, 119, 165, 166]. Recent theoretical analyses indicate that if a network is formed whilst being subject to attack, or subject to fluctuating loads, the optimal form will contain loops [58, 59, 119]. More specifically, Katifori et. al [119] consider the family of networks where a number of sink nodes are distributed on a surface along with a single source node, the flows across the network are assumed to be driven by potential differences, and $\sum_{i,j} \kappa_{ij}^{\gamma} = 1$, where

κ_{ij} is the conductance of the edge ij and γ is a tunable parameter. The authors use stochastic simulations to identify the network that minimizes the total power dissipated over time, where each time step one edge is temporarily 'cut' (so κ_{ij} is set to zero for the duration of that time step), and the currents f_{ij} and the power dissipated $\sum_{ij} \frac{f_{ij}^2}{\kappa_{ij}}$ are calculated using basic circuit theory (see Section 2.3). Alternatively, they identify the network that minimizes the total power dissipated over time where every time step a different, randomly selected node is chosen to act as the sink.

Optimization under damage to edges implies the formation of loops almost by definition, as if there were only one route connecting the source and a given sink, an infinite amount of power would be dissipated when that route is cut. Robustness to damage can be conferred by a (topologically minimum) ring joining the outermost nodes [165], and more generally it is well known that redundant edges can confer a degree of robustness to a transport network [18, 31, 81, 82, 125, 160, 165, 166, 195]. Leaves and fungi are under constant attack, from the elements as well as pathogens and a wide variety of grazing animals [30, 34, 165, 166]. If fungal networks were branching trees, severing any branch would disconnect the network. Likewise, if the leaf vascular network was treelike, damage to any vein would result in the death of all the leaf sections downstream from that vein. The value of redundant edges is therefore quite clear, but the results of Katifori et. al. go beyond that relatively simple observation, as they show that optimality under robustness to damage can produce hierarchical, recursively nested loops [119], as can be found in actual leaf venation networks [165, 166].

Katifori et. al. [119] and Corson et. al. [58, 59] also show the importance of fluctuating demand for optimal transport networks. Many definitions of optimality yield treelike structures, with a single path connecting any two points [11, 13, 14, 30, 35, 73, 74, 173, 203]. In this light, the many loops found in leaf venation networks, fungal networks or vascular networks could be interpreted as a compromise between transport efficiency and other requirements, such as tolerance to damage. However, Katifori et. al. and Corson et. al. show that the optimality of branching trees is contingent on the assumption of a stationary flow through the network.

Somewhat surprisingly, they found that optimization under a varying load leads can lead to the formation of dense, recursively looped structures [58, 59, 119]. More specifically, when time variations or fluctuations are allowed for, the resulting optimal structures contain loops, although they do share the hierarchical organization that is characteristic of treelike optimal networks.

This result is biologically very significant, as in general biological transport networks operate in the face of considerable spatiotemporal irregularities. For example, it is well known from functional magnetic resonance imaging that brain vasculature has evolved to deliver changing fluxes under constantly varying load [8, 149]. There is a similar phenomenon in the case of leaves, called stomatal patchiness, which refers to the fact that stomatal apertures (and thus water evaporation and photosynthetic activity) varies in space and time across the surface of the leaf blade [58, 59, 119, 165, 166]. Likewise, as fungal networks grow and the supporting mycelium matures, different parts of the growing margin will need to be supplied with resources at different times. If fungal networks have indeed evolved to maximize transport efficiency, they should be optimal in relation to a history of transport demands, and we should not expect that at any instant the network is the best way of linking the sites of resource uptake with the sites of resource demand.

1.5 Outline of Thesis

In Chapter 2 we review some of the important features of fungal morphology, and propose a model for translocation in fungi. This model was presented in the Proceedings of the Royal Society B [100], and we apply our model to empirical data obtained by imaging the temporal evolution of networks formed by *Phanerochaete velutina*. The key idea is that the effective incompressibility of the fluids within fungi means there must be a flow of fluids from the sites of water uptake to the sites of growth. In effect, we take a series of networks with empirically determined volumes, and at each stage we calculate the unique set of currents that account for the observed changes in cord volume, while minimising the work required to overcome

viscous drag. In other words, we treat each fungal network as a hydraulic system, with pressure driven flows. As we shall see in Section 2.6, predicted speeds are in reasonable agreement with experimental data, and the pressure gradients needed to produce these flows are small. Furthermore, we found that cords that were predicted to carry fast-moving or large currents were significantly more likely to increase in size than cords with slow-moving or small currents.

In Chapter 3 we consider the distribution of resource that arises when material moves through a network by a process of advection and diffusion, while the resource in question is lost or delivered out of the network at some given, local rate. The fact that the material of interest is consumed *en route* is critical to understanding nutrient delivery. In most existing models of optimal transport networks, the network is optimized under the constraint that there must be at least some minimal flow to each sink node of the network [14, 58, 68, 68, 160, 161, 203], but the consumption of the resource carried by those flows is not itself an integral part of the model. To understand nutrient transport we think that the appropriate modelling technique is to couple advection, diffusion and delivery, as the process of delivery is a key component of the dynamics, especially in capillary beds or leaves, where we might expect to see significant variation in nutrient concentrations [90, 123, 194, 207]. The effect of including a delivery term can be significant and somewhat counter-intuitive. For example, in Section 6.3 we will see that there are circumstances in which increasing the number of blood vessels in a region can actually decrease the amount of glucose that is delivered to that region.

We develop two methods that enable us to calculate how the concentration in a network will vary in both space and time, if the resource within in it is subject to advection, diffusion and delivery. The first approach is to operate in Laplace space, which is computationally efficient, because of the wide range of velocities in the networks we are interested in analyzing. In particular, we are interested in analyzing fungal networks that shrink and grow over time, so we also develop an algorithm for finding the concentration of resource in a network where the cross-sectional areas of the edges vary continuously over time. The second method employs a finite

difference scheme, but simple versions of this approach are computationally problematic in the case where the advective velocities are much greater in some parts of the network than others.

In Chapter 4 we investigate the claim that growth-induced mass flows are sufficient to supply the growing tips with the resources they require. We do this by modelling advection, diffusion and delivery over empirically determined fungal networks, and by comparing model predictions with experimental data gathered using radio-labeled tracers. Our results lead us to suggest that in well insulated, foraging fungi, growth-induced mass flow is sufficient to account for long distance transport. This analysis supports the conclusion that additional, active transport mechanisms may only be required at the very end of the transport pathway, near the growing tips.

One problem with higher fungi as experimental systems is that it can take weeks or months for fungal networks to grow, and imaging the translocation of radio-labelled materials with scintillation screens is expensive. By exploring the patterns of growth that are observed *in silico*, we can better determine which experiments are most worth performing. With that motivation, we built on the preceding chapters by developing a model for growing *in silico* fungi, and in Chapter 5 we use our model to help explain some empirical observations concerning fungal growth. As far as possible we use empirically determined parameter values for our model, and we advance the methodology of Boswell et. al. [37, 38, 39, 40, 41] by following their mixed,'tip and bond' approach.

In Chapter 6 we consider ways in which our research could be further developed. In Section 6.1 we discuss experimental work that we have performed and that could be undertaken, which could help to elucidate the process of translocation across fungal networks, and in Section 6.2 we consider how our model of a growing fungal network could be further developed. In Section 6.3 we note that the mathematical machinery developed in Chapter 3 could be used to analyze models of many biological systems, and in particular, we present a simple model of glucose delivery through a vascular network. By analyzing our model we can show that in certain circumstances, increasing the volume of blood and the number of glucose

transporters can actually decrease the total rate of glucose delivery. This somewhat paradoxical result is of particular bio-medical interest, as glucose delivery is essential to the survival of tumours and healthy tissue, and understanding the functional consequences of anti-angiogenic drugs is key to the effective treatment of vascular tumours [3, 10, 51, 54, 69, 120, 121, 151, 153, 175, 184, 194, 201, 207, 209]. As we shall see, to appreciate how the number of blood vessels in a region affects the total rate of glucose delivery, it is essential that we consider the topology of the network, and the local rate of delivery is also critical in a non-trivial manner. Finally, we conclude by reviewing the major findings of the thesis, and the ways in which our research could be further developed.

Chapter 2

Growth-Induced Mass Flows in Fungal Networks

Multi-cellular organisms have evolved sophisticated systems to supply individual cells with the resources necessary for survival. In particular, cord-forming fungi form extensive networks that continuously adapt to maintain an efficient transport system. It is essential that fungi control the osmotic forces that they are subject to [4, 5, 49, 93, 115, 127, 128, 135, 156], and in the literature there has been some preliminary speculation as to how fungi are able to co-ordinate the concentration of osmolytes across the mycelium [49, 115, 156]. As osmotically driven water uptake is often distal from the tips, and aqueous fluids are incompressible, we propose that growth itself induces mass flows across the mycelium, whether or not there are intrahyphal concentration gradients. In this chapter we review some of the important features of fungal morphology, and propose a model for translocation in fungi. This model was presented in the Proceedings of the Royal Society B [100], and in this chapter we apply our model to empirical data obtained by imaging the temporal evolution of networks formed by *Phanerochaete velutina*. At each stage we calculate the unique set of currents that account for the observed changes in cord volume, while minimising the work required to overcome viscous drag.

Predicted speeds are in reasonable agreement with experimental data, and the pressure gradients needed to produce these flows are small. Furthermore, we found that cords that were predicted to carry fast-moving or large currents were signifi-

cantly more likely to increase in size than cords with slow-moving or small currents. The incompressibility of the fluids within fungi means there is a rapid global response to local fluid movements. Hence velocity of fluid flow is a local signal that conveys quasi-global information about the role of a cord within the mycelium. We conclude the chapter by suggesting that fluid incompressibility and the coupling of growth and mass flow are critical physical features that enable the development of efficient, adaptive, biological transport networks.

2.1 Biophysics of Fungal Growth

Fungi are composed of hyphae: tubular structures which can draw water from their environment by means of osmotic forces. As far back as 1892, Reinhardt noted that fungi grow by a process of apical extension, and that as the tips of the hyphae expand, the movement is always perpendicular to the cell wall [159]. Contemporary experiments have confirmed his observations [22], and the fact that expansion is at all points perpendicular to the cell wall strongly suggests that turgor pressure is responsible for forcing out the cell wall.

Although maintaining a suitable turgor pressure is a critical process for fungi [4, 5, 49, 93, 115, 127, 128, 135, 156], turgor pressure does not appear to be rate limiting for growth, as hyphae experiencing different turgor pressures can grow at the same rate [135]. Indeed, some oomycytes can grow in the absence of turgor pressure, which suggests that the cytoskeleton may play a role in forcing the tip of the hyphae forward [135]. Regardless of turgor pressure, fungi cannot grow faster than the rate of growth of the fungal wall. Mathematical models [20, 21, 22, 23, 135, 181] and biochemical analyses [202] indicate that the localized deposition of chitin and β-glucans are particularly critical in determining the characteristics of hyphal expansion.

The details vary considerably between fungal species, but in each case an elaborate cellular dance ensures that vesicles containing materials that will become integrated into the cell wall undergo exocytosis specifically at the tips [20, 21, 22, 23,

127, 202]. These vesicles are thought to arise in the endoplasmic reticulum far behind the tips, and they pass through Golgi equivalents before being transported to the tips where they undergo exocytosis [202]. In some cases the fusion of vesicles with the cell wall is cordinated by an apical body known as the Spitzenkörper (an organelle that is found in all of the fungal species specifically mentioned in this thesis), and in all cases microtubules and other cytoskeletal elements have been implicated in this carefully controlled process.

Atomic force microscopy has indicated that hyphal tips are relatively plastic [202], and as such they can be significantly deformed by the forces produced by turgor pressure. Over the course of tens of seconds, the chitin and β-glucans molecules that have been added to the apex are modified within the domain of the wall. Covalent crosslinks are formed between these two polymers, and hydrogen bonds link homologous polymer chains [202], leading to the formation of chitin microfibrils crosslinked to a glucan matrix. This process converts an initially plastic wall into a rigid wall capable of withstanding turgor pressure, and it is this process which ensures that localized exocytosis results in polar, apical growth. Indeed, hyphae that stop growing attain a wall over the apex that is indistinguishable from the mature, cylindrical wall [202], and it has been observed that interupting growth for as little as one minute can permanently block the elongation of hyphae [163].

Foraging fungal mycelia continuously re-model their morphology, and as a transport network the mycelium must adapt to changing local environmental conditions and patchy resource availability [27, 32, 33, 49, 50, 81, 93, 115, 200]. Hyphae grow by tip extension and then branch sub-apically to form a diffuse tree-like mycelium [92, 134, 135, 181]. As the colony continues to grow, hyphal fusions or anastomoses occur, producing a more reticulate, net-like structure (see Fig. 2.1). Ascomycete fungi have partial septa or septal pores which allow cytoplasmic continuity and organelle movement across the intact mycelium [127]. For example, the nuclei of *N. crassa* migrate across the mycelium. Basidiomycete fungi such as *P. velutina* are septate, and although these septa are perforated by a central pore (so the cytosol can

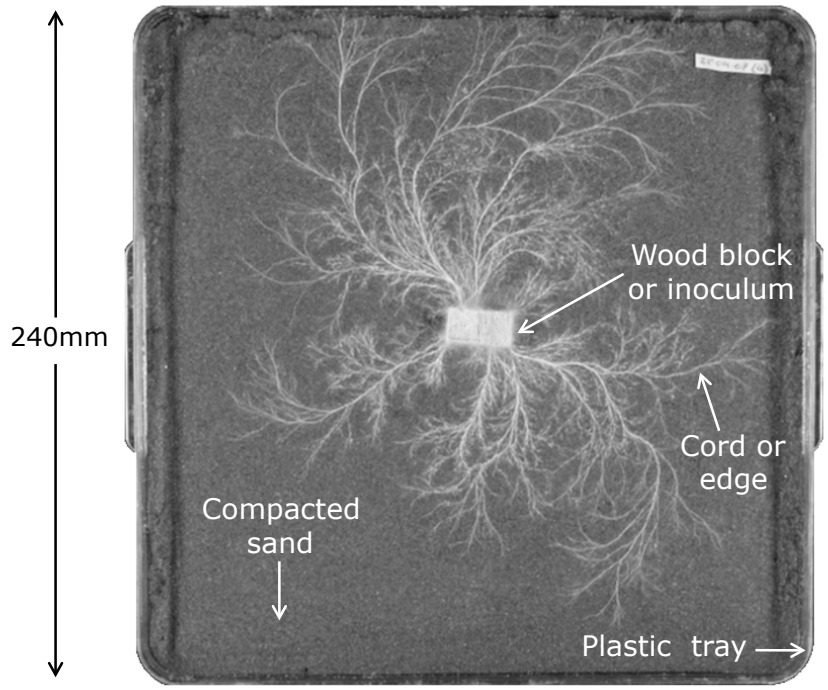

Figure 2.1: **Microcosm and mycelium of *Phanerochaete velutina***

flow between adjacent cells), a swelling at the septal wall or dome-shaped membrane covers the pore, so in these species the nuclei do not travel among adjacent cells [66]. Although we think it is reasonable to model a fungal mycelium as a network of tubes, it is worth noting that pores can be quickly blocked by nearby Woronin bodies or organelles following damage [114]. Furthermore, closing septal pores will alter the hydraulic conductance of that part of the network, and may redirect or halt mass-flows.

As some hyphae expand and mature, other regions of the mycelium regress. The process of autophagy (self-eating) appears to be critical to enabling fungi to forage effectively in highly heterogeneous environments, as by this process they can recycle redundant material to support new growth [77, 78, 81, 146]. While some hyphae are consumed by the process of autophagy, others undergo a limited form of differentiation, as hyphal aggregates form specialized, high-conductivity channels within root-like structures known as rhizomorphs or cords. [50]. Crucially, these structures are well-insulated from the environment due to the presence of a tough,

hydrophobic rind [42, 49, 115, 156, 157]. Rhizomorphs have a thick melanized rind, and the whole organ extends from the tip [157]. Mature mycelial cords also have hydrophobic rinds, but the whole organ does not extend apically; rather, it develops behind a mycelial margin of diffuse hyphae, each of which extends apically [33].

The internal anatomy of cords is believed to be similar for all basidiomycetes [48, 49, 75, 94, 116, 157]. In all cases, cords form behind a front of normal apically-extending hyphae, with the degree of hyphal aggregation within the growing front varying interspecifically [157]. Within the growing front both large and smaller diameter hyphae are normally present, with many branches and anastomoses interconnecting both hyphal types. Close to the growing front, large diameter hyphae appear to contain cytoplasm, with progressive cellular disorganisation and appearance of empty vessel hyphae with distance from the front [48, 49, 157]. The extent to which mature cords have a clear structure varies interspecifically, but in *P. velutina* and many other species, the central region (the inner medulla) is distinct because it contains numerous rigid, hollow vessel hyphae, with very few septal pores [75, 94, 116]. There is interspecific variation in hyphal size and the relative dimensions of the cortex and medulla, but the general structured pattern of cords or rhizomorphs is similar in all basidiomycetes [48]. Vessel hyphae typically have a diameter of 10 - 15 μm, and the inner medulla is known to be the path of translocation for radioisotopes [43]. In contrast to the inner medulla, the outer medulla contains loosely packed hyphae which are only about 2 μm wide (see Fig. 2.2).

Whilst direct uptake and intra-hyphal nutrient diffusion may be sufficient to sustain short-range local growth when resources are abundant [146], long-distance translocation is required to deliver nutrients at a sufficient rate to growing tips, particularly in non-resource restricted fungi that are too large to distribute nutrients through diffusion alone [37, 38, 39, 41, 56, 63, 75, 116, 197, 198]. Remarkably little is known about the mechanism(s) underpinning such long-distance nutrient translocation, or the quantitative contribution of different potential transport pathways, such as cytoplasmic streaming, vesicle transport or mass flow, to net fluxes and overall nutrient dynamics [49, 81, 115]. There is abundant evidence that fluid flows within

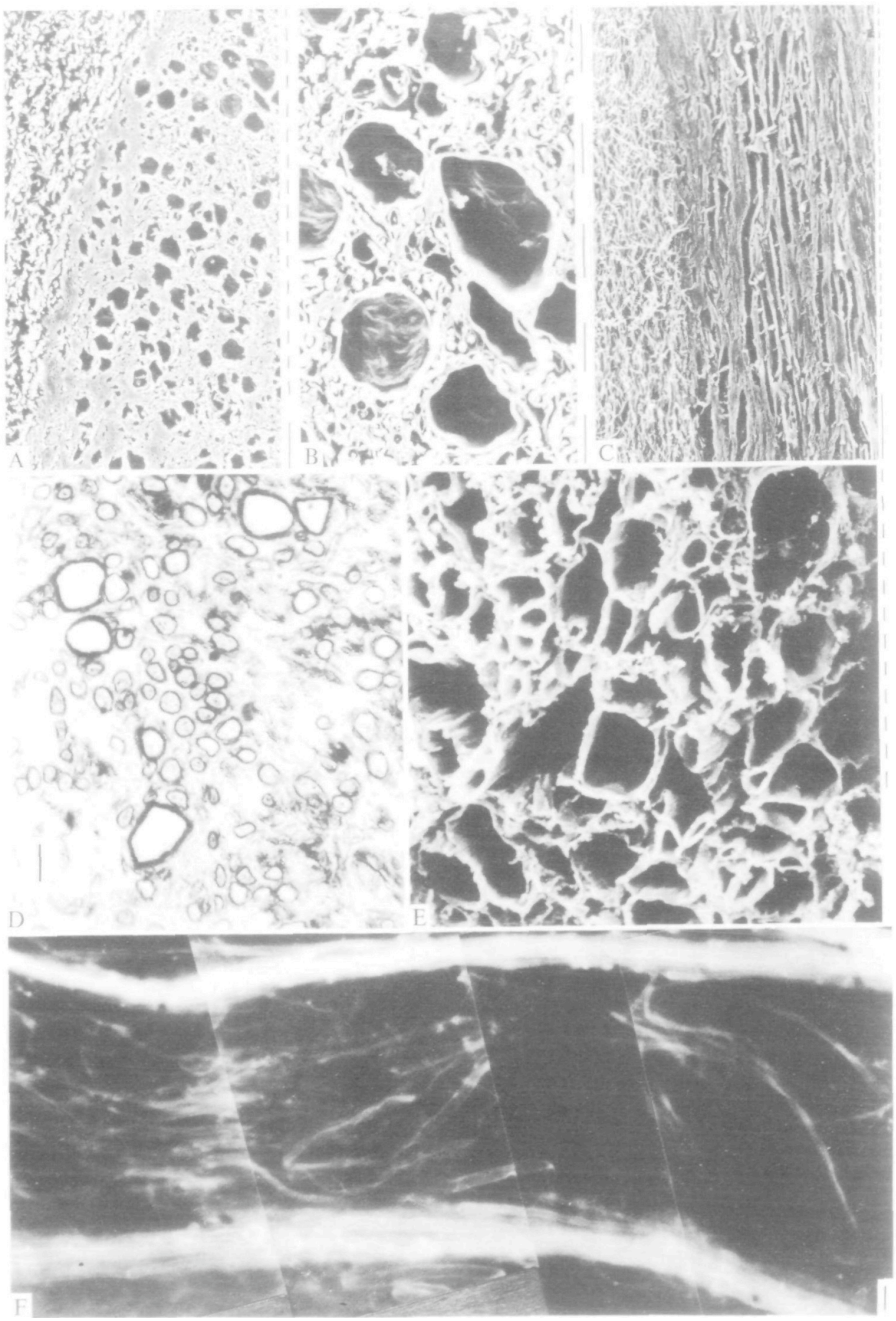

Figure 2.2: **Scanning electron micrographs, taken from [75]** (A-C) Scanning electron micrographs of rhizomorphs of *Armillaria mellea*. (A) Transverse section of medulla showing two distinct regions. Scale bar $10\mu m$. (B) Transverse section showing details of inner medullary region, including wide diameter vessel hyphae. Scale bar $10\mu m$. (C) Longitudinal section of medullary region. Scale bar $10\mu m$. (D-E) Transverse sections of mature cords of *Phallus impudicus*. (D) Light micrograph. Scale bar $10\mu m$. (E) Scanning electron micrograph. Scale bar $1\mu m$. (F) Mycelium of Serpula lacrimans stained with 001% (w/v) sodium fiuorescein and photographed with U.V. radiation. Scale bar $20\mu m$.

fungal networks are critical to the transport process [4, 5, 42, 43, 49, 115, 126, 130, 147, 191, 198, 208], and our modelling approach is to conceive of the mycelium as a network of connected tubes.

A critical observation is that regardless of intra-hyphal concentration gradients, mass flow only takes place when water is able to exit the translocation pathway through either localized exudation (e.g. *Serpula lacrymans*), evaporation, or by moving into a region of new growth. In this section we present a model for quantifying the last of these phenomena, which we have termed growth-induced mass flow. By way of physical analogy consider a rigid tube filled with salty water that is blocked at one end by a semi-permeable membrane, while the other is blocked by a thin rubber cap. If this apparatus is submerged in water, the osmotic gradient across the semi-permeable membrane will induce turgor pressure, and the pressure within the tube will force the rubber cap to begin to bulge outwards. As aqueous fluids are essentially incompressible, the column of fluid within the tube can only move forward at the same rate as the rubber cap, and this movement indicates the presence of a pressure gradient (Fig. 2.3a).

Injected oil droplets in individual hyphae of *Neurospora* provide evidence for this kind of growth-coupled mass flow, as in the apical compartment the average rate of movement ($\sim 0.2\mu\text{ms}^{-1}$) matches the rate of tip extension [126]. Likewise, nuclei in the apical compartment of mature hyphae of wild-type or mutant *Neurospora crassa* migrate towards the growing tips at the same rate (on average) as the tips extend [154]. Such movement would be consistent with mass flow driven by the continuous sub-apical water influx required to sustain volume increases at the tip during growth. Taken together, these lines of evidence suggest growth-coupled mass flow may have a significant role in water and nutrient translocation in larger mycelial systems.

Model development

To quantify the scale of growth-induced mass flow we developed two models, the

'uniform model' and the 'time-lapse model', and applied these models to measured examples of mycelial growth. To obtain a sample of fungal networks, Jessica Lee and Mark Fricker (Department of Plant Sciences, Oxford) allowed *P. velutina* to grow over experimental microcosms for a four week period, taking photographs every three days. They then used an image analysis program to convert the sequence of photographs into a sequence of networks, comprising cords of measured length and volume. Given the measured volumes and changes in volume, we used these models to calculate a flow or current for each edge. The currents calculated by the uniform model reflect the topology of the network. The time-lapse model produces an estimate for the minimum flow of material that is consistent with the measured changes in volume, under the assumption that the inoculum is the sole source of water and nutrients.

We found that the cords with higher currents or higher speeds of mass flow were more likely to increase in thickness than the other cords (see Section 2.7). This suggests that our model is correctly identifying the high current cords, since thickening the high current cords is an efficient way to remodel a fungal network. This follows because increasing the thickness and conductance of any cord will reduce the cost of overcoming viscous drag, but it is much more efficient to thicken cords which carry large currents rather than thickening the cords with small currents.

Before outlining the models of growth-induced mass flows, it may be helpful to define some basic terminology. By definition a network is a collection of nodes together with the edges that connect those nodes. A node that is connected to a single edge is called a 'tip', and we refer to all other edges as 'cords'. By this definition a cord is a cylindrical, linear structure, while any branching fungal form is described as a network of cords. We use letters such as i and j to index nodes, and pairs of letters ij index the edge (or cord) between nodes i and j. In this section two models are described that can be unfolded over a given network: the 'uniform model' and the 'time-lapse model'. Both models take as their inputs experimentally determined networks extracted from images; how these image data are used to calculate currents differs between the two cases. Furthermore, both models have been defined for water

uptake at a single location (the inoculum), but could be adapted for growth involving more than one source of nutrients and water.

The thickness of branches on a tree are related to their position within the structure. For example, the trunk is predictably thicker than any of the branches. The uniform model was designed to assess whether or not the thickness of cords relates to their position within the network structure in an analogous fashion. As we are interested in seeing whether or not we can predict the thickness of cords, this model throws away all detail about the thickness of cords (but not their lengths) and supposes they are of uniform thickness. It calculates currents by supposing that all tips grow at the same rate. Given any network, the output of the uniform model is a 'current' for each cord. This quantity reflects the topological location of the cords, and the currents predicted by the uniform model reflect the number of tips 'downstream' from each of the given cords (see Fig. 2.4a). As well as studying fungi, we could also apply the uniform model to trees, representing each leaf with a unit sink, while the trunk is the source. The cross-sectional area of each branch of a tree is approximately proportional to the number of leaves supported by that branch [133, 170, 173], so there is a very high correlation between the currents assigned by the uniform model and the thickness of branches on a tree. In the case of fungal networks, we found that cords with a large current tend to be thicker than cords with a small current.

While the uniform model calculates currents by assuming that all tips grow at the same rate, the time-lapse model uses observed changes in volume between successive pairs of aligned networks. We effectively derive a minimal set of currents that are consistent with the measured growth. A key principle behind the time-lapse model is that if an object (e.g. a thickening cord) is composed of incompressible material, the rate of increase in the volume of that object must equal the rate of flow into that object minus the rate of flow out of that object. Growth requires the flow of materials, and the time-lapse model was designed to quantify the extent to which changes in volume generate mass flows through the supporting mycelial network. The currents we will calculate represent a minimal total flux, found by calculating

the unique set of currents that account for the observed changes in cord volume, while minimising the work required to overcome viscous drag.

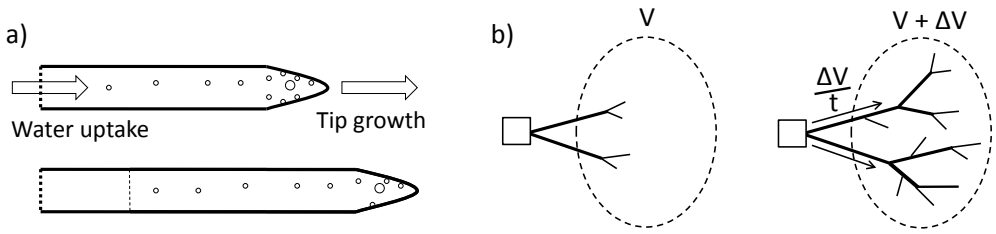

Figure 2.3: **Physical principles of growth-induced mass flow. (a)** Turgor pressure is induced by an osmotic gradient at the site of water uptake. Vesicles (circles) move towards the tip faster than it recedes, while the cytosol behind the growing tip moves forward at the rate of tip growth [126]. The conservation of volume dictates that as the tip expands, fluid flows towards the tips from the site of water uptake. This mass flow demonstrates the presence of a pressure gradient. **(b)** Suppose that a fungus grows out of an inoculum (square) and into a region (oval). Some of the material that becomes part of the fungi may come from within the oval region. The rest of the material must have travelled along the cords (edges) that cross the region's boundary. If the volume of fungi within the region increases by ΔV over a period of time t, and none of the material is drawn from within the region, it follows that the average current flowing into the region is $\frac{\Delta V}{t}$. Furthermore, if the total cross-sectional area of the boundary crossing cords is a, the mean velocity of flow will be $\frac{\Delta V}{at}$.

2.2 Modelling Fluid Flows: The Uniform Model

The 'uniform model' described in this section takes as its input an empirically observed fungal network, where each cylindrical cord in the network has a measured length. We have called it the uniform model because we assume uniform conductance (cross-sectional area) throughout the network, and assume a unit current outflow at every tip.

The rules governing the uniform model are as follows:

1. We assume unit growth at every tip, so there is a unit current flowing towards each tip.

2. The net current flowing away from the inoculum is equal to the total number of tips. In other words, water uptake occurs at the inoculum, and the rate of water uptake equals the total rate of growth.

3. All cords have the same resistance per unit length. In other words, the conductance of each cord is inversely proportional to its length.

Current effectively enters the network at the inoculum (source) and exits at the tips (sinks). Elsewhere the currents of an incompressible fluid must obey Kirchhoff's law, which states that the total current flowing into a point must equal the total current flowing out. In other words, the net current must be zero. It follows that where w_i is the net current flowing out of node i,

$$w_i = \begin{cases} -1 & \text{if node } i \text{ is a tip} \\ m & \text{if node } i \text{ is the inoculum (where } m \text{ is the number of tips)} \\ 0 & \text{otherwise.} \end{cases} \tag{2.1}$$

Note that the net current at the inoculum is positive, because the flow is directed away from the inoculum. Basic circuit theory tells us that the current in a cord is equal to the pressure drop times the conductance. We can use this fact to sum the currents that flow in or out of node i, so we have

$$\sum_j (p_i - p_j)\kappa_{ij} = w_i, \tag{2.2}$$

where p_i is the pressure at node i and κ_{ij} is the conductance of the cord between nodes i and j. In the uniform model,

$$\kappa_{ij} = \begin{cases} 0 & \text{if nodes } i \text{ and } j \text{ are not directly connected, and} \\ 1/l_{ij} & \text{if there is a cord } ij \text{ of length } l_{ij}. \end{cases} \tag{2.3}$$

As we shall see in the following section, if we are given the conductance of each cord and the net current flowing out of each node, we can uniquely determine the pressure difference between any pair of nodes, and hence we can uniquely determine the currents in the network.

2.3 Pressure Gradients, Hydraulic Conductance, Current and Velocity

The relationships between pressure gradients, hydraulic conductance, current and velocity are fundamental to understanding fluid flows in plants and fungi. We note,

however, that there is no close analogy between flows in open-ended plant vessels which are permeable along their lengths and close-ended fungal vessels which have hydrophobic coatings along their length. In plants, concentration gradients draw water from the companion cells in the surrounding tissue into, and out of, the phloem vessels all along their lengths. By contrast, fungal cords have hydrophobic coatings, and we suppose that such cords do not directly draw fluid from their surrounding environment (in our model, water uptake only occurs at the inoculum). In plants one expects flow between two points to be explained by a chemical potential difference. Similarly, in fungi there is a chemical potential difference between the environment and the hyphae responsible for water and nutrient uptake, and the fungus must do work to maintain such osmotic gradients [4, 5, 16, 128]. However, flows between two points *within* the fungus need not be caused by chemical potential differences between those points. The physical effects of growth, turgor pressure and fluid incompressibility may suffice to create flows across the mycelium.

The models in this chapter make no assumptions concerning the mechanisms of fungal growth: fluid incompressibility means that volume is conserved regardless of the mechanisms driving fungal fluid flows. We make the simplifying assumption that the inoculum is the sole source of extra fluid, and the presence of this fluid enables the volume change we observe in the growing fungus. Of the possible set of current flows consistent with the observed changes in volume, we parsimoniously identify the unique flows which minimize energy losses to resistance. Since the fluid flows within fungi are laminar (see Section 2.8), it is appropriate to apply the Hagen-Poiseuille equation, which accurately describes the laminar flow of incompressible fluids along an insulated tube.

By definition (and by analogy with Ohm's law) the current in a cord must be equal to the pressure drop times the conductance [141, 173, 194]. The size of the conducting vessels within a cord does not vary significantly with the size of the cord. We are therefore motivated to assume that all cords contain tubes of some fixed radius, and that the number of tubes within a cord is proportional to its cross-sectional area. The Hagen-Poiseuille equation tells us that the total current f through

a cord comprised of n tubes will satisfy the equation

$$f = \Delta P \kappa = \Delta P \frac{n\pi r^4}{8\eta l} = \sigma \Delta P A, \tag{2.4}$$

where ΔP is the pressure drop between the ends of the cord, κ is the hydraulic conductance of cord, r is the radius of the tubes, η is the dynamic viscosity of the fluid, l is the length of the cord, A is the cross-sectional area of the cord and σ is a constant of proportionality. The conductance of a cord is proportional to the number of tubes it contains, and if we assume a constant density of tubes, conductance is proportional to cross-sectional area.

Viscosity, velocity and laminar flow

To assess whether the flows in fungi are laminar, we first estimate the Reynolds number (Re). This is defined as the ratio of inertial to viscous forces [141], that is

$$\mathrm{Re} = \frac{\rho v d}{\eta}, \tag{2.5}$$

where ρ is the density of the fluid (approximately equal to that of water: $1\mathrm{gml}^{-1}$), v is the mean velocity of the fluid, d is the diameter of the hypha or transport vessel, and η is the dynamic viscosity of the fluid. The viscosity of cytoplasm is reported to be similar to that of water, $1\mathrm{gs}^{-1}\mathrm{m}^{-1}$ [85], but the fluids within fungi could plausibly be as viscous as 1.5 M sucrose solution, which has a viscosity of $7\mathrm{gs}^{-1}\mathrm{m}^{-1}$ [16]. Here we use a value of $\eta = 2\mathrm{gs}^{-1}\mathrm{m}^{-1}$.

The velocity of fluid flow and the diameter of the tubular vessels within the cords may vary considerably throughout the fungi, but even the most extreme of the plausible values yield a Reynolds number several orders of magnitude smaller than one [126]. This tells us that smooth, laminar flow is occurring [126, 141, 194].

Calculating the pressure at each node

Recall that the current in a cord is equal to the pressure drop times the conductance

of the cord. That fundamental relationship implies Equation (2.2), which states that for each node i,

$$\sum_j (p_i - p_j)\kappa_{ij} = w_i,$$

where p_i is the pressure at node i, w_i is the net current flowing out of node i and κ_{ij} is the conductance of the cord between nodes i and j. This relationship between the pressure and net current at each node can be summarized by defining the following symmetric matrix $\mathbf{A}$:

$$\begin{aligned} A_{ii} &= \sum_k \kappa_{ik} \quad \text{and} \\ A_{ij} &= -\kappa_{ij}. \end{aligned} \tag{2.6}$$

Letting $\overline{p}$ be the vector form of the pressures p_i and $\overline{w}$ the vector form of the currents w_i, we know by Equation (2.2) that $\overline{p}$ satisfies the equation

$$\mathbf{A}\overline{p} = \overline{w}. \tag{2.7}$$

Since each row of $\mathbf{A}$ sums to zero, $\mathbf{A}$ has no inverse and we cannot uniquely determine $\overline{p}$. However, it is the pressure differences which are of interest, not the absolute value of $\overline{p}$. We are therefore free to fix the pressure at any one node. Once we have done this, Equation (2.7) uniquely determines the pressure at every other node. More specifically, suppose that our network contains N nodes. In that case Equation (2.7) represents a system of N linear equations in N unknowns, but as each row and column sums to zero, the N'th equation is a linear combination of the other $N-1$ equations. Setting $p_N = 0$ gives us a system of linear constraints on the values for $p_1, \ldots, p_{N-1}$, namely

$$\begin{pmatrix} A_{11} & \cdots & A_{1(N-1)} & A_{1N} \\ \vdots & \ddots & \vdots & \vdots \\ A_{(N-1)1} & \cdots & A_{(N-1)(N-1)} & \\ A_{N1} & \cdots & & A_{NN} \end{pmatrix} \begin{pmatrix} p_1 \\ \vdots \\ p_{N-1} \\ 0 \end{pmatrix} = \begin{pmatrix} w_1 \\ \vdots \\ w_{N-1} \\ w_N \end{pmatrix}. \tag{2.8}$$

This is equivalent to the following system of linear constraints on the values for $p_1, \ldots, p_{N-1}$,

$$\begin{pmatrix} A_{11} & \cdots & A_{1(N-1)} \\ \vdots & \ddots & \vdots \\ A_{(N-1)1} & \cdots & A_{(N-1)(N-1)} \end{pmatrix} \begin{pmatrix} p_1 \\ \vdots \\ p_{N-1} \end{pmatrix} = \begin{pmatrix} w_1 \\ \vdots \\ w_{N-1} \end{pmatrix} \tag{2.9}$$

plus an additional equation

$$A_{(N-1)1}p_1 + A_{(N-1)2}p_2 + \ldots + A_{(N-1)(N-1)}p_{N-1} = w_N. \tag{2.10}$$

Because the rate of water uptake is equal to the rate of growth, the total in-current is equal to the total out-current. In other words, $\sum w_i = 0$. We therefore know that $w_N = -w_1 - \ldots - w_{N-1}$. We can use Equation (2.9) to eliminate each of the w_i (as $w_i = A_{i1}p_1 + A_{i2}p_2 + \ldots + A_{i(N-1)}p_{N-1}$), and this shows that Equation (2.10) is redundant. In other words, given that the total in-current is equal to the total out-current, Equation (2.9) is sufficient to determine our solution. It contains $N-1$ linear equations in $N-1$ unknowns, and in the case of a connected network (where $\sum_j \kappa_{ij} \neq 0$ for all i) Equation (2.9) uniquely determines the current in each edge.

2.4 Modelling Fluid Flows: The Time-Lapse Model

Each experiment yielded a sequence of eleven digitized networks. Unlike the uniform model, the time-lapse model does not assume that the tips are growing at constant rate. Instead we calculate currents by looking at how each network changes from one time-step to the next. The networks in each sequence must be aligned, and all nodes are considered to be present at all times (so some nodes in a network may not be connected to any edges/cords). We are given the time-lapse t between the earlier and later networks, and each cord has a given length l_{ij}, a volume in the earlier network v^0_{ij} (though this volume may equal zero), and a volume in the later network v^1_{ij}.

To calculate the currents we must know the relative conductances of the cords, and the net current at each node. By Equation (2.4) the conductance of cords is

proportional to their cross-sectional area. Where σ is an arbitrary constant of proportionality and δ is small compared to the cross-sectional areas of the cords, the conductance κ_{ij} of cord ij is defined to be

$$\kappa_{ij} = \begin{cases} 0 & \text{if nodes } i \text{ and } j \text{ are not connected,} \\ \sigma a_{ij}/l_{ij} & \text{if } i \text{ and } j \text{ are connected in the earlier network, and} \\ \sigma\delta/l_{ij} & \text{if } i \text{ and } j \text{ are only connected in the later network.} \end{cases} \tag{2.11}$$

In the uniform model the inoculum is the source, and each tip is a sink. In the time-lapse model thickening cords are also sinks, while thinning cords and the inoculum are sources. Now, the volume of cord ij changes from v_{ij}^0 to v_{ij}^1 over a period of time t. Therefore the current flowing into ij must be $(v_{ij}^1 - v_{ij}^0)/t$ greater than the current flowing out of ij. As a simplifying assumption, we put half of edge ij's demand for current (sink) at node i, and half at node j. In other words, we suppose that the current flowing into node i is $(v_{ij}^1 - v_{ij}^0)/2t$ greater than the current flowing out of node i, and likewise for node j (see Equation 2.12).

In both the uniform model and the time-lapse model the conservation of volume leads us to suppose that the rate of water uptake equals the total rate of growth. Hence the net current at the inoculum must be such that the total net current is zero. There is one final consideration behind the definition of the net currents in the time-lapse model. To make an unbiased analysis of the relationship between current and changes in cross-sectional area, we calculate the current induced in cord $\alpha\beta$ by the changes in volumes of all the cords excluding cord $\alpha\beta$ and any of its immediate neighbours. When we are calculating the current in $\alpha\beta$, we disregard the changes in volume in the edges connected to nodes α and β, as it would not be appropriate to use information about the change in volume of $\alpha\beta$ (or its immediate neighbours) when that is what we are trying to predict. In other words, when we are calculating the current in edge $\alpha\beta$, we suppose that the net current flowing out of node i is

$$w_i = \begin{cases} -\sum_{j\neq i} w_j & \text{if node } i \text{ is the inoculum, and} \\ \\ \sum_{i,j\neq\alpha,\beta} \frac{v_{ij}^0 - v_{ij}^1}{2t} & \text{otherwise.} \end{cases} \tag{2.12}$$

Note that the first sum is over the set of all nodes, while the second sum is over the

set of all the cords ij directly connected to node i, excluding any cords connected to nodes α or β. As in the uniform model, we can use the conductance of each cord and the net current flowing out of each node to uniquely determine the pressure difference between any pair of nodes (see Section 2.3). Given the pressure drop between the nodes, we can use Equation (2.4) to uniquely determine the current in each cord. The currents that emerge from this calculation only depend on the empirically determined pair of networks, while the velocities and pressure gradients scale with the model parameters.

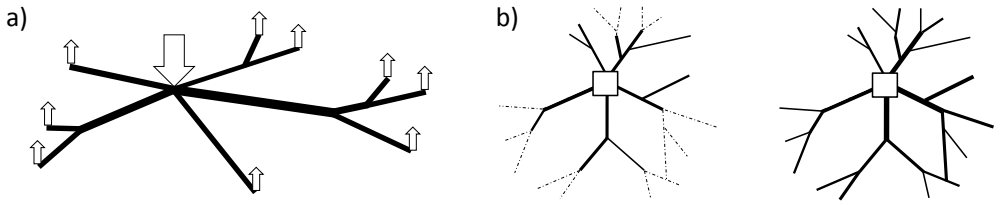

	a) Uniform Model	**b) Time Lapse Model**
Input	A network where each cord has a measured length, and one node is designated as the inoculum.	A pair of networks such that the 'earlier network' grows into the 'later network' over a period of time t. Each cord in these two networks has a measured length and volume.
Assumptions	1) Water uptake only occurs at the inoculum. 2) There is a unit current in every tip. 3) All cords in the network have unit resistance per unit length. 4) Fluid follows the path of least resistance. 5) The total volume of fluid is conserved.	1) Water uptake only occurs at the inoculum. 2) The current flowing into a cord minus the current flowing out of a cord equals the rate of change of volume for that cord. 3) The conductance of cords is proportional to their cross-section. 4) Fluid follows the path of least resistance. 5) The total volume of fluid is conserved.
Output	Each cord has a current. In tree-like networks, the current is equal to the number of cords 'downstream'.	Each cord has a current, and a mean velocity of mass flow. The current in the cord of interest is calculated without referring to the change in volume of that cord.

Figure 2.4: **Models of growth-induced mass flow.**

The parameters of the time-lapse model

Recall that by definition, the conductance of a newly formed cord is $\sigma\frac{\delta}{l_{ij}}$, where l_{ij} is the length of the cord and the parameter σ specifies the conductance per unit area for each cord in the network. The value of σ does not affect the calculated currents, as it is the relative conductance of cords that determines the distribution of currents. However, the pressure gradients predicted by this model will be inversely proportional to σ. We require the parameter δ because newly forming cords must have some conductance, or else they would not be connected to the rest of the network, and their growth could not induce currents. The precise value of δ is not significant, but the calculation of currents requires that all cords have a non-zero conductance.

Alternatively, we could remove the parameter δ by supposing that the conductance of cord ij is $\frac{\sigma(v_{ij}^0+v_{ij}^1)}{2l_{ij}}$. Since an extension of a cord can be represented as a new cord, the length of cords does not change. Hence this formula is equivalent to supposing that the cross-sectional area of cord ij is halfway between the cord's cross-section in the initial network and its cross-section in the resulting network. However, in that case cords that increase in size would carry more current than cords that do not, precisely because in this alternate model, cords that become large are assigned a larger conductance. This is undesirable (and not the method we employ in this chapter), because we want an unbiased estimate of current to correlate with changes in area. We could also have avoided the parameter δ by saying that newly forming cords are not part of the network, but in that case we would have to devise an additional algorithm for assigning out-current to the cords from which the new cords grow: something we 'get for free' by using our model with δ.

Varying the parameter values σ and δ does not significantly affect our calculation of the currents induced by growth. However, we do need to make a significant assumption concerning the relationship between conductance and cross-sectional area. We assume that conductance is proportional to cross-sectional area, because fungal cords are composed of bundles of transport vessels [106], and there is no evidence that the size of these transport vessels systematically varies with the size of the entire cord.

Furthermore, the assumption that the conductance of cords is proportional to their cross-sectional area is only of consequence when the network provides a number of alternate routes between the site of water uptake and the site of growth. Because our boundary conditions are fixed in terms of currents, the current in part of a branching tree will not depend on the conductance of the network. For example, if there is a certain current flowing out of the tips of a branching tree, the specified current has to flow through a given sequence of cords regardless of their conductance, as in the absence of loops there is only one route from trunk to tip. In practice, the fungal networks we are studying are composed of branching trees connected to a net-like core. Within the net-like structure more current will tend to flow through the larger cords, as fluids naturally follow the 'path of least resistance'.

2.5 Digitizing Empirical Fungal Networks

Experimental microcosms

Cultures of *P. velutina* (DC.) Parmasto were maintained in the Department of Plant Sciences, University of Oxford, by Mark Fricker and the members of his laboratory. The fungus was grown on 2% malt agar (2% no. 3 agar, 2% malt extract, Oxoid, Cambridge, UK) at $22 \pm 1^{\circ}$C in darkness in a temperature-controlled incubator. To create wood inoculae, 1cm^3 autoclaved beech (*Fagus sylvatica*) blocks (Bagley Wood sawmill, Kennington, UK) were placed on top of *P. velutina* mycelium in the agar culture plates and incubated at 22°C, to allow penetration of the blocks by hyphae. Inoculated wood blocks were placed on a compressed bed of 33% sterile white sand, 50% sterile black sand, and 17% water by weight in a 24-cm square culture dish. Two inoculated blocks were placed side-by-side in the centre of each dish and allowed to grow at $21 \pm 0.5^{\circ}$C in the dark. While the fungal networks were growing, we maintained the weight of the microcosm by spraying a fine mist of water droplets to replace any moisture that had been lost by evaporation.

As well as relying on the fungal networks produced by other members of the

group, I also grew some fungi myself, and to improve the contrast between the fungi and the microcosm I suggested that the medium in the trays should be changed. Instead of using glassy and reflective black sand, we switched to using 75% white sand, 5% charcoal powder and 20% water by weight.

Producing digital networks from the experimental microcosms

The growing mycelium was photographed every three days, and the sequence of images was manually marked to record the location of nodes or junctions, as well as the presence or absence of edges. The cords were not sufficiently well resolved to make direct measurements of their diameter from the digitized images. However, the reflected intensity, averaged over a small user-defined kernel at either end of the cord, correlated well with microscope-based measurements of cord thickness. The observed relationship between image intensity and thickness was therefore used to estimate cord thickness across the mycelium (linear regression, $r2 = 0.77$, $df = 195$, $p < 0.0001$). Mark Fricker was therefore justified in using this calibration to estimate the width of cords, while the volume of the mycelium was calculated by assuming that the cords were cylindrical [27, 81, 83, 113].

Three duplicate experiments, photographed over 36 days, were used to generate the results discussed in this section. In each case the inoculum and resource units were represented as a single node, as the internal mycelial organization was not visible. Estimates for the diameter of cords range from 48 μm to 480 μm, although fine hyphae and cords smaller than 100 μm are likely to be missing from the digitised network.

Measuring the total amount of growth

The total volume of the networks increased in an approximately linear fashion, so the proportional growth dropped significantly over time. The mean rate of increase over the first 21 days was $0.61\text{mm}^3\text{h}^{-1}$ in the first experiment, $0.51\text{mm}^3\text{h}^{-1}$ in the second experiment and $1.14\text{mm}^3\text{h}^{-1}$ in the third experiment (see Fig. 5.6). The total

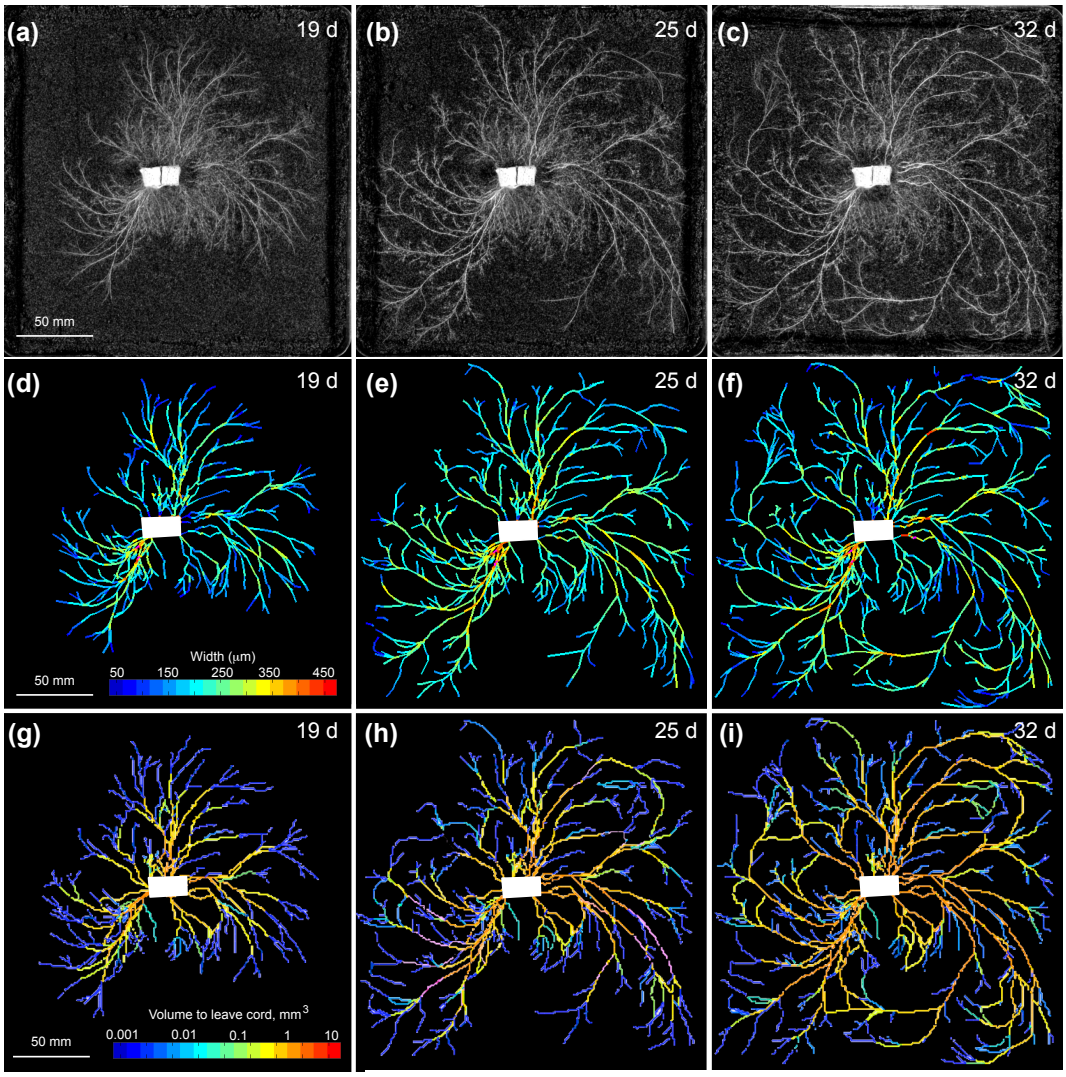

Figure 2.5: **Network development and predicted currents in *P. velutina*.** Images (a) to (c) show network development in *P. velutina* after 19 days, 25 days and 32 days respectively. The image intensity of cords was used to estimate their thickness, enabling the production of the weighted, digitized networks (d) to (f). These are colour-coded to show the estimated thicknesses of all sections of all edges, while the white block represents the inoculum. Images (g) to (i) are colour coded according to the total volume that has passed through each cord, as calculated by using the time-lapse model.

number of nodes and cords also increased in an approximately linear fashion, with around two cords and two nodes appearing every hour. The number of tips increased at about half that rate. In two of the experiments the total recorded volume of the network eventually decreased, and in all cases growth significantly slowed after 24 days. The time-lapse model was only applied while the fungi continued to grow at a rate of at least 0.1mm^3 per hour: a period of 21 days in Experiment 1, and 27 days in Experiments 2 and 3.

2.6 Distribution of Currents and Speeds

Both the uniform model and the time-lapse model indicate that many cords carried small currents while a few cords carried much larger currents. Furthermore, the cords that carry exceptionally large currents are sufficiently prevalent to dominate the mean. In fact, 78% of edges carry a current smaller than the mean, and 70% of edges carry a current that is smaller than half the mean. In other words, the distribution of currents is heavy tailed, and somewhat similar to the case of a branching tree where one branch carries a current of $1\text{mm}^3\text{s}^{-1}$, two branches carry currents of $1/2\text{mm}^3\text{s}^{-1}$, four branches carry currents of $1/4\text{mm}^3\text{s}^{-1}$, and so on, (see Fig. 2.6). Although edges with a large current tend to be thicker (see Section 2.7) the distribution of predicted speeds was also heavy tailed, with many small velocities and a few much larger velocities.

As well being interested in the general distribution of the currents and velocities in the network, we are also interested in the particular values predicted for the velocity of translocation. The speeds were calculated using the time-lapse model, with the additional assumption that 10% of the cross-sectional area of each cord was occupied by the interior of the vessels that carry mass flows ($\lambda = 0.1$). Under this assumption, 63% of edges carried a current whose mean velocity was less than $1\mu\text{m s}^{-1}$ (3.6mm hour^{-1}), and 5% of edges carried a current whose mean velocity was greater than $10\mu\text{m s}^{-1}$ (36mm hour^{-1}). This is comparable to the kinds of velocities observed experimentally in the major cords of *P. velutina* (see Chapter 4

for a detailed comparison between model predictions and experimental data in *P. velutina*). For comparison, velocities in the range $4.4 - 9.8\mu$m s^{-1} have been measured in *Armillaria mellea* [49, 95, 115], and velocities as large as $55 - 69\mu$m s^{-1} have been measured in *Serpula lacrimans* [42, 49, 115].

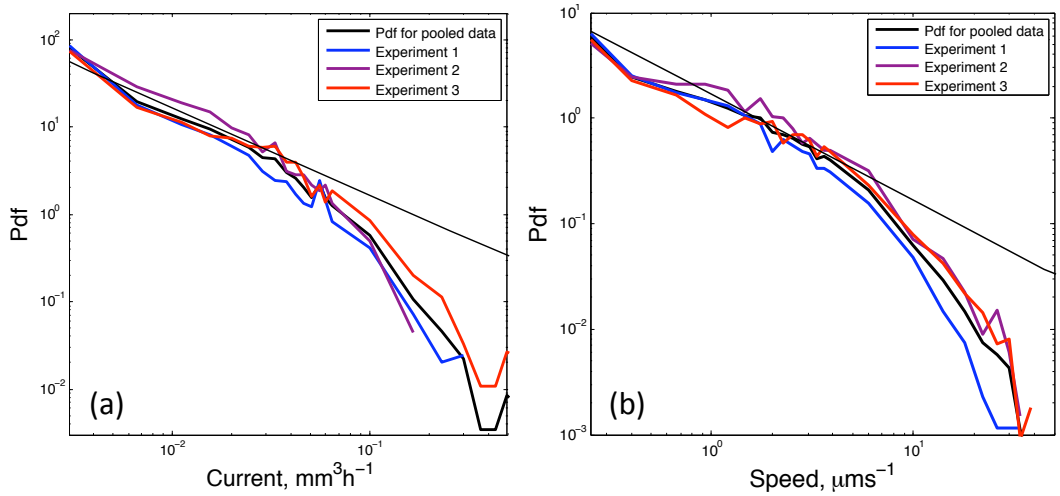

Figure 2.6: **Log-log plot of the probability density function (pdf) of (a) the predicted current, and (b) the predicted speed, calculated using the time-lapse model.** The black curve indicates the pdf for the pooled data, and the coloured curves indicate the pdfs for individual experiments. For comparison, the straight lines in figures **(a)** and **(b)** represent the pdf for a finite branching tree where each branch has the same cross-sectional area, and one branch carries a current of 1mm^{3}s^{-1}, two branches carry currents of $1/2$mm^{3}s^{-1}, four branches carry currents of $1/4$mm^{3}s^{-1}, and so on. The mean current in such a branching tree is dominated by the small fraction of cords which carry large currents, and the distribution of currents in the fungal networks is similarly heavy tailed. However, the pdf obtained from the time-lapse model decays more rapidly than a straight line, and the best fit power law is one that decays more rapidly than that of a branching tree, so the distribution of currents is somewhat more uniform than that extreme case.

We cannot yet provide a full quantitative analysis of the predicted velocities as our imaging techniques do not have sufficient resolution to map the fine hyphae that fan out ahead of the developing cords. Thus the actual volume increase at one of the notional 'tips' characterised here may well be several-fold greater than the volume of the terminal cord that we can measure. Nevertheless, the distribution of predicted currents should reflect the actual currents to the extent that the regions with large amounts of sub-resolution hyphal growth are also regions where the cords develop and thicken. For example, if we assume that 0.1mm^3 of fine hyphae grows

out of each tip each day, the predicted growth-induced currents would approximately double, as would the predicted velocities. This estimate of the volume of fine hyphal growth corresponds to each tip growing a fan of 10μm thick hyphae, which cover an area of 10mm^2 per day. If this coarse estimate of the quantity of fine hyphal growth is accurate, the volume of the digitised cords is only 50-60% of the total fungal volume.

2.7 Correlations Between Currents and Growth

Correlations between the cross-sectional area of cords and topological traits

To assess the relationship between the topological organisation of the network and the cross-sectional area of the cords, we used the uniform model, with unit current at each tip and a constant conductance per unit length, to calculate a current for each cord. When using the uniform model, the network at each time point is effectively an independent experiment, and in all cases the calculated currents were correlated with the measured cross-sectional areas. Note that because the currents predicted by the uniform model are based on the assumption that all the edges have the same thickness, this correlation is non-trivial. By definition, Pearson's linear correlation coefficient (r) between $X_1,\ldots,X_n$ and $Y_1,\ldots,Y_n$ is

$$r = \frac{\sum_i (X_i - \bar{X})(Y_i - \bar{Y})}{\sqrt{\sum_i (X_i - \bar{X})^2 (Y_i - \bar{Y})^2}}, \tag{2.13}$$

where $\bar{X}$ is the mean of $X_1,\ldots,X_n$. If the raw values X_i, Y_i are converted to ranked variables x_i, y_i, we can find the Spearman's rank correlation coefficient (ρ) between $X_1,\ldots,X_n$ and $Y_1,\ldots,Y_n$, as by definition

$$\rho = \frac{\sum_i (x_i - \bar{x})(y_i - \bar{y})}{\sqrt{\sum_i (x_i - \bar{x})^2 (y_i - \bar{y})^2}} \tag{2.14}$$

Over the set of all networks the mean value for r between the current as predicted by the uniform model and the cross-sectional area was 0.38 for Experiment 1, 0.42 for Experiment 2 and 0.49 for Experiment 3. When we pooled the data from all three experiments, the value of r was 0.41. Over the set of all networks, the mean value

for ρ was 0.34 for Experiment 1, 0.38 for Experiment 2 and 0.52 for Experiment 3, and when we pooled the data from all three experiments, the value of ρ was 0.37.

As we have three experiments, eleven time steps, and each network contains hundreds or even thousands of edges, the correlation between topology and edge thickness is statistically significant, with p-values much smaller than 1%. More specifically, if we randomly shuffle the values for edge thickness and recalculate the linear correlation coefficient, the absolute value of the new r value is smaller than absolute value of the original r value more 99% of the time. Given the number of data points even a small correlation coefficient can be statistically significant in this sense, but the correlation coefficient between the thickness of the edges and the current as calculated by the uniform model is quite large ($r = 0.41$), and this result compares favourably with previously used network measures. For example, it has been noted that as the mycelium is a kind of biological transport network, we might reasonably expect that edges with a large betweeness centrality will be thicker than edges with a low betweeness centrality [81]. That is to say, we can calculate the shortest path between each node and the inoculum, and the local betweenness centrality of a given edge is the fraction of those shortest paths which pass through the edge in question.

We might expect that edges with a high betweenness centrality will also be relatively thick, because if resource follows a shortest path (as we might expect in an efficient system), edges with a high betweeness centrality will need to carry more resources than edges with a low betweenness centrality. Over the set of all networks, the mean value for r between cross-sectional area and local edge betweeness was 0.31 for Experiment 1, 0.29 for Experiment 2 and 0.38 for Experiment 3. When we pooled the data from all three experiments, the value of r was 0.32. Over the set of all networks, the mean value for ρ between cross-sectional area and local edge betweeness was 0.29 for Experiment 1, 0.34 for Experiment 2 and 0.36 for Experiment 3. When we pooled the data from all three experiments the value of ρ was 0.30, and this level of correlation is statistically significant with a p-value smaller than 1%.

In each experiment we found that cords that were closer to the inoculum tended to be thicker, and older edges also tended to be thicker. These levels of correlation are statistically significant with p-values smaller than 1%. However, current was a significantly better predictor of area than either distance or age (see Fig. 2.7), as over the set of all networks the value of r between the distance to the inoculum and the cross-sectional area of each cord was -0.31, and the value of ρ was -0.29. Over the set of all networks (excluding those from the first time step, where, to our knowledge, all edges are the same age) the value of r between the age and cross-sectional area of the cords was 0.34, and the value of ρ was 0.33. As the relationship between current and area was reasonably consistent over time and over the three data sets (Fig. 2.7), it is possible to use this relationship to predict the size of cords given nothing more than the topology of a fungal network.

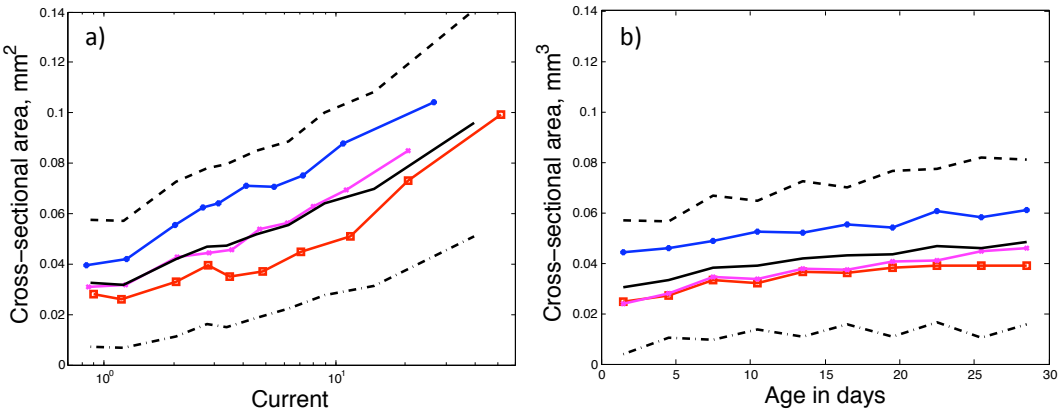

Figure 2.7: **Correlation between cord cross-sectional area and (a) the current predicted by the uniform model, or (b) cord age.** Both graphs indicate the mean over all networks (continuous black line), plus and minus one standard deviation (dashed black lines). Other lines indicate the mean values for individual experiments. **(a)** There was a positive correlation between cross-sectional area and the current in a cord, where current is calculated by applying a unit current to each tip, and we assume constant conductance per unit length. The graph was produced by taking data from all time steps and partitioning it into bins. The first data point marks the mean cross-sectional area for cords with a current of one or less (as was the case for 30% of cords), while the second cross marks the mean cross-sectional area for cords with a current between one and two (as was the case for 25% of cords). The remaining cords were partitioned into bins of equal size according to the calculated current, and each symbol marks the mean current and mean area of one of these bins. **(b)** Although most cords thicken over time, there was only a weak correlation between the age of a cord and its cross-sectional area.

Correlations between area and the total volume passing through cords

Having reviewed the results for the uniform model, we now turn our attention to the time-lapse model. At each time step we used the time-lapse model to calculate the total volume to pass out of each cord over its history to date. There was a strong, positive correlation between the total volume flowing through a cord and its cross-sectional area (Fig. 2.5 and 2.8). Pearson's linear correlation coefficient r was 0.55, 0.60 and 0.46 in the individual experiments, and $r = 0.45$ for the pooled data. This level of correlation is statistically significant with a p-value smaller much than 1%. Spearman's rank correlation coefficient ρ was 0.53, 0.58 or 0.63 in the individual experiments, and $\rho = 0.58$ for the pooled data. The vast majority of cords had a volume between 0.1 and 1mm^3, and if we select a random edge at a random point in time, there was a 56% chance that the total volume to leave the cord was greater than the volume of the cord itself.

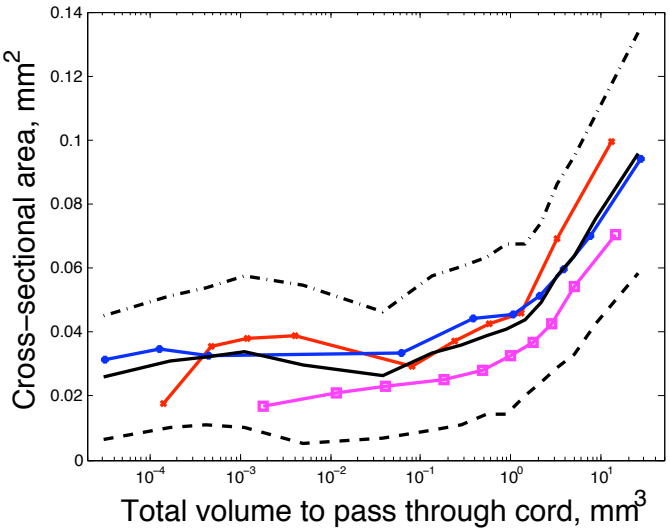

Figure 2.8: **Correlation between cross-sectional area and the total volume to pass through each cord.** The data from all experiments and all time steps were partitioned into bins according to the total volume of fluid that had passed through each cord over its history up to each time point. The mean area (continuous black line) plus and minus one standard deviation (dashed black lines) have been plotted for each bin. The coloured lines indicate the means for individual experiments.

Correlations between speed of flow and changes in cross-sectional area

Under the time-lapse model, cords that were predicted to carry a high velocity current were significantly more likely to increase in size than cords with a low velocity current (Fig. 2.9a). Pearson's linear correlation coefficient r between speed and change in area was 0.18, 0.15 or 0.31 in the individual experiments, and $r = 0.23$ for the pooled data. This level of correlation is statistically significant with a p-value much smaller than 1%. The value of ρ between speed and change in area was 0.24, 0.16 or 0.37 in the individual experiments, and $\rho = 0.29$ for the pooled data. There was also a positive correlation between current and change in cross-sectional area (Fig. 2.9b), with r equal to 0.46, 0.45 or 0.43 in the individual experiments, with $r = 0.39$ for the pooled data. The value of ρ was 0.43, 0.47 or 0.56 in the individual experiments, with $\rho = 0.49$ for the pooled data. Thicker cords tend to carry greater current, but this is to be expected precisely because thicker cords have greater conductance. However, we also found that given a pair of equally thick cords, the cord that is predicted to carry a greater current is the one that is more likely to thicken (see Fig. 2.10).

Cords with high current or velocity increase in area

Mass flows are required to maintain a sufficient supply of nutrients throughout the mycelium, but there are limits to the current that can pass along an individual hypha. High velocities require high pressure gradients, and increasing the velocity of flow means that greater amounts of work must be done by the fungi to overcome viscous drag. Thickening cords and the formation of high conductivity, aseptate channels may represent effective responses to these challenges.

By employing the time-lapse model we have observed a characteristic relationship between the total current that has passed through a cord, and the thickness of that cord (Fig. 2.5 and 2.8). We have also observed a correlation between the currents and the flux densities predicted by our model and the extent to which cords thicken over time (Fig. 2.9). Given the further assumption that *P. velutina* has

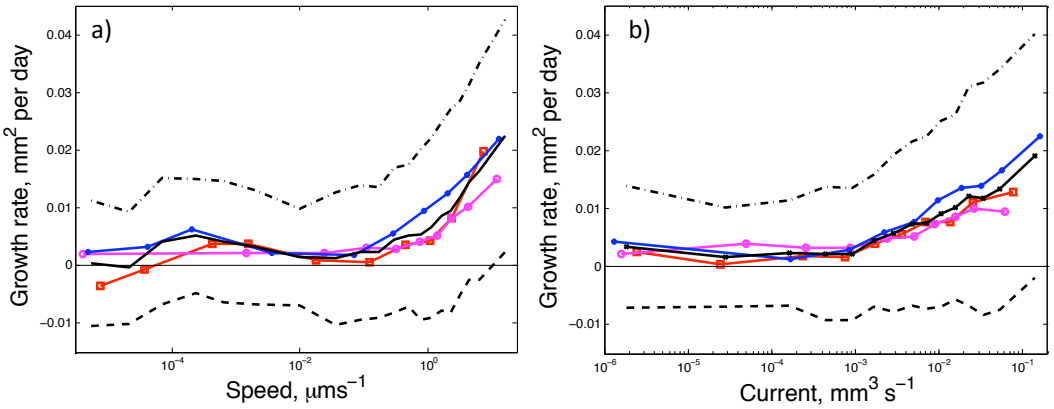

Figure 2.9: **Correlation between the change in cross-sectional area and the predicted flow.** The graphs were produced by using the time-lapse model to calculate the current in each cord. The flux density or speed of flow was calculated by assuming that the interior of the vessels carrying the mass flows occupies half the total cross-sectional area. These graphs were produced by partitioning the data from all experiments and all time steps into ten bins of equal size according to the calculated speed or current. Each point on the curve indicates the mean speed **(a)** or mean current **(b)**, plotted against the mean change in cross-sectional area for one of these bins. The solid black lines indicate the mean over all experiments, plus and minus one standard deviation (dashed black lines). The coloured lines indicate the mean values for individual experiments. Also note that the shape of the left hand half of each graph is not particularly significant, as all of the data points correspond to edges that carry a current at very low velocity, or with a negligible current.

adapted to reduce the work needed to overcome viscous drag, we should expect to see preferential thickening of the high current cords. This follows because, where there is a distribution of currents, significantly greater energy savings can be made by thickening the high current cords (as opposed to thickening the low current cords).

There is an element of positive feedback inherent in these observations, as any differential thickening of two parallel transport pathways will automatically increase flow through the cord with greater hydraulic conductivity. However, while we should expect that larger cords will carry greater currents (precisely because they have greater conductance), we have also found that given a pair of equally thick cords, the cord that is predicted to carry a greater current is the one that is more likely to thicken (see Fig. 2.10).

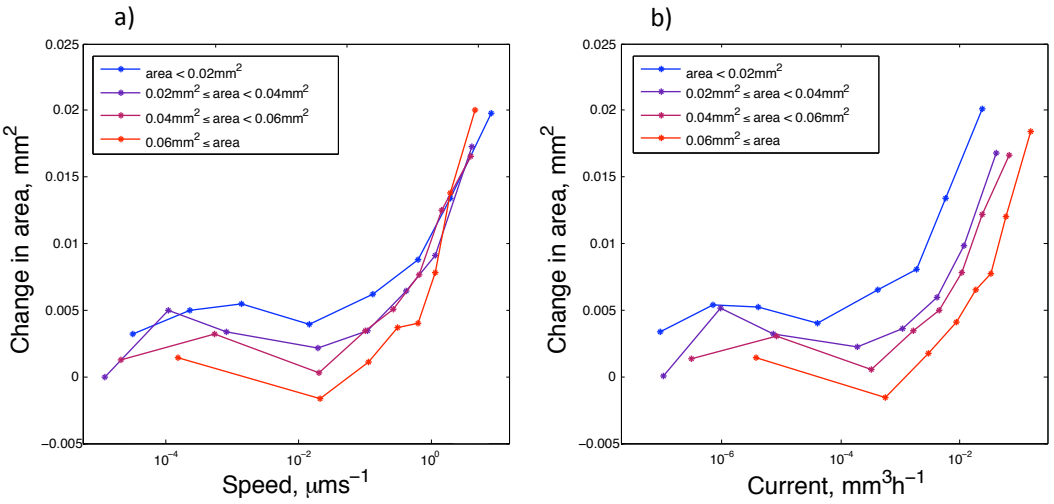

Figure 2.10: **Correlation between the change in cross-sectional area and the predicted flow for edges of similar thickness.** The data from all experiments and all time steps were partitioned into four bins according to the cross-sectional area of the cords. Each of these bins was then subdivided into ten subsets of equal size, according to the calculated speed **(a)** or current **(b)**. Each marker indicates the mean speed and mean change in cross-sectional area for one of these subsets. **(a)** Regardless of cross-sectional area, there was a similar relationship between the speed of flow in a cord and the change in cross-sectional area. Note that fewer large cords have a very low speed (less than 10^{-2}, say). **(b)** Larger cords tended to carry more current, but regardless of cross-sectional area, there was a qualitatively similar relationship between predicted current and the measured change in area.

2.8 Pressure Gradients and Wall Shear Stress

Pressure gradients and speed of flow

Suppose that a cord has a cross-sectional area a and carries a current f. The mean speed of flow within the cord as a whole will be f/a. However, only a fraction λ of the cross-sectional area of each cord will be occupied by the interior of the vessels that carry mass flows. Thus the mean speed within the vessels will be $f/\lambda a$. If we want to use our model to obtain estimates for the speeds of mass flow we need to choose an appropriate value for λ. Similarly, if we want estimates of the pressure gradients we need to choose a sensible value for the constant of proportionality between cross-sectional area and conductance per unit length. In each cord we have

$$v = \frac{f}{\lambda a}, \tag{2.15}$$

where v is the mean velocity of mass flow, f is the current through the cord and λa is the cross-sectional area through which the current passes. Furthermore, the Hagen-Poiseuille equation tells us that the pressure gradient dP/dx must satisfy the equation

$$\frac{\mathrm{d}P}{\mathrm{d}x} \equiv \frac{\Delta P}{l} = f\frac{8\eta}{n\pi r^4} = f\frac{\pi r^2}{\lambda a}\frac{8\eta}{\pi r^4} = v\frac{8\eta}{r^2}, \tag{2.16}$$

where η is the dynamic viscosity of the fluid, n is the number of tubes within the cord and r is the radius of each tube. Here we assume that the vessels within each cord have an internal radius of $6\mu m$, and in the following discussion we also assume that $\lambda = 0.1$. By adopting these parameter values we are effectively assuming that for every square mm of cord, there are 884 transport vessels.

Deriving pressure gradients from the time-lapse model

To estimate the pressure gradients needed to drive the flows predicted by the time-lapse model, we need estimates for the conductances of cords. Electron micrographs [75, 94, 116] indicate that a significant fraction of each cord is occupied by transport vessels that run along the length of the cord, and these vessels have an internal diameter in the range $10-15\mu$m (see Fig. 2.2). The fraction of each cord that is occupied by functional transport vessels is difficult to quantify, because of the technical difficulty in determining precisely where the flows are occurring. As a simplifying assumption, we suppose that all transport vessels an internal radius of 6μm, and that these vessels occupy 10% of the cross-sectional area of each cord. This results in an estimate of the hydraulic conductance of cords that is towards the lower end of the range of plausible conductivities [75], but as we shall see in Chapter 4, experiments with radio-labelled tracers give some empirical support for the figure of 10%.

To calculate the pressure gradient required to produce the velocities predicted by the time-lapse model, we also require an estimate for the viscosity of the moving fluids. Here we assume that the viscosity was $2\mathrm{gs}^{-1}\mathrm{m}^{-1}$ [75, 106, 126]. By Equation

(2.16), these values give us the relationship

$$\frac{\mathrm{d}P}{\mathrm{d}x} \approx 2v \times 10^{-4}, \tag{2.17}$$

where v is measured in μm s^{-1}, and dP/dx is measured in bar cm^{-1}. Our estimate of conductance per unit area tells us that maintaining a velocity of 1μm s^{-1} only requires a pressure gradient of around 2×10^{-4} bar cm^{-1}. This is very small compared to the hydrostatic pressure of hyphae, which is about $4-5$ bar [5, 126, 128, 134]. Pressure gradients of this scale could plausibly be maintained over tens or even hundreds of metres.

In *Neurospora crassa* the cytoplasm moves forward with the growing tips at a rate of $0.2-0.5\mu$m s^{-1}. Mass flows in the hyphae behind the tips typically reach 5μm s^{-1}, and currents as fast as 60μm s^{-1} have also been directly observed [126]. In *P. velutina* the highest reported velocities are around 900μm s^{-1} [198], though because the rind of cords is opaque, obtaining accurate estimates of velocity is a major challenge. Our estimate for the conductance of cords implies that maintaining a velocity as large as 900μm s^{-1} requires a pressure gradient of around 0.2 bar cm^{-1}. This is a significant pressure gradient compared to the hydrostatic pressure of hyphae, and without increasing the diameter of vessel hyphae, pressure gradients of this scale could only be sustained over a few tens of centimetres.

Deriving wall shear stresses from the time-lapse model

As a result of the friction between moving fluids and the static vessel walls, fluid flows induce wall shear stresses on the vessels within cords. A good estimate for the wall shear stress τ_v can be obtained using the formula

$$\tau_v = \frac{4\eta v}{r}, \tag{2.18}$$

where η is the dynamic viscosity of the fluid, v is the mean velocity of fluid flow and r is the radius of the vessels within cords [173]. Using the previously indicated values for η and r tells us that $\tau_v \approx v \times 10^{-3}$Nm^{-2}, where the mean velocity v is

measured in μm s^{-1}. By way of comparison, the wall shear stresses in mammalian arterial systems are in the range $0.2-2$Nm^{-2} [117, 164].

It is widely accepted that a local adaptive response to wall shear stress is a key mechanism that enables the optimization of mammalian vascular systems [117, 151, 152, 164, 173]. By analogy it is certainly plausible that hyphae could detect and respond to velocities of the order $100-1000\mu$m s^{-1}, as we estimate that mass-flows in the transport vessels moving at these velocities would induce wall shear stresses of the order $0.1-1$Nm^{-2}. Furthermore, experiments have indicated that hyphal tips exposed to flow rates of 400μm s^{-1} preferentially orient themselves towards the upstream of the flowing medium, and this tropic response may also occur at lower velocities, despite the absence of a detectable gradient in the pH or oxygen concentration of the flowing medium [144]. This strongly suggests that hyphae are sensitive to the asymmetry in the forces exerted on their exterior by the flowing fluid, though the molecular mechanisms involved have not been identified. It is therefore plausible that fungi are sensitive to the forces produced by fluid flows within the hyphae, especially if the velocity of fluid flow is as large as 100μm s^{-1}. Moreover, the wall shear stresses will significantly greater in the septal pores compared to the rest of the hyphae, because at that point the same current that is passing through the hyphae or transport vessels must pass though a smaller channel, which means the mean velocity of flow must be greater. If the mass-flows also pass through the much smaller vessels that are found within cords [75, 94, 116], or if the wall shear stress is detected at the septal pores, fungi could plausibly detect velocities of the order 10μm s^{-1}. It is less likely that fungi can detect the difference between currents with a mean velocity much smaller than this, as the corresponding changes in wall shear stress would be very modest.

Curvature and the Dean number

The curvature of vessels can have a profound effect on the fluid flows within them [194]. When fluid flows around a bend, inertial forces push against the outer wall,

and that is a force that is not present in the case of a straight, cylindrical tube. Flow in a curved cylindrical vessel is governed by two, dimensionless ratios. The first significant ratio is between the tube radius r and the radius of curvature R, and the ratio $\delta = \frac{r}{R}$ essentially summarizes the geometry of the tube. The second term, called the Dean number, captures the relative importance of inertial forces, and by definition

$$\mathrm{De} = \sqrt{\delta}\,\mathrm{Re}, \tag{2.19}$$

where Re is the Reynolds number [194]. In the case of a straight tube $R = \infty$, so $\mathrm{De} = \delta = 0$. In general, the velocity profile and distribution of wall shear stress within a vessel does not differ significantly from the case of a straight tube unless r is similar to R, or $\mathrm{De} \gg 1$. In the major curved arteries of the human vascular system the values for δ are in the range 0.02 - 0.2, and the Dean numbers are in the range 20 - 700 [194]. In that parameter range curvature has a considerable effect, and significant errors may arise if we model the fluid flows without considering the effect of curvature. In the case of fungal networks the Reynolds number is very small, as is the radius of the transport vessels, so $\mathrm{De} \ll 1$, $r \ll R$, and the effect of curvature on fluid flows is negligible.

Turgor pressure and intramural stress

As well as experiencing wall shear stress, the vessels within pressure driven vascular systems also experience intramural stress (see Fig. 2.11). This force per unit area is experienced throughout the vessel wall (and not just on the inside surface), as the vessel must resist the tendency to expand or burst. Where ΔP is the transmural pressure (that is, the pressure drop between the inside and outside of the vessel), r is the internal radius and d is the thickness of the vessel wall, the Law of Laplace [172] tells us that the mean intramural stress is

$$\tau_P = \Delta P \frac{r}{d}. \tag{2.20}$$

Hyphae and transport vessels are subject to several atmospheres of pressure (about $4-5$ bar) [5, 126, 128, 134], and the fluids within these structures flow at a very modest rate [4, 75, 83, 95, 126, 147, 188, 189, 198]. Consequently, the intramural stress will be orders of magnitude greater than the shear wall stress. Nevertheless, this does not mean that it is implausible that fungi are sensitive to changes in wall shear stress. The cell wall must be rigid enough to withstand the intramural stress [99, 127, 135, 202], but proteins embedded in the lipid membranes of tethered organelles, or in the septal pores (where the velocity of flow and the wall shear stress will be greatest) may be sensitive to the scale of flows within a fungal network.

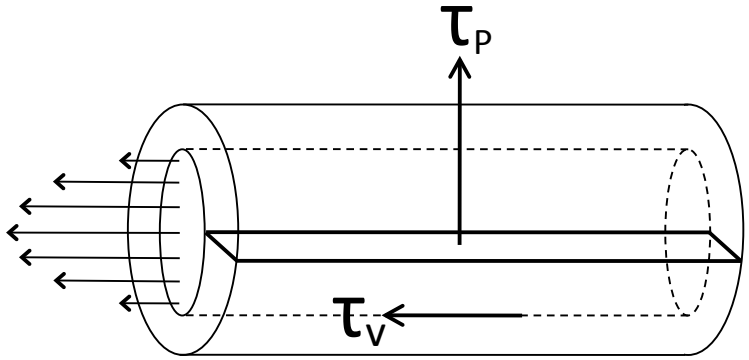

Figure 2.11: **Stress and pressure in a cylindrical vessel.** Intramural stress is the mean force per unit area within the vessel wall, perpendicular to both the axis of the vessel and the vessel's circumference. Wall shear stress is the force per unit area experienced on the inside of the vessel, as the moving fluid tends to stretch the vessel in the direction of flow.

2.9 The Biological Significance of Growth-Induced Mass Flows

Transport velocities are determined by the network architecture

The network architecture will affect the velocity of growth-induced mass flows. In this regard, it is instructive to compare a growing linear network to a growing branching tree (see Fig. 2.12).

Suppose that the tips in both of the model networks illustrated in Fig. 2.12 grow a unit distance from the inoculum per unit time, and that each edge has unit length and

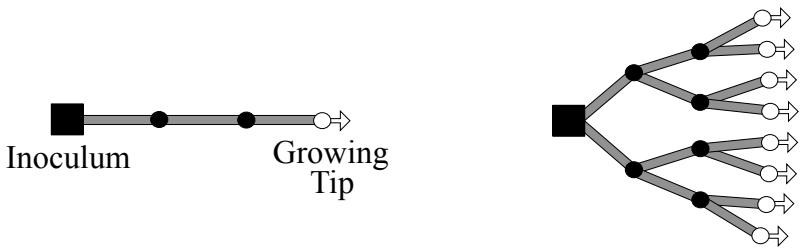

Figure 2.12: **Network structure and the efficacy of growth-induced mass flows as a means of transport.** Two contrasting examples of networks with growth-induced mass flows.

volume. In the case of a linear network, and in the absence of diffusion, it will take n units of time for the resource to travel from the inoculum to the nth edge. It follows that if the resource in the network is consumed over the time-scale n, growth-induced mass flows in a linear network cannot supply resource over length scales greater than n. In the case of a branching tree where each edge has the same volume, the total volume of the nth generation is greater than the total volume of all the preceding generations (see Fig. 2.12). This implies that it will take less than a unit of time for resource to travel from the inoculum to the nth generation. Provided that the concentration of resource at the inoculum remains sufficiently high, there is no limit to the size of branching tree that can be filled with resource by growth-induced mass flows, even if the local rate of resource delivery is high. Also note that if mothers and daughters have the same cross-sectional area (as is the case for individual hyphae), the velocity of flow in a vessel with n generations of offspring will be 2^n times greater than the rate of tip growth. In principle, this explains how water uptake and growth can induce mass flows at speeds that are orders of magnitude greater than the rate of individual tip growth.

More generally, the cross-sectional area of the supporting network is critical. If water uptake only occurs at the inoculum, the current out of the inoculum is equal to the volumetric rate of growth, and the mean velocity of flow by the inoculum is inversely proportional to the total cross-sectional area of edges by the inoculum. This suggests that a major advantage of autophagy is that it reduces the cross-sectional

area of the supporting mycelium, which increases the velocity of growth-induced mass flows. For example, if the branching network in Fig. 2.12 were such that the total cross-sectional area of each generation were constant, at the point in time where there are n generations, the current in each member of the i'th generation would be 2^{n-i}, but the velocity would be constant throughout.

Our analysis suggests that the distribution of currents across fungal networks is somewhat akin to a branching network (see Fig. 2.6 a), with many cords carrying small mass flows, while some cords carry large mass flows. There is also quite a wide spread of velocities, with many edges carrying low velocity mass flows, and a few edges carrying high velocity mass flows (see Fig. 2.6 b). As we shall see in Chapter 4, most edges are predicted to carry a small current and contribute little to the transport process, but the patterns of translocation observed using radio-tracers can be explained by the few edges that are predicted to carry a significant current.

Growth-induced mass flows do not deliver resource to the tips

In the absence of diffusion, the fluid exactly at the growing tips is never replaced by the fluid entering at the inoculum. Rather, the fluid in the apical compartment advances along with the tip itself [126]. This implies that growth-induced mass flows alone cannot supply resource to the growing tips: diffusion and specific transport mechanisms are essential for transporting resource across the newest generation of edges. On the other hand, growth-induced mass flows can account for a significant fraction of the long range movement of resource. The extent to which growth-induced mass flows can account for long range transport in fungal networks is investigated in some detail in Chapter 4.

The importance of localizing water uptake

Fungal colonies form integrated hydraulic systems, and so the increase in volume that results from hyphal growth requires an equivalent uptake of water, or a reduction in the volume of another part of the mycelium. Furthermore, the efficiency of

growth-induced mass flows as a means of transport depends upon the fact that water uptake and growth are spatially separated. If growth occurs exclusively at the tips, but water uptake occurs throughout the network, growth-induced mass flows will still occur, but the scale of advection will be significantly reduced. In the case of a linear network, switching from water uptake at one end to water uptake throughout the edge will half the scale of mass-flow (see Fig. 2.13).

In the case of a branching network the change in the scale of advection can be much greater. For example, if water uptake occurs throughout a branching network of unit cross-sectional area (see Fig. 2.13) the velocity of mass flow can equal the velocity of tip growth v in every edge (regardless of its generation). That contrasts dramatically with the case where all the water uptake occurs in the trunk, as in the case where there are n generations in total and the edge in question is part of generation i, the mean velocity is $v2^{n-i}$ rather than v (see Fig. 2.13).

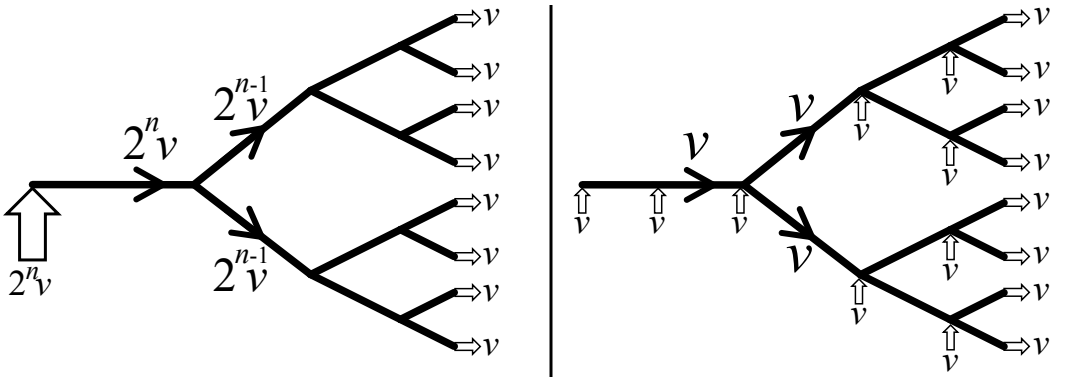

Figure 2.13: **Velocities in a branching network with different patterns of water uptake.** If water uptake only occurs in the trunk, the velocity of mass flow halves from one generation to the next. If water uptake occurs throughout the network, the velocity may be constant throughout.

In actual fungal networks water uptake occurs over entire regions, and not just at individual points. Nevertheless, in species such as *P. velutina*, patches of fine hyphae (where growth and water uptake both occur) are connected by cords with a tough, hydrophobic barrier [49, 75, 94, 115, 116, 156]. These rinds insulate the hyphae within cords from their environment, and they are a distinctive feature of most foraging fungi. The tough, outer layers of such structures offer some protection

from mycophagic insects, but our analysis suggests that the hydrophobic coating may also facilitate transport by increasing the distance between water uptake and growth.

Summary of results

In conclusion, we note that the incompressibility of the fluids within fungi ensures that there is a rapid global response to local fluid movements. Furthermore, velocity of fluid flow is a local signal that can convey quasi-global information about the role of a cord within the mycelium. We have found a correlation between the thickening of cords and the speeds or flux densities predicted by our model (Fig. 2.9a and 2.10a). Similarly, there was a positive correlation between predicted current and the thickening of cords (Fig. 2.9b and 2.10b). This is consistent with the plausible assumption that *P. velutina* has evolved to reduce the work needed to overcome viscous drag, as significantly greater energy savings can be made by preferentially thickening the high current cords.

The speeds predicted by our model are consistent with experimental data. For example, a radiolabelled source of carbon has been measured moving at a velocity $7\mu ms^{-1}$ away from the inoculum [95]. This is the same order of magnitude that our model predicts for a major cord, and in Chapter 4 I show that there is good empirical agreement between our model and experimental data using radio-labelled tracers. We note that the pressure gradients required to produce the predicted flows are very modest (see 2.8). More importantly, contrary to previous analyses [115, 128, 155], we suggest that intrahyphal concentration gradients are not strictly necessary for the production of mass flows.

In the phloem in plants water leaves the surrounding tissue and enters the phloem vessels at points where they contain a high concentration of osmolytes, and water exits the phloem at points of low osmolyte concentration [16, 76, 141, 186, 211]. In contrast the major transport vessels of fungi are insulated from their environment, and so regardless of any concentration gradients across the mycelium, fluid does not

enter or exit the cords along their length. The uptake of water and the maintenance of turgor pressure require an osmotic gradient between the hyphae and their environment, but the incompressibility of aqueous fluids ensures that there will be a mass flow from the sites of water uptake to the sites of growth, regardless of the concentration gradients within the mycelium itself. We also suggest that local responses to flux density and nutrient concentration might govern the development of these remarkable self-organizing, efficient, adaptive, growing transport networks.

In the next chapter we develop mathematical machinery to analyze how resource will become dispersed over a network, given the mean velocity of flow and the dispersion coefficient for each edge, and given that the resource in question is consumed at a given rate. This enables us to further probe the plausibility of the claim that growth-induced mass flows account for a significant proportion of the long range transport in fungal networks, as we can use that machinery to make predictions about how resource will become distributed over time, given the currents predicted by the time-lapse model. As we shall see in Chapter 4, we can use the time-lapse model and the machinery described in Chapter 3 to make predictions about how a radiolabelled tracer will spread out over time, and have found that there is compelling agreement between our model predictions and the empirical data.

Chapter 3

Advection, Diffusion and Delivery: Mathematical Methods

In this chapter we consider the distribution of resource that arises when material moves through a network by a process of advection and diffusion, while the resource in question is lost or delivered out of the network at some given, local rate. We are interested in solving such systems of equations, as they arise in the models of transport within fungal networks that are describe in Chapters 4 and 5. In this chapter we develop two methods that enable us to calculate how the concentration in a network of tubes will vary in both space and time. The first approach is to operate in Laplace space, which is computationally efficient, because of the wide range of velocities in the networks we are interested in analyzing. In particular, we are interested in analyzing fungal networks that shrink and grow over time, so we also develop an algorithm for finding the concentration of resource in a network where the cross-sectional areas of the edges vary continuously over time. The second method employs a finite difference scheme, but simple versions of this approach are computationally problematic in the case where the advective velocities are much greater in some parts of the network than others.

3.1 Fundamental Equations and Assumptions

Many biological, geophysical and technological systems involve the transport of material over a network by advection and diffusion [29, 45, 121, 131, 168]. Indeed, fluid

transport systems are found in the vast majority of multicellular organisms, as the component cells of such organisms require resources for metabolism and growth, and diffusion alone is only an effective means of exchange at microscopic length scales [125]. Molecules of interest are carried by advection and diffusion through the cardio-vascular networks of animals [25, 26, 90, 91, 121, 173, 175, 184, 194], the mycelial networks of fungi [49, 115], the xylem and phloem elements of tracheophytes (vascular plants) [133, 166, 186], and various body cavities of many different animals. For example, oxygen is transported through the lungs of mammals and the trachea of insects, while suspension feeding animals (including sponges, clams, brachiopods, many arthropods, fish, ascidians and baleen whales) pass water through various chambers of their bodies, capturing the organic particles that are needed for survival [125]. Similar mechanisms of transport are also found in geological and technological systems, such as rivers and drainage networks [14], gas pipelines, sewer systems and ventilation systems.

In all of these cases the particles of interest diffuse within a moving fluid, which is constrained to flow within a given network. The bulk movement of fluid is referred to as advection, convection or mass flow, and in general the fluid in question travels with a mean velocity that varies over the network. The mean velocity of fluid flow may vary by several orders of magnitude, as, for example, the velocity of human blood drops from 1m s^{-1} in the aorta to around 1mm s^{-1} in the capillaries [46, 61]. Given a network and a distribution of velocities, we may wish to calculate how an initial distribution of resource changes over time. For example, we might want to know how a patch of pollutant will spread within a drainage network [29, 131, 168], how a drug will spread within the cardio-vascular system [25, 26, 90, 91, 173, 175, 194], or how nutrients will be translocated within a fungal network [49, 115]. In Chapter 4 I use the mathematical machinery developed in this chapter to model the translocation of nutrients in a fungal network, and in Chapter 6 I use the same machinery to model the delivery of glucose via a vascular network.

Koplik et. al. [122] describe an effective method for calculating the exact moments of the transit times for a neutral tracer across an arbitrary network that contains

a flowing medium, but which initially contains no tracer. The moments of transit time are of particular interest, because they reflect the structure of the network, and the range of paths that can be followed through the network. For example, if fluid is pumped through porous rock and there is a large variance in the transit time of a pulse of tracers, that can constitute evidence for the presence of a reservoir of fluid which an individual tracer may or may not enter [122, 167, 168]. We have advanced the methods of Koplik et. al. to handle resources that may be consumed or delivered out of the network, while the resource that remains in the network moves by advection and diffusion. More specifically, we suppose that each edge in the network has a local delivery rate R_{ij}, which represents the probability per unit time that any given unit of resource will be consumed, lost or delivered out of the network.

The fact that the material of interest is consumed *en route* is critical to understanding nutrient delivery. In most existing models of optimal transport networks, the network is optimized under the constraint that there must be at least some minimal flow to each sink node of the network [14, 58, 68, 68, 160, 161, 203], but the consumption of the resource carried by the fluid flow is not itself an integral part of the model. To understand nutrient transport we think that the appropriate modelling technique is to couple advection, diffusion and delivery, as the process of delivery is a key component of the dynamics, especially in capillary beds or leaves, where we might expect to see significant variation in nutrient concentrations [90, 123, 194, 207]. The effect of including a delivery term can be significant and somewhat counter-intuitive: we will see, for example, that there are circumstances in which increasing the number of blood vessels in a region can actually decrease the amount of glucose that is delivered to that region (see Section 6.3). This problem is of particular bio-medical interest, as glucose delivery is essential to the survival of tumours and healthy tissue [51, 54, 121, 175, 194]. As we shall see, to appreciate how the number of blood vessels in a region effects the total rate of glucose delivery, it is essential that we consider both the rate of delivery of resource out of the network and the topology of the transport network itself.

To enable the assessment of the transport characteristics of arbitrary networks, with velocities that may vary over several orders of magnitude, we have developed a method that utilizes the Laplace transform.

Preliminary assumptions

We are interested in calculating the distribution of resource across a network of tubes, where the resource in question has a molecular diffusion coefficient D_m, and where we are given four essential properties for each edge in the network (see Fig. 3.1). The edge connecting nodes i and j has:

1. A cross-sectional area, denoted $S_{ij}(t)$. We initially assume that $S_{ij}(t)$ is piece-wise constant, though in Section 3.8 we consider the more complex case where $S_{ij}(t)$ varies continuously.

2. A length, denoted l_{ij}. As the location of the nodes does not vary over time, l_{ij} is constant.

3. A mean velocity, denoted $u_{ij}(t)$. This represents the mean velocity of the fluid in the edge, and we say that $u_{ij}(t)$ is positive if and only if the current flows from node i to node j (so $u_{ij}(t) = -u_{ji}(t)$). By assumption, for each edge ij, $u_{ij}(t)$ is piece-wise constant.

4. Finally, we suppose that resource in edge ij is delivered out of the network at a rate R_{ij}, so if a particle is in ij for a short period of time Δt, the probability that it is delivered out of the network in that time is $R_{ij}\Delta t$.

We are interested in quantifying motion along the length ij. The term u_{ij} tells us the mean velocity of particles, but while there is a global value for the molecular diffusion coefficient D_m, the dispersion coefficient $D_{ij}(t)$ may be different for each edge. This is because the value of $D_{ij}(t)$ captures the tendency of adjacent particles to spread out within ij: they not only diffuse along the length of the transport vessels that comprise the edge ij, but they also spread out because they can diffuse between

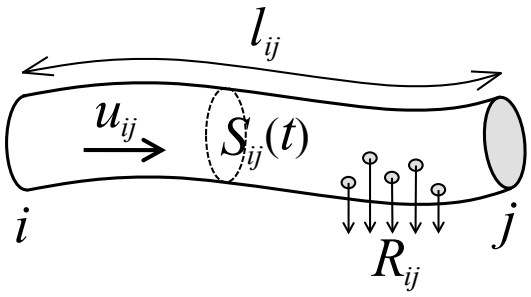

Figure 3.1: **Properties of a single edge in a resource distribution network.** $S_{ij}(t)$ denotes the cross-sectional area of edge ij at time t, l_{ij} denotes the length of the edge, resource and medium flows along the edge with a mean velocity $u_{ij}(t)$, and resource is delivered out of the network at a rate R_{ij}. Note that resource travels *along* each edge (and into other edges) by advection and diffusion, but the total rate at which resource in the edge is delivered *out* of the network is simply R_{ij} times the quantity of resource present in the edge. Also note that we do not need to assume that the edges in our network are straight, but we do assume that a single length scale l_{ij} captures the distance that particles must travel to move from i to j.

the slow moving fluid by the edge of the vessels, and the relatively fast moving fluid in the centre of each vessel.

If we consider the case where each edge ij is composed of some number of cylindrical tubes of radius r_{ij} (see Fig. 3.2), and if the Reynold's number is small, we can calculate $D_{ij}(t)$ by using Taylor's dispersion coefficient for laminar flow in a cylindrical tube [6, 185]. This formula tells us that

$$D_{ij}(t) = D_m + u_{ij}(t)^2 \frac{r_{ij}^2}{48 D_m}. \tag{3.1}$$

In the case of a vascular network r_{ij} is simply the lumen radius of the edge ij, so we have $S_{ij} = \pi r_{ij}^2$. In plants, fungi or neural tissue each edge in the transport network can be modelled as a bundle of cylindrical tubes; in which case r_{ij} is the characteristic radius of the component transport vessels, and S_{ij} is the total cross-sectional area of the transport vessels.

Fundamental equations

We suppose that resource decays while it moves across the network by advection and diffusion, resulting in changing concentrations at every point. We will only consider

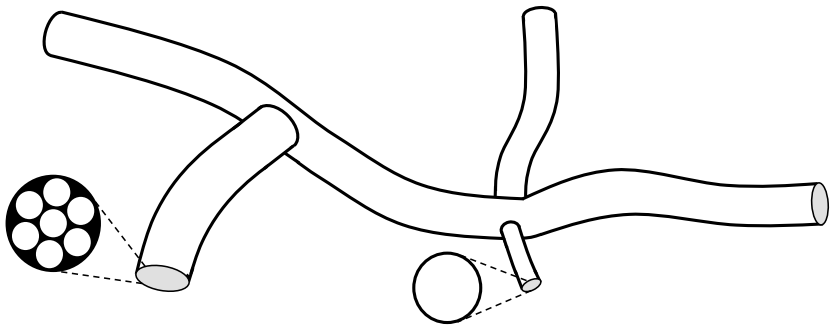

Figure 3.2: **Properties of an arbitrary resource distribution network.** Each edge in the network comprises a single vessel or a bundle of transport vessels, and each edge has a length l_{ij}, a total cross-sectional area $S_{ij}(t)$, a mean velocity of flow $u_{ij}(t)$ and a local delivery rate R_{ij}. Each edge also has a dispersion coefficient $D_{ij}(t)$, as described by Equation (3.1). Note that the values of $D_{ij}(t)$ depend on the molecular diffusion coefficient D_m, the velocities $u_{ij}(t)$ and the radius of the transport vessels within the edge ij. The nodes represent the point of contact between the edges: we assume that there is perfect mixing at each node, and we require a consistent concentration at node i whether we consider it to be one end of edge ij, or one end of any other edge connected to node i.

longitudinal coordinates along the edge ij, using real numbers x to denote distances from node i, where $0 \leq x \leq l_{ij}$. Each edge contains a quantity of resource, which must satisfy the one-dimensional advection-diffusion-delivery equation

$$\frac{\partial q_{ij}}{\partial t} + R_{ij}q_{ij} + u_{ij}\frac{\partial q_{ij}}{\partial x} - D_{ij}\frac{\partial^2 q_{ij}}{\partial x^2} = 0, \tag{3.2}$$

where q_{ij} is the quantity of resource per unit length, u_{ij} is the mean velocity, D_{ij} is the dispersion coefficient and R_{ij} is the rate at which a unit of resource is lost, or delivered out of the network. In other words, at time t and location x, the amount of resource in a Δx long slice of the edge is $q_{ij}(x,t)\Delta x$. The distribution of resource within each edge will vary over space and time, but if there is no direct link between the nodes i and j, we let $S_{ij}(t) = 0$ and $q_{ij}(x,t) = 0$. This ensures that the sums in the following equations are properly defined for all pairs of nodes i and j.

Crucially, the concentration at node i must be consistent across the edges ij, ik, etc, and we let $c_i(t)$ denote the concentration at node i at time t (amount of resource per unit volume). For each edge ij we have

$$c_i(t) = \frac{q_{ij}(0,t)}{S_{ij}(t)} \qquad \text{and} \qquad c_j(t) = \frac{q_{ij}(l_{ij},t)}{S_{ij}(t)}, \tag{3.3}$$

where $S_{ij}(t)$ denotes the cross-sectional area at time t. We also assume that there is perfect mixing at the nodes, and that the nodes have an infinitesimal volume. In other words, the edge ij is only affected by the rest of the network via the concentrations at nodes i and j.

It follows from our assumptions that the concentration profile in edge ij is completely determined by Equation (3.2) together with the initial condition $q_{ij}(x,0)$ and the boundary conditions $S_{ij}(t)c_i(t)$ and $S_{ij}(t)c_j(t)$. By Fick's Law the rate at which resource leaves node i along edge ij is given by

$$J_{ij}(t) = \left[u_{ij}(t)q_{ij}(x,t) - D_{ij}\frac{\partial q_{ij}(x,t)}{\partial x}\right]_{x=0}. \tag{3.4}$$

Our framework can accommodate the case where resource is introduced at node i at some given rate $I_i(t) > 0$. If node i is not an inlet node (that is, a point where resource enters the network), the quantity of resource entering node i is equal to the quantity of resource leaving node i, so we have $I_i(t) = 0$. In either case, Equation (3.4) implies that the net rate at which resource leaves node i is

$$I_i(t) = \sum_j \left[u_{ij}(t)q_{ij}(x,t) - D_{ij}\frac{\partial q_{ij}(x,t)}{\partial x}\right]_{x=0}. \tag{3.5}$$

Note that we may be concerned with both the quantity of resource and the quantity of fluid that passes a given point per unit time. Henceforth the term current is reserved for the quantity of resource that passes a given point per unit time, while medium-current refers to the volume of the advecting medium that passes a given point per unit time.

Critical time scales for advection, diffusion and delivery

For an edge of length l, mean velocity $u > 0$, dispersion coefficient D and local delivery rate R, there are three critical time scales:

$$t_A = \frac{l}{u} \text{ is the time taken to advect across the edge,}$$

$$t_D = \frac{l^2}{D} \text{ is the mean diffusion time for the edge and}$$

$$t_T = \frac{1}{R} \text{ is the time scale of transport out of the edge.}$$

The ratio $\frac{t_D}{t_A} = \frac{ul}{D}$ is the macroscopic Péclet number for the edge [122, 194]. If $\frac{t_D}{t_A} \gg 1$ then advection is the dominant form of transport across ij, and almost all of the material that leaves ij will pass to locations downstream from ij. It is also generally true that in the case of high Péclet numbers large concentration gradients can persist within each edge [194]. If $\frac{t_D}{t_A} \ll 1$ then diffusion is the dominant form of transport across ij, which means that the concentration within ij will tend to vary smoothly from node i to j.

If $t_T \ll t_A$ and $t_T \ll t_D$, then the bulk of the resource will be delivered out of the transport network before it transits the edge in question. As a general rule, an efficient transport network will utilize resource over a time scale t_T which is similar to the time scales over which resource transits the network. For example, in the case of vascular networks, the oxygen affinity of haemoglobin varies with body size, and is related to the circulation time for the species in question [194, 203]. This makes sense, because if the oxygen affinity of haemoglobin were too low for a given body size, red blood cells would become deoxygenated too rapidly, and too little oxygen would be carried to the tissues distant from the heart and lungs. On the other hand, if a large proportion of the haemoglobin were to remain as oxyhaemoglobin throughout the vascular system, only a small fraction of the oxygen in red blood cells would be transported to the surrounding tissue.

3.2 Advection, Diffusion and Delivery in Laplace Space

By assumption, the resource in each edge of a given network is subject to advection, diffusion and delivery, as described by Equation (3.2). Given this system of fundamental equations we want to find the quantity of resource throughout the network, which may vary over time. It is convenient to follow the approach of

[122], which entails the application of the Laplace transform. This operation enables the efficient handling of the different time scales over which resource may move from one node to another, which is important, as the networks in question may contain resource that is carried at a wide range of different velocities. In particular, we take advantage of the following properties of the Laplace transform $\mathscr{L}\big(q_{ij}(x,t)\big) = \int_0^\infty q_{ij}(x,t)e^{-st}dt = Q_{ij}(x,s)$:

$$\mathscr{L}(\frac{\partial q_{ij}(x,t)}{\partial t}) = sQ_{ij}(x,s) - q_{ij}(x,0), \qquad \text{and} \tag{3.6}$$

$$\mathscr{L}(\frac{\partial q_{ij}(x,t)}{\partial x}) = \frac{\partial}{\partial x}Q_{ij}(x,s). \tag{3.7}$$

If u_{ij} and D_{ij} are constant over time, it follows from Equation (3.2) that

$$(s+R_{ij})Q_{ij} + u_{ij}\frac{\partial Q_{ij}}{\partial x} - D_{ij}\frac{\partial^2 Q_{ij}}{\partial x^2} = q_{ij}(x,0). \tag{3.8}$$

Furthermore, Equations (3.5), (3.6) and (3.7) imply that

$$\Upsilon_i(s) = \sum_j \left[u_{ij}Q_{ij}(x,s) - D_{ij}\frac{\partial}{\partial x}Q_{ij}(x,s)\right]_{x=0}, \tag{3.9}$$

where $\Upsilon_i(s)$ denotes the Laplace transform of $I_i(t)$, the net current flowing out of node i.

Zero initial conditions in an edge

We begin by considering an initially empty edge, before extending our results to the more complex case of non-zero initial conditions. We let $q_{ij}(x,0) = 0$, and consider the homogeneous case for Equation (3.8):

$$(s+R_{ij})Q_{ij} + u_{ij}\frac{\partial Q_{ij}}{\partial x} - D_{ij}\frac{\partial^2 Q_{ij}}{\partial x^2} = 0. \tag{3.10}$$

To find the steady state solution, we try a solution of the form $Q_{ij}(x,s) = e^{\lambda x}$. Equation (3.10) tells us that

$$e^{\lambda x}(s + R_{ij} + u_{ij}\lambda - D_{ij}\lambda^2) = 0.$$

It follows that for every s, there is some pair of constants A and B such that

$$Q_{ij}(x,s) = Ae^{\frac{u_{ij}+\alpha_{ij}(s)}{2D_{ij}}x} + Be^{\frac{u_{ij}-\alpha_{ij}(s)}{2D_{ij}}x}, \tag{3.11}$$

where

$$\alpha_{ij}(s) = \sqrt{u_{ij}^2 + 4D_{ij}(s+R_{ij})}. \tag{3.12}$$

Note that the Laplace variable s represents a rate, and that $\alpha_{ij}(s) = \alpha_{ji}(s)$ is positive, and dimensionally equivalent to speed. Roughly speaking, $\alpha_{ij}(s)$ represents the speed at which resource travels over the time scale $1/s$, with a correction term to account for delivery. Since s and D_{ij} are positive and R_{ij} is non-negative, we always find that $\alpha_{ij}(s) > |u_{ij}|$. In particular, when $s = \frac{u_{ij}^2}{4D_{ij}} - R_{ij}$, Equation (3.12) implies that $\alpha_{ij}(s) = \sqrt{2u_{ij}^2}$. The value of $\alpha_{ij}(s)$ depends on u_{ij}, D_{ij} and R_{ij} over most time scales, but for very short time scales ($s \gg \frac{u_{ij}^2}{4D_{ij}} - R_{ij}$) almost all the movement is due to diffusion, $\alpha_{ij} \gg u_{ij}$ and $\alpha_{ij}(s) \approx \sqrt{4D_{ij}(s+R_{ij})}$.

Equation (3.11) tells us that for any positive number s, we can find A and B and express $Q_{ij}(x,s)$ in terms of the quantity of resource at either end of the edge. For any given s, we denote the quantity of resource at the ends of each edge by

$$\begin{aligned} X_{ij}(s) &\equiv Q_{ij}(0,s) \quad \text{and} \\ X_{ji}(s) &\equiv Q_{ji}(0,s) = Q_{ij}(l_{ij},s). \end{aligned} \tag{3.13}$$

For each edge ij, it is convenient to define two, dimensionless ratios between time scales:

$$g_{ij} = \frac{u_{ij}l_{ij}}{2D_{ij}} \quad \text{and} \quad h_{ij}(s) = \frac{\alpha_{ij}(s)l_{ij}}{2D_{ij}}. \tag{3.14}$$

Setting $x = 0$ and $x = l_{ij}$ tells us that

$$\begin{aligned} X_{ij} &= A + B \quad \text{and} \\ X_{ji} &= Ae^{(g_{ij}+h_{ij})} + Be^{(g_{ij}-h_{ij})}. \end{aligned} \tag{3.15}$$

A, B, X_{ij}, X_{ji}, α_{ij} and h_{ij} are all functions of the Laplace variable s, but this dependence is omitted for the sake of clarity. Equation (3.15) tells us that

$$Ae^{(g_{ij}+h_{ij})} + (X_{ij} - A)e^{(g_{ij}-h_{ij})} = X_{ji}, \quad \text{so} \tag{3.16}$$

$$A = \frac{X_{ji}e^{-g_{ij}} - X_{ij}e^{-h_{ij}}}{2\sinh(h_{ij})} \quad \text{and likewise} \tag{3.17}$$

$$B = \frac{X_{ij}e^{h_{ij}} - X_{ji}e^{-g_{ij}}}{2\sinh(h_{ij})}. \tag{3.18}$$

Note that if u_{ij} is negative, the medium-current flows towards node i and the macroscopic Péclet number for the edge ij is $\frac{u_{ji}l_{ij}}{D_{ij}} = -2g_{ij}$ [122, 194]. Assuming that edge ij is initially empty, we can find $Q_{ij}(x,s)$ by substituting Equations (3.14), (3.17) and (3.18) into Equation (3.11), giving us

$$\begin{aligned} Q_{ij}(x,s) &= \frac{1}{2\sinh(h_{ij})}\left[\left(X_{ji}e^{-g_{ij}} - X_{ij}e^{-h_{ij}}\right)e^{\frac{(u+\alpha)x}{2D}} + \left(X_{ij}e^{h_{ij}} - X_{ji}e^{-g_{ij}}\right)e^{\frac{(u-\alpha)x}{2D}}\right] \\ &= \frac{1}{2\sinh(h_{ij})}\left[X_{ij}e^{\frac{ux}{2D}}\left(e^{\frac{\alpha(l-x)}{2D}} - e^{\frac{-\alpha(l-x)}{2D}}\right) + X_{ji}e^{\frac{-u(l-x)}{2D}}\left(e^{\frac{\alpha x}{2D}} - e^{\frac{-\alpha x}{2D}}\right)\right] \\ &= X_{ij}\frac{\sinh(\frac{l_{ij}-x}{l_{ij}}h_{ij})}{\sinh(h_{ij})}e^{\frac{x}{l_{ij}}g_{ij}} + X_{ji}\frac{\sinh(\frac{x}{l_{ij}}h_{ij})}{\sinh(h_{ij})}e^{\frac{x-l_{ij}}{l_{ij}}g_{ij}}. \end{aligned} \tag{3.19}$$

Given any Laplace constant s and the Laplace transform of the quantity of resource at either end of edge ij, Equation (3.19) tells us the Laplace transform of the quantity of resource at any point within edge ij. Equation (3.19) only applies when the initial condition of edge ij is zero, but as we shall see in the following section, we can use this equation to calculate the Laplace transform of the concentration of each node in a given network.

3.3 Advection, Diffusion and Delivery in an Initially Empty, Static Network

Having examined the case of a single edge, we now turn to the problem of coupling the edges of a network such that the concentrations vary continuously as we move from one edge to another. For each node i we let $C_i(s) = \int_0^\infty c_i(t)e^{-st}dt$. Assuming that the cross-sectional areas S_{ij} are constant, Equations (3.3) and (3.13) imply that for all edges ij we have

$$C_i(s) = \frac{X_{ij}(s)}{S_{ij}} \quad \text{and} \quad C_j(s) = \frac{X_{ji}(s)}{S_{ij}}. \tag{3.20}$$

Enforcing this equation ensures that the Laplace transform of the concentration at node i is consistent for all edges ij, ik, and so on. In general, we may not know the Laplace transform of the node concentrations $\bar{C}(s) = \{C_1(s), \ldots, C_m(s)\}$, where m is the number of nodes. However, given $\bar{I}(t) = \{I_1(t), \ldots, I_m(t)\}$ (the net current of resource leaving each node), we can calculate $\bar{\Upsilon}(s) = \{\Upsilon_1(s), \ldots, \Upsilon_m(s)\}$ (the Laplace transform of $\bar{I}$), and, in the following manner, calculate $\bar{C}(s)$. If we substitute Equation (3.11) into Equation (3.9), and note that $x = 0$, we find that

$$\begin{aligned}\Upsilon_i(s) &= \sum_j \left[u_{ij}\big(A+B\big) - D_{ij}\big(\frac{u_{ij}+\alpha_{ij}}{2D_{ij}}A + \frac{u_{ij}-\alpha_{ij}}{2D_{ij}}B\big)\right] \\ &= \sum_j \frac{\alpha_{ij}}{2}\big(B-A\big) + \frac{u_{ij}}{2}\big(A+B\big).\end{aligned}$$

Equations (3.14) and (3.15) imply that $A+B = X_{ij}$, and

$$B - A = \frac{1}{2\sinh(h_{ij})}\left[X_{ij}e^{h_{ij}} - X_{ji}e^{-g_{ij}} - X_{ji}e^{-g_{ij}} + X_{ij}e^{-h_{ij}}\right],$$

so we have

$$\Upsilon_i(s) = \sum_j \left[\frac{\alpha_{ij}}{2\sinh(h_{ij})}\left(X_{ij}\cosh(h_{ij}) - X_{ji}e^{-g_{ij}}\right) + \frac{u_{ij}}{2}X_{ij}\right]. \tag{3.21}$$

Equations (3.20) and (3.21) imply that

$$\Upsilon_i(s) = \sum_j \left[C_i(s)S_{ij}\left(\frac{u_{ij}}{2} + \frac{\alpha_{ij}}{2\tanh(h_{ij})}\right) - C_j(s)S_{ij}\left(\frac{\alpha_{ij}e^{-g_{ij}}}{2\sinh(h_{ij})}\right)\right]. \tag{3.22}$$

In other words, for each node i we have a linear equation in $C_1(s), C_2(s), \ldots, C_m(s)$. Hence where $\bar{C}(s)$ and $\bar{\Upsilon}(s)$ are column vectors, we thus have

$$\mathbf{M}(s)\bar{C}(s) = \bar{\Upsilon}(s), \tag{3.23}$$

where

$$\mathbf{M}_{ij}(s) = \begin{cases} \sum_k S_{ik}\left[\frac{u_{ik}}{2} + \frac{\alpha_{ik}}{2\tanh(h_{ik})}\right] & \text{if } i = j, \\ \frac{-S_{ij}\alpha_{ij}e^{-g_{ij}}}{2\sinh\left(h_{ij}\right)} & \text{otherwise.} \end{cases} \tag{3.24}$$

We refer to the matrix $\mathbf{M}(s)$ as the propagation matrix, and it contains a row and column for each node in the given network. Given $\mathbf{M}(s)$ and $\bar{\Upsilon}(s)$ we can calculate $\bar{C}(s)$ using various efficient algorithms, including the stabilized biconjugate gradient method (BiCGStab). In most cases this is the most efficient algorithm to use, as our matrix $\mathbf{M}(s)$ is non-symmetric and sparse [67].

Equation (3.12) implies that the diagonal elements $\mathbf{M}(s)$ are all positive. Furthermore, $\mathbf{M}_{ij}(s) = 0$ if and only if there is no edge between i and j, and the other off-diagonal elements are negative. We note that if there is resource at node j, it may be transported along ij, bringing resource to i and reducing $\Upsilon_i(s)$ (the Laplace transform of the net current flowing out of node i). Resource can only reach node i along the edges ij, ik, etc, so $\Upsilon_i(s)$ is completely determined by the concentration at i and the concentrations that flow through the nodes adjacent to i. As $\Upsilon_i(s)$ is the Laplace transform of the net current flowing out of node i, and resource at nodes $j \neq i$ can flow into node i, the off-diagonal elements of $\mathbf{M}(s)$ are negative, and zero if i and j are not directly connected.

Multiplying $\left|\mathbf{M}_{ij}(s)\right|$ by $C_j(s)$ gives us the Laplace transform of the current of resource flowing from j to i, so roughly speaking, $\left|\mathbf{M}_{ij}(s)\right|$ represents the size of the volumetric current from j to i, over the time scale $1/s$. Note that if u_{ij} is positive, then the medium-current flows from i to j, $\left|\mathbf{M}_{ij}(s)\right| < \left|\mathbf{M}_{ji}(s)\right|$, and there is a greater flow from i to j than the other way around. That is to say, when the medium-current is from i to j, the value of $C_i(s)$ has a greater influence on the value of $\Upsilon_j(s)$ than the influence of $C_j(s)$ on the value of $\Upsilon_i(s)$. Also note that the ratio of $\mathbf{M}_{ij}(s)$ to $\mathbf{M}_{ji}(s)$ depends on the Péclet number $\frac{u_{ij}l_{ij}}{D_{ij}} = 2g_{ij}$, as $\mathbf{M}_{ij}(s) : \mathbf{M}_{ji}(s)$ is equal to $1 : e^{2g_{ij}}$.

For very short time scales we have a very large s, and by Equation (3.12), $\alpha_{ij} \gg u_{ij}$ and $\alpha_{ij} \approx \sqrt{4D_{ij}s}$. In this case the off-diagonal elements of $\mathbf{M}$ are very small, and $\mathbf{M}_{ii} \approx \sum_k S_{ik}\frac{\alpha_{ik}}{2} \approx \sum_k S_{ik}\sqrt{D_{ik}s}$. In other words, over very short time scales resource is lost from the nodes by a process of diffusion, but it does not have time to reach the other nodes. Over longer time scales the difference between u_{ij} and α_{ij} is smaller, the off-diagonal elements of $\mathbf{M}$ are larger, and effect of advection is greater.

Finally, note that in the advective limit where the Péclet number $\frac{u_{ij}l_{ij}}{D_{ij}} \gg 1$ for all ij, we have

$$\mathbf{M}_{ij}(s) \approx \begin{cases} \sum_k S_{ik} \frac{u_{ik}+\alpha_{ik}}{2} & \text{if } i = j, \\ -S_{ij}\alpha_{ij} e^{\frac{-(\alpha_{ij}+u_{ij})l_{ij}}{2D_{ij}}} & \text{if } i \neq j \text{ and } u_{ij} < 0 \\ 0 & \text{otherwise.} \end{cases} \tag{3.25}$$

If the Péclet number $\frac{u_{ij}l_{ij}}{D_{ij}} \ll 1$, diffusion is the dominant form of transport through each edge. We can ignore the slight diffusive bias of $u_{ij} \neq 0$ provided that the delivery rate is great enough or the time scale $\frac{1}{s}$ is short enough. That is to say, if $\max\left[s, R_{ij}\right] \gg \frac{u_{ij}^2}{4D_{ij}}$ for all ij, we may be justified in making the approximation $u_{ij} = 0$. In that case $\alpha_{ij}(s) = \sqrt{4D_{ij}(s+R_{ij})}$, and Equation (3.24) tells us that

$$\mathbf{M}_{ij}(s) = \begin{cases} \sum_k S_{ik} \frac{\sqrt{D_{ik}(s+R_{ik})}}{\tanh\left(l_{ik}\sqrt{\frac{s+R_{ik}}{D_{ik}}}\right)} & \text{if } i = j, \\ -S_{ij} \frac{\sqrt{D_{ij}(s+R_{ij})}}{\sinh\left(l_{ij}\sqrt{\frac{s+R_{ij}}{D_{ij}}}\right)} & \text{otherwise.} \end{cases} \tag{3.26}$$

We now have a method for finding the Laplace transform of various quantities, and in the following section we consider how to transform these quantities into the time domain. We have seen that for a given Laplace value s, we can find $\mathbf{M}(s)$ and $\bar{\Upsilon}(s)$. We can therefore use Equation (3.23) to find $\bar{C}(s) = \{C_1(s), \ldots, C_m(s)\}$, the Laplace transform of the concentrations at each node. Furthermore, we can use Equation (3.19) to calculate $Q_{ij}(x,s)$ in terms of the boundary conditions $X_{ij}(s) = \mathscr{L}\left(q_{ij}(0,t)\right)$ and $X_{ji}(s) = \mathscr{L}\left(q_{ij}(l_{ij},t)\right)$. In other words, for each edge and each Laplace variable s, we can find an algebraic expression for $Q_{ij}(x,s)$ in terms of the boundary conditions $X_{ij}(s)$ and $X_{ji}(s)$, but we have yet to show how we can numerically invert such quantities into the time domain.

3.4 Inverting From Laplace Space

As we can calculate any sequence of real valued sample points in Laplace space and we wish to calculate the corresponding value at a given point in time, it is appropriate

and efficient to apply the Gaver-Stehfest algorithm [2, 64]. The key idea behind this algorithm (and other, related algorithms) is the notion of constructing a sequence of linear combinations of exponential functions in order to form a weighted delta convergent sequence [2, 64, 212, 213]. That is to say, we consider a sequence of functions $\delta_n(x,t)$ such that for any function q that is continuous at t, we have

$$\int_0^\infty \delta_n(v,t)q(v)dv = t\tilde{q}_n(t), \tag{3.27}$$

where $\tilde{q}_n(t) \to q(t)$ as $n \to \infty$. As we shall see, there are weighted delta convergent sequences of functions such that $\delta_n(v,t)$ is of the form

$$\delta_n(v,t) = \sum_{i=1}^{n} \omega_i e^{\frac{-\theta_i v}{t}}, \tag{3.28}$$

where $\theta_i > 0$ for all i, and the terms θ_i and ω_i do not depend on t. Now, if we suppose that our function q does not increase exponentially, then the Laplace transform $Q(s) = \int_0^\infty e^{-sv}q(v)dv$ is well defined for all positive numbers s. Hence the existence of $Q(s)$ for all positive s is a reasonable assumption, given the context in which our functions q arise. Assuming that $Q(s)$ is well defined for all positive numbers s, Equations (3.27) and (3.28) imply that

$$\begin{aligned} \tilde{q}_n(t) &= \frac{1}{t}\int_0^\infty \sum_{i=1}^{n} \omega_i e^{\frac{-\theta_i v}{t}} q(v)dv \\ &= \frac{1}{t}\sum_{i=1}^{n} \omega_i Q\big(\frac{\theta_i}{t}\big). \end{aligned}$$

Gaver [89] employed the sequence of functions

$$\delta_n(v,t) = \ln 2 \frac{(2n)!}{n!(n-1)!}(1-e^{-\frac{v\ln 2}{t}})^n (e^{-\frac{v\ln 2}{t}})^n, \tag{3.29}$$

but the resulting terms $\tilde{q}^n(t)$ converge to $q(t)$ logarithmically slowly. Gaver also showed that the quantity $\tilde{q}^n(t) - q(t)$ can be expanded in terms of inverse powers of n, which enabled him to accelerate the convergence of his original sequence of approximations [89]. The most useful formula for finding an accurate estimate of $q(t)$ based on a linear combination of the Gaver estimates was derived by Stehfest [179], who stated that

$$q(t) \approx \tilde{q}_\Omega(t) = \frac{\ln 2}{t}\sum_{n=1}^{\Omega} \kappa_n Q(n\frac{\ln 2}{t}), \quad \text{where} \tag{3.30}$$

$$\kappa_n = (-1)^{n+\Omega/2} \sum_{k=[(n+1)/2]}^{\min(n,\Omega/2)} \frac{k^{\Omega/2}(2k)!}{(\Omega/2-k)!k!(n-k)!(2k-n)!}, \tag{3.31}$$

and Ω is even. Note that the terms κ_n can be extremely large, and that the value of κ_n depends on the parameter Ω. Furthermore, increasing the parameter Ω increases the accuracy of our estimate $q(t) \approx \tilde{q}_\Omega(t)$, provided that we have sufficient system precision to utilize the exact values for κ_n.

The Gaver-Stehfest algorithm is very efficient and accurate, but it requires high system precision for the weights κ_n if it is to yield accurate estimates for $q(t)$. Indeed, if we wish to produce an estimate of $q(t)$ that is accurate to N significant digits, we must calculate the values of κ_n with an accuracy of about $2.5N$ significant digits [1, 2]. Fortunately, to calculate $q(t)$ accurately we do not require such a disproportionately high level of accuracy in the values of $Q(s)$.

If the transform $Q(s)$ has all its singularities on the negative real axis, and if the function $q(t)$ is infinitely differentiable for all $t > 0$, extensive experimentation [1, 2] indicates that the relative error

$$\left| \frac{q(t) - \tilde{q}_\Omega(t)}{q(t)} \right| \approx 10^{-0.45\Omega}, \tag{3.32}$$

provided that the values κ_n have been calculated with sufficient precision [1, 2]. If the function q does not satisfy the above conditions $\tilde{q}_\Omega(t)$ may converge to $q(t)$ rather more slowly, but as a rule of thumb setting $\Omega = 10$ and using standard double precision for the weights κ_n will ensure that the Gaver-Stehfest algorithm produces inversions that are accurate to at least three significant digits.

3.5 Non-Zero Initial Conditions in a Single Edge

We now consider advection, diffusion and delivery along a single edge ij, where the initial condition $q_{ij}(x,0)$ is non-zero. We let the length of ij equal l, the longitudinal dispersion coefficient is D, the local delivery rate is R and the mean velocity is u.

We have seen that for any positive Laplace constant s, $Q_1(x,s) = e^{(g+h)\frac{x}{l}}$ and $Q_2(x,s) = e^{(g-h)\frac{x}{l}}$ satisfy the homogeneous analog, Equation (3.10). Furthermore,

the Wronskian

$$\begin{aligned} W_{ij}(x,s) &= Q_1(x,s)\frac{\partial Q_2(x,s)}{\partial x} - \frac{\partial Q_1(x,s)}{\partial x}Q_2(x,s) \\ &= e^{\frac{u_{ij}+\alpha_{ij}}{2D_{ij}}x} e^{\frac{u_{ij}-\alpha_{ij}}{2D_{ij}}x}\left(\frac{u_{ij}-\alpha_{ij}}{2D_{ij}} - \frac{u_{ij}+\alpha_{ij}}{2D_{ij}}\right) \\ &= \frac{-\alpha e^{2g\frac{x}{l}}}{D}. \end{aligned}$$

By the method of variation of parameters,

$$\begin{aligned} f\big(x,s,q_{ij}(y,0)\big) &= -Q_1(x,s)\int_0^x \frac{Q_2(y,s)q_{ij}(y,0)}{D_{ij}W_{ij}(y,s)}dy \\ &\quad +Q_2(x,s)\int_0^x \frac{Q_1(y,s)q_{ij}(y,0)}{D_{ij}W_{ij}(y,s)}dy, \\ &= \frac{e^{(g-h)\frac{x}{l}}}{\alpha}\int_0^x e^{(h-g)\frac{y}{l}}q_{ij}(y,0)dy \\ &- \frac{e^{(g+h)\frac{x}{l}}}{\alpha}\int_0^x e^{-(g+h)\frac{y}{l}}q_{ij}(y,0)dy \end{aligned} \tag{3.33}$$

is a particular solution to the fundamental Equation (3.8).

Note that $f(0,s,q)=0$ for all initial conditions q. Also note if $q=q_1+q_2$ then $f(x,s,q)=f(x,s,q_1)+f(x,s,q_2)$. Since $f\big(x,s,q_{ij}(y,0)\big)$ is a particular solution of Equation (3.8), for each edge ij there is a pair of constants A and B such that

$$Q_{ij}(x,s) = Ae^{(g+h)\frac{x}{l}} + Be^{(g-h)\frac{x}{l}} + f\big(x,s,q_{ij}(y,0)\big). \tag{3.34}$$

Because $f(0,s,q)=0$ for all initial conditions q, Equations (3.14) and (3.34) imply that

$$X_{ij} \equiv Q_{ij}(0,s) = A+B, \qquad \text{and} \tag{3.35}$$

$$X_{ji} \equiv Q_{ij}(l_{ij},s) = Ae^{(g+h)} + Be^{(g-h)} + f\big(l,s,q_{ij}(y,0)\big). \tag{3.36}$$

We can therefore express A and B in terms of X_{ij} and X_{ji}. Indeed, substituting Equation (3.35) into Equation (3.36) and multiplying both sides by e^{-g} tells us that

$$X_{ji}e^{-g} = A\big(e^h - e^{-h}\big) + X_{ij}e^{-h} + e^{-g}f\big(l,s,q_{ij}(y,0)\big). \tag{3.37}$$

At this point it is convenient to define a constant

$$\beta_{ij}(s) \equiv \frac{-\alpha_{ij}(s)e^{-g_{ij}}}{2\sinh\big(h_{ij}(s)\big)}f\big(l,s,q_{ij}(y,0)\big), \tag{3.38}$$

whose physical significance is explained in Section 3.6. As is the case with the terms α_{ij} and h_{ij}, β is a function of the Laplace constant s, but this dependence is omitted for clarity. Now, Equations (3.35) and (3.37) imply that

$$\begin{aligned} A &= \frac{X_{ji}e^{-g} - X_{ij}e^{-h}}{2\sinh(h)} + \frac{\beta_{ij}}{\alpha} \qquad \text{and} \\ B &= \frac{X_{ij}e^{h} - X_{ji}e^{-g}}{2\sinh(h)} - \frac{\beta_{ij}}{\alpha}, \end{aligned} \tag{3.39}$$

and substituting Equation (3.39) into Equation (3.34) tells us that for any initial condition $q_{ij}(y,0)$,

$$\begin{aligned} Q_{ij}(x,s) &= \left(\frac{X_{ji}e^{-g} - X_{ij}e^{-h}}{2\sinh(h)} + \frac{\beta_{ij}}{\alpha}\right)e^{(g+h)\frac{x}{l}} \\ &\quad + \left(\frac{X_{ij}e^{h} - X_{ji}e^{-g}}{2\sinh(h)} - \frac{\beta_{ij}}{\alpha}\right)e^{(g-h)\frac{x}{l}} + f\big(x,s,q_{ij}(y,0)\big). \end{aligned} \tag{3.40}$$

Having analyzed the case of a single edge with a non-zero initial condition, we now move on to consider the case of an entire network, under the assumption that there is perfect mixing at each node.

3.6 Non-zero Initial Conditions Over a Network

The first step is to note that Equation (3.33) implies that

$$\begin{aligned} \frac{\partial f\big(x,s,q_{ij}\big)}{\partial x} &= -\frac{(u+\alpha)}{2D\alpha}e^{\frac{u+\alpha}{2D}x}\int_0^x e^{\frac{-(u+\alpha)}{2D}y}q(y,0)dy \\ &\quad + \frac{(u-\alpha)}{2D\alpha}e^{\frac{u-\alpha}{2D}x}\int_0^x e^{\frac{-(u-\alpha)}{2D}y}q(y,0)dy. \\ &\quad - \frac{(u+\alpha)}{2D\alpha}e^{(g+h)\frac{x}{l}}\int_0^x e^{-(g+h)\frac{y}{l}}q_{ij}(y,0)dy \\ &\quad + \frac{(u-\alpha)}{2D\alpha}e^{(g-h)\frac{x}{l}}\int_0^x e^{(h-g)\frac{y}{l}}q_{ij}(y,0)dy, \end{aligned}$$

where for the sake of clarity we drop the subscript ij from u_{ij}, α_{ij}, l_{ij}, g_{ij}, h_{ij} and D_{ij}. Note that for any initial condition $q_{ij}(y,0)$, we have $\frac{\partial f\left(x,s,q_{ij}(y,0)\right)}{\partial x}\big|_{x=0} = 0$. It follows that

$$\left.\frac{\partial Q_{ij}(x,s)}{\partial x}\right|_{x=0} = \frac{u+\alpha}{2D}\left(\frac{X_{ji}e^{-g_{ij}} - X_{ij}e^{-h_{ij}}}{2\sinh(h_{ij})} + \frac{\beta_{ij}}{\alpha}\right)$$

$$+\frac{u-\alpha}{2D}\left(\frac{X_{ij}e^{h_{ij}}-X_{ji}e^{-g_{ij}}}{2\sinh(h_{ij})}-\frac{\beta_{ij}}{\alpha}\right),$$

$$\begin{aligned}=\ & \frac{\beta_{ij}}{D}+\frac{u+\alpha}{2D}\left(\frac{X_{ji}e^{-g}-X_{ij}e^{-h}}{2\sinh(h)}\right)\\ & +\frac{u-\alpha}{2D}\left(\frac{X_{ij}e^{h}-X_{ji}e^{-g}}{2\sinh(h)}\right).\end{aligned} \tag{3.41}$$

Now, recall that $\Upsilon_i(s)$ denotes the Laplace transform of the net current of resource flowing away from node i, and that $\Upsilon_i(s)=0$ unless i is an inlet node. Substituting Equation (3.41) into Equation (3.9) gives us

$$\begin{aligned}\Upsilon_i(s) &= \sum_j u_{ij}X_{ij}-\sum_j D_{ij}\left[\frac{u_{ij}+\alpha_{ij}}{2D_{ij}}\left(\frac{X_{ji}e^{-g_{ij}}-X_{ij}e^{-h_{ij}}}{2\sinh(h_{ij})}\right)\right.\\ &+ \left.\frac{u_{ij}-\alpha_{ij}}{2D_{ij}}\left(\frac{X_{ij}e^{h_{ij}}-X_{ji}e^{-g_{ij}}}{2\sinh(h_{ij})}\right)+\frac{\beta_{ij}}{D_{ij}}\right],\end{aligned}$$

$$= \sum_j X_{ij}\left[\frac{u_{ij}}{2}+\frac{\alpha_{ij}}{2\tanh(h_{ij})}\right]-\sum_j X_{ji}\frac{\alpha_{ij}e^{-g_{ij}}}{2\sinh(h_{ij})}-\sum_j \beta_{ij}(s). \tag{3.42}$$

Assuming that the cross-sectional areas S_{ij} are constant, Equations (3.20) and (3.42) imply that

$$\begin{aligned}\Upsilon_i(s) &= C_i(s)\sum_j S_{ij}\left(\frac{u_{ij}}{2}+\frac{\alpha_{ij}}{2\tanh(h_{ij})}\right)\\ &\quad -\sum_j C_j(s)S_{ij}\frac{\alpha_{ij}e^{-g_{ij}}}{2\sinh(h_{ij})}-\sum_j \beta_{ij}(s).\end{aligned} \tag{3.43}$$

In matrix form we have

$$\mathbf{M}(s)\bar{C}(s)=\bar{\rho}(s), \qquad \text{where} \tag{3.44}$$

$$\bar{C}(s)=\{C_1(s),C_2(s),\ldots,C_m(s)\}^{\mathrm{T}}, \tag{3.45}$$

$$\rho_i(s)=\Upsilon_i(s)+\sum_j \beta_{ij}(s) \tag{3.46}$$

and $\mathbf{M}(s)$ is the propagation matrix as in Equation (3.24). Note that the effect of the initial conditions on the concentration at the nodes is completely captured by the terms $\beta_{ij}(s)$, and that, as before, the propagation matrix $\mathbf{M}(s)$ relates the concentrations at the nodes to the net currents flowing out of the nodes. Furthermore, by

comparison with Equation (3.24), we can see that the concentration at the nodes is the same as would be the case if the network were initially empty, and the Laplace transform of the net current leaving node i was $\rho_i(s)$ rather than $\Upsilon_i(s)$.

In effect, the formalism of the propagation matrix enables us to substitute an initial condition in the edges around node i for a boundary condition at node i. For each node i and each Laplace variable s, this boundary condition is of the form $\sum_j \beta_{ij}(s)$. Intuitively speaking, the term $\beta_{ij}(s)$ represents the Laplace transform of the quantity of resource that first leaves edge ij by arriving at node i. Note that we have not calculated the impact of the initial condition $q_{ij}(x,0)$ on the future concentration profile $q_{ij}(x,t)$ for $t > 0$: we have simply calculated the impact of the initial conditions on the concentrations at the nodes (see Section 3.7).

Since $\alpha_{ij}(s) \gg u_{ij}$ and $h_{ij}(s) \gg g_{ij}$ for large s, for very short time steps t we have $\sinh(h_{ij}) \gg \max\left[e^{g_{ij}}, e^{-g_{ij}}\right]$. It follows that over short time scales, the off-diagonal elements of $\mathbf{M}(s)$ will be very small. If the entries in the ith column of $\mathbf{M}(s)$ are very small, it may be numerically difficult to calculate $C_i(s)$, as any error in our estimate for $C_i(s)$ would have very little impact on the value of $\mathbf{M}(s)\bar{C}(s)$.

In practice this is not a significant problem, as when we solve the above system of linear equations to identify $C_i(s)$, we make the initial guess that $C_i(s) = c_i(0)/s$, which would be the correct value if the concentration at node i remained constant. For numerical reasons we may not be able to identify the exact value of $C_i(s)$, but this problem only arises when the bulk of resource around node i does not leave the edges around node i over the time scale $1/s$. As we shall see in Section 3.7, those are precisely the circumstances under which the value of $C_i(s)$ has little impact on our calculation of the distribution of resource within the edges at a given time $t \approx 1/s$.

3.7 Efficient Calculation of Resource Distribution

If we wish to find the concentration at various points in the network other than the nodes, there are two ways we can proceed. The first method is to suppose that each edge contains several nodes in addition to its terminal points. The problem with this

approach is that introducing additional nodes increases the size of the propagation matrix, and finding $\bar{C}(s)$ by inverting the matrices $\mathbf{M}(s)$ is the major computational cost of the propagation matrix algorithm. Furthermore, although this approach can be used to find the exact concentration at each of a given set of points, it does not provide a means of finding the exact quantity of resource between a given pair of points. We could approximate the total quantity of resource between two points by assuming that the concentration varies in a linear manner from one point to the next, but as the exact solution may contain boundary layer effects, we might require a very high spatial resolution to ensure that such a linear approximation is accurate.

A different approach, which is outlined in this section, provides an exact solution for the total quantity of resource within each section of the network, regardless of the spatial resolution. The key conceptual step involves partitioning the resource into two parts, as we can imagine that the resource is composed of particles, which either leave or do not leave a given edge over a given time scale. We let $\hat{q}_{ij}(x,t)$ denote the quantity of resource per unit length at the point $0 \leq x \leq l_{ij}$ in edge ij and time t, where we only consider particles that have passed through a node (any node) by time t after initialization. In each edge, this quantity is complemented by $\tilde{q}_{ij}(x,t)$: the quantity of resource per unit length at the point $0 \leq x \leq l_{ij}$ and time t, where we only consider particle that have not reached a node by time t after initialization.

To calculate $\hat{q}_{ij}(x,t)$ we work in Laplace space, and let $\mathscr{L}\big(\hat{q}_{ij}(x,t)\big) = \hat{Q}_{ij}(x,s)$. This term denotes the Laplace transformed concentration profile that would occur if the network was initially empty, and if the Laplace transform of the net current leaving each node was $\rho_i(s) = \Upsilon_i(s) + \sum_j \beta_{ij}(s)$, rather than $\Upsilon_i(s)$. As we have seen in Section 3.6, the impact of the initial condition on the concentration at the nodes is completely captured by the constants $\beta_{ij}(s)$. However, $\hat{Q}_{ij}(x,s)$ and $\hat{q}_{ij}(x,t)$ do not fully capture the influence of the initial condition $q_{ij}(x,0)$ on the concentration profile $q_{ij}(x,t)$ for $t > 0$. In addition to $\hat{q}_{ij}(x,t)$ (the quantity of resource that has reached a node over the time scale t), we must also consider the resource that starts in edge ij, and which does not reach node i or j over the time scale t. We let $\tilde{q}_{ij}(x,t)$

denote the quantity of such resource at the point $0 \leq x \leq l_{ij}$ in edge ij and time t, where by definition

$$q_{ij}(x,t) = \tilde{q}_{ij}(x,t) + \hat{q}_{ij}(x,t). \tag{3.47}$$

We can calculate the concentration at each node by calculating $\beta_{ij}(s)$ for every i and j, and by using the propagation matrix. Furthermore, because at time 0 none of the resource in edge ij has had time to reach a node, we can apply Equation 3.19, and find $\hat{Q}_{ij}(x,s)$ in terms of the boundary conditions $X_{ij}(s)$ and $X_{ji}(s)$. Given $\hat{Q}_{ij}(x,s)$ for $s = \frac{\ln 2}{t}, \ldots n\frac{\ln 2}{t}$, we can apply the Gaver-Stehfest algorithm and find $\hat{q}_{ij}(x,t)$. In addition, we solve a separate PDE for each edge, which tells us how the resource that stays within each edge has evolved over a given time step t. That is to say, for each edge ij we find $\tilde{q}_{ij}(x,t)$, given that $\tilde{q}_{ij}(x,t)$ satisfies the fundamental advection-diffusion-delivery Equation (3.2), $\tilde{q}_{ij}(x,0) = q_{ij}(x,0)$, $\tilde{q}_{ij}(0,t) = 0$ and $\tilde{q}_{ij}(l_{ij},t) = 0$. Finally, Equation (3.47) tells us that $q_{ij}(x,t) = \tilde{q}_{ij}(x,t) + \hat{q}_{ij}(x,t)$.

In particular, we consider the case where the initial condition is stepwise constant, and edge ij is divided into N_{ij} sections of equal length. We let $k_{ij}^{(n)}(t)$ denote the mean quantity of resource per unit length in the nth section at the given time t, where by convention the first section is next to node i and the Nth section is next to node j. For any $t > 0$, we can employ the following algorithm to find an exact solution for the updated mean quantities per unit length,

$$k_{ij}^{(n)}(t) = \frac{N_{ij}}{l_{ij}} \int_{\frac{n-1}{N_{ij}} l_{ij}}^{\frac{n}{N_{ij}} l_{ij}} q_{ij}(x,t)dx. \tag{3.48}$$

Stepwise constant initial conditions

We are interested in calculating how the quantity of resource in a network changes over time, given that the resource decays and is subject to advection and diffusion. It is particularly convenient to consider a stepwise constant initial condition, as we can then calculate how the total quantity of resource in each segment of the network has changed by time t. The first step in this calculation is to find the Laplace transform of the concentrations at each node $\bar{C}(s)$. As we have seen, to calculate $\bar{C}(s)$ we

must first find $\mathbf{M}_{ij}(s)$ and $\bar{\Upsilon}(s)$, which do not depend on the initial condition. For each sample point s and each edge ij we must also calculate $\beta_{ij}(s)$ and $\beta_{ji}(s)$, which capture the effect of the initial condition $q_{ij}(x,0)$ on the nodes i and j. We start this subsection by considering the case where the initial condition is

$$q_{ij}(x,0) = \begin{cases} k & \text{if } \frac{n-1}{N} l_{ij} \leq x < \frac{n}{N} l_{ij} \\ 0 & \text{otherwise,} \end{cases} \tag{3.49}$$

where $n \leq N$. We will find our solutions for other initial conditions by summing the solutions for various initial conditions of this form. For the sake of clarity we drop the subscripts ij from l_{ij}, N_{ij}, g_{ij} and h_{ij}, and note that Equation (3.33) tells us that for this initial condition

$$\begin{aligned} f\big(l,s,q_{ij}\big) &= -\frac{ke^{g+h}}{\alpha_{ij}} \int_{\frac{n-1}{N}l}^{\frac{n}{N}l} e^{-(g+h)\frac{x}{l}} dx + \frac{ke^{g-h}}{\alpha_{ij}} \int_{\frac{n-1}{N}l}^{\frac{n}{N}l} e^{(h-g)\frac{x}{l}} dx, \\ &= \frac{2D_{ij}ke^{g+h}}{\alpha_{ij}(u_{ij}+\alpha_{ij})} \left(e^{\frac{-n}{N}(g+h)} - e^{\frac{-(n-1)}{N}(g+h)} \right) \\ &\quad -\frac{2D_{ij}ke^{g+h}}{\alpha_{ij}(u_{ij}-\alpha_{ij})} \left(e^{\frac{n}{N}(h-g)} - e^{\frac{(n-1)}{N}(h-g)} \right). \end{aligned} \tag{3.50}$$

Substituting into Equation (3.38) yields

$$\begin{aligned} \beta_{ij}(s) &= \frac{ke^{\frac{1-n}{N}g}}{4(s+R_{ij})\sinh(h)} \times \\ &\quad \left[e^{\frac{N-n}{N}h} \big(e^{\frac{h}{N}} - e^{\frac{-g}{N}}\big)\big(\alpha_{ij}-u_{ij}\big) + e^{\frac{n-N}{N}h} \big(e^{\frac{-h}{N}} - e^{\frac{-g}{N}}\big)\big(\alpha_{ij}+u_{ij}\big) \right]. \end{aligned} \tag{3.51}$$

Recall that $f(x,s,q_1+q_2) = f(x,s,q_1) + f(x,s,q_2)$. Since Equation (3.38) is linear, it follows that if the initial condition contains several blocks of resource, each block makes its own separate contribution to $\beta_{ij}(s)$ and $\beta_{ji}(s)$. Let $x_0 = 0, x_1 = \frac{l}{N}, x_2 = \frac{2l}{N}, \ldots, x_N = l$, and suppose that for all $1 \leq n \leq N$ we have

$$q_{ij}(x,0) = k_{ij}^{(n)} \quad \text{for all} \quad x_{n-1} < x < x_n. \tag{3.52}$$

Given such a stepwise constant initial condition, we can calculate $\beta_{ij}(s)$ by summing the contribution of each of the blocks of resource. That is to say, Equation (3.51) becomes

$$\begin{aligned}\beta_{ij}(s) &= \sum_{n=1}^{N} \frac{k_{ij}^{(n)} e^{\frac{1-n}{N} g_{ij}}}{4(s+R_{ij})\,\sinh(h_{ij})} \times \\ &\left[e^{\frac{N-n}{N} h_{ij}} \left(e^{\frac{h_{ij}}{N}} - e^{\frac{-g_{ij}}{N}} \right) \left(\alpha_{ij} - u_{ij} \right) + e^{\frac{n-N}{N} h_{ij}} \left(e^{\frac{-h_{ij}}{N}} - e^{\frac{-g_{ij}}{N}} \right) \left(\alpha_{ij} + u_{ij} \right) \right].\end{aligned} \tag{3.53}$$

We can find $\beta_{ji}(s)$ by using the above formula, substituting $-g_{ij}$ for g_{ji}, $-u_{ij}$ for u_{ji} and $k_{ij}^{(N-n+1)}$ for $k_{ji}^{(n)}$. It follows that

$$\begin{aligned}\beta_{ji}(s) &= \sum_{n=1}^{N} \frac{k_{ij}^{(N-n+1)} e^{\frac{n-1}{N} g_{ij}}}{4(s+R_{ij})\,\sinh(h_{ij})} \times \\ &\left[e^{\frac{N-n}{N} h_{ij}} \left(e^{\frac{h_{ij}}{N}} - e^{\frac{g_{ij}}{N}} \right) \left(\alpha_{ij} + u_{ij} \right) + e^{\frac{n-N}{N} h_{ij}} \left(e^{\frac{-h_{ij}}{N}} - e^{\frac{g_{ij}}{N}} \right) \left(\alpha_{ij} - u_{ij} \right) \right].\end{aligned} \tag{3.54}$$

Resource that leaves its initial edge

If a particle leaves edge ij and reaches node i or j over the relevant time scale, it contributes to $\beta_{ij}(s)$ or $\beta_{ji}(s)$, and hence it contributes to our solution $C_i(s)$, $C_j(s)$ and $\mathscr{L}\left(\hat{q}_{ij}(x,t)\right) = \hat{Q}_{ij}(x,s)$. On the other hand, at time 0 none of the resource has reached the nodes, so the initial condition $\hat{q}_{ij}(x,0) = 0$. It follows that if the cross-sectional areas are held constant, we can apply Equation (3.19). In other words, we can find $\hat{Q}_{ij}(x,s)$ by effectively considering an initially empty network, where resource is introduced at the nodes at a rate which exactly matches the rate at which resource reaches the nodes in the case where the network has the given non-zero initial condition. Equation (3.19) also accounts for the impact of any inlet nodes, in the case where resource is being added to the network.

We can therefore use Equations (3.44), (3.54) and (3.55) to find the terms $\bar{C}(s) = \{C_1(s), \ldots, C_m(s)\}$, and in the case where the cross-sectional areas are constant, we can use Equations (3.19) and (3.20) to express $\hat{Q}_{ij}(x,s)$ in terms of the boundary conditions $X_{ij} = S_{ij}C_i(s)$ and $X_{ji} = S_{ij}C_j(s)$. Since $\mathscr{L}\left(\int \hat{q}_{ij}(x,t)dx\right) = \int \hat{Q}_{ij}(x,s)dx$,

we can find $\int \hat{q}_{ij}(x,t)dx$ by calculating $\int \hat{Q}_{ij}(x,s)dx$ for $s = \ln 2/t, \ldots, N\ln 2/t$ and applying the Gaver-Stehfest algorithm.

We suppose that edge ij is divided into N_{ij} sections of equal length, and for the sake of clarity we drop the subscripts ij from D_{ij}, l_{ij} and N_{ij}. We let $y_{ij}^{(n)}(t)$ denote the mean value of $\hat{q}_{ij}(x,t)$ in the nth section of edge ij, and note that by definition

$$y_{ij}^{(n)}(t) = \frac{N}{l}\int_{\frac{n-1}{N}l}^{\frac{n}{N}l} \hat{q}_{ij}(x,t)dx. \tag{3.55}$$

We let $Y_{ij}^{(n)}(s) \equiv \mathscr{L}\big(y_{ij}^{(n)}(t)\big)$ and note that we have

$$\begin{aligned}
Y_{ij}^{(n)}(s) &= \frac{N}{l}\int_{\frac{n-1}{N}l}^{\frac{n}{N}l} \hat{Q}_{ij}(x,s)dx \\
&= \frac{NX_{ij}}{l\,\sinh(h_{ij})}\int_{\frac{n-1}{N}l}^{\frac{n}{N}l} \sinh\big(h_{ij}\frac{l-x}{l}\big)e^{g_{ij}\frac{x}{l}}dx \\
&+ \frac{NX_{ji}}{l\,\sinh(h_{ij})}\int_{\frac{n-1}{N}l}^{\frac{n}{N}l} \sinh\big(h_{ij}\frac{x}{l}\big)e^{g_{ij}\frac{x-l}{l}}dx \\
&= \frac{NS_{ij}C_i(s)}{2l\,\sinh(h)}\int_{\frac{n-1}{N}l}^{\frac{n}{N}l} e^{h}e^{\frac{(u-\alpha)}{2D}x} - e^{-h}e^{\frac{(u+\alpha)}{2D}x}dx \\
&+ \frac{NS_{ij}C_j(s)}{2l\,\sinh(h)}\int_{\frac{n-1}{N}l}^{\frac{n}{N}l} e^{-g}e^{\frac{(u+\alpha)}{2D}x} - e^{-g}e^{\frac{(u-\alpha)}{2D}x}dx \\
&= \frac{ND}{l\,\sinh(h_{ij})}\left[\frac{X_{ij}e^{h_{ij}} - X_{ji}e^{-g_{ij}}}{u_{ij}-\alpha_{ij}}e^{(g_{ij}-h_{ij})\frac{x}{l}}\right. \\
&\qquad \left. + \frac{X_{ji}e^{-g_{ij}} - X_{ij}e^{-h_{ij}}}{u_{ij}+\alpha_{ij}}e^{(g_{ij}+h_{ij})\frac{x}{l}}\right]_{\frac{n-1}{N}l}^{\frac{n}{N}l}.
\end{aligned}$$

This implies that

$$\begin{aligned}
Y_{ij}^{(n)}(s) &= \eta_{ij}(s)\big(\alpha_{ij}+u_{ij}\big)\Big[X_{ij}\big(e^{\frac{n-1}{N}(g_{ij}-h_{ij})} - e^{\frac{n}{N}(g_{ij}-h_{ij})}\big) \\
&+ X_{ji}\big(e^{\frac{n-N}{N}g_{ij}-\frac{n+N}{N}h_{ij}} - e^{\frac{n-N-1}{N}g_{ij}-\frac{n+N-1}{N}h_{ij}}\big)\Big] \\
&+ \eta_{ij}(s)\big(\alpha_{ij}-u_{ij}\big)\Big[X_{ij}\big(e^{\frac{n-1}{N}g_{ij}-\frac{2N-n+1}{N}h_{ij}} - e^{\frac{n}{N}g_{ij}-\frac{2N-n}{N}h_{ij}}\big) \\
&+ X_{ji}\big(e^{\frac{n-N}{N}(g_{ij}+h_{ij})} - e^{\frac{n-N-1}{N}(g_{ij}+h_{ij})}\big)\Big],
\end{aligned} \tag{3.56}$$

where

$$\eta_{ij}(s) = \frac{N_{ij}e^{h_{ij}}}{4(s+R_{ij})l_{ij}\,\sinh\big(h_{ij}\big)}. \tag{3.57}$$

Resource that remains in its initial edge

Over the time scale t, not all of the resource within edge ij will reach node i or j. To find $\tilde{q}_{ij}(x,t)$, the quantity of resource that has not left edge ij, we must solve the advection, diffusion, delivery problem for each separate edge ij, where nodes i and j are absorbing boundaries and the initial condition $\tilde{q}_{ij}(x,0) = q_{ij}(x,0)$. The resulting solution accounts for those particles which do not reach a node in the relevant time-scale. In particular, we consider the case where the initial condition is stepwise constant, as in Equation (3.52).

The fundamental Equation (3.2) tells us that for each edge

$$\frac{\partial}{\partial t}\tilde{q}_{ij} = D_{ij}\frac{\partial^2}{\partial x^2}\tilde{q}_{ij} - u_{ij}\frac{\partial}{\partial x}\tilde{q}_{ij} - R_{ij}\tilde{q}_{ij}. \tag{3.58}$$

We now try solutions of the form $f(x,t) = Ae^{\lambda t+\eta x}$, and note that Equation (3.58) implies that

$$\lambda e^{\lambda t+\eta x} = (D_{ij}\eta^2 - u_{ij}\eta - R_{ij})e^{\lambda t+\eta x}. \tag{3.59}$$

It follows that for any given value of λ, we have

$$\eta = \frac{u_{ij} \pm \sqrt{u_{ij}^2 + 4D_{ij}(R_{ij}+\lambda)}}{2D_{ij}}. \tag{3.60}$$

Hence if η were real we would have $\tilde{q}_{ij}(x,0) = Ae^{\eta x}$, but by definition $\tilde{q}_{ij}(0,0) = \tilde{q}_{ij}(l_{ij},0) = 0$. It follows that η is complex, and we let

$$iC_\lambda = \frac{\sqrt{u_{ij}^2 + 4D_{ij}(R_{ij}+\lambda)}}{2D_{ij}}, \tag{3.61}$$

where C_λ is a real number. For any real number λ, we have

$$\begin{aligned} f(x,t) &= e^{\lambda t+\frac{g_{ij}x}{l}}\big(\hat{A}\cos(C_\lambda x) + i\hat{A}\sin(C_\lambda x) \\ &+ \hat{B}\cos(C_\lambda x) + i\hat{B}\sin(C_\lambda x)\big), \end{aligned}$$

but we are looking for a real valued function $\tilde{q}_{ij}(x,t)$, so we have

$$f(x,t) = e^{\lambda t+\frac{g_{ij}x}{l}}\big(A\sin(C_\lambda x) + B\cos(C_\lambda x)\big). \tag{3.62}$$

Since $\tilde{q}_{ij}(0,t) = 0$, it follows that $B = 0$ for any choice of λ. Furthermore, as $\tilde{q}_{ij}(l_{ij},t) = 0$ for all t, it follows that for each positive integer m we have a potential solution of the form

$$f_m(x,t) = A^m e^{\lambda t + \frac{g_{ij}x}{l}} \sin\left(\frac{m\pi x}{l_{ij}}\right). \tag{3.63}$$

Given that $iC = \frac{\sqrt{u_{ij}^2 + 4D_{ij}(R_{ij}+\lambda)}}{2D_{ij}}$ and $C = \frac{m\pi}{l_{ij}}$, it follows that

$$\frac{-m^2\pi^2}{l_{ij}^2} = \frac{u_{ij}^2 + 4D_{ij}(R_{ij}+\lambda_{ij}^m)}{4D_{ij}^2} \quad \text{and} \tag{3.64}$$

$$\lambda_{ij}^m = -\left(m^2\frac{D_{ij}\pi^2}{l_{ij}^2} + \frac{u_{ij}^2}{4D_{ij}} + R_{ij}\right). \tag{3.65}$$

We can therefore express $\tilde{q}_{ij}(x,t)$ in the following form:

$$\begin{aligned} \tilde{q}_{ij}(x,t) &= e^{\frac{u_{ij}}{2D_{ij}}x} \sum_{m=1}^{\infty} A^m e^{\lambda_{ij}^m t} \sin\left(\frac{m\pi x}{l_{ij}}\right), \\ \text{where} \quad \lambda_{ij}^m &= -\left(m^2\frac{D_{ij}\pi^2}{l_{ij}^2} + \frac{u_{ij}^2}{4D_{ij}} + R_{ij}\right). \end{aligned} \tag{3.66}$$

The parameters A^m can be found by taking Fourier transforms. More specifically, we know that $\tilde{q}_{ij}(x,0) = q_{ij}(x,0)$, so

$$\begin{aligned} \sum_{n=1}^{\infty} A^m \sin\left(\frac{m\pi x}{l_{ij}}\right) &= q_{ij}(x,0)e^{-g_{ij}\frac{x}{l_{ij}}} \quad \text{and} \\ \int_0^l \sin\left(\frac{m\pi x}{l_{ij}}\right) \sin\left(\frac{n\pi x}{l_{ij}}\right) dx &= \begin{cases} 0 & \text{if } m \neq n, \\ \frac{l_{ij}}{2} & \text{if } m = n. \end{cases} \end{aligned}$$

It follows that for every positive integer m,

$$A^m = \frac{2}{l_{ij}} \int_0^{l_{ij}} \sin\left(\frac{m\pi x}{l_{ij}}\right) q_{ij}(x,0) e^{-g_{ij}\frac{x}{l_{ij}}} dx. \tag{3.67}$$

In the case where the initial condition is stepwise constant, and of the form described by Equation (3.52), we have

$$\begin{aligned} A^m &= \mu_{ij}^m \sum_{n=1}^{N_{ij}} k_{ij}^{(n)} \left[e^{-g_{ij}\frac{x}{l_{ij}}} \left(\frac{-g_{ij}}{\pi m} \sin\left(\frac{m\pi x}{l_{ij}}\right) - \cos\left(\frac{m\pi x}{l_{ij}}\right) \right) \right]_{\frac{n-1}{N_{ij}} l_{ij}}^{\frac{n}{N_{ij}} l_{ij}} \\ &= - \mu_{ij}^m \sum_{n=1}^{N} k_{ij}^{(n)} \left[e^{\frac{-unl}{2DN}} \left(\frac{g_{ij}}{\pi m} \sin\left(\frac{mn\pi}{N}\right) + \cos\left(\frac{mn\pi}{N}\right) \right) \right] \end{aligned}$$

$$+ \quad \mu_{ij}^m \sum_{n=0}^{N-1} k_{ij}^{(n+1)} \left[e^{\frac{-unl}{2DN}} \left(\frac{g_{ij}}{\pi m} \sin\left(\frac{mn\pi}{N}\right) + \cos\left(\frac{mn\pi}{N}\right) \right) \right]$$

$$= \quad \mu_{ij}^m \left(k_{ij}^{(1)} - k_{ij}^{(N_{ij})} e^{-g_{ij}} (-1)^m \right) \tag{3.68}$$

$$+ \quad \mu_{ij}^m \sum_{n=1}^{N_{ij}-1} \left[e^{\frac{-n}{N_{ij}} g_{ij}} \left(k_{ij}^{(n+1)} - k_{ij}^{(n)} \right) \left(\frac{g_{ij}}{\pi m} \sin\left(\frac{mn\pi}{N_{ij}}\right) + \cos\left(\frac{mn\pi}{N_{ij}}\right) \right) \right],$$

where

$$\mu_{ij}^m = \frac{8D_{ij}^2 \pi m}{u_{ij}^2 l_{ij}^2 + 4D_{ij}^2 \pi^2 m^2}. \tag{3.69}$$

We are now in a position to find

$$z_{ij}^{(n)}(t) = \frac{N_{ij}}{l_{ij}} \int_{\frac{n-1}{N_{ij}} l_{ij}}^{\frac{n}{N_{ij}} l_{ij}} \tilde{q}_{ij}(x,t) dx, \tag{3.70}$$

as Equation (3.66) implies that

$$\begin{aligned}
z_{ij}^{(n)}(t) &= \frac{N_{ij}}{l_{ij}} \int_{\frac{n-1}{N_{ij}} l_{ij}}^{\frac{n}{N_{ij}} l_{ij}} e^{\frac{g_{ij} x}{l_{ij}}} \sum_{m=1}^{\infty} A^m e^{\lambda_{ij}^m t} \sin\left(\frac{m\pi x}{l_{ij}}\right) dx \\
&= \frac{N_{ij}}{l_{ij}} \sum_{m=1}^{\infty} A^m e^{\lambda_{ij}^m t} \frac{4D^2 l^2}{u^2 l^2 + 4D^2 \pi^2 m^2} \times \\
&\quad \left[e^{\frac{g_{ij} x}{l}} \left(\frac{u}{2D} \sin\left(\frac{m\pi x}{l}\right) - \frac{m\pi}{l} \cos\left(\frac{m\pi x}{l}\right) \right) \right]_{\frac{n-1}{N} l}^{\frac{n}{N} l} \\
&= \frac{N_{ij}}{2} e^{g_{ij} \frac{n}{N_{ij}}} \sum_{m=1}^{\infty} \mu_{ij}^m A^m e^{\lambda_{ij}^m t} \left[\frac{g_{ij}}{\pi m} \left(\sin\left(\frac{mn\pi}{N_{ij}}\right) - e^{\frac{-g_{ij}}{N_{ij}}} \sin\left(\frac{m(n-1)\pi}{N_{ij}}\right) \right) \right. \\
&\quad + \left. \left(e^{\frac{-g_{ij}}{N_{ij}}} \cos\left(\frac{m(n-1)\pi}{N_{ij}}\right) - \cos\left(\frac{mn\pi}{N_{ij}}\right) \right) \right].
\end{aligned} \tag{3.71}$$

Note that $\mu_{ij}^m \to \frac{2}{\pi m}$ as $m \to \infty$, and likewise $A^m \in O(m^{-1})$. In contrast $e^{\lambda_{ij}^m t}$ tends to zero much more rapidly. Indeed, we note that

$$\begin{aligned}
\sum_{m=\Omega'}^{\infty} e^{\lambda_{ij}^m t} &= e^{-\left(\frac{u_{ij}^2}{4D_{ij}} + R_{ij}\right) t} \sum_{m=\Omega'}^{\infty} e^{-\frac{D_{ij}\pi^2 t}{l_{ij}^2} m^2} \\
&< \frac{e^{-\left(\frac{u_{ij}^2}{4D_{ij}} + R_{ij}\right) t}}{\Omega'} \int_{\Omega'}^{\infty} x e^{-\frac{D_{ij}\pi^2 t}{l_{ij}^2} x^2} dx \\
&< \frac{e^{-\left(\frac{u_{ij}^2}{4D_{ij}} + R_{ij}\right) t}}{M} \left[-\frac{l_{ij}^2 e^{-\frac{D_{ij}\pi^2 t}{l_{ij}^2} x^2}}{2D_{ij}\pi^2 t} \right]_M^{\infty} \\
&< \frac{l_{ij}^2}{2\Omega' \pi^2 D_{ij} t} e^{\lambda_{ij}^{\Omega'} t}.
\end{aligned} \tag{3.72}$$

It follows that the relative error

$$\left| \frac{\sum_{m=1}^{\infty} e^{\lambda_{ij}^m t} - \sum_{m=1}^{\Omega'} e^{\lambda_{ij}^m t}}{\sum_{m=1}^{\infty} e^{\lambda_{ij}^m t}} \right| < \frac{\sum_{m=\Omega'}^{\infty} e^{\lambda_{ij}^m t}}{\sum_{m=1}^{\infty} e^{\lambda_{ij}^m t}} < \varepsilon \tag{3.73}$$

whenever we have

$$e^{\lambda_{ij}^{\Omega'} t} < \varepsilon \frac{2\Omega' \pi^2 D_{ij} t}{l_{ij}^2} \sum_{m=1}^{\Omega'} e^{\lambda_{ij}^m t}. \tag{3.74}$$

We can therefore be confident that if we truncate the sum in Equation (3.71) at $m = \Omega'$, the relative errors in our estimates for $z_{ij}^{(n)}(t)$ will be smaller than ε provided that Ω' satisfies Equation (3.74). Also note that Equation (3.66) tells us that if $D_{ij}t > l_{ij}^2$ then $e^{\lambda_{ij}^m t}$ decreases rapidly, so Ω' does not need to be large unless $D_{ij}t \ll l_{ij}^2$. Furthermore, if $u_{ij}^2 t^2 > l_{ij}^2$ then most of the resource will leave edge ij over the time scale t, and $\tilde{q}_{ij}(x,t)$ will only make a small contribution to the total value of $q_{ij}(x,t)$. In that case using a small value of Ω' will produce very accurate estimates for $k_{ij}^{(n)}(t)$ even if $D_{ij}t \ll l_{ij}^2$.

Calculating the total quantity of resource in each segment of a network

Suppose that we wish to calculate the mean concentration per unit length in each segment of a network at time t, such that each part of our final answer has a relative error $\varepsilon < 10^{-0.45\Omega}$, where Ω is an even integer. The first step is to set $s = \Omega \ln 2/t$, and apply Equations (3.54) and (3.55) to find $\beta_{ij}(s)$ and $\beta_{ji}(s)$ for each edge ij. We then compute $\mathbf{M}(s)$ and $\bar{\rho}(s)$, and employ the BiCGStab algorithm to find $\bar{C}(s_\Omega)$, starting with the initial guess that for each i,

$$C_i(s_\Omega) \approx \frac{\tau}{\Omega \ln 2} c_i(0) = \frac{\tau}{\Omega \ln 2} \frac{\sum_j k_{ij}^{(1)}}{\sum_j S_{ij}(0)}. \tag{3.75}$$

This initial guess for the value of $\bar{C}(s_\Omega)$ would be correct if the concentration at the nodes was constant, and making such a guess can help to speed up the process of finding the true value of $\bar{C}(s_\Omega)$. At each step, when we have identified $\bar{C}(s)$ such that $\mathbf{M}(s)\bar{C}(s) = \bar{\rho}(s)$, we store the vector $\bar{C}(s)$ and repeat for $s = s_{\Omega-1}, \ldots, s_1$, where $s_n = n \ln 2/t$. The only difference is that for subsequent applications of the BiCGStab

algorithm, we can take advantage of the approximation

$$C_i(s_n) \approx \frac{n+1}{n} C_i(s_{n+1}). \tag{3.76}$$

This is generally a better initial guess than that provided by Equation (3.75), so the BiCGStab algorithm converges on the solution more rapidly. Given $C_i(s_n)$ and $C_j(s_n)$, we can use Equation (3.56) to calculate $Y_{ij}^{(m)}(s_n)$ for each section in the edge ij. Having found $Y_{ij}^{(m)}(s_n)$ for each $1 \leq n \leq \Omega$, we can apply the Gaver-Stehfest algorithm to obtain $y_{ij}^{(m)}(t)$, and we repeat this process for each edge in the network. Finally, for each edge ij we can use Equations (3.66), (3.69) and (3.69) to calculate a sequence of values for $e^{\lambda_{ij}^m t}$, μ_{ij}^m and A^m until we reach an integer Ω' such that $e^{\lambda_{ij}^{\Omega'} t}$ satisfies Equation (3.74). We then employ Equation (3.71) to find $z_{ij}^{(1)}(t), \ldots, z_{ij}^{(N_{ij})}(t)$ (the mean quantity of resource in ij that has not reached a node), and note that for each section of the network the mean quantity of resource per unit length

$$k_{ij}^{(n)}(t) = y_{ij}^{(n)}(t) + z_{ij}^{(n)}(t). \tag{3.77}$$

Unless there are many sections in each edge, finding the vectors $\bar{C}(s)$ such that $\mathbf{M}(s)\bar{C}(s) = \bar{\rho}(s)$ is the most time consuming step of the computation, as it involves solving m simultaneous, linear equations, where m is the number of nodes. We also note that Equation (3.24) implies that if h_{ij} is larger than 10 (say), then the matrix $\mathbf{M}(s)$ may be close to singular, making it computationally difficult to calculate $\bar{C}(s)$. Fortunately this problem is easy to avoid, as we can simply introduce an additional node k at the midpoint of edge ij. This increases the size of the matrix $\mathbf{M}(s)$, but the lengths l_{ik} and l_{kj} will be half the length l_{ij}. As we have seen, the ratio $\mathbf{M}_{ij}(s) : \mathbf{M}_{ji}(s)$ is equal to $1 : e^{2g_{ij}}$ (where $g_{ij} = \frac{u_{ij} l_{ij}}{2D_{ij}}$), so adding additional nodes greatly reduces the ratio between the entries of $\mathbf{M}(s)$, and can make it significantly easier to find the vector $\bar{C}(s)$.

In the case where we wish to find the concentration of resource in a changing network (see Section 4.2), we simply vary all the parameters in a stepwise manner, finding the distribution of resource at the end of each time step, and treating that distribution as an initial condition for the following time step. The terms $k_{ij}^{(n)}(t)$

provide an exact solution for the quantity of resource in the given region at time t, so this approximation does not lead to significant errors unless the spatial resolution is such that a single term $k_{ij}^{(n)}(t)$ summarizes the concentration in a region with a significant concentration gradient. Modelling changing cross-sectional areas as step-wise constant might also produce errors, but in the following section I outline a variant of this algorithm in which the cross-sectional areas vary continuously over time. However, in the case of the fungal networks that are analyzed in Chapter 4, both approaches yield very similar results.

3.8 Resource Distribution in a Changing Network.

In this section we describe how we calculate the spatial distribution of resource in a network of tubes with cross sectional areas that vary over time, where the resource in question is lost or delivered out of the network at a given rate, while being subject to advection and diffusion. More specifically, we consider the case where each cross-sectional area $S_{ij}(t)$ varies monotonically over time, while the lengths l_{ij}, mean velocities u_{ij}, local delivery rates R_{ij} and dispersion coefficients D_{ij} remain constant. Equation (3.1) tells us that the dispersion coefficients D_{ij} will be constant and equal to the molecular diffusion coefficient D_m if the edges are sufficiently narrow or the velocities sufficiently low. Alternatively, D_{ij} and u_{ij} would remain constant despite the changing cross-sectional areas in the case where the edges are composed of some variable number of tubes of fixed radius r_{ij}, while the pressure at each node remains constant over time. In that case the conductance of edge ij will be proportional to $S_{ij}(t)$, so the medium-current at time t will be proportional to the pressure drop times $S_{ij}(t)$, and the velocity u_{ij} will be constant.

More generally, if we are considering advection, diffusion and delivery over a network where the parameters u_{ij}, S_{ij}, R_{ij} and D_{ij} change over time, it is reasonable to assume that u_{ij}, R_{ij} and D_{ij} are piece-wise constant provided that the time scales for transiting the edges ij are small compared to the time scales over which u_{ij}, R_{ij} and D_{ij} are changing. For example, in the case of vascular networks the cross-

sectional areas of capillaries, the velocity of blood flow and the rates of resource delivery may vary over time, but such changes occur over time scales that are large compared to the time it takes to transit a capillary. In such a case R_{ij} might represent the local rate of glucose delivery per unit of glucose in the blood (for example), and the following algorithm enables us to calculate the concentrations that arise at times t_1, t_2, etc, as we vary $S_{ij}(t)$ in a continuous manner, while u_{ij}, R_{ij} and D_{ij} vary in a stepwise manner, being held constant between each of the time points of interest.

Now, suppose that we want to know how the spatial distribution of resource in a network changes over a time-scale τ. We let $S_{ij}(t)$ denote the area of edge ij at time t, and where $S_{ij}(0)$ and $S_{ij}(\tau)$ are given quantities, it is mathematically convenient to set

$$\begin{aligned} S_{ij}(t) &= \big(2S_{ij}(\tau) - S_{ij}(0)\big) + \big(2S_{ij}(0) - 2S_{ij}(\tau)\big)e^{\frac{-\ln 2}{\tau}t} \\ &= a_{ij} + b_{ij}e^{\frac{-\ln 2}{\tau}t}. \end{aligned} \tag{3.78}$$

By adopting this functional form for $S_{ij}(t)$, we are assuming that the cross-sectional areas S_{ij} vary in an approximately linear manner over the time scale of interest τ. More precisely, the rate of change $\frac{d}{dt}S_{ij}$ halves over the time scale $0 \le t \le \tau$. Also note that if the given cross-sectional areas $S_{ij}(0)$ and $S_{ij}(\tau)$ are non-negative, it follows that $S_{ij}(t) \ge 0$ for all $0 \le t \le \tau$. However, as $t \to \infty$, $S_{ij}(t) \to 2S_{ij}(\tau) - S_{ij}(0)$, which may be negative. Since the value of $S_{ij}(t)$ has little effect on our calculations for $t > \tau$, we are not introducing a major source of error when we allow the possibility of negative values for $S_{ij}(t)$ at time points beyond the time of interest.

Propagation matrices for a changing network

Suppose that the cross-sectional areas $S_{ij}(t)$ are of the form described by Equation (3.78), and u_{ij} and D_{ij} are constant. By definition we have $q_{ij}(x,t) = S_{ij}(t)c_{ij}(x,t)$, so taking Laplace transforms gives us

$$Q_{ij}(x,s) = \mathscr{L}\big(a_{ij}c_{ij}(x,t)\big) + \mathscr{L}\big(b_{ij}e^{\frac{-\ln 2}{\tau}t}c_{ij}(x,t)\big)$$

$$= \quad a_{ij}C_{ij}\big(x,s\big) + b_{ij}C_{ij}\big(x,s+\ln 2/\tau\big). \tag{3.79}$$

We then let $s' = s + \ln 2/\tau$, and define

$$X_{ij}(s) \equiv Q_{ij}(0,s) = a_{ij}C_i(s) + b_{ij}C_i(s') \qquad \text{and} \tag{3.80}$$

$$X_{ji}(s) \equiv Q_{ij}(l_{ij},s) = a_{ij}C_j(s) + b_{ij}C_j(s'). \tag{3.81}$$

Substituting Equations (3.80) and (3.81) into Equation (3.42) tells us that

$$\begin{aligned}\Upsilon_i(s) \quad &= \quad \sum_j \Big(a_{ij}C_i(s) + b_{ij}C_i(s')\Big)\left(\frac{u_{ij}}{2} + \frac{\alpha_{ij}}{2\tanh\big(h_{ij}\big)}\right) \\ &- \quad \sum_j \Big(a_{ij}C_j(s) + b_{ij}C_j(s')\Big)\frac{\alpha_{ij}e^{-g_{ij}}}{2\sinh\big(h_{ij}\big)} \\ &- \quad \sum_j \beta_{ij}(s).\end{aligned} \tag{3.82}$$

In matrix form we have the equivalent of Equation (3.44):

$$\mathbf{V}(s)\bar{C}(s) + \mathbf{W}(s)\bar{C}(s+\ln 2/\tau) = \bar{\rho}(s), \tag{3.83}$$

$$\text{where} \quad \bar{C}(s) = \{C_1(s), C_2(s), \ldots, C_m(s)\}^{\mathrm{T}}, \tag{3.84}$$

$$\rho_i(s) = \Upsilon_i(s) + \sum_j \beta_{ij}(s), \tag{3.85}$$

$$\mathbf{V}_{ij}(s) = \begin{cases} \sum_k a_{ij}\left[\frac{u_{ik}}{2} + \frac{\alpha_{ik}}{2\tanh(h_{ik})}\right] & \text{if } i = j, \\ \frac{-a_{ij}\alpha_{ij}e^{-g_{ij}}}{2\sinh\big(h_{ij}\big)} & \text{otherwise,} \end{cases} \tag{3.86}$$

and

$$\mathbf{W}_{ij}(s) = \begin{cases} \sum_k b_{ij}\left[\frac{u_{ik}}{2} + \frac{\alpha_{ik}}{2\tanh(h_{ik})}\right] & \text{if } i = j, \\ \frac{-b_{ij}\alpha_{ij}e^{-g_{ij}}}{2\sinh\big(h_{ij}\big)} & \text{otherwise.} \end{cases} \tag{3.87}$$

Calculating $\bar{C}(s)$ in a changing network

To find the boundary conditions $X_{ij}(s)$ and $X_{ji}(s)$ for each edge, we must first calculate the Laplace transform of the concentration at each node. Furthermore, in order to apply the Gaver-Stehfest algorithm, we need to calculate $\bar{C}(s)$ for $s = s_1, \ldots, s_\Omega$ where $s_n = n \ln 2/\tau$. As in the case where the cross-sectional areas of the network remain constant, we can calculate $\mathbf{V}(s)$, $\mathbf{W}(s)$ and $\bar{\rho}(s)$ for any positive integer s. Since $s_{n+1} = s_n + \ln 2/\tau$, we can use Equation (3.83) to relate the vectors $\bar{C}(s_{n+1})$ and $\bar{C}(s_n)$. That is to say, for each n we have

$$\mathbf{V}(s_n)\bar{C}(s_n) = \bar{\rho}(s_n) - \mathbf{W}(s_n)\bar{C}(s_{n+1}). \tag{3.88}$$

To begin this iterative process of finding $\bar{C}(s_n)$ from $\bar{C}(s_{n+1})$, we must first estimate the value of $\bar{C}(s_\Omega)$ for some integer Ω. In finding such an approximation the first point to note is that the value of $C_i(s_\Omega)$ is predominantly determined by the value of $c_i(t)$ over the time-scale $0 \le t \le \frac{\tau}{\Omega}$: the value of $c_i(t)$ for $t > \frac{\tau}{\Omega}$ is relatively inconsequential.

The second point to note is that by Equation (3.78), the cross-sectional area at time $\frac{\tau}{\Omega}$ is

$$\begin{aligned} S_{ij}\big(\frac{\tau}{\Omega}\big) &= \big(2S_{ij}(\tau) - S_{ij}(0)\big) + \big(2S_{ij}(0) - 2S_{ij}(\tau)\big)e^{\frac{-\ln 2}{\Omega}} \\ &= S_{ij}(0)\big(2^{\frac{\Omega-1}{\Omega}} - 1\big) + S_{ij}(\tau)\big(2 - 2^{\frac{\Omega-1}{\Omega}}\big). \end{aligned}$$

If $\Omega = 13$ (say), we have $S_{ij}\big(\frac{\tau}{\Omega}\big) \approx 0.9S_{ij}(0) + 0.1S_{ij}(\tau)$. We can estimate $C_i(s_\Omega)$ by assuming that the cross-sectional area of each edge does not vary over time, but remains constant at $S_{ij}\big(\frac{\tau}{\Omega}\big)$. This enables us to apply Equation (3.44), and thereby obtain an estimate for $C_i(s_\Omega)$. For each node i we make the initial guess that

$$C_i(s_\Omega) = \int_0^\infty c_i(t)e^{\frac{-\Omega \ln 2}{\tau}t}dt \quad \approx \quad \frac{\tau}{\Omega \ln 2}c_i(0), \tag{3.89}$$

(an approximation that would hold exactly if the concentration at the nodes remained constant). We can then employ the BiCGStab algorithm to home in on a more accurate solution to $\mathbf{M}(s_\Omega)\bar{C}(s_\Omega) = \bar{\rho}(s_\Omega)$. Once we have obtained an estimate for $\bar{C}(s_\Omega)$,

we can employ Equation (3.88) to find $\bar{C}(s_{\Omega-1}),\ldots,\bar{C}(s_1)$. Also note that when the relative change in cross-sectional area is small, b_{ij} is small compared to a_{ij}, so the elements in the vector $\mathbf{W}(s_{n+1})\bar{C}(s_n)$ are small compared to the corresponding elements in $\mathbf{V}(s_n)\bar{C}(s_n)$ and $\bar{\rho}(s_n)$. This means that when the relative change in cross-sectional area is small, any errors in our estimate for $\bar{C}(s_\Omega)$ have little effect on the calculated values for $\bar{C}(s_{\Omega-1})$.

Advection, diffusion and delivery in a changing network

We now combine the preceding observations, and present an algorithm for calculating the concentration in each section of a network with changing cross-sectional areas after a given time τ. More specifically, we suppose that for each edge in our network the mean velocity u_{ij} and the dispersion coefficient D_{ij} remain constant, while the cross-sectional areas $S_{ij}(t)$ vary smoothly from $S_{ij}(0)$ to $S_{ij}(\tau)$ in accordance with Equation (3.78). The first step in our algorithm is to pick an odd integer Ω. This determines the scale of the errors in our final answer, and the ratio of the errors to the true values which will be of the order $\varepsilon = 10^{-0.45(\Omega-1)}$. As a rule of thumb setting $\Omega = 13$ and using standard double precision for the weights κ_n will ensure that the our final answers are accurate to at least three significant digits.

We let $s_\Omega = \frac{\Omega \ln 2}{\tau}$ and assume that the cross-sectional area of edge ij is held constant at $S_{ij}\left(\frac{\tau}{\Omega}\right)$. These cross-sectional areas can be used to find a propagation matrix $\mathbf{M}(s_\Omega)$, as described by Equation (3.44). Furthermore, the given initial condition can be used to calculate $\bar{\rho}(s_\Omega)$, as described by Equations (3.46), (3.54) and (3.55).

Equation (3.44) tells us that $\mathbf{M}(s_\Omega)\bar{C}(s_\Omega) = \bar{\rho}(s_\Omega)$, so we are now in a position to find $\bar{C}(s_\Omega)$ by employing the BiCGStab algorithm, starting with the initial guess that for each i,

$$C_i(s_\Omega) \approx \frac{\tau}{\Omega \ln 2} c_i(0) = \frac{\tau}{\Omega \ln 2} \frac{\sum_j k_{ij}^{(1)}}{\sum_j S_{ij}(0)}. \tag{3.90}$$

If the concentration at the nodes remained constant, this estimate would equal the exact solution. Once we have run the BiCGStab algorithm, we store the vector

$\bar{C}(s_\Omega)$, and use Equations (3.44), (3.54), (3.55), (3.86) and (3.87) to find $\mathbf{V}(s_n)$, $\mathbf{W}(s_n)$ and $\bar{\rho}(s_n)$ where $n = \Omega - 1$.

These matrices are related to one another by Equation (3.88), so once again we can employ the BiCGStab algorithm to find $\bar{C}(s_n)$. As in the case of a network with constant cross-sectional areas, the matrices tend to be close to singular if any of the terms $\frac{l_{ij}\alpha_{ij}(s)}{2D_{ij}}$ are large (greater than 10, say). This makes it computationally difficult to calculate $\bar{C}$, but this problem is easy to avoid as we can simply introduce additional nodes along the edge ij, thereby reducing the lengths l_{ij}. Having described the network in terms of nodes and sufficiently short edges, we start the BiCGStab algorithm with the initial guess that for each i,

$$C_i(s_n) \approx \frac{n+1}{n} C_i(s_{n+1}). \tag{3.91}$$

This process is iterated until we have found $\bar{C}(s_\Omega), \ldots, \bar{C}(s_1)$. Now, for each edge and each integer $n = \Omega - 1, \ldots, 1$, we can use Equations (3.80) and (3.81) to find the boundary conditions $X_{ij}(s_n)$ and $X_{ji}(s_n)$. As in the case of constant cross-sectional areas, the Laplace transform of resource that has reached a node is denoted by $Q_{ij}^N(x, s_n)$, and this quantity is related to $X_{ij}(s_n)$ and $X_{ji}(s_n)$ by Equation (3.19). We can therefore use Equation (3.56) to find $Y_{ij}^{(n)}(s) = \mathscr{L}\left(y_{ij}^{(n)}(t)\right)$, the mean value of $Q_{ij}^N(x,s)$ in the n'th section of the edge ij.

Having found $Y_{ij}^{(n)}(s)$ for each section in the network, we can apply the Gaver-Stehfest algorithm to obtain $y_{ij}^{(n)}(t)$. Finally, we note that the quantity of resource within each edge only changes because of advection, diffusion and delivery. Varying the cross-sectional area of an edge will affect the quantity of resource that enters that edge, but it will not directly affect the quantity or distribution of resource that remains in ij without reaching nodes i or j over the time-scale t. For example, if an edge ij is shrinking and the fluid within ij is leaving that edge, it is assumed that the effect of this mass flow is entirely captured by calculating the appropriate velocity term u_{ij}. Given that this is so, for each edge ij we can use Equations (3.65), (3.69) and (3.69) to calculate a sequence of values for $e^{\lambda_{ij}^m t}$, μ_{ij}^m and A^m until we reach an integer Ω' such that $e^{\lambda_{ij}^{\Omega'} t}$ satisfies Equation (3.74). This ensures that when we

employ Equation (3.71) to find $z_{ij}^{(1)}(t), \ldots, z_{ij}^{(N_{ij})}(t)$ (the mean quantity of resource in ij that has not reached a node), the errors are very small. Finally, we note that for each section of the network the mean quantity of resource per unit length

$$k_{ij}^{(n)}(t) = y_{ij}^{(n)}(t) + z_{ij}^{(n)}(t). \tag{3.92}$$

Resource distribution with fixed and varying cross-sectional areas

We have presented two algorithms for calculating the concentration in a network as it changes over time, with resource subject to advection, diffusion and local delivery out of the network. In the first, cross-sectional areas and the medium-currents in each edge change in a stepwise manner, while in the second the cross-sectional areas and medium-currents in each edge vary continuously. The former algorithm is about twice as fast, and experimentation indicates that it is more numerically stable.

By design, the total medium-current to pass through each edge in a given time step is the same whether the cross-sectional areas vary continuously or in a stepwise manner. Consequently, if the concentration at each node does not change dramatically over a given time step, the amount of resource to pass through each edge over the time step in question will be similar whichever of the two algorithms we apply. However, the two algorithms may give very different results for the concentration profile within a given edge, if there is a difference in the initial concentration at the nodes at either end.

3.9 Alternate Methods of Solution

In the preceding sections I described an efficient method for calculating the changing distribution of resource throughout a given network, where the resource in question is subject to advection, diffusion and delivery. There are several methods that could be applied to solve such a system of equations, and as a check on the Laplace transform method and my computer program for implementing that method, I also wrote a program that utilizes a different (less efficient) method. One alternative to taking

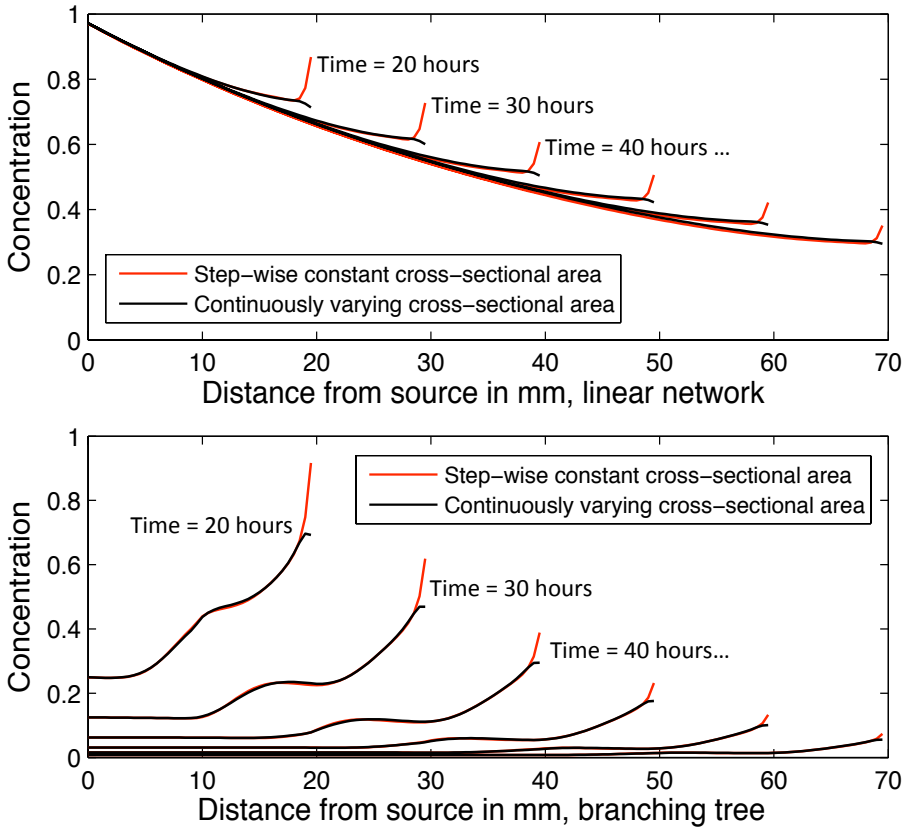

Figure 3.3: **Concentration in a linear network and branching tree.** In each case resource is added at the source at a constant rate, the local delivery rate throughout each network is 0.02 hour^{-1}, and the diffusion coefficient is $D_m = 6.7 \times 10^{-4}$mm^{2}s^{-1}. Every hour, both networks grow 1mm further from the source, and the branching tree bifurcates every 10mm. The cross-sectional area of each new edge either varies in a stepwise manner from 0 to 6μm (red lines), or the cross-sectional area varies continuously from 0 to 6μm (black lines). Note that the same amount of resource is contained within the linear network and the branching tree, but the branching tree has a greater volume. After 70 hours the mean concentration in the linear network is over 18 times greater than the mean concentration in the branching tree, but the concentration near the tips is only about 5 times as great.

Laplace transforms is to model the movement of resource by taking a particle based approach, where a large number of particles move across the network, and the path taken by each particle is determined probabilistically, as is the time taken to travel from one node to the next [168].

The problem with such particle based approaches is the challenge of avoiding under-sampling in the regions of the network that contain a low concentration of resource. This problem occurs because, in a finite simulation, the low probability

paths are of course less well sampled, but the fact that such regions are part of the network may exert a significant effect on the movement of resource, particularly on the higher moments of the transit-times for particles moving across the network [65, 122, 158]. Indeed, that is why the dispersion of tracers can be used to probe the structure of networks, and why tracer dispersion plays such a critical role in geophysical surveying techniques [131, 167, 168].

Another possible approach is to employ a finite difference scheme. However, in a network where the transport velocities vary over several orders of magnitude, straight-forward applications of such an approach are not efficient. The problem is that the time scale for updating the concentrations is essentially determined by the fastest edge; for stability the distance travelled by advection per time step must be smaller than the spatial resolution (i.e. the Courant number must be less than one). Using such a small time step may be very inefficient in the slower moving regions of the network [60, 176].

Finite difference methods

To solve Equation (3.2) by finite difference methods, we let $c(x,t)$ denote the concentration at point x at time t, and suppose that $x^{(i-1)}$, $x^{(i)}$, $x^{(i+1)}$, ... are points in space Δx apart, while times t_{j-1}, t_j, t_{j+1}, ... are Δt apart. The central difference approximation tells us that

$$\left.\frac{\partial c}{\partial x}\right|_{x^{(i)},t_j} \approx \frac{c(x^{(i+1)},t_j)-c(x^{(i-1)},t_j)}{x^{(i+1)}-x^{(i-1)}} = \frac{c(x^{(i+1)},t_j)-c(x^{(i-1)},t_j)}{2\Delta x}. \tag{3.93}$$

The second derivative at the point $x^{(i)}$ may be approximated by using the formula $\frac{\partial^2 c}{\partial x^2} = \lim_{\Delta x\to 0}\frac{\Delta\left(\frac{\partial c}{\partial x}\right)}{\Delta x}$. We can evaluate this derivative at the (fictitious) points $x^{(i+\frac{1}{2})}, x^{(i-\frac{1}{2})}$, defined in the obvious way. Then by using the central difference approximations for the spatial derivatives evaluated at these points, we find that

$$\left.\frac{\partial c}{\partial x}\right|_{x^{(i+\frac{1}{2})},t_j} \approx \frac{c(x^{(i+1)},t_j)-c(x^{(i)},t_j)}{\Delta x}, \qquad \text{and}$$

$$\left.\frac{\partial c}{\partial x}\right|_{x^{(i-\frac{1}{2})},t_j} \approx \frac{c(x^{(i)},t_j)-c(x^{(i-1)},t_j)}{\Delta x}.$$

This implies that

$$\frac{\partial^2 c}{\partial x^2} \approx \frac{\left.\frac{\partial c}{\partial x}\right|_{x^{(i+\frac{1}{2})}} - \left.\frac{\partial c}{\partial x}\right|_{x^{(i-\frac{1}{2})}}}{x^{(i+\frac{1}{2})} - x^{(i-\frac{1}{2})}} = \frac{c(x^{(i+1)},t_j) - 2c(x^{(i)},t_j) + c(x^{(i-1)},t_j)}{(\Delta x)^2}. \tag{3.94}$$

We can approximate derivatives with respect to time in the same way. For example, the forward difference approximation for $\partial c/\partial t$ at the point (x_i,t_j) is

$$\left.\frac{\partial c}{\partial t}\right|_{x^{(i)},t_j} \approx \frac{c(x^{(i)},t_{j+1}) - c(x^{(i)},t_j)}{t_{j+1}-t_j} = \frac{c(x^{(i)},t_{j+1}) - c(x^{(i)},t_j)}{\Delta t}.$$

For each edge ik, we let $x_{ik}^{(1)},\ldots,x_{ik}^{(N)}$ denote the sequence of points from node i to node j (see Fig. 3.4). Furthermore, Fick's Law tells us the flux at point x is $u\frac{\partial c}{\partial x} - D\frac{\partial^2 c}{\partial x^2}$. As the volume of each 'point' is $\Delta x S_{ik}$, Fick's Law, Equation (3.93) and Equation (3.94) imply that between time t_j and t_{j+1}, the quantity of resource that leaves 'point' $x_{ik}^{(n)}$ to pass into 'point' $x_{ik}^{(n-1)}$ is equal to

$$c(x_{ik}^{(n)},t_j)S_{ik}\Delta x\left(D_{ik}\frac{\Delta t}{(\Delta x)^2} - \frac{u_{ik}}{2}\frac{\Delta t}{\Delta x}\right). \tag{3.95}$$

Likewise, the quantity of resource that leaves point $x_{ik}^{(n)}$ for $x_{ik}^{(n+1)}$ is equal to

$$c(x_{ik}^{(n)},t_j)S_{ik}\Delta x\left(D_{ik}\frac{\Delta t}{(\Delta x)^2} + \frac{u_{ik}}{2}\frac{\Delta t}{\Delta x}\right). \tag{3.96}$$

Note that these equations do not include the term R_{ik}. They are derived from Fick's Law, and they imply that the total flux at point $x_{ik}^{(n)}$ and time t_j is

$$D_{ik}\frac{c(x^{(i+1)},t_j) - 2c(x^{(i)},t_j) + c(x^{(i-1)},t_j)}{(\Delta x)^2} - u_{ik}\frac{c(x^{(i+1)},t_j) - c(x^{(i-1)},t_j)}{2\Delta x}.$$

In the case where $R_{ik} = 0$ the finite difference scheme ought to conserve the total quantity of resource. We also assume that for every pair of edges ik and in and at every time point t, we have $c(x_{ik}^{(1)},t) = c(x_{in}^{(1)},t)$. In other words, we assume that the concentration at node i is consistent over all of the edges $ik,\ldots,in$. At time t_j, the total amount of resource in the 'points' $x_{ik}^{(1)},\ldots,x_{in}^{(1)}$ is $\sum_k c(x_{ik}^{(1)},t_j)S_{ik}\Delta x$. For each edge ik we know how much resource is passed between points $x_{ik}^{(1)}$ and $x_{ik}^{(2)}$, so by

the conversation of resource we have

$$c(x_{ik}^{(1)},t_{j+1}) = \frac{1}{\sum_k S_{ik}}\sum_k \Bigg[c(x_{ik}^{(1)},t_j)S_{ik}\big(1-D_{ik}\frac{\Delta t}{(\Delta x)^2}-\frac{u_{ik}}{2}\frac{\Delta t}{\Delta x}\big) + c(x_{ik}^{(2)},t_j)S_{ik}\big(D_{ik}\frac{\Delta t}{(\Delta x)^2}-\frac{u_{ik}}{2}\frac{\Delta t}{\Delta x}\big)\Bigg]. \quad (3.97)$$

In the case where resource enters the network at node i at a rate $U(i)$, over time Δt a total of $U(i)\Delta t$ is added to the network, and that resource is spread between the points $x_{ik}^{(1)},\ldots,x_{in}^{(1)}$. It follows that we have

$$c(x_{ik}^{(1)},t_{j+1}) = \frac{1}{\sum_k S_{ik}}\Bigg(U(i)\frac{\Delta t}{\Delta x}+\sum_k \Bigg[c(x_{ik}^{(1)},t_j)S_{ik}\big(1-D_{ik}\frac{\Delta t}{(\Delta x)^2}-\frac{u_{ik}}{2}\frac{\Delta t}{\Delta x}\big) + c(x_{ik}^{(2)},t_j)S_{ik}\big(D_{ik}\frac{\Delta t}{(\Delta x)^2}-\frac{u_{ik}}{2}\frac{\Delta t}{\Delta x}\big)\Bigg]\Bigg). \quad (3.98)$$

We now consider the case where $R_{ik}\neq 0$, and note that over a short period of time Δt, a fraction $R_{ik}\Delta t$ of the resource in edge ik will be delivered out of the network. It follows from Equations (3.95) and (3.96) that when $x_{ik}^{(n)}$ is a point with two neighbours, we have

$$\begin{aligned} c(x_{ik}^{(n)},t_{j+1}) &= c(x_{ik}^{(n)},t_j)\big(1-R_{ik}\Delta t\big)\big(1-2D_{ik}\frac{\Delta t}{(\Delta x)^2}\big) \\ &+ c(x_{ik}^{(n+1)},t_j)\big(1-R_{ik}\Delta t\big)\big(D_{ik}\frac{\Delta t}{(\Delta x)^2}-\frac{u_{ik}}{2}\frac{\Delta t}{\Delta x}\big) \\ &+ c(x_{ik}^{(n-1)},t_j)\big(1-R_{ik}\Delta t\big)\big(D_{ik}\frac{\Delta t}{(\Delta x)^2}+\frac{u_{ik}}{2}\frac{\Delta t}{\Delta x}\big). \end{aligned} \quad (3.99)$$

If resource is added to node i at a constant rate $U(i)$ for a period of time Δt, a fraction $R_{ik}\frac{\Delta t}{2}$ of that resource will be delivered out of the network. Equation (3.97) therefore implies that at the points $x_{ik}^1,\ldots,x_{in}^1$,

$$\begin{aligned} c(x_{ik}^{(1)},t_{j+1}) &= \frac{1}{\sum_k S_{ik}}\Bigg(U(i)\frac{\Delta t}{\Delta x}\Big(1-R_{ik}\frac{\Delta t}{2}\Big) \\ &+ \sum_k \Bigg[c(x_{ik}^{(1)},t_j)S_{ik}\big(1-R_{ik}\Delta t\big)\big(1-D_{ik}\frac{\Delta t}{(\Delta x)^2}-\frac{u_{ik}}{2}\frac{\Delta t}{\Delta x}\big) \\ &+ c(x_{ik}^{(2)},t_j)S_{ik}\big(1-R_{ik}\Delta t\big)\big(D_{ik}\frac{\Delta t}{(\Delta x)^2}-\frac{u_{ik}}{2}\frac{\Delta t}{\Delta x}\big)\Bigg]\Bigg). \end{aligned} \quad (3.100)$$

This scheme is consistent in the sense that the finite difference approximations have a truncation error that approaches zero as $\Delta t\to 0$, $\Delta x\to 0$. Moreover, it can

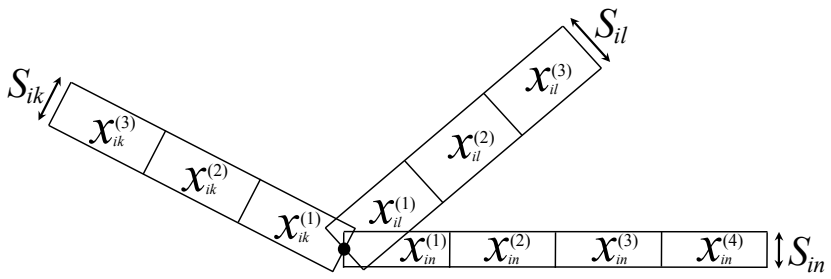

Figure 3.4: **Finite difference scheme over a network.** By assumption, the concentration is the same at each of the points $x_{ik}^{(1)},\ldots,x_{in}^{(1)}$.

be shown [176] that this scheme is convergent to the exact solution and does not magnify errors provided that

$$\Delta x < \frac{2D}{|u|} \tag{3.101}$$

(so the Péclet number at the scale Δx is small, and diffusion dominates the transport of resource between adjacent points),

$$\frac{D\Delta t}{(\Delta x)^2} < 1/2 \tag{3.102}$$

(so there is not too much diffusion between neighbours per time step), and

$$R\Delta t \ll 1 \tag{3.103}$$

(so resource delivery is accurately modelled). Finally, it is essential that the resource does not travel by advection further than Δx in time Δt, which is to say that the Courant number $|u|\frac{\Delta t}{\Delta x}$ must be less than one [60]. In fact, Hindmarsh and Sousa [104, 178] have shown that in order for the scheme to be stable, we require

$$\left(\frac{u\Delta t}{\Delta x}\right)^2 \leq 2\frac{D\Delta t}{(\Delta x)^2} < 1. \tag{3.104}$$

Note the coarsest spatial resolution that produces a stable scheme is given by Equation (3.101). For any given spatial resolution Δx, Equations (3.102) and (3.104) imply that in order to be stable, we must have

$$\Delta t < \min\left(\frac{\Delta x^2}{2D}, \frac{2D}{u^2}\right). \tag{3.105}$$

Experiments with radio-labelled tracers and our model of growth-induced mass flows both indicate that the velocity of flow in some fungal cords is of the order 0.01mms^{-1} [42, 49, 95, 100, 115]. Furthermore, as we shall see in Chapter 4, when modelling the movement of ^{14}C-labeled α aminoisobutyric acid (AIB) through a fungal network, we let $D_m = 3.5 \times 10^{-4}\text{mm}^2\text{s}^{-1}$ [194]. Equation (3.101) tells us that our spatial resolution must be such that $\Delta x < 0.07$mm, or diffusion would not dominate, and we would incorrectly calculate how resource leaves each node. Given these values for Δx, D and u, Equation (3.105) implies that we require a temporal resolution such that $\Delta t < 3$s. The time scale of delivery in fungal networks is of the order of days or weeks, and so at that temporal resolution, a very small fraction of the resource is delivered per time step, and to avoid error it is necessary to store the concentrations at high precision.

The fungal networks that we are analyzing are tens of centimeters wide, and the total length of cords within our digitized networks was 8.3m in Experiment 1, 12.2m in Experiment 2 and 12.5m in Experiment 3. Furthermore, the networks grow over a period of weeks, and the radio-label experiments take days to complete, so modelling those experiments by finite difference methods would require a vector of more than 10^5 data points, which is updated about 10^5 times. Even greater precision would be required to obtain an accurate solution, as the above limits only guarantee convergence, not accuracy [104, 176, 178]. It is much more efficient to operate in Laplace space, and so that is the approach that we adopt.

Chapter 4

Nutrient Transport in Fungal Networks

The mobility of nitrogen and phosphate within fungal networks is crucial to their roles as decomposers and root symbionts [33, 50, 86, 196]. Fungi specialized to utilize wood show a number of nitrogen-conserving strategies, including nitrogen recycling from old to new mycelium [129, 196], selective depletion of cell materials under nitrogen starvation and the ability to utilize and select between many different chemical compounds of nitrogen [47]. The uptake and translocation of phosphate is also critical, and there is some evidence to suggest that the phosphate within fungal cords is relatively immobile [56]. The relative absence of translocation of phosphate after influx into the cord may reflect immediate storage of phosphate within the hyphae, possibly as polyphosphate, or within some compartment not readily accessible to the translocation stream.

In the preceding chapters we have argued that the fungal body or mycelium can be understood as a network of fluid filled tubes or hyphae, which grow by osmotically drawing water from their surroundings while adding material to the cell wall specifically at the tips of the growing hyphae [20, 21, 22, 23, 66, 135]. As the network grows there is water uptake from the inoculum. Because aqueous fluids are incompressible, it follows that there is a mass flow from the sites of water uptake to the sites of growth [100]. In this chapter we investigate the claim that this form of growth-induced mass flow is sufficient to supply the growing tips with the re-

sources they require. We do this by modelling advection, diffusion and delivery over empirically determined fungal networks, and by comparing model predictions with experimental data gathered using radio-labeled tracers. Our results lead us to suggest that in foraging fungi, growth-induced mass flow is sufficient to account for long distance transport, if the system is well insulated. This analysis supports the conclusion that additional, active transport mechanisms may only be required at the very end of the transport pathway, near the growing tips.

4.1 Experimental Evidence for Transport in Fungi

Many species of fungi are capable of foraging in heterogeneous environments [27, 32, 41, 66, 77, 78, 81, 146]. In order to grow over a metabolically inert substrate, some kind of transport process is required to move the resources needed for growth from the source of nutrients, to the growing margin. Diffusion may be sufficient to sustain short-range local growth when resources are abundant, but foraging fungi such as *Phanerochaete velutina* can grow hundreds of millimeters away from a food source over metabolically inert surfaces [27, 49, 147].

These observations strongly suggest that long-distance transport mechanisms are required to deliver nutrients to the growing tips at a sufficient rate, though there are many open questions concerning the mechanism(s) of transport involved [38, 49, 62, 115, 127, 147]. Vesicles moved by motor proteins [180, 181], contractile elements [115], diffusion through the vacuole system [62] and carefully regulated osmotic gradients [49, 115] have all been proposed as mechanisms for driving long range transport in fungi. Though a fundamental physiological question, which (if any) of these mechanisms is important is still a topic of debate.

Mass flows within apical hyphae can be observed directly, using a pressure-probe apparatus to impale the hyphae and inject droplets of a low-viscosity silicone oil to observe flow of the cytoplasm [126]. These inert droplets move at the same rate as the other contents of the hyphae, indicating that a mass flow of fluid is responsible for much of the observed motion, not motor proteins, the cytoskeleton

or some other specific interaction. At the microscopic scale GFP tagged proteins, chemical stains and quantum dots [49, 115, 126, 208] suggest that hyphae contain advecting fluid, and that near the tips fungi employ active transport mechanisms (eg. there is interaction between lipid vesicles, motor proteins and the cytoskeleton). In particular, there is evidence that microtubule related motor proteins play a role in nuclear migration and positioning in filamentous fungi [110, 150, 183, 210], but live imaging of growing hyphae of *N. crassa* and other fungal species indicates that mass flow of the cytoplasm is the dominant factor driving nuclear translocation [126, 154]. At a larger scale, radio-labelled carbon and phosphate have been observed to move over distances and time scales that cannot be explained by diffusion alone [42, 43, 49, 56, 57, 83, 95, 115, 130, 147, 187, 188, 191, 197, 198], and they provide an experimental system to evaluate model predictions.

We have imaged the pattern of nutrient transport by adding the non-metabolised ^{14}C-labeled amino-acid analogue, α aminoisobutyric acid (AIB) to the inoculum. A semi-translucent scintillation screen was gently placed onto the fungal network and movement of the radio-label was imaged using a photon-counting camera [83, 190, 191, 196]. As AIB is not metabolized, the ^{14}C-label faithfully reports the distribution of the amino acid analogue, and so the density of photons arriving from each region of the network can be used to estimate the distribution of AIB (see Fig. 4.1b). To obtain intensity values for each edge, the digitized network was aligned with the image from the photon counting camera and used to sample pixel intensities on each of the links. The empirically determined intensities could then be compared with the predictions of the advection, diffusion, delivery (ADD) model.

4.2 Modelling Advection, Diffusion and Delivery of Radio-labelled AIB

Transportation of radio-labelled AIB in *P. Velutina*

The empirical data consist of a pair of networks where each edge has a length and

volume at time T and time $T+\tau$. We wish to make a prediction for the total number of photons emitted from each edge, which we assume is proportional to mean concentration of radio-labeled AIB over the time period in question. The prediction of our ADD model is based on the following assumptions:

1. The edges in our fungal networks are composed of bundles of hyphae and transport vessels [75], as described in Section 2.1. We therefore assume that mass flows occur in transport vessels of radius 6μm, which occupy some fraction λ of the cross-sectional area of each edge.

2. We let the diffusion coefficient $D_m = 3.5 \times 10^{-6}\text{cm}^2\text{s}^{-1}$, which is the diffusion coefficient of AIB in water [194], and we use Equation (3.1) to calculate the dispersion coefficient D_{ij} for each edge.

3. Growing edges are sinks for fluid, while shrinking edges and the inoculum are sources, as described in Section 2.4. It is assumed that each edge continues to grow or shrink at the rate that was measured between times T and $T+\tau$.

4. The hydraulic conductance of each edge is assumed to be proportional to its cross-sectional area at time $T+\tau$, and given the distribution of sources and sinks, circuit theory is used to calculate the current in each edge (see Section 2.4).

5. We assume that radio-labeled AIB enters the network at the inoculum at a constant rate, and as AIB is not metabolized (and there is negligible decay of ^{14}C), we let the local delivery rate $R = 0.05$ day^{-1}, though very similar results are obtained for any small value of R. The rate of AIB uptake at the inoculum does not affect the relative concentration of points in the network, and we assume that the number of photons leaving node i between times T and $T+\tau$ is proportional to $\int_T^{T+\tau} c_i(t)dt$, where $c_i(t)$ denotes the concentration at node i at time t.

We let $c_i'(t) = c_i(T+t)$, and note that by definition, $\int_T^{T+\tau} c_i(t)dt$ is equivalent to the convolution of $c_i'(t)$ with the unit function. The convolution theorem [124] therefore implies that

$$\mathscr{L}\Big(\int_0^{\tau} c_i(t)dt\Big) = \frac{1}{s}\mathscr{L}\big(c_i'(\tau)\big). \tag{4.1}$$

The method described in Section 3.3 enables us to find $C_i(s) = \mathscr{L}\big(c_i'(\tau)\big)$ for $s = \frac{\ln 2}{\tau}, \ldots n\frac{\ln 2}{\tau}$, and so by Equation (4.1) we can find $\mathscr{L}\big(\int_T^{T+\tau} c_i(t)dt\big)$ for $s = \frac{\ln 2}{\tau}, \ldots n\frac{\ln 2}{\tau}$. We can therefore use the Gaver-Stehfest algorithm to calculate $\int_T^{T+\tau} c_i(t)dt$, and we assume that the mean concentration in edge ij is halfway between the mean concentrations at nodes i and j.

Comparing predictions of the ADD model to empirical data

Although the mycelium formed a branching network spanning most of the microcosm, the distribution pattern for ^{14}C-AIB was remarkably asymmetric, with high levels in part of the network growing in the lower left quadrant, lower levels in the lower right quadrant and almost none in the upper quadrants, apart from one short section of cord. The explanation for this behaviour is not readily apparent from the static architecture of the network, as regions with low label still have substantial cords. However, when the growth of the network over the last time step is considered using the ADD model, there is an impressive degree of congruency between the model predictions for different values of λ and the empirical determination of nutrient distribution (see Fig. 4.1).

In the experiment shown in Fig. 4.1, if we exclude those points in the network that are not covered by the scintillation screen, 29% of points emit photons at a rate greater than the mean background intensity plus three standard deviations. In the case of the ADD model where we set $\lambda = 0.1$, 27% of the points in the network are predicted to have a mean intensity that is significantly greater than zero. That fraction drops to 17% when we let $\lambda = 0.2$. In a duplicate experiment, 28% of points contain enough AIB to produce a significant signal, compared to a prediction

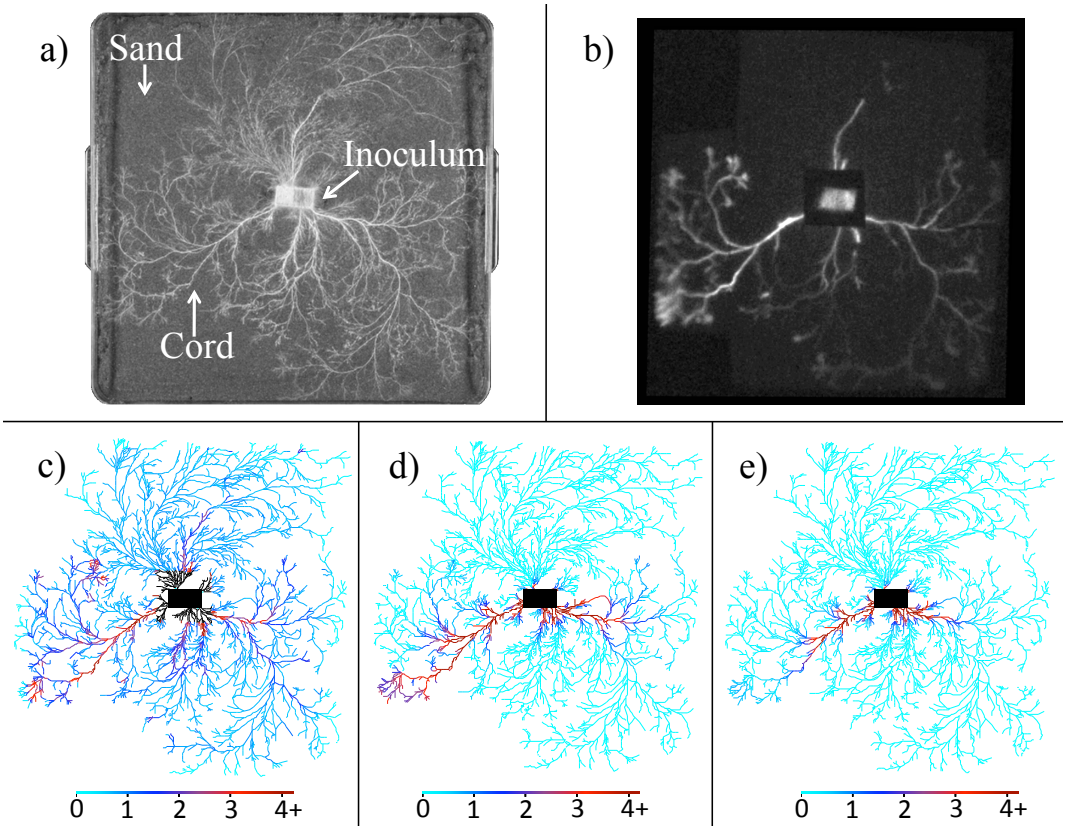

Figure 4.1: **Measured and predicted intensities.**
(a) *Phanerochaete velutina* in a 24 cm $\times$ 24 cm microcosm, photographed just before radio-labeled AIB was dripped onto the inoculum.
(b) Data from the photon counting camera. The brightness of the image reflects the total number of photons emitted from each region over the period of time starting 5.6 hours after the AIB was added, and finishing 37.6 hours after the AIB was added.
(c) Digitized network, coloured to indicate the density of photons reaching the camera from each region of the network. Luminosity is measured in arbitrary units, and edges that were not covered by the scintillation screen are coloured black.
(d) Predicted intensity measured in arbitrary units, under the assumption that AIB enters the network at the inoculum at a constant rate, each edge in the final network continues to grow (or shrink) at the same rate that was observed over the final time step, and $\lambda = 0.1$ (so we assume that 10% of each edge is occupied by transport vessels).
(e) Predicted intensity in arbitrary units under the same assumptions as diagram d), except that in this case we let $\lambda = 0.2$.

of 32% when $\lambda = 0.1$ and 18% for $\lambda = 0.2$. By setting λ such that our model predicts the correct number of points with a significant amount of AIB, we find that $\lambda \approx 0.1$ in both replicates. Note that we can vary the number of points that are predicted to contain a significant amount of resource by varying the free parameter

λ, but for any reasonable value of λ, our model is successful at predicting which points will contain a significant amount of resource (see Fig. 4.1 and Table 4.1). Indeed, our model does significantly better that simply predicting that the points nearest the source will contain a significant amount of resource, and we found the best fit between our model's prediction and the empirical data when we let $\lambda \approx 0.1$.

The claim that 10% of each cord is occupied by transport vessels is at the lower end of biologically plausible values [75], and we suspect that agreement between the ADD model and the empirical data was better in the first experiment because in the second experiment, the mycelium had reached the edges of the microcosm by the time the AIB was added, which made it more difficult to accurately measure growth. Also note that the fact that we found the best agreement for $\lambda = 0.1$ does not mean that we predict that 10% of each cord is occupied by transport vessels, or that we believe that growth-induced mass flows are the only transport process occurring within fungi. The vacuole system [62], transport between organelles [180], and interactions between vesicles and motor proteins [181] will affect the distribution of materials within fungi (with some key materials being sequestered or actively transported), but we argue that the evidence suggests that growth-induced mass flows dominate the transport process at the centimetre scale. Also note that our method of imaging only captures cords, and not the growth of fine hyphae, so we expect that our model underestimates the scale of growth and growth-induced mass flows (see Section 2.7), and expect that more than 10% of each cord is occupied by transport vessels.

λ	**Experiment 1**	**Experiment 2**
0.05	0.45	0.38
0.10	0.56	0.31
0.15	0.56	0.31
0.20	0.55	0.30

Table 4.1: Pearson's linear correlation coefficient ρ between the predicted intensity and the empirical data. By way of comparison, we can calculate the Euclidean distance from each point to the centre of the inoculum, and the value of ρ between those distances and the empirical data was -0.27 in Experiment 1, and -0.28 in Experiment 2.

4.3 Modelling the Distribution of Resource Over the Duration of Experiments

Modelling the currents in fungal networks

We wish to know whether growth-induced mass flows are sufficient to carry resource from the inoculum to the growing tips over the time-scale of growth. We are therefore motivated to consider how the distribution of resource changes over the entire duration of the experiment, given the assumption that there is a constant supply of a generic resource needed for growth originating at the inoculum. To calculate the currents in the growing network, we suppose that all the water and other materials which form the mycelium ultimately originate from the inoculum, and as before we suppose that some fraction λ of each edge is composed of transport vessels, each of which has a radius of 6μm [75]. However, as we wish to investigate whether growth-induced mass flows are sufficient to carry resource from the inoculum to the tips over the time-scale of growth, in this section we set $\lambda = 1$. In other words, given values for the medium-currents, we consider the worst case scenario by letting λ be as large as possible, so that the velocities of growth-induced mass flow are as small as possible.

Modelling resource uptake and delivery

The length and volume of each edge at times $t_1, \ldots, t_n$ is determined empirically, and by the assumptions outlined in the previous section, and the method described in Section 2.4, we can find $u_{ij}(t)$: the mean velocity of the fluid in edge ij at time t. We assume that resource enters the network at the inoculum, and is distributed throughout the network by advection and diffusion, but in order to calculate the quantity of resource $q_{ij}(x,t)$ in each edge, we must make some assumptions about both the rate of resource uptake, and the rate at which resource is consumed. From the beginning of each experiment, the inoculum is filled with wood-degrading hyphae (see Fig. 2.1), so we assume that resource enters the network at the inoculum (node 1) at a constant rate $I_1(t) = K$. The rate of water uptake at the inoculum corresponds to the total rate of growth, so our assumptions imply that the amount of water entering the network per unit of resource is not constant, but is proportional to the rate of growth. We also make the simplifying assumption that throughout the network resource is metabolised at a constant rate R: a term that is intended to capture the metabolic cost of growing and maintaining the network. In other words, where $Q(t)$ denotes the total amount of resource in the network, we suppose that

$$\frac{d}{dt}Q(t) = K - RQ(t). \tag{4.2}$$

As $Q(0) = 0$, Equation (4.2) implies that $Q(t) = \frac{K}{R}\left(1 - e^{-Rt}\right)$.

In our experimental set-up the fungal networks attain a maximum volume as the fungi only have access to a finite supply of resource. This is reflected in our assumptions, as if the uptake rate K and the local delivery rate R are both constants, the total quantity of resource in the network accumulates over a time-scale $\frac{1}{R}$, and then approaches a steady state $\frac{K}{R}$. To obtain a reasonable value for the constant R, we suppose that resource accumulates in the network over a time-scale that is equal to the time-scale of growth, so that over the course of the experiment the mean concentration is approximately constant. More specifically, we let V_{F} denote the maximum volume attained by the mycelium, and we measure the time τ that elapses

before the mycelium attains a volume $\frac{1}{2}V_{\mathrm{F}}$. We then assume that $Q(\tau)$ is half the maximum quantity of resource $\frac{K}{R}$, which implies that

$$R = \frac{\log(2)}{\tau}. \tag{4.3}$$

Given this system of equations, the concentrations at all points in space and time are proportional to K, and so the relative concentrations are independent of K.

Modelling the spatial distribution of resource in empirical networks

To apply our minimal model for the distribution of resource in a growing fungal network, we require empirical values for V_{F} (the maximum volume attained by the network) and τ (the time taken to grow to volume $\frac{1}{2}V_{\mathrm{F}}$). We also require the adjacency matrix of the network, the lengths l_{ij} and the cross-sectional areas $S_{ij}(t_n)$ for each edge ij and each time point $t_1, \ldots, t_N$.

For each time interval, the first step is to calculate the unique set of medium-currents which are consistent with the observed changes in volume, and which minimize the work required to overcome viscous drag (see Section 2.4). We suppose that over the time interval $t_n < t \leq t_{n+1}$ the cross-sectional area is

$$S_{ij}(t) = \frac{1}{2}\big[S_{ij}(t_n) + S_{ij}(t_{n+1})\big], \tag{4.4}$$

and as the edges are composed of a bundle of transport vessels, we suppose that the conductance of each edge is proportional to its cross-sectional area. Finally, we calculate whether each of the nodes is a source or a sink. Where F_i denotes the net medium-current flowing out of node i, we let

$$F_i = \begin{cases} -\sum_{j \neq i} F_j & \text{if node } i \text{ is the inoculum,} \\ \sum_{ij} \frac{S_{ij}(t_n) - S_{ij}(t_{n+1})}{2(t_{n+1} - t_n)} & \text{otherwise.} \end{cases} \tag{4.5}$$

If the edges around node i are growing, then F_i is negative and node i is a sink. If the edges around node i are shrinking, or if node i is the inoculum, then F_i is positive and node i is a source. Circuit theory tells us that we can use the conductance of

each edge and the net current flowing out of each node to determine the pressure difference between any pair of nodes (see Section 2.3). Furthermore, given the conductance of edge ij and the pressure drop between nodes i and j, we can uniquely determine the medium-current $F_{ij}(t)$ for each edge in the network. This medium-current is constant over the time interval $t_n < t \leq t_{n+1}$, and it does not depend on the constant of proportionality between the cross-sectional area of the edges and the conductance of the edges.

We are interested in finding the distribution of a generic source of energy and carbon, so we let $D_m = 6.7 \times 10^{-4}\text{mm}^2\text{s}^{-1}$ (the molecular diffusion coefficient of glucose), as this is representative of the diffusion coefficient of a small molecule. We also assume that in each edge the advection and diffusion of resource occurs within some number of transport vessels of radius 6μm [75], so once we have found the mean velocity of flow $u_{ij}(t)$, we can use Equation (3.1) to find the piece-wise constant dispersion coefficient $D_{ij}(t)$.

The delivery rate per unit of resource is assumed to be the same in every edge, and the value of $R_{ij} = R$ is given by Equation (4.3). The rate K at which resource enters the network does not affect the relative concentration of points across the network, but a value of $K = 1.125\mu\text{mol hour}^{-1}$ was chosen to produce sensible values for the mean concentration. The nutrient and water content of woodblocks can vary, resulting in more or less vigorous growth. In the first replicate we found that the volume of the mycelium $V_\text{F} = 393\text{mm}^3$ (equivalent to 20% of the volume of the woodblock) and $\tau = 242$ hours. In the second we found that $V_\text{F} = 372\text{mm}^3$ (19% of the volume of the woodblock) and $\tau = 468$ hours. In the third we found that $V_\text{F} = 616\text{mm}^3$ (31% of the volume of the woodblock) and $\tau = 367$ hours.

Finally, the Laplace transform of the net quantity of resource leaving the inoculum is assumed to be $\Upsilon_1(s) = \frac{K}{s}$, and for every other node $\Upsilon_i(s) = 0$. We now have all the parameters we need to implement the algorithms described in Section 3.7. That is to say, we can calculate the spatial distribution of resource that would arise if the cross-sectional areas of the edges vary in either a step-wise or continuous manner, where the volumetric currents are determined by the measured changes in vol-

ume. Whichever algorithm we employ, at each time t_n we record the resulting spatial distributions of resource by dividing each edge into N_{ij} line segments such that $\frac{l_{ij}}{N_{ij}} \leq 1$mm. These quantities of resource per unit length are then treated as an initial condition over the following time step, and the concentrations at time t_n are identified by dividing $q_{ij}(x,t_n)$ by $S_{ij}(t_n)$. By programming in MATLAB and running the algorithm on a laptop with a 2.4 GHz Intel core, we can calculate the growth-induced currents in a network with 3,000 edges in a couple of seconds. It takes about 4 hours to calculate the resulting concentrations in such a network, though we suspect that this running time could be significantly improved.

Results of the simulation

Three fungal networks were grown and digitized, and the observed changes in fungal volume were used to determine the minimal currents consistent with the changing volume, as well as the uptake rate and decay rate of a generic form of resource. In each of three experiments our model suggests that the growth-induced mass flows were sufficiently large to spread the resource from the inoculum out to the growing tips over the time-scale of growth (see Figs. 4.2 and 4.3).

This result is somewhat counter-intuitive, as in most of the edges the mean velocity of the growth-induced mass flows is very low (see Section 2.6). Indeed, if we consider the worst case scenario and let $\lambda = 1$ and pool the data from all three experiments and over all time steps, 70% of the edges have a mean velocity that is so small that over the course of one week, resource travelling at that velocity would move *less* than the 20mm that resource would typically travel by diffusing in one dimension (75% of edges in Experiment 1, 59% in Experiment 2 and 64% in Experiment 3). Over the time-scale of two hours, only 4% of edges have a velocity great enough to carry resource further than the 2.2mm that is typically travelled by diffusion alone (2% in Experiment 1, 6% in Experiment 2 and 6% in Experiment 3).

Even if we set λ to the more realistic value of 0.1 (which increases our predictions of the advective velocities 10 fold), most edges are predicted to carry currents

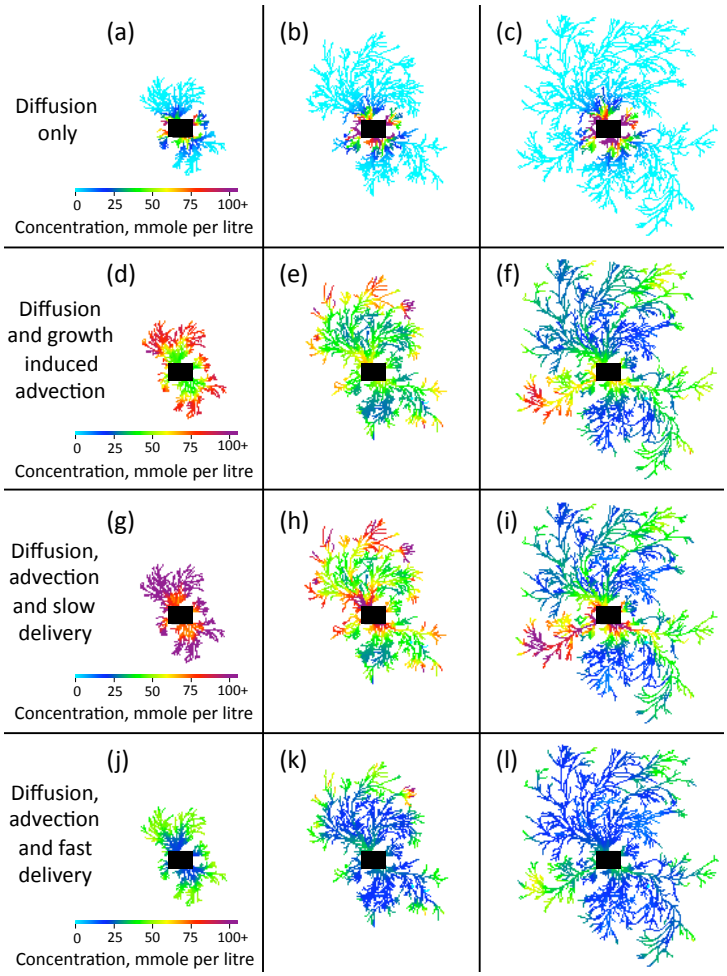

Figure 4.2: **Concentration of resource in Experiment 1.** Experiment 1 after 6 days (a, d, g and j), 12 days (b, e, h and k) and 18 days (c, f, i and l). Diagrams (a - c) illustrate the concentration of resource that would occur in the absence of advection, where resource enters at the inoculum at a rate of $K = 1.125\mu$mole hour^{-1}, and $\tau = 242$ hours. Diagrams (d - f) illustrate the concentration of resource where fluid and resource enter the network at the inoculum, and the medium-currents are consistent with the observed changes in volume, while minimising the work required to overcome viscous drag (see Section 4.3). As before, resource enters at the inoculum at a rate of $K = 1.125\mu$mole hour^{-1}, and $\tau = 242$ hours. Note that at any point in time, the concentration near the tips can be greater than the concentration near the inoculum. This is possible because resource enters the network at a constant rate, but the rate of water influx at the inoculum corresponds to the total volumetric rate of growth. Consequently, as the total volumetric rate of growth increases, the concentration of resource in the fluid near the inoculum decreases. We cannot directly measure the delivery rate of resource, so to assess the sensitivity of our model to the parameter R, we also consider the cases where we half and double the delivery rate R. Diagrams (g - i) illustrate the concentrations that occur when the medium-currents and rate of uptake are as before, but the local delivery rate has been halved. Diagrams (j - l) illustrate the concentrations that occur when the medium-currents and rate of uptake are as before, but where the local delivery rate has been doubled.

at very modest velocity (see Section 2.6). Despite the modest scale of the advection in most of the edges, the fraction of edges in which the mean velocity is significant suffices to spread the resource from the inoculum out to the growing tips (see Figs. 4.2 and 4.3). We also calculated the distribution of resource that results if the cross-sectional areas $S_{ij}(t)$ vary continuously over each time step (see Section 3.8), but the results were almost identical to the simpler case where the cross-sections are varied in a stepwise manner.

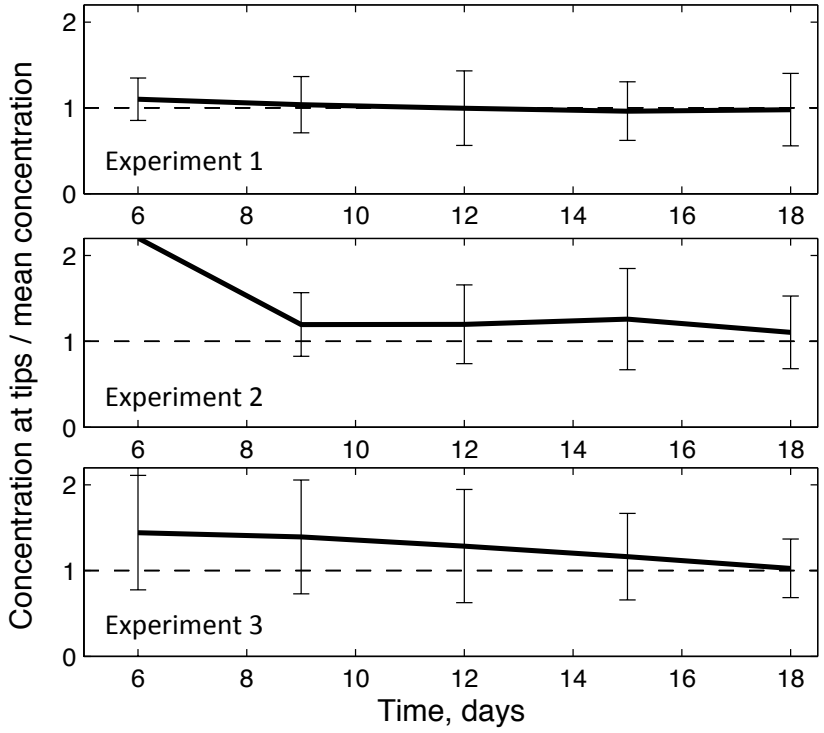

Figure 4.3: **Concentration in the tips relative to the concentration elsewhere.** To produce this figure we let $\lambda = 1$ and $R = \frac{\log(2)}{\tau}$, where τ is the time it takes for the mycelium to obtain half its maximum volume. In each of the three experiments, the concentration at the tips (nodes of order one) was larger than the mean concentration in the network as a whole.

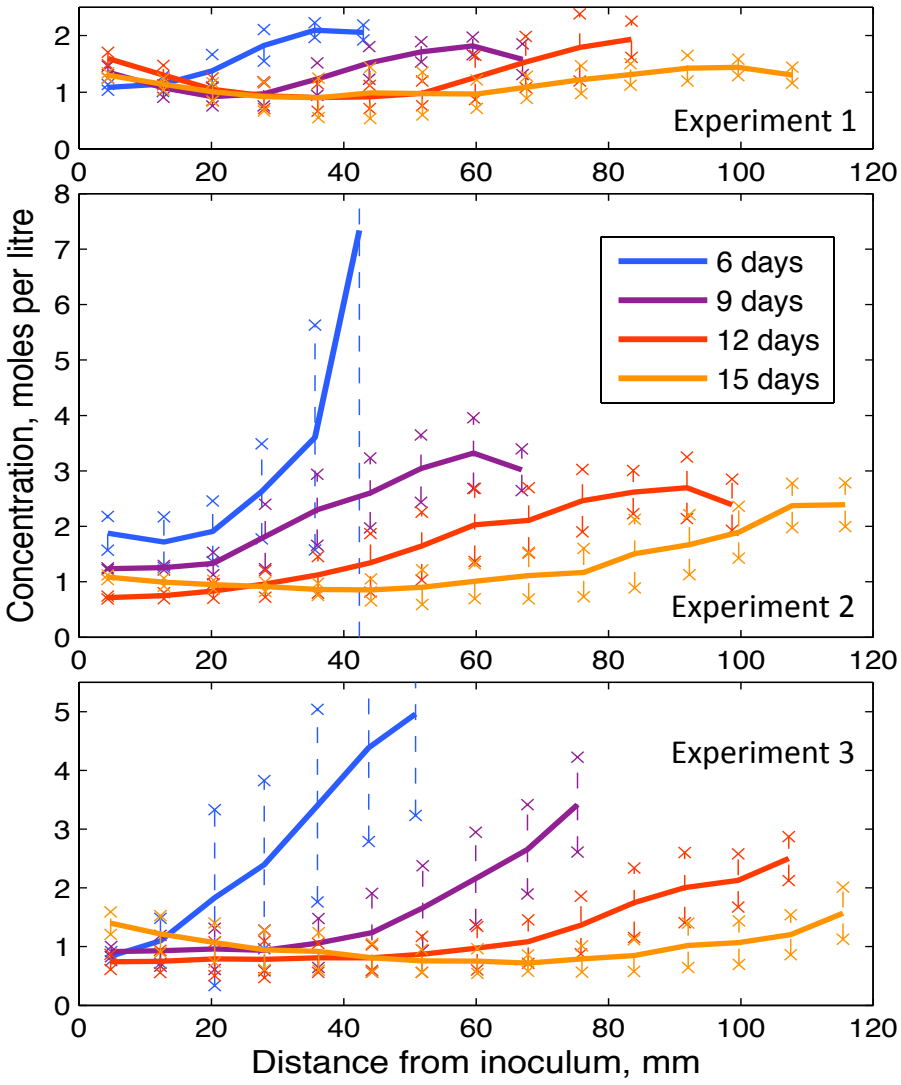

Figure 4.4: **Concentration varies with distance from the inoculum.** To produce these graphs, points in the network at each time step are divided into bins according to the Euclidean distance from the given point to the inoculum. Each bin produces a data point, and its location on the x-axis indicates the mean Euclidean distance from the given points to the inoculum, while its location on the y-axis indicates their mean concentration, plus or minus one standard deviation. Note that our means of setting the decay rate R effectively normalizes the mean concentration over time (see Section 4.3).

4.4 Implications and Limitations of Our Modelling Approach

In the ADD model we assume that resource diffuses and is carried by growth-induced mass flows, and we also assume that resource is consumed or metabolized at

a rate that is constant throughout the network. It could be argued that the total rate of resource delivery in an edge should be proportional to the volume of that edge, rather than being proportional to the quantity of resource contained within that edge. However, as our model results in a fairly constant concentration throughout the network, changing from first order to zero order delivery is unlikely to make a significant difference to the concentration at the tips (unless, of course, we change the mean amount of time that elapses between resource entering the network and the resource being consumed). It might also be argued that the growing hyphal tips are responsible for a significant fraction of the resource consumption [37, 38, 39, 40, 41, 145]. After all, as material is added to the growing cell wall, the concentration of that material in the cytoplasm must be depleted near the region of growth. Although our model does not include a term for consumption due to growth, it does indicate that growth-induced mass flows are sufficient to carry resource across the network over the time-scale of growth.

While advective mass flows carry resource over long distances from the inoculum out towards the growing tips [49, 115, 147], diffusion and active transport mechanisms may be essential near the sites where the cell wall is expanding. This follows because the cytosol within the apical hyphae moves forward at the same rate as the growing tips [126], but to transport resource from the base of the hyphae to the growing tips, the resource has to move faster than the rate of growth. Complex cellular machinery regulates the addition of material to the cell walls, ensuring that the growing hyphae exhibit polar growth, and only expand at the hyphal tips [20, 127, 135, 180, 181]. The presence of motor proteins and the cytoskeleton will affect the distribution of materials within fungal networks [110, 150, 183, 210], and the possibility of sequestering resources in organelles or the vacuole system will also influence the distribution of materials [62, 66]. We note, however, that our model suggests that the minimum currents consistent with the observed growth would effectively transport resource from the inoculum to the growing tips over the time-scale of growth. This suggests that the active transport mechanisms observed in the growing tips of fungal networks may not be required for long range transport.

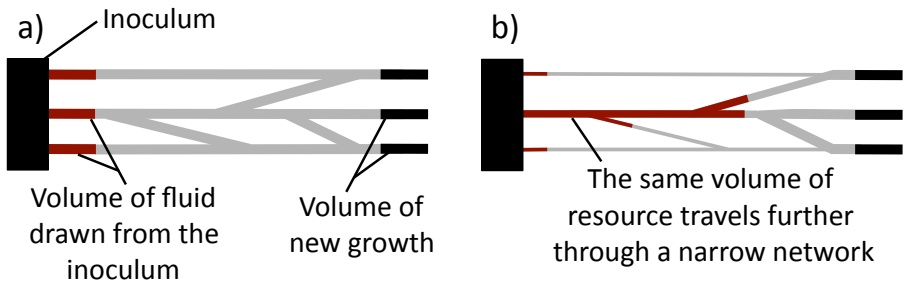

[h!]

Figure 4.5: **Reducing the cross-sectional area of the supporting network increases the velocity of mass-flows. a)** If water uptake only occurs at the inoculum, the current out of the inoculum is equal to the volumetric rate of growth. **b)** The volumetric current through a tube is equal to the mean velocity of flow times its cross-sectional area, so if a tube is carrying a given current, we can increase the velocity by decreasing the cross-sectional area. We therefore suggest that fungi can increase the velocity of transport by reducing the cross-sectional area of the transport stream, either by thinning the supporting mycelium through the process of autophagy, or by restricting the mass-flows to transport vessels that occupy less that the whole cord.

More generally, our analysis suggests that the cross-sectional area of the supporting network is a critical feature in determining the time it takes for resource to travel across the mycelium. The ability of fungi to recycle redundant material to support new growth is thought to be crucial for enabling them to forage effectively in heterogeneous environments [77, 78, 81, 146], and we suggest that autophagy is a useful ability for three principle reasons. First, autophagy enables fungi to recoup some of the metabolic cost of growing the mycelium. Second, by digesting parts of the mycelium that are not essential for transport, fungi can reduce the volume of metabolically active mycelium, and thereby reduce the amount of energy needed to maintain the given structure. Third, reducing the cross-sectional area of the supporting mycelium means that the volumetric currents that are required by growth can travel at a greater velocity (see Fig. 4.5).

The observation that the rate of water uptake across the whole mycelium must be commensurate with the volumetric rate of growth also helps to explain previously challenging experimental observations, most notably, the occurrence of sudden route switching [83] and the observation that when fungi encounter a new source of nutrients, there is often a local increase in the growth rate, while growth is inhibited

in parts of the mycelium away from the new source of nutrients [189, 199]. This latter claim requires further justification, but it is well known that the rate of hyphal branching increases when tips encounter resource rich environments [38, 41, 77, 93, 145, 196]. Turgor pressure and the build up of vesicles have both been implicated, but whatever the mechanism behind this response, differential branching rates may constitute a unique kind of foraging strategy. There is an obvious efficiency to increasing the growth rate when hyphae encounter a resource rich environment, because by doing so the fungi will increase the proportion of the mycelium that has immediate access to nutrients. Furthermore, this pattern of growth enables the fungi to utilize resources that might otherwise be consumed by a competing organism.

It is not surprising that fungi grow more vigorously in those parts of the environment that are relatively rich in resources: the interesting questions relate to the effects induced by asymmetries in the rate of growth. Regions of the mycelium that encounter nutrients are expected to produce a relatively large number of growing tips, so if growth induces mass-flows, we should expect to see a disproportionate amount of fluid flowing towards the regions of high nutrient concentration. Our central observation is that the rate of water uptake across the whole mycelium must be commensurate with the volumetric rate of growth, and so an increase in the growth rate in one part of the network can directly result in an increase in the rate of water uptake elsewhere in the network (see Fig. 4.6). More specifically, for a topology as in Fig. 4.6a, the flux towards region B will be $\frac{IV_B}{V_A+V_B}$, where V_A and V_B are the volumetric growth rates of regions A and B respectively (see Fig. 4.6a).

We could try to replicate the experimental details of this phenomenon by means of a complex model, and in the following chapter we develop a modelling framework that can be used to explore the complex relationship between growth, mass-flows, and local resource concentration. However, the principle at work can be also illustrated in a relatively simple manner (see Fig. 4.6).

Note that if the source of nutrients and water is some distance from the growth regions A and B, it may take a significant amount of time before an increase in the growth rate of region A affects the concentration and growth rate of region B. In

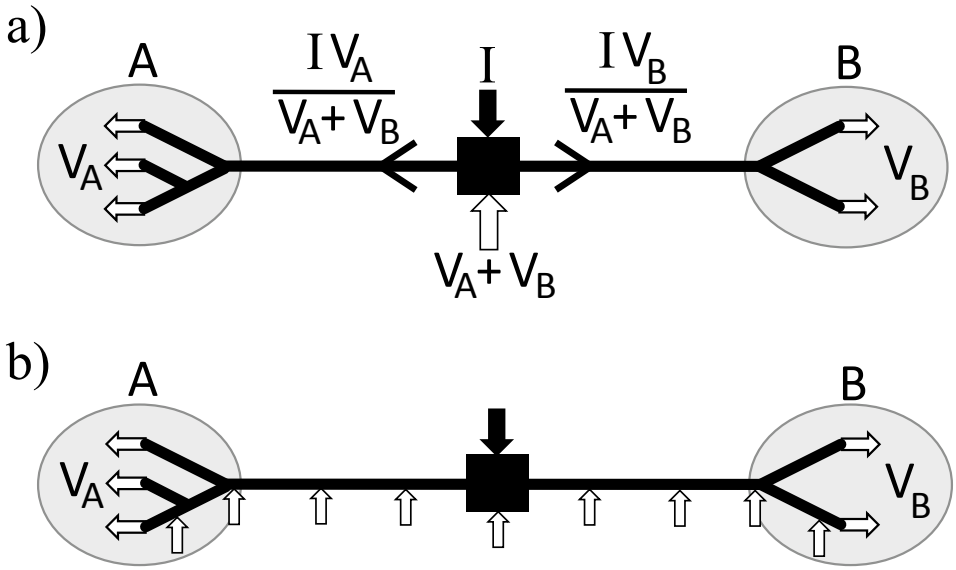

Figure 4.6: **A local increase in the growth rate can inhibit growth elsewhere. a)** If resource and water only enter the network at the inoculum, and if the rate of water uptake equals the total rate of growth, an increase in the growth rate in region *A* results in a reduction of the flux of material flowing towards region *B*. **b)** If an increase in the growth rate in region *A* produces an increase in the rate of water uptake in the tips of region *B*, local growth in one region could rapidly inhibit growth elsewhere.

actual fungal networks there may be water uptake by any of the hyphae, though it should be noted that in our experimental set up the majority of the hyphae are within the inoculum, and once a bundle of hyphae have matured into cords, they are insulated from the environment and so do not take up water. As the total rate of water uptake must be commensurate with the total rate of growth, an increase in the rate of growth in one part of the network will result in an increase in the total rate of water uptake. If an increase in the growth rate in region *A* produces an increase in the rate of water uptake in the tips of region *B* (see Fig. 4.6b), we should expect to see a relatively rapid reduction in the concentration in the tips of region *B*. If this drop in concentration results in a lower rate of growth, we will find that increasing the growth rate in region *A* rapidly produces a reduction in the growth rate in region *B*.

We speculate that regions of the mycelium that do not carry a sufficient flux of materials tend to regress, and that the resulting networks constitute an efficient re-

sponse to the given resource environment. In the following chapter we develop a model for growing *in silico* fungal networks, which can be used to investigate the complex relationship between local nutrient concentration, growth rates, the transport of resources and the network structures that emerge as a result of those interactions. Such models require a large number of parameters, many of which are phenomenological in character, and cannot be measured directly. Nevertheless, the modelling framework that we present can be used to describe fungal growth at a range of scales, and we explain how many of the parameters can be calibrated using empirical fungal networks.

Chapter 5

In Silico Fungal Networks

In this chapter we develop a family of models for growing *in silico* corded fungal networks. As far as possible we use empirically determined parameter values for our model and, in the simulations presented here, we have calibrated our model to recapitulate the growth of *P. velutina*. The framework we present here could also be used to model a hyphal network (as opposed to a network of cords) and it is based on the mixed 'tip and bond' approach described by Boswell et. al. [39, 40, 41]. This model represents a growing network by showing the number and location of cords and hyphal tips, as well as the concentration over a network of some growth-limiting resource. Many chemical elements are necessary for fungal growth, but carbon is particularly critical because of its central role in biosynthesis and energy-yielding metabolism. For the sake of simplicity, in our model all of the materials necessary for growth are modelled as a single generic element.

The models presented here were used to investigate the ideas developed in the preceding chapters, and in particular, we wanted to explore the complex relationship between local nutrient concentration, growth rates, the transport of resources and the network structures that emerge as a result of those interactions in a hydraulically coupled system. We have worked to develop *in silico* models from the beginning of my research, but although that process was helpful in shaping our thinking, none of the results produced by our models are central to this thesis. Rather, we include this detail here for completeness, because it reflects a large body of code, and represents a test bed for developing ideas that can and will be refined in further work. Indeed,

our principle results concern our methods for comparing simulated and empirical networks, which can be used to constrain the parameter values. We note further that there are a number of parameters which remain only lightly constrained: this motivates further experiment and an exhaustive computational study. A full and careful treatment of the parameter uncertainties and their relationship to empirical data could be developed by placing priors over the parameters, identifying important empirical characteristics which need to be reproduced and then using approximate Bayesian computation [192], but such an analysis is beyond the scope of this thesis.

In Section 5.1 we outline the details of our modelling approach, which we have adapted from the models described by Boswell et. al [39, 40, 41]. The parameters of our most complex model are listed in Table 5.1, and a flowchart describing the algorithm is presented in Figure 5.2. As in the models of Boswell et. al, each tip is represented as an agent, whose behaviour depends on the local concentration of resource. These agents move over a hexagonal lattice leaving a pattern of bonds that represent the growing fungal network. Tips are created by a process of branching, and they are destroyed when a tip grows into an existing cord (anastomosis). In a departure from the models of Boswell et. al. we suppose that the edges of our network can thicken or thin, and in line with the empirical findings presented in Chapter 2, we assume that cords that carry high velocity mass flows are significantly more likely to thicken than cords that carry low velocity mass flows. More specifically, we try to reflect this behaviour with a minimal number of parameters, so we suppose that the extent of cord thickening is a linear function of the velocity of mass flow passing through the given edge.

Once the cross-sectional area of each edge is known for times t and $t+\Delta t$, the medium-currents through the network are calculated by treating the network like an electrical circuit, where the conductance of each edge is proportional to its cross-sectional area and inversely proportional to its length, and the sources and sinks are determined by the pattern of water uptake and growth. At each time step the mean velocity of flow in each edge can be calculated by following the method described in Section (2.3), and given the diffusion coefficient of the resource in question, the

dispersion coefficients D_{ij} can be calculated by using Equation (3.1). Finally, we describe a method for finding appropriate values for the local delivery rates R_{ij}, and for the rates of resource uptake from the inoculum and from the edges undergoing autophagy. We now have all the parameters we require to apply the mathematical machinery described in Chapter 3, and so we can calculate how the quantity of resource per unit length has changed at the end of the given time step.

In Section 5.2 we list the model parameters and summarize the implementation of our model. In Section 5.4 we explain how the growth rate, branching rate, anastomosis rate and curvature of cords can all be determined from the empirical data. We also suggest ways of using the empirical data to find appropriate values for the local delivery rates and the local rates of resource uptake. Finally, in Section 5.4 we compare our model networks to empirical fungal networks. Our current data are preliminary, and our methods are more important that the absolute values of our results, but we emphasise that given the branching rate of the empirical networks, there are surprisingly few anastomosis points. Our model does a better job of replicating the distribution of edge lengths and cross-sectional areas of the empirical networks, but further data are needed to produce statistically robust results.

5.1 Tip and Bond Models

The basic modelling framework that we have adopted is a 'bond' and 'cell'-type hybrid model, as described by Boswell et. al. [41] in their model of the hyphal network of *Rhizoctonia solani*. The network is modelled as growing over a hexagonal array, utilising a generic metabolic substrate as it grows. Hyphal tips grow from the centre of one hexagon to the centre of a neighbouring hexagon, which is to say that there is a triangular lattice of possible locations for the hyphae or cords. Such an approach is preferable to a strictly cellular model, which would force all adjacent, occupied 'cells' to be connected to each other, unlike an actual fungal network, which can have parallel, adjacent cords that are not directly connected. This particular lattice configuration has the further desirable property that the angle between branches is

60°, which is a better approximation to the actual hyphal branching characteristics than would be obtained through the use of a square lattice.

Growing tips follow biased random walks

The first parameter choices in running the simulation involve selecting a spatial and temporal resolution, defined by the size of time step Δt, and the grid size Δx. The latter is defined as being the distance between the centres of adjacent hexagonal cells. A physical interpretation of Δx is that it can be no smaller than the diameter of a cord (or adjacent cords would necessarily be in contact), and in the simulations presented here, a value of $\Delta x = 1$ mm were typically used.

We use the term 'tip' to refer to the terminal point of an edge, which can move forward over time, and we use the term 'tip-section' to refer to the edge of length Δx that connects the tip to the rest of the network. Tip growth is modelled as a Poisson process, such that where v is the mean speed at which the tips extend, the probability that a given tip will grow by Δx over a time step of length Δt is equal to $v\frac{\Delta t}{\Delta x}$. This growth event may also be a branching event, as we explain in the following subsection. This kind of stochastic model is more realistic than constant deterministic growth, as experimental evidence indicates that individual tips grow in spurts, and there is random variation between the different tips [169]. Because the tip growth mechanism included in this model produces a random 'move/do not move' event at each time step, some random variation in the tip extension rate is introduced. Also note that if growth is being modelled as a Poisson process, there is a non-zero probability that a given tip will grow by more than Δx over a given time period Δt. However, our method of simulation does not allow for this possibility, so if we want the mean rate of growth to be independent of our choice of the parameter Δt, we must chose a value such that $(v\Delta t/\Delta x)^2$ is negligibly small.

The growth of a tip requires the expenditure of energy, and the consumption of resources. We suppose that growing by a volume α costs α units of resource, and this resource is removed from the tip-section whenever there is tip growth. To avoid

the absurd scenario of negative concentrations, tips that do not contain enough resource to pay this cost have a zero probability of growing. Note that this assumption of unit cost per unit volume does not result in a loss of generality: it merely reflects an arbitrary choice for the units in which concentration is measured.

Both cords and the hyphal tips of most mycelial fungi, including *P. velutina*, grow in a predominantly straight line, though they occasionally undergo small directional changes. This kind of directed growth is a consequence of the structure of the hyphal walls and the manner in which new wall material is incorporated at the hyphal tip [127, 162, 181]. In our model tip movement is essentially viewed as a biased random walk on the vertices of the embedded triangular lattice, with most growth events extending the tip in the direction it was already headed (see Fig. 5.1).

The Matlab program handles this process on the basis that each hexagonal cell containing a tip necessarily contains a single cord, and the orientation of this cord determines from which cell the tip has originated. Over most growth events the cord that is growing continues along its current orientation. However, there is also a probability that when it grows, the tip will deviate by 60° to the left or right. Since hyphae do not exhibit any sharp bends when growing in unconstrained domains, the probability of bending by more than 60° was set to be zero (see Fig. 5.1). Where the parameter d denotes the mean number of degrees deflection between the beginning and the end of an edge of unit length, then we assume that the probability that a given growth event introduces a 60° bend is equal to $\frac{d\Delta x}{60^\circ}$. Given that $\frac{1}{\Delta x}$ growth events are required to produce a unit length, the expected number of bending events per unit length will equal $\frac{d}{60}$ mm^{-1}, and the expected deflection per unit length will be d° mm^{-1}.

Branching

New hyphal tips are created by branching, which can be observed to occur in three distinct patterns within the filamentous fungi [92]. The first kind of branching is dichotomous branching, where a growing tip splits to produce two tips. The second

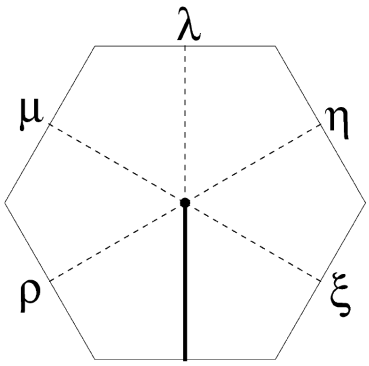

Figure 5.1: **Modelling tip growth.** Hyphae do not exhibit sharp bends, and so we suppose that given its initial orientation, the probability that the tip will grow in direction ρ or ξ is equal to zero. We suppose that the probability of growing in the direction μ is equal to the probability of growing in the direction η, and where d represents the average number of degrees deflection per unit length, these probabilities equal $d\frac{\Delta x}{120^\circ}$. It follows that the probability of growing in direction λ is equal to $1 - d\frac{\Delta x}{60^\circ}$. The empirical data indicate that 6° mm^{-1} is a reasonable choice for the parameter d, and for any given value of d, we must choose Δx such that $d\frac{\Delta x}{60^\circ} < 1$.

is known as subapical branching, where a new tip emerges just behind a growing tip. The third kind is lateral branching, where new tips emerge from the sides of hyphae, some distance behind the tips. Most of the tips produced by *P. velutina* arise subapically, although lateral branching also occurs. However, given the millimeter scale over which this model is operating, it is reasonable to model subapical branching as though it were dichotomous. This is because the cords that are recorded as being present or absent are in fact composed of multiple hyphae, and cords a short distance back from the tips either resolve into a branch point or they resolve into a single cord.

Both turgor pressure and the buildup of tip vesicles have been implicated in the commencement of the branching process [93]. Fungi that are growing in a homogeneous, nutrient rich environment typically cover the source of nutrients with a dense, mycelial network, with diffuse growing margins that fully exploit the available resources. In nutrient poor environments the mycelium is relatively sparse, and branching rates are lower [32, 33, 127, 202]. As in Boswell et. al's model [37, 39, 40, 41], we assume that internal substrate is responsible for branching and,

in the absence of any experimental evidence to the contrary, we assume that the branching rate is linear with respect to the amount of internal substrate. We let b denote the branch rate per unit concentration, which is to say that when there is a unit concentration in the tip-sections, there are on average b branch points per unit distance. In other words, if at time t the quantity of resource per unit length in the tip-section ij is $q_{ij}(t)$, then the probability that there is a branching event at tip i given that there was a growth event is equal to $\frac{bq_{ij}(t)\Delta x}{S_{ij}(t)}$.

Newly formed edges are oriented in directions that are determined by the orientation of the edge from which they branched. Specifically, consistent with the physiology of *P, velutina* and other fungal species, a new branch is assumed to only arise at acute angles to the direction of hyphal growth. If a given growth event is in fact a branching event, the existing tip extends by a single hexagon in the direction it was heading, and a second tip also emerges from the hexagon in question. This second tip is equally likely to grow 60° to the left or right, and could be viewed as a tip that has emerged subapically Δx back from the tip that has just grown, and which has itself grown by Δx. Branching events are twice as costly as ordinary growth events, and as in the case of ordinary growth events, an amount of resource equal to the total volume of the newly formed tips is removed from the tip-section as soon as we know that there is going to be a branching event. To avoid the absurd scenario of negative concentrations, tip-sections that do not contain enough resource to pay this cost have a zero probability of branching.

Anastomosis, cord thickening and autophagy

When a tip grows into a hexagon that is already occupied, we assume that anastomosis occurs. Fusion is assumed to occur at the very end of the time step, which means we need to keep track of two different adjacency matrices. One adjacency matrix reflects the network just before anastomosis occurs. A second adjacency matrix contains the same edges, but in this case the adjacency matrix reflects the fact that anastomosis has occurred. We use the first adjacency matrix when calculating

how resource is redistributed by advection, diffusion and consumption, but it is the second network that we adopt at the beginning of the next time step.

We have now described how we model branching and anastomosis. The final developmental process that we can include in our model is the process of edge thickening or thinning. The capacity of fungi to vary the thickness and transport capacity of various parts of the mycelium has a significant impact on their transport efficiency [27, 82]. The thinning of edges is associated with the process of autophagy (self-eating), and the ability of fungi to recycle redundant material to support new growth is believed to be crucial for enabling them to forage effectively in heterogeneous environments [77, 78, 81, 146]. As we are calibrating the model parameters to recapitulate the growth of *P. velutina*, our model must allow for the fact that the thickness of edges may vary considerably. In the case where the parameters are chosen in order to model the growth of a hyphal network, it may be more appropriate to suppose that edges do not grow thicker than some given cross-sectional area (the cross-section of a large hypha). However, even if we are modelling a hyphal network in which the edges all have a similar cross-section, we should allow the possibility of edge thinning, as that is how we model autophagy.

In line with the empirical findings presented in Chapter 2, we note that there is little correlation between the size of a cord and the rate at which it grows (or shrinks), but cords that carry high velocity mass flows are significantly more likely to thicken than cords that carry low velocity mass flows. To reflect this behaviour with a minimal number of parameters, we suppose that the extent of cord thickening is a linear function of the velocity of mass flow passing through the given edge. In other words we suppose that mass flows across the network induce changes in cross-sectional area, which in turn produce growth-induced mass flows. It is necessary to introduce a small time lag Δt between the presence of a high velocity current and the resulting edge thickening, because in order to calculate the growth-induced mass flows at a given time step, we first need to know how the cross-sectional areas of the edges are changing over that time step.

To describe the linear relationship between velocity and change in cross-sectional area, we require two parameters. We let $\delta > 0$ denote the maximum possible rate at which an edge can shrink, and we let ω denote the velocity at which the cross-sectional area of an edge will not change. Finally, to avoid producing negative cross-sectional areas, we impose a minimal cross-sectional area $S_{\min}$ for any edge. Note that by setting $S_{\min} > 0$ we can ensure that the network remains connected, which is important, because our method for calculating the velocity of flow depends upon the assumption that the network is connected.

As in the case of tip growth, the cost of thickening an edge is equal to the change in volume of that edge, and when an edge shrinks, we assume that some fraction μ of the cost of growing that edge is recouped. In other words, we assume that autophagy recoups a fraction μ of the cost of growth, and in the absence of experimental measurements of the efficiency of autophagy, we assume that $\mu = 0.5$. This parameter can of course be varied, but it should be noted that even when $\mu = 0$, there is still an energy benefit to reducing the cross-section of edges, as the cost of maintaining a large edge will be greater than the cost of maintaining a small edge. To restate these assumptions in equation form, we let

$$S'_{ij} = S_{ij}(t) + \Delta t \left(\frac{\delta f_{ij}(t - \Delta t)}{\omega S_{ij}(t)} - \delta \right), \tag{5.1}$$

where $S_{ij}(t)$ is the cross-sectional area at time t and $f_{ij}(t)$ is the absolute value of the medium-current in edge ij between time t and $t + \Delta t$. For each edge at each time step, we put

$$S_{ij}(t + \Delta t) = \begin{cases} \max\left[S'_{ij}, S_{\min}\right] & \text{if } S'_{ij} < S_{ij}(t) \text{ and} \\ \min\left[S'_{ij}, q_{ij}(t) + S_{ij}(t)\right] & \text{otherwise,} \end{cases} \tag{5.2}$$

where $q_{ij}(t)$ is the quantity of resource per unit length at time t. Having calculated the cross-sectional area of edge ij at the end of the given time step, we immediately update the quantity of resource per unit length in edge ij to reflect the cost of growth, letting

$$q'_{ij}(t) = q_{ij}(t) + S_{ij}(t) - S_{ij}(t + \Delta t). \tag{5.3}$$

Note that by definition $S_{ij}(t+\Delta t) \leq q_{ij}(t) + S_{ij}(t)$, so for every edge ij we have $q'_{ij}(t) \geq 0$. Our model accounts for the metabolic cost of growth, but due to the process of autophagy, shrinking edges are a source of nutrients, and this should be reflected in our model. We let $U_i(t)$ denote the rate at which resource enters the network at node i between times t and $t+\Delta t$, and let

$$U_i(t) = I(i) + \sum_j \max\left[\frac{\mu\Delta x\big(S_{ij}(t) - S_{ij}(t+\Delta t)\big)}{2\Delta t}, 0\right], \tag{5.4}$$

where μ denotes the fraction of the cost of growth that is recouped by autophagy, and $I(i)$ denotes the rate of resource uptake from the environment at node i.

Newly formed edges tend to carry relatively small currents at relatively low velocity, and we found that if we implement the algorithm described above, newly formed edges are the ones that are most likely to shrink. This behaviour is not found in empirical fungal networks, as there is invariably a time lapse between the formation of a cord and the shrinkage of that cord by the process of autophagy. We therefore do not allow edges to shrink until a time $t_{\min} = 48$ hours after their formation, as an allowance for the developmental changes that are required before autophagy is possible. As we shall see in Section 5.4, our models were successful at reproducing the distribution of edge lengths and cross-sectional areas found in empirical networks. More generally, we found that networks that are initially uniform in cross-sectional area mature by forming major transport routes, while other parts of the network thin, much as we found with empirical fungal networks.

Resource uptake and the cost of maintaining edges

Resource is expended both by maintaining existing structures and by the growth of new edges. We assume that the cost of growing an edge is equal to its volume, the cost of maintaining an edge is proportional to its volume, and the local rate of delivery $R_{ij}(t)$ cannot be greater than some maximum $R_{\max}$. To calculate the local rate of delivery $R_{ij}(t)$ for each edge ij, we require a second parameter τ, which is equal to the period of time over which the cost of maintaining a volume α is equal

to the cost of growing a volume α. In other words, for each edge and at each time step we recalculate $R_{ij}(t)$, and where $q_{ij}(t)$ denotes the mean quantity of resource per unit length in edge ij at time t, we let

$$R_{ij}(t) = \min\left[\frac{S_{ij}(t)}{q_{ij}(t)\tau}, R_{\max}\right]. \tag{5.5}$$

Note that if $R_{ij} < R_{\max}$ and the quantity of resource in edge ij remains constant between times t and $t+\Delta t$, then we have a quantity $q_{ij}(t)\Delta x$ of resource being delivered at a rate $R_{ij}(t)$, so over the time step the total amount of resource lost from edge ij is equal to $\Delta x S_{ij}(t)\frac{\Delta t}{\tau}$. Also note that newly formed edges do not have any resource in them at the beginning of the time step, so their local delivery rate at the time step in which they are formed is $R_{\max}$.

Resource enters the network from the environment, and in the case where we model the growth of a fungal network from an inoculum over an inert substrate, we simply assume that there is constant rate of resource uptake I at node 1 (that is, the node which represents the inoculum). Note that as we define one unit of resource to be the quantity of resource required to grow a unit volume, I represents the maximum (sustainable) volumetric rate of growth. More generally, we can consider the growth of fungal networks in environments with widely distributed resources that become depleted over time. In that case, we can follow the models developed by Boswell et. al. [37, 38, 39, 40, 41], and assume that the rate of resource uptake is a function of the surface area of the edges within the hexagon i, the concentration of internal resource in those edges, and the amount of external resource at that point in the environment. These modelling assumptions are justified on the grounds that internal substrate must be used to acquire external substrate by active transport across the plasma membrane.

Water uptake and velocities of mass flow

In order to calculate the velocities of mass flow within the fungal network, we employ the mathematical machinery described in Section 2.3. Essentially, we assume

that the conductance of edge ij between time t and $t+\Delta t$ is proportional to the mean cross-sectional area of the edge over the given time step, and inversely proportional to the length of the edge. We also assume that growing edges are sinks, while shrinking edges and sites of water uptake are sources. We can either assume that all water uptake occurs at the inoculum, or alternatively, we can assume that water uptake at each node i is proportional to the total surface area of the edges connected to node i.

More precisely, if edge ij first appears between time t and $t+\Delta t$, growing from node j to node i, we let the net medium-current (volume per unit time) $w_i(t)$ flowing out of node i at time t be given by

$$w_i(t) = \frac{\beta \Delta x}{\Delta t}, \tag{5.6}$$

where β is the cross-sectional area of newly formed edges. This ensures that the volume of medium flowing into edge ij between times t and $t+\Delta t$ is equal to the volume of edge ij. The thickening and thinning of edges will also produce sources and sinks, and this should be reflected in the values for the net currents at the nodes. Equation (5.6) tells us the net current at the newly formed tips. At every other node, the net current is determined by both water uptake, and the growth and shrinking of the edges connected to that node. We suppose that the net medium-current flowing out of node i due to shrinkage and growth is

$$\tilde{w}_i(t) = \sum_j \frac{l_{ij}(t)S_{ij}(t) - l_{ij}(t-\Delta t)S_{ij}(t-\Delta t)}{2\Delta t}, \tag{5.7}$$

and we denote the net-current at node i by $w_i(t)$. If there is no water uptake at node i, then $w_i(t) = \tilde{w}_i(t)$, and we assume that the total volume of water is conserved, which is to say that at every time step t, $\sum_i w_i(t) = 0$. Note that the factor of 2 arises because the change in volume of edge ij induces a current at node i and node j. If we assume that all water uptake occurs at the inoculum (node 1), we simply set $w_i(t) = \tilde{w}_i(t)$ for all $i > 1$, and we let

$$w_1(t) = \sum_{i>1} -w_i(t). \tag{5.8}$$

This ensures that the rate at which water enters the network is equal to the total rate of growth, but this modelling assumption is not appropriate in the case where the total volume is decreasing. If we are modelling the growth of a hyphal network (as opposed to a network of cords), it may be more appropriate to assume that water uptake occurs throughout the network, and that the water uptake at node i is proportional to the total surface area of edges connected to node i. In that case the net current at tips that have grown over the given time step is given by Equation (5.6), and at every other edge the net current due to shrinkage and growth is given by Equation (5.7). The rate of water uptake also contributes to w_i, and we assume that the total rate of water uptake is equal to the volumetric rate of growth, and that the rate of water uptake at each node is proportional to the total surface area of the edges connected to that node. In other words we let

$$w_i(t) = \tilde{w}_i(t) - \frac{\sum_j l_{ij}(t)\sqrt{S_{ij}(t)}}{\sum_i \sum_j l_{ij}(t)\sqrt{S_{ij}(t)}} \sum_i \tilde{w}_i(t). \tag{5.9}$$

Given the net current at each node, we can calculate the medium-current in each edge by following the method described in Section (2.3). Finally, the mean velocity of flow in the transport vessels of edge ij between times t and $t+\Delta t$ is defined to be

$$u_{ij}(t) = \frac{2f_{ij}(t)}{\lambda\left(S_{ij}(t) + S_{ij}(t+\Delta t)\right)}, \tag{5.10}$$

where $f_{ij}(t)$ denotes the medium-current in edge ij over the given time-step, and λ denotes the fraction of each edge that is occupied by transport vessels.

5.2 List of model parameters

Δx. This denotes the width of each hexagon in the grid. This should be small in comparison to the mean distance between branch points, and in our simulations based on the growth of *P. velutina*, the typical value chosen for Δx was 1mm.

Δt. This denotes the length of each time step in the simulation. Where v is the mean velocity of tip extension, we must pick a value for Δt such that $(\frac{v\Delta t}{\Delta x})^2$ is small. In our simulations, a typical value for Δt was 1hour.

Parameter	Physical interpretation	Value
Δx	Distance between points on grid	1 mm
Δt	Duration of time steps	1 hour
v	Velocity of tip growth	0.2mm hour^{-1}
b	Branching rate per unit concentration	*0.01* mm^{-1}unit^{-1}
d	Curvature of cords	6°mm^{-1}
D_m	Molecular diffusion rate	3.5×10^{-6}cm^{2}s^{-1}
λ	Fraction of each edge that is occupied by transport vessels	0.1
r	Internal radius of transport vessels	6μm
β	Cross-sectional area of newly formed edges	0.02 mm^2
δ	Maximum rate at which an edge can shrink	*0.001* mm hour^{-1}
ω	Velocity at which the cross-sectional of an edge will not change	*0.5*mm hour^{-1}
$S_{\min}$	Minimum cross-section	0.001 mm
$t_{\min}$	Age at which edges can shrink	*48* hours
I	Rate of resource uptake from the inoculum	*2* units hour^{-1}
τ	Time over which the cost of maintaining a given volume is equal to the cost of growth	*500* hours
$R_{\max}$	Maximum rate of resource delivery	*0.05* hour^{-1}
μ	Proportion of growth cost that can be recouped by autophagy	*0.5*

Table 5.1: **List of parameters and typical parameter values.** Parameters in italics are weakly constrained. Further details about the parameters and our reasons for choosing the given values can be found in the following text.

v. This denotes the mean velocity at which tips extend. In our simulations we let the velocity $v = 0.2$mm hour^{-1}. Note that at this rate of growth, it would take about 21 days to grow 10 cm, which reflects the empirical data [83, 189]. In our model tip-sections must have sufficient internal resource to grow, so simulated networks that run low on resource may exhibit mean grow rates that are smaller than this value.

b. This denotes the branch rate per unit concentration, which is to say that when there is a unit concentration in the tip-sections, there are on average b branch points per unit distance. In other words, if at time t the concentration at the tip-section connected to tip i is $c_{ij}(t)$, then the probability that there is a branching event at tip i given that there was a growth event is equal to $bc_{ij}(t)\Delta x$. This parameter is intended

to capture the phenomenological fact that fungi grow more densely in nutrient rich environments, though we do not have direct experimental evidence showing the relationship between branching rate and nutrient levels in the cytosol. However, as we shall see in Section 5.3, we can estimate the mean branching rate from empirical networks, and can use those values to choose appropriate values for b.

d. The curvature of cords is captured by the parameter d, and in our simulations we let $d = 6°\text{mm}^{-1}$. The empirical data tell us the number of degrees deflection per mm of growth, and we replicate that in our model by saying that when a tip grows a distance Δx without branching, the probability that the growth produced a 60° bend is $\frac{d\Delta x}{60}$.

D_m. The resource in the network moves by advection and diffusion, and we let the molecular diffusion coefficient $D_m = 3.5 \times 10^{-6}\text{cm}^2\text{s}^{-1}$: a typical rate of diffusion for small molecules in an aqueous solution [62, 140, 147, 194].

λ. This denotes the fraction of each edge that is occupied by transport vessels. In the case where the parameters are being chosen to model a hyphal network, λ should equal the ratio between the external and internal radius of one of the hyphae. As we are modelling a network of cords, we let $\lambda = 0.1$, reflecting the evidence concerning *P. velutina* presented in Section 4.2.

r. This denotes the internal radius of the transport vessels in each edge. We let $r = 6\mu\text{m}$, and use this value when calculating the dispersion coefficient for a given edge, in accordance with Equation (3.1).

β. This denotes the cross-sectional area of newly formed edges, and in our simulations we let $\beta = 0.02\ \text{mm}^2$, because this is a typical thickness for newly formed cords in the empirical networks that we analyzed.

δ. This denotes the maximum possible rate at which an edge can shrink. This can be estimated from the empirical data in a straightforward manner, and we let

$\delta = 0.001$ mm hour^{-1}

ω. We assume that the rate of change of the cross-sectional area of a cord between times t and $t+\Delta t$ is an increasing, linear function of the mean velocity in edge ij between times $t-\Delta t$ and t. If the mean velocity is zero the edge is assumed to shrink at a rate δ, while ω denotes the mean velocity at which the cross-sectional area of edge ij will not change. If $\omega < v$ no edges are likely to thin, as velocities are relatively small in the tips. Since we let $v = 0.2$mm hour^{-1}, we let ω be in the range $0.3-1$mm hour^{-1}, as this ensures that a reasonable proportion of the edges thin over time.

$S_{\min}$. This is the minimum cross-sectional area of any edge, and to ensure that the network remains connected, we let $S_{\min} > 0$. The constant $S_{\min}$ ought to be significantly smaller than β, so the edges can indeed shrink. Moreover, $S_{\min}$ should not be too small, as to calculate the medium-currents in the network we need to solve Equation (2.6). The constants in this system of linear equations $Ax = b$ depend upon the conductances of the edges, and if $S_{\min}$ is too small, we may find that the matrix A is close to singular, which makes the medium-currents hard to calculate. We let $S_{\min} = 0.001$ mm, but any small value produces similar results.

$t_{\min}$. Once an edge has formed, it cannot shrink until a period of time $t_{\min}$ has elapsed. To ensure that some edges shrink, $t_{\min}$ must be smaller than the duration of the simulation. If $t_{\min}$ is small compared to the time it takes a tip to branch, the network just behind the tips thins. We let $t_{\min} = 48$ hours.

I. This denotes the rate of resource uptake at the inoculum, which is a difficult quantity to measure experimentally. Note that the units in which quantity of resource is measured are fixed by the assumption that growing a volume α 'costs' α units of resource, so I represents the maximum (sustainable) volumetric rate of growth. The rate of volumetric growth observed in our experiments was almost always less than 2 mm^3 hour^{-1}, so we let $I = 2$ units hour^{-1}.

τ. This denotes the period of time over which the cost of maintaining a volume α is equal to the cost of growing a volume α. This parameter is also difficult to measure experimentally, but since it has a clear physical interpretation, we can constrain this parameter to a sensible range. In our simulations we assume that $\tau = 500$ hours, as this value minimizes the variation in our predictions for the total metabolic expenditure of our empirical networks (see Section 5.3). A better assessment of appropriate values for τ could be obtained by measuring the metabolic rate of the species being modelled, at various stages of growth.

$R_{\max}$. This denotes the maximum local rate of resource delivery, which pertains in the case where an edge has been starved of resource. We let $R_{\max} = 0.05$ hour^{-1}, which means that resource entering an edge that has been starved of resource has a half life of 14 hours. The precise values of τ and $R_{\max}$ are not very significant, as we are operating in the parameter range where over the course of our simulations, most of the metabolic costs will be associated with growth. As we found that most of the resources are consumed by growth, changing the parameters associated with the cost of maintaining edges has a relatively small effect.

μ. This denotes the efficiency of autophagy, so if it costs one unit of resource to grow a unit volume, an amount of resource equal to μ is recouped when that unit of volume is lost. In the absence of empirical data, we let $\mu = 0.5$.

Outline of the algorithm

In many ways our model resembles the ones proposed by Boswell et. al. [39, 40, 41], as both consider growth, branching, anastomosis, resource uptake, costs for growing and maintaining hyphae, but never-the-less, there are several key differences. First, the models proposed by Boswell et. al. contain 'active' and 'inactive' hyphae: active hyphae contribute to the transport process and they require resources in order to be maintained, while inactive hyphae do not have a maintenance cost, and they do not contribute to the transport process. Active hyphae become inactivated if the

concentration at that point drops below a given parameter value, and inactive hyphae are removed from the network by a Poisson process. In our model edges thicken or thin, rather than switching between active and inactive. Thicker edges have a greater transport capacity, but changes in cross-sectional area are a function of the velocity of mass-flow as well as concentration (recall that in our model edges cannot thicken if they do not contain sufficient resource to do so).

The other crucial difference is the way in which we model the transport of resources. In Boswell et. al's model resource diffuses through the active hyphae, and whenever there is a cell adjacent to a tip, a fraction of the resource in that cell is passed on to the tip. This effectively makes the tips function as sinks, as the cells adjacent to the tips become depleted of resource. In our model we also have diffusive transport, as well as advective transport that is directed towards the tips. Crucially we do not suppose that the individual hyphae have any global knowledge, as both the scale and direction of advective transport is determined by the location and scale of water uptake and growth, and the conductance of the network.

5.3 Calibrating Model Parameters From Empirical Data

In order to reduce the number of free parameters in this model, as many as possible were extracted from the literature or from data gathered using digital images of *P. velutina*. Jessica Lee and Mark Fricker (Department of Plant Sciences, Oxford) have converted photographs of *P. velutina* into adjacency matrices by marking the branch or anastomosis points as nodes, as well as marking numerous points along the length of the cords. A program was written that labels the nodes and then uses the marked points to calculate the lengths of the cords between them. Since manual delineation of the network was required to produce the adjacency matrices and other network summaries, the available data were limited, but were sufficient to provide rough estimates of the curvature and branching rate in networks of *P. velutina*. Given recent developments in automated network extraction (see Section 6.1), and the likelihood

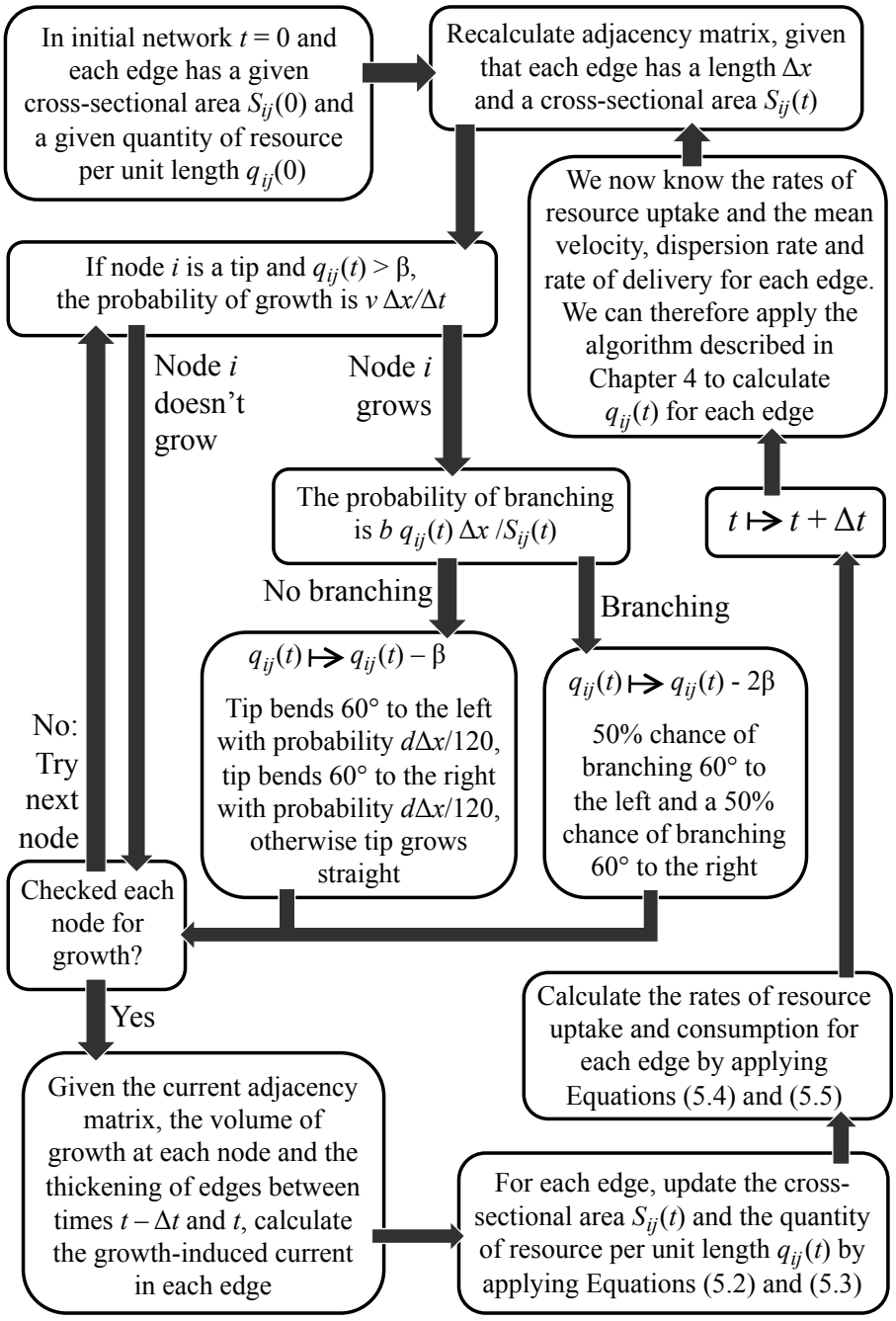

Figure 5.2: **Outline of algorithm.** Algorithm can be continued until the network reaches a given size, or for a given number of time steps.

of much more data becoming available, the methods used to calibrate our parameters are of much greater interest than the absolute values, as these are likely to be refined with higher resolution data.

Estimating the number of anastomosis points

The digital images used to calibrate the model do not distinguish between branch points and anastomosis points. However, they do contain information on the total number of tips and the total number of nodes. We let n_t, n_a and n_b denote the number of tips, the number of anastomosis points and the number of branching points respectively. Following an argument that is closely related to Euler's proof of his polyhedral formula, we note that whenever a branching event occurs the number of tips increases by one, and the number of branch nodes also increases by one. Similarly, when an anastomosis event occurs the number of tips is reduced by one while the number of anastomosis points is increased by one. Crucially, the sum $n_t - n_b + n_a$ does not change when we increase n_t and n_b by one (as in the case where a tip branches), or when we increase n_a and decrease n_t by one (as in the case where a tip grows into an existing edge).

Any network can be built by starting with three tips connected to a central node, followed by some sequence of tip extension, branching and anastomosis. Since our initial network is such that $n_t - n_b + n_a = 2$, and this total is not changed by branching or anastomosis, it follows that for every network

$$n_t - n_b + n_a = 2. \tag{5.11}$$

When calculating the number of anastomosis points, we assume that each anastomosis or branching event produces a new node. In that case every node that is not a tip would be of order 3, while by definition each tip is of order 1. The empirical networks that we analyze contain nodes whose order is greater than 3. However, a node of order $n > 3$ can effectively be represented as $n-2$ nodes of order 3 (see Fig. 5.3). The only slight miscalculation arises from the fact that fungal cords can grow

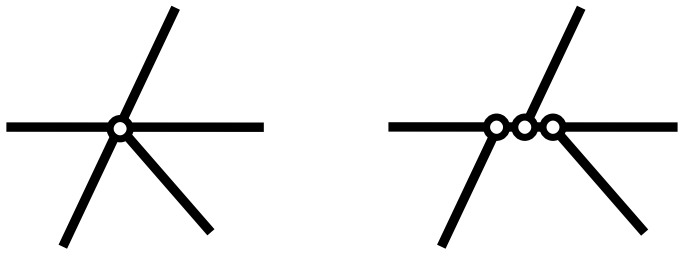

Figure 5.3: **Representation of nodes with more than three edges.** To calculate the mean branching rate of an empirical network we must count the number of nodes, the number of tips (that is, edges that terminate in a node of order 1) and we must also calculate the total length of edges. These quantities are calculated by representing nodes of order $n > 3$ as an assembly of $n-2$ nodes.

over one another and then subsequently fuse at the overlap point, leaving a node of order four produced by a single anastomosis event. However, to satisfy the terms of the above analysis we must represent this sequence of events by having four edges that are joined by a pair of nodes, one of which will be counted as an anastomosis node while the other is counted as a branching node.

Given any network we can count the number of tips n_t and we can count the total number of nodes. As we are interested in estimating the number of branching events and the number of anastomosis events, we do not simply count the number of nodes, we count $N = n_a + n_b + n_t$. That is to say, nodes of order four are counted as two nodes, nodes of order five are counted as three nodes, and so on (see Fig. 5.3). We can then use Equation (5.11) to estimate the number of anastomosis points n_a and the number of branch points n_b, because some elementary algebra indicates that

$$n_a = \frac{N - 2n_t + 2}{2} \qquad \text{and} \qquad n_b = \frac{N-2}{2}. \tag{5.12}$$

Estimating branching rates

Once the number of anastomosis nodes, branching nodes and tips has been calculated, we can produce an estimate for the mean branching rate by assuming that branch nodes appear at a fixed rate λ_b mm^{-1}, and the mean distance between branch

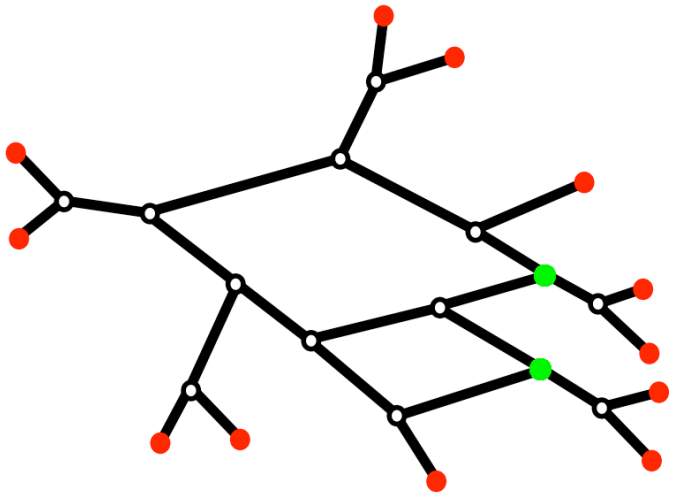

Figure 5.4: **Estimating branching rates.** We are interested in finding the number of branching events per unit distance, which is smaller than the total number of nodes per unit distance.

points is $E(Y) = \frac{1}{\lambda_b}$ mm. To find the branching rate we need to know the mean distance between branch points, which is not the same quantity as the mean distance between nodes, as some nodes are tips, and others are formed by anastomosis events (see Fig. 5.4). In order to estimate the branching rate we simply measure the total length of all the edges, and divide by the number of branch points. Where $\sum L$ denotes the total length of the edges, n_t denotes the total number of tips and N denotes the total number of nodes, Equation (5.12) implies that an unbiased estimate of the branching rate $\bar{\lambda}_b$ is

$$\bar{\lambda}_b = \frac{n_b}{\sum L}. = \frac{N-2}{2\sum L}. \tag{5.13}$$

Note that $\sum L$, n_t and N can all be measured in an empirical network, and so although we cannot distinguish between nodes that are produced by anastomosis and nodes that are produced by branching, we can obtain an estimate of the branching rate of an empirical network over time (see Fig. 5.5). Recall that actual fungal networks are not expected to have a constant branching rate, as the branching rate is higher when the mycelium is well supplied with nutrients [93]. In our model of fungal growth we do not choose a fixed branching rate λ_b, but let the branching rate equal $bc(i,t)$, where $c(i,t)$ is the concentration at tip i at time t. We do not know

the concentration at the tips of empirical networks, and so we cannot find suitable estimates for the parameter b directly, but by using Equation (5.13) we can check that the mean branching rates of our *in silico* networks are similar to the mean branching rates of the empirical networks that we wish to model.

In the case of Experiment 1 we found that there were 0.11 branch points per mm, while in Experiments 2 and 3 there were 0.06 branch points per mm (see Fig. 5.5). These branching rates vary by about 10% over the course of the experiments (between 0.104 to 0.127 branch points per mm in Experiment 1, 0.054 to 0.065 branch points per mm in Experiment 2 and 0.054 to 0.062 branch points per mm in Experiment 3). However, it should be noted that these branching rates reflect the resolution with which the networks were digitized. Moreover, when we measure branching rates using the method outlined in this section, they can appear to change as a result of biomass recycling, as once a cord is removed from the system it no longer exerts any influence on our estimate of the branching rate. However, in the case of the experiments we analyzed we found that including the edges that had been lost through autophagy changed our estimate of the branching rate by less than 1%.

Estimating curvature

To estimate the extent to which hyphae bend as they grow, a program was written that takes each cord in the fungal network and identifies three points along its length. For each such triplet a uniquely determined fourth point was identified, such that the first three points all lie a distance r mm from the fourth. Essentially each cord is modelled as lying on the unique circular arc that passes through the three given points. Under this assumption the length of the cord will be $\frac{\pi r\theta}{180}$ mm, where θ is the angle in degrees subtended between the first given point, the centre of the circle and the third given point. Over this distance the cord is assumed to have deflected by θ°, so its curvature is $\frac{180^\circ}{\pi r}$ mm^{-1}.

To confirm that the use of a hexagonal grid does not make the three-point Gaussian measure of curvature entirely inappropriate, a simple program was written that

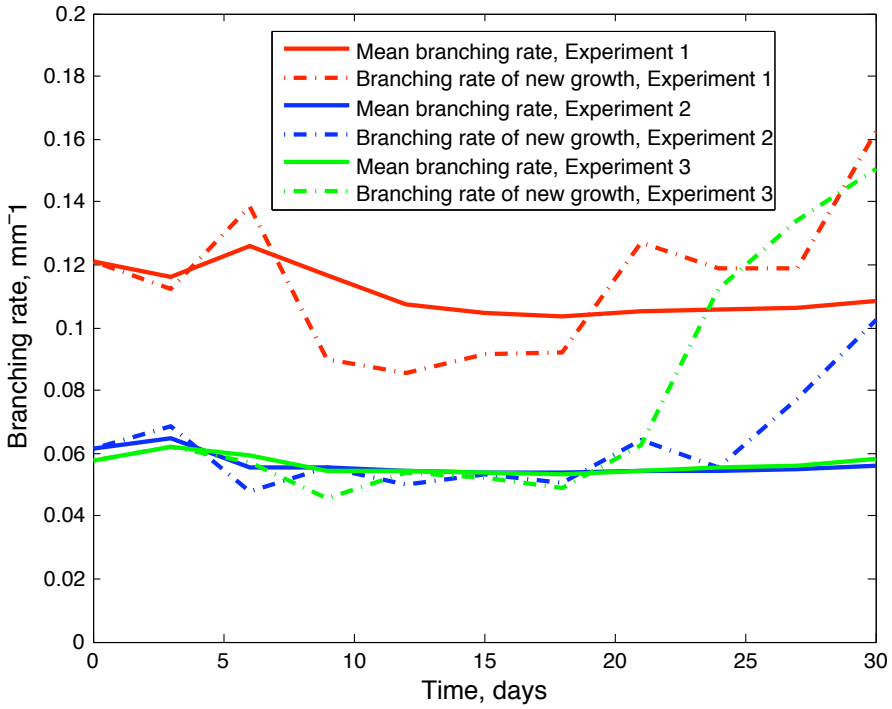

Figure 5.5: **Branching rates in empirical networks.** The branching rates for the new growth are obtained by dividing the total length of the newly formed edges by the change in the total number of branch points. Note that branching rates appear to increase slightly over time, even though the volumetric rate of growth decreases over time (see Fig. 5.6). In other words the rate of growth slows significantly, but the number of branch points per mm of cord increases slightly over time. This may be a result of lateral branching, as cords sometimes grow out of existing cords, and such growth events will clearly result in an increase in our measured branching rate.

produces a series of lines of unit length with a sixty degree bend in them. The two endpoints, together with a point a distance x along the line, were fed into the algorithm outlined above, and the calculated curvature was plotted as a function of x. The algorithm gives a maximum estimate for the curvature when x is the point at which the line bends, and when x and the bend point are both drawn randomly from a uniform distribution the expected measure of the curvature of the line was 60° with a standard deviation of 23°. This indicates that our algorithm produces networks that have the intended mean deflection per unit length (provided that only a small proportion of edges contain more than one bend), and so our algorithm can produce networks that have the same mean deflection per unit length as the empirical

networks.

Growth costs and maintenance costs

We assume that growing a unit volume 'costs' one unit of resource: an assumption that effectively determines the units of concentration. We also assume that the cost of maintaining a unit volume is equal to $\frac{1}{\tau}$ hour^{-1}. Note that where $V(t)$ denotes the volume of the network at time t, we are effectively assuming that the total metabolic cost of growing and maintaining the network between time t and $t+\Delta t$ is

$$M(t) = V(t+\Delta t) - V(t) + \frac{\Delta t}{\tau}\frac{V(t+\Delta t)+V(t)}{2}, \tag{5.14}$$

and the metabolic rate over this time period is $\frac{M(t)}{\Delta t}$. If we suppose that our fungi obtain and use energy at a reasonably constant rate, we can determine a sensible value for the parameter τ by examining the empirical rate of growth, and calculating how the metabolic rates will vary over time (see Fig. 5.6). In the case of Experiment 1, the volume increased over time while the growth rate diminished. In this case, we found that setting $\tau = 470$ hours produces a sequence of metabolic rates that have no correlation with time (that is to say, the straight line that minimizes mean squared error is horizontal). In Experiments 2 and 3 the growth rate barely diminishes over time, so for any value of τ the metabolic rate increases over time. However, by choosing $\tau = 500$ hours we find that the metabolic cost of maintaining the largest networks is similar to the metabolic cost of sustaining the fastest growth. Apart from two outliers the maximum rate of growth does not exceed 2 mm^3 hour, and when $\tau = 500$ hours, the maximum maintenance cost is 1.7 units hour^{-1}. We therefore let the rate at which resource enters the network $I = 2$ units hour^{-1}, because under this assumption the fungus obtains resource at about the same rate at which it is consumed.

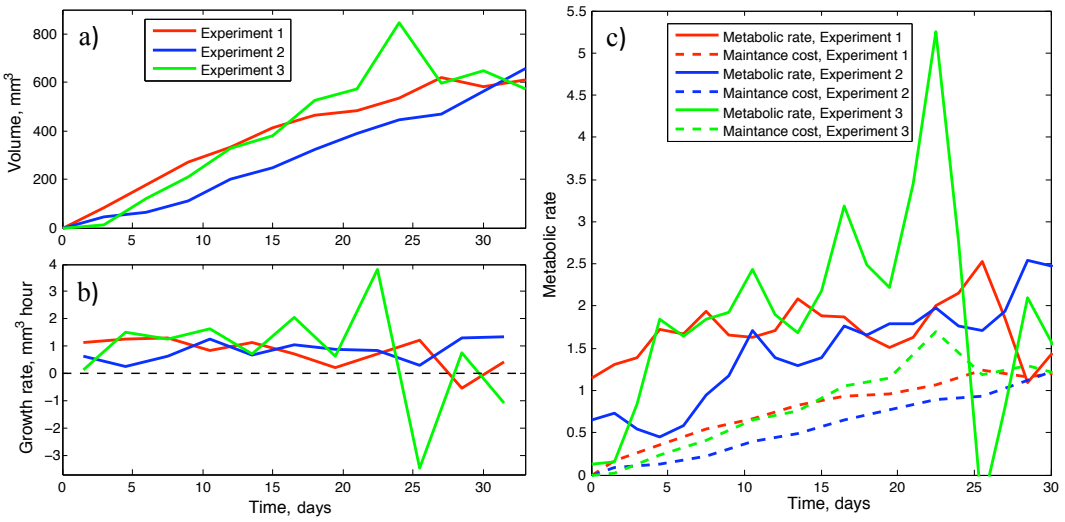

Figure 5.6: **Volume, growth rate and total metabolic expenditure.** **a)** The volume of three empirical networks over time. **b)** The volumetric rate of growth over time. **c)** The total metabolic rate per unit time, which is calculated by employing the following assumptions. First we assume that growing a volume of 1 mm^3 costs one unit of resource, while reducing in volume by 1 mm^3 supplies half a unit of resource. The second component of total metabolic cost is the cost of maintaining the network. Here we assume that it costs $1/500$ units of resource to maintain 1 mm^3 for one hour. In other words, we let $\tau = 500$ hours.

5.4 Geometric Comparisons Between Fungi and the Simulations

Because of the complexity of this model, the parameter space is considerable, though many of the parameters can be constrained within some sensible range. The resulting structure will of course depend on the parameter values, and within some regions of parameter space the branching rate drops significantly as the tips grow further from the inoculum, while in others the concentration in the network as a whole tends to increase over time, which results in an increase in branching rate (at least over some period of time). If we disregard the concentrations in the network and simply suppose that the growth rate and branching rate are constant, and equal to the values extracted from empirical data, the parameter space is significantly reduced. In this section we use our family of models to generate an ensemble of networks, and we assess the extent to which our models can recapitulate the structure and development of actual fungal networks.

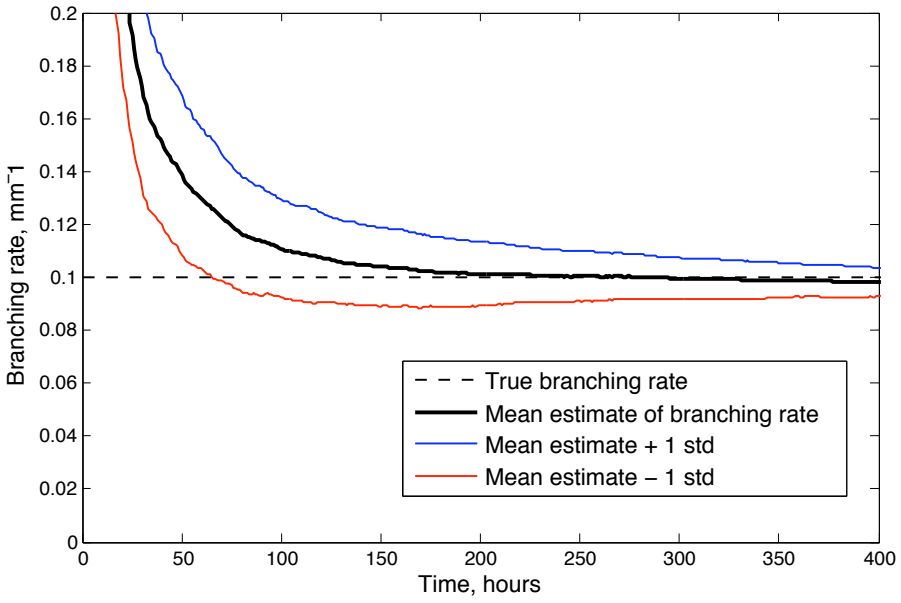

Figure 5.7: **Estimated branching rates converge on the true value.** If we generate *in silico* networks with a fixed branching rate λ_b, Equation (5.13) produces an estimate for the branching rate that approaches the true value as the number of tips and nodes increases. Note that the initial estimate of the branching rate is very high, because our simulations begin with six edges of length Δx radiating out of a single hexagon. In other words, regardless of the branching rate λ_b, our simulations begin with 4 branch nodes and a total edge length equal to $6\Delta t$.

Curvature and branching rates

Insufficient data were available to make statistically robust estimates for the branching rate and curvature of *P. velutina*, but as we have seen, reasonable parameter values of 0.06 mm^{-1} and 6°mm^{-1} respectively could be obtained from the empirical data. Furthermore, if we use our algorithm to grow an *in silico* network with a constant branching rate λ_b and then estimate the branching rate by examining the resulting network, Equation (5.13) returns a value $\bar{\lambda}_b$ that tends towards λ_b as N tends to infinity (see Fig. 5.7).

Number of loops in the network

There are a two standard ways of measuring the extent to which a network is filled with loops, normalized to account for the size of the network. The gamma index of

a network is equal to the ratio between the number of edges E and the maximum number of edges that the network could contain, given the number of nodes. In the case of a planar network, Euler's polyhedral formula implies that the maximum number of edges in a network with N nodes is $3N-6$ [18]. We therefore let

$$\gamma_p = \frac{E}{3N-6}. \tag{5.15}$$

An alternative measure is the alpha index, which equals the ratio between the number of elementary cycles or loops and the maximum number of loops, given the number of nodes. The number of elementary cycles is equal to the number of anastomosis nodes, or $E-N+1$ (where E is the number of edges and N is the number of nodes). Given a network with N nodes the maximum number of elementary loops is $2N-5$ [18], so we have

$$\alpha = \frac{E-N+1}{2N-5}. \tag{5.16}$$

As one elementary cycle is formed every time there is an anastomosis event, the value of α is an increasing function of the number of anastomosis events. Likewise, as anastomosis reduces the number of tips, α is a decreasing function of the number of tips. Using the definition of the average degree $< k >= \frac{2E}{N}$, in the limit case of large N we have

$$\alpha \approx \frac{< k > -2}{4} \quad \text{and} \quad \gamma_p \approx \frac{< k >}{6}. \tag{5.17}$$

A potentially significant geometric difference between the actual fungal networks and the simulations is that the latter quite rapidly reach the point where the anastomosis points outnumber the tips, producing relatively large values for the alpha and gamma indices. In simulations with a branching rate equal to that of the empirical networks, the percentage of nodes that are anastomosis points increases over time, and begins to level out at around 30%, compared to 20% tips and 50% branch points. In contrast, the actual fungi maintained a significantly higher proportion of tips over the period that they were photographed (see Fig. 5.8a). It has been observed that hyphal tips at the edges of a fungal colony tend to display negative autotropic behaviour, which reduces the amount of anastomosis that occurs, while tips

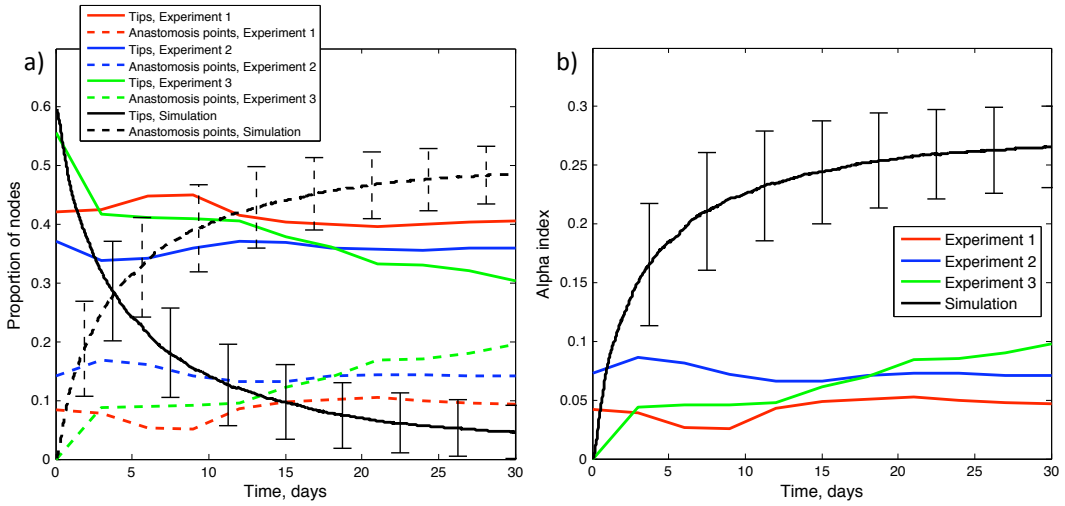

Figure 5.8: **Loops in empirical and model networks. a)** Fraction of nodes that are tips, and fraction of nodes that are anastomosis points in empirical and simulated networks. In the case of the simulated networks we have shown the mean fraction of nodes of each type, plus or minus one standard deviation. If most edges do not contain bends, the number of tips approaches 4% of the total number of nodes, while α approaches 0.27, over a time scale that is determined by the velocity of tip growth and the branching rate. **b)** Alpha index for empirical and model networks, plus or minus one standard deviation. Note that the number of loops in the empirical networks is only about 30% of the number of loops in a simulated network with an equivalent branching rate.

behind the leading-edge of the colony do fuse with other hyphae [103]. This may explain why our empirical networks have more tips and fewer anastomosis points than equivalently densely branching *in silico* networks. The relatively large number of tips in the empirical fungal networks is reflected in relatively small values for α (see Fig. 5.8b).

Distribution of lengths and cross-sectional areas

Although our model does not do a very good job of reproducing the ratio of loops to tips in a growing fungal network, with the appropriate choice of parameter values our model does produce networks with distributions of edge lengths and cross-sectional areas that are very similar to the empirical case (see Fig. 5.9). However, it should be noted that both the branching rates and the distribution of lengths and cross-sectional areas depend on the resolution of the process by which we digitize the

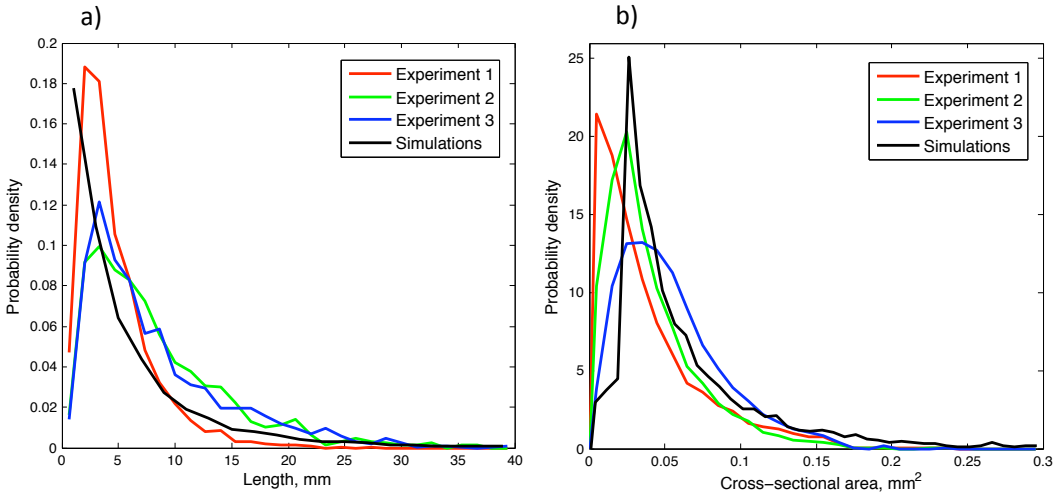

Figure 5.9: **Distribution of edge lengths and cross-sectional areas in empirical and model networks.** **a)** Probability density function for the length of edges. Increasing the branching rate in our model decreases the mean length of edges, but for any parameter value, the distribution of edge lengths is approximately exponential. Note that in the absence of anastomosis the distribution of edge length would be precisely exponential, as we assume that branching is a Poisson process. **b)** Probability density function for the area of edges. The distribution of cross-sectional areas in the model networks depends on the choice of parameter values (chosen here to fit the empirical data), but the most frequently occurring cross-sectional area is β: the cross-sectional area of newly formed edges. Recall that the parameter ω represents the velocity at which the edges will not grow or shrink. If ω is too small all the edges will thicken over time, while if ω is too large all the edges will shrink, and most edges will be smaller than β. In this case we let $\beta = 0.02$ mm^2, while $\omega = 0.4$mm hour^{-1}, which is double the mean velocity of tip growth.

network. Significantly, our algorithm for changing the cross-section of edges over time means that a network that is initially uniform in cross-sectional area matures by forming major transport pathways, while other parts of the network thin (see Fig. 5.10). This lends support to the idea that the developmental fate of hyphae is partially determined by the currents that they carry.

Concluding remarks

We have presented a modelling framework that was intended to capture the complex interplay between growth, mass-flows, and resource concentration. Many of the parameters can be calibrated by analyzing empirical networks, and our models were successful at reproducing the distribution of edge lengths and cross-sectional areas

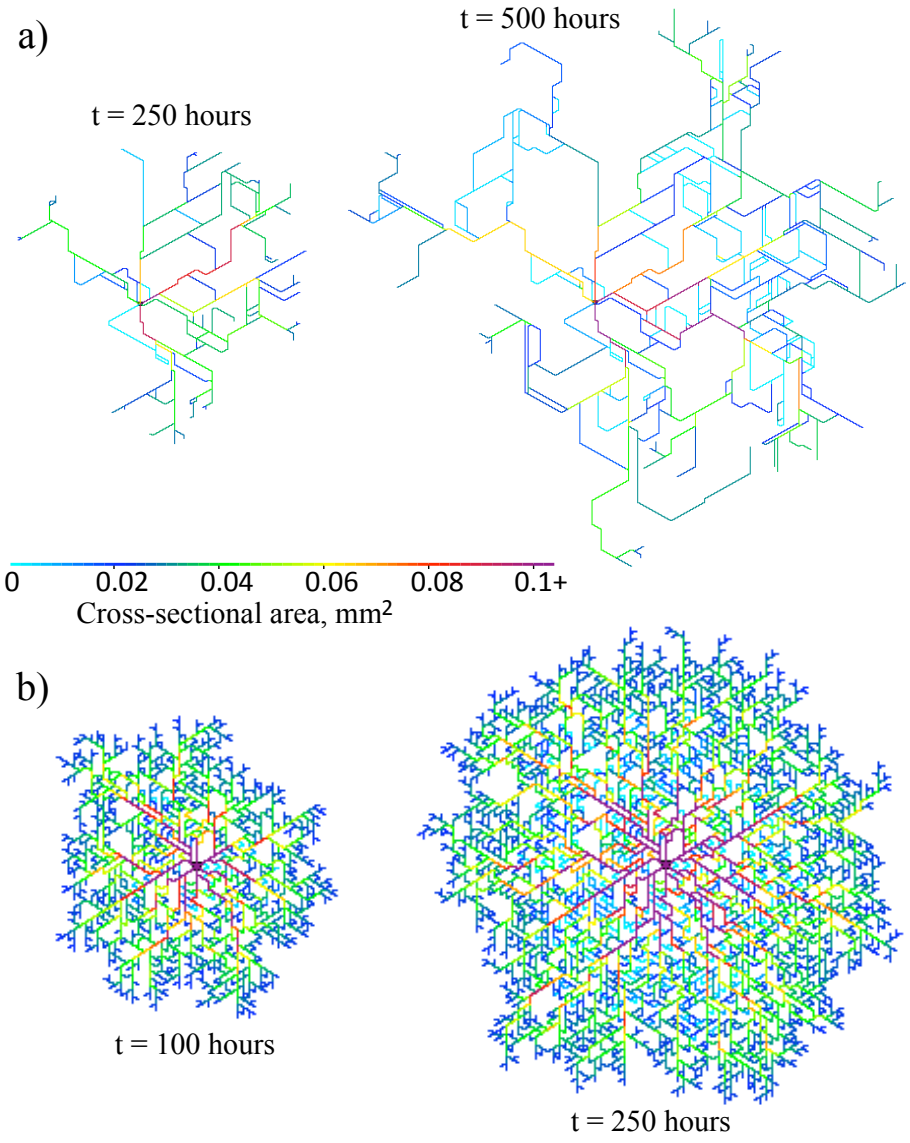

Figure 5.10: **Examples of a network generated by our model. a)** This network was generated using the parameter values listed in Section 5.2, with a branching rate equal to 0.05 branch points per mm. **b)** This network was generated using the same parameter values, apart from the branching rate, which was set to equal 0.5 branch points per mm. Note that changing the branching rate has a significant effect on the distribution of edge lengths, but the distribution of cross-sectional areas that emerge from the model is not very sensitive to the branching rate.

found in empirical networks (see Fig. 5.9), with some edges thinning while others thicken over time. This lends support to the idea that the developmental fate of hyphae is partly determined by the currents that they carry, as we found that networks that are initially uniform in cross-sectional area mature by forming major transport routes, while other parts of the network thin (see Fig. 5.10). Given the branching rate of empirical networks, we found that they contain surprisingly few loops. Model networks with the same branching rate contain far fewer tips, and form a much larger number of loops (see Fig. 5.8).

Due to the complexity of our model, and the large parameter space, our analysis of the morphologies that emerge in different nutrient environments is at a preliminary stage. Nevertheless, it is clear that the hydraulic coupling of the network ensures that growth in one region has an impact on the nutrient concentration in other parts of the network. If these changes in concentration are sufficient to change the pattern of growth, then increasing the growth rate in one part of the network will inhibit growth elsewhere, as has been observed in actual fungal networks [189, 199]. In the following chapter we present some ways in which our research could be further developed, including various ways in which our *in silico* model of fungal growth could be extended. As well as discussing models that we could develop, we also consider experiments that might elucidate transport processes in fungi, and we also consider a completely different application for our mathematical machinery for solving advection, diffusion and delivery equations over a network.

Chapter 6

Further Work

In this chapter we describe some of the ways in which our research could be further developed. In Section 6.1 we discuss the experimental work that we have carried out and which could be undertaken, to elucidate the process of translocation across fungal networks. In particular, we discuss automated network extraction, bidirectional transport and the use of quantum dots. In Section 6.2 we review some of the ways in which our *in silico* model of fungal growth could be extended. For example, we could incorporate more detailed interactions between the hyphae and their environment, and we could explore the relative foraging success of a range of variants in a range of environments. One problem with fungi as experimental systems is that it can take weeks or months for fungal networks to grow, and imaging the translocation of radio-labelled materials with scintillation screens is expensive. By exploring the patterns of growth that are observed *in silico*, we can better determine which experiments are most worth performing.

A further important point is that the formalism of advection, diffusion and delivery could be used to model many physical systems. As noted in Chapter 3, molecules of interest are carried by advection and diffusion through the cardio-vascular networks of animals [25, 26, 90, 91, 121, 173, 175, 184, 194], the xylem and phloem elements of tracheophytes (vascular plants) [133, 166, 186], and various body cavities of many different animals. Similar mechanisms of transport are also found in geological and technological systems, such as rivers and drainage networks [14], gas pipelines, sewer systems and ventilation systems. In Section 6.3 we employ the

machinery we have developed to analyze simple models of glucose delivery through a vascular network. This work has been placed in a chapter entitled 'Further Work' because we have not yet connected our model to any empirical data. Nevertheless, we believe that are results are biologically relevant, and the methods presented in Chapter 3 should make it computationally feasible to solve our model equations over empirically determined vascular networks. In the absence of empirical data we have considered very simple networks, subject to a wide range of local delivery rates, but even these toy models can reveal the importance of network structure, and the impact of local delivery on the dynamics of resource distribution.

A notable feature of this model is the fact that we can use it to show that in certain circumstances, increasing the volume of blood and the number of glucose transporters can actually decrease the total rate of glucose delivery. This somewhat paradoxical result is of particular bio-medical interest, as glucose delivery is essential to the survival of tumours and healthy tissue, and understanding the functional consequences of anti-angiogenic drugs is key to the effective treatment of vascular tumours [51, 120, 151, 201]. As we shall see, to appreciate how the number of blood vessels in a region affects the total rate of glucose delivery, it is essential that we consider both the rate of delivery of resource out of the network and the topology of the transport network itself. We conclude Section 6.3 with an analysis of the bio-medical implications of the insights we have gained from our modelling approach. Finally, in Section 6.4 we review the major findings of the thesis, and assess the ways in which our research could be further developed.

6.1 Future Work: Experiments

We have seen that experiments with radio-labelled tracers reveal transport on a scale that is comparable with the flows that we predict on the basis of our model of growth-induced mass flows. Moreover, the asymmetric distribution of tracers and the occurrence of sudden route switching can also be explained by the fact that we observe patchy, stochastic growth, which is expected to induce significant currents in some

cords but not others. More data are needed to make statistically robust correlations between growth, mass-flows and cord thickening, and the process of gathering more data will be greatly assisted by new methods of automatically extracting digital networks from a sequence of photographs [142, 143]. This process also enables us to describe the networks in much greater detail, improving our measurements of the changing volume of the network.

Further confirmation of the validity of our modelling approach could be obtained by directly measuring the velocity of flow in a hyphal network (which are relatively small and transparent), as opposed to a network of cords. For example, video footage of *N. crassa* clearly indicates that the cytosol is moving [103, 126], and if the technical difficulties of resolving an entire network could be overcome, these empirically determined velocities could be compared to the velocities predicted by our model. As with any model, our account of transport in fungal networks is based on an idealization, and there are numerous features of actual fungal networks that we have ignored. In particular, we suppose that the entire network is connected, and that some fixed fraction of each cord is occupied by transport vessels. In reality, fungi include numerous compartments where materials could be sequestered, and in particular, the vacuole system may have a significant impact on the distribution of various molecules throughout a fungal network [62]. Quantum dots are a promising technology for investigating transport pathways within fungal networks, and further developments in microscopy should help to elucidate the scale and structure of the transport pathways. For example, it may be possible to obtain an independently determined figure for the fraction of each cord that is occupied by transport vessels.

In our model the currents in each edge are directed from the sites of water uptake to the sites of growth. This pattern of flow is pressure driven, and material only ever flows from high pressure to low pressure, so transport is directed and material does not move in loops. There is evidence that in actual fungal networks, transport can be bidirectional, with some material passing from source A to source B, while at the same time there is a flow of material from source B to source A [57, 130]. It is not clear whether the two materials are traveling along different routes (which

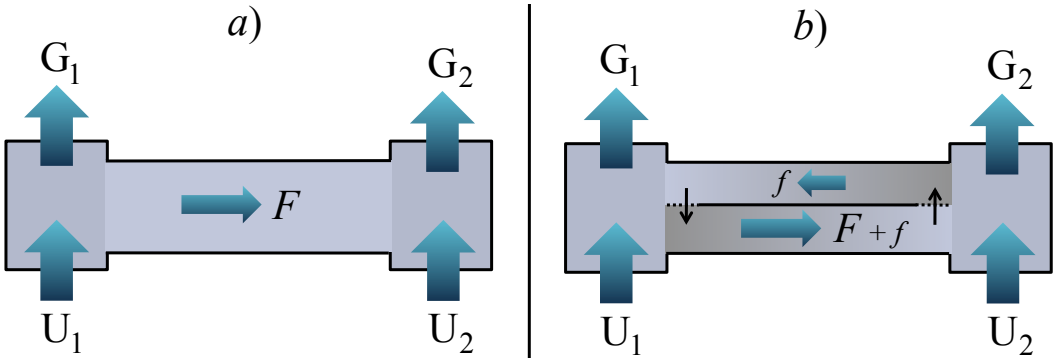

Figure 6.1: **Bidirectional flows in an insulated cord.** In the case where an insulated cord is the only link between two regions, the net current from region 1 to region 2 must be $F = U_1 - G_1 = G_2 - U_2$, where U_i denotes the volumetric rate at which water and other materials enter region i and G_i denotes the rate of growth of region i. Both scenarios **a)** and **b)** have the same net current, but in case **b)**, a concentration gradient across semi-permiable membranes produce a flow of water molecules into a transport vessel at one point, and out at another. The fungi would have to work to maintain the concentration gradients needed to drive the counter-flow f. It is not clear whether fungi actually expend energy to maintain such flows, but in any case, the conservation of volume ensures that there must be a net flow of fluid towards the growing tips.

could be consistent with the picture of transport in each cord being unidirectional), or whether a single cord can carry flows that are moving in opposite directions. My experiments to determine which of these is the case were inconclusive, but we note that if a cord is not changing in volume, the net current entering the cord must equal zero. The pattern of flows must be consistent with the changing distribution of volume, but if fungi work to maintain concentration gradients between adjacent hyphae, osmotic forces could produce counter flows, much as plants produce mass flows in the phloem [116, 141, 211]. Such flows could be an important part of fungal transport pathways, but the possible distribution of currents across the mycelium is constrained by the fact that aqueous fluids are incompressible in this regime, so in any case there must be a net flow from the sites of water uptake to the sites of growth (see Fig. 6.1).

Automated network extraction

In order to analyze fungal networks, we require a digitized description of them.

More specifically, we require an adjacency matrix where each edge has a measured length and volume. The networks analyzed in this thesis were obtained by a labour-intensive, semi-automated process, carried out by Jessica Lee and other members of Mark Fricker's laboratory (Department of Plant Science, University of Oxford). Much more data could be obtained by using a fully automated process, and an obvious first step in segmenting or extracting a network structure from a digital photograph is to find the component lines of the network by identifying the directions in which the image intensity is brightest. The problem with such simple, intensity-based methods of network segmentation is that they tend to be very sensitive to changes in absolute intensity or changes in image contrast.

Very recently, a fully automated method of network extraction has been developed by Boguslaw Obara (e-Research Centre, University of Oxford) [142, 143]. This algorithm converts the image into Fourier space, and compares the phase of different frequencies at different parts of the image. Near a linear structure such as a cord, the phases of different frequencies will be very similar in the direction perpendicular to the line, but there is no reason why the phases should be correlated in the direction parallel to the line. Moreover, the values of phase congruency are minimally affected by changes in image contrast. Thus by using information about phase congruency as well as image intensity, B. Obara has shown that we can do a much better job of segmenting a network containing thick and thin lines.

It is essential to our model that the network is connected, and a graph representation of the network is constructed by pruning any disconnected edges. We can also assign edge weights based on the Euclidean lengths of the lines, and on estimates of edge thickness derived from sampling the local intensity. This approach provides a rapid, robust and extremely effective means to extract fungal networks [142, 143]. This will mean a huge amount of new data is available for analysis, but at present, each photograph yields a separate network, rather than a time series of networks where each edge has an empirically determined volume that changes over time.

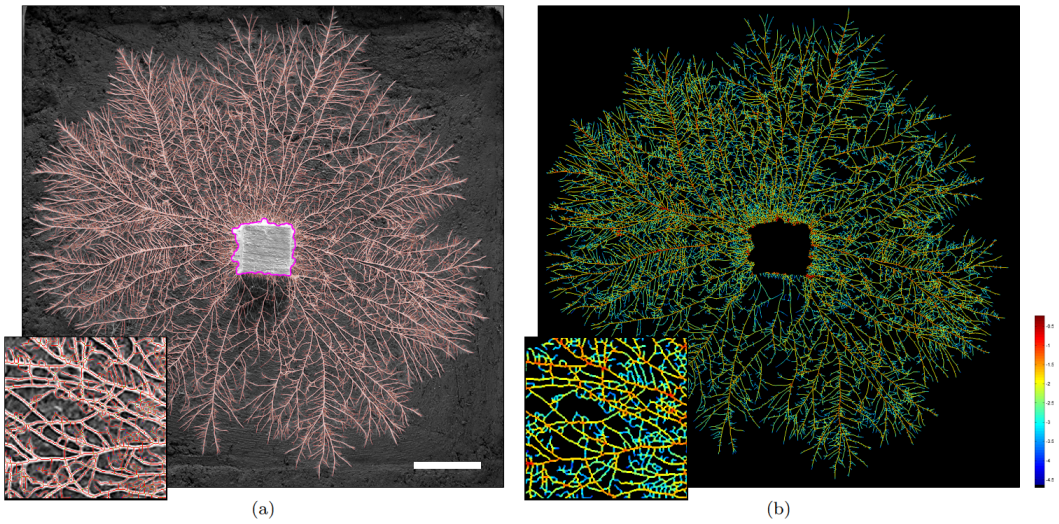

Figure 6.2: **Automated extraction of digital networks**. **a)** A photograph of a network formed by*Phallus impudicus*, grown on compressed soil over a period of 20 days. The network extracted by B. Obara's image analysis program has been overlaid with centre lines shown in red, branch points in green, end points in blue, and the food-source boundary lines has been marked in magenta. **b)** The digitized network, with edges coloured by the image intensity of the photograph along the lines in question. The scale bar corresponds to 2 cm, and the digitized network contains about 10^6 edges.

Velocities of cytoplasmic flow, growth and topology of *N. crassa*

In many ways *P. velutina* is less than ideal as a choice of species with which to assess our model of growth-induced mass flows. *P. velutina* is of interest because it forages over significant distances, but its cords are opaque, and it is very difficult to accurately measure the velocity of mass flows within the fungal network. In contrast, it is relatively straightforward to accurately measure the velocity of particles within the hyphae of species such as *Neurospora crassa* [103, 126]. As has been demonstrated by Roger Lew and members of his laboratory, in the apical compartments of *N. crassa* the mean velocity of mass flow matches the velocity of tip growth, as predicted by our model [126]. Measurements of the velocity of mass flow can be obtained from video footage of organelles and silicon droplets moving through the hyphal networks of *N. crassa* , and it is apparent that the velocity of mass flow away from the growing tips can be significantly greater than the velocity of tip growth [103]. It would be interesting to systematically compare the velocities predicted by

our model with the measured velocities. The technical difficulty is that in order to apply our model, we either require a snapshot of the entire network complete with estimates of the rates of growth or, failing that, we require measurements of a fragment of the network in which the rates of growth are known, as are all the volumetric currents flowing into the measured fragment.

Measuring the local velocities requires close up video footage, and simultaneously capturing the structure of the surrounding network is a significant technical challenge, not least because such networks will not lie in a single focal plane. However, by automating the imaging process, it may be possible to ensure that a complete network (or fragment of a network) has been captured, at which point we would be able to assess the accuracy of our model. It should be noted that the model described in Chapter 4 assumes that all water uptake occurs at the inoculum, which is reasonable because the cords have hydrophobic coatings, and the inoculum is filled with hyphae that do in fact draw water into the mycelium by means of osmotic forces. In the case where we are modelling a hyphal network (as opposed to a network of cords) it would be more appropriate to assume that there is a more even pattern of water uptake.

Microscopy and quantum dots

One promising technique to investigate the flow of nutrients within fungi and between fungi, plants, microorganisms and soil is the use of quantum dots [208]. Quantum dots (QDs) are nanoscale semiconductors that fluoresce in different colors depending on their size (ranging between $2-20$nm), and they can be bound to amino or carboxyl groups within organic compounds. QDs are not susceptible to photobleaching, and by binding them to a range of organic compounds, the movement of those compounds can be imaged and tracked. For example, QDs have been used to demonstrate that arbuscular mycorrhizal fungi may have a more significant effect on organic nitrogen dynamics than previously believed [208]. QDs could be used to assess the difference in translocation pathway between different molecules

of interest, and they might also be used to identify the parts of cords that actually carry molecules moving from one part of the mycelium to another.

Bidirectional flow in *P. Velutina*

There is evidence that when a fungal network connects two or more sources of nutrient (sources A and B, say), translocation of phosphate and other molecules occurs in both directions [57, 130]. It is not clear whether individual cords can accommodate bidirectional transport, with material moving in both directions in a single cord, or whether currents flowing in different directions are carried through different cords. In order to answer this question, we devised a series of experiments that were ultimately inconclusive. First we placed autoclaved beech (*Fagus sylvatica*) blocks on *P. velutina* mycelium in malt agar culture plates, and incubated at 22°C until the fungi had thoroughly penetrated the wood blocks. We then placed pairs of inoculated wood blocks 10cm apart in a sand filled microcosm (33% sterile white sand, 50% sterile black sand, and 17% water by weight), and while we waited for a fungal network to form, we maintained the weight of the microcosm by spraying water to replace any that was lost by evaporation. Once there was a network connecting the two woodblocks, some scintillation screen was cut into 1cm wide strips, the plastic side was coloured with a black marker pen, and the strips were glued onto a long strip of scintillation screen with a gap of 1cm between them. The cords connecting the two wood blocks were then covered with these striped scintillation screens, and we dripped ^{14}C-AIB onto one wood block, and ^{32}P on the other. The decay energy of ^{14}C is 0.16MeV, compared to 1.71MeV for ^{32}P, and only the electrons ejected by ^{32}P can penetrate the screen where it has two layers. In contrast, where the screen has only one layer we can detect both the ^{14}C and the ^{32}P.

Our original intention was to calibrate the quantities of ^{14}C-AIB and ^{32}P in our fungal networks such that both tracers would cause the emission of similar numbers of photons. The hope was that we could then separate the signal produced by 32^P from the signal produced by ^{14}C-AIB, and track the movement of the two different

kinds of tracer. Unfortunately, the experimental microcosms were too small, and the time needed to produce a significant signal from the ^{14}C-AIB was similar to the time it took the ^{32}P to transit from one wood block to other (about 8 hours). Consequently, it was not possible to unambiguously detect the moving fronts of both radio-tracers, and for individual cords, we could not determine whether or not there was bidirectional movement of tracers. Increasing the concentration of radio-label would improve our ability to track the movement of materials within in fungi, as if a larger number of photons were emitted, we could reduce the period of time over the which we need to integrate the photon count. Performing the experiment in a larger microcosm should also improve the results, assuming that it would long for the tracers to move between wood blocks that are further apart.

6.2 Future Work: Models

Growth in heterogenous environments

The distribution of nutrients in the environment has a critical impact on fungal growth [28, 32, 145, 156]. Most fungi grow in soils, which exhibit spatio-temporal, nutritional and structural heterogeneity. The structural heterogeneity in soils is largely determined by the relative location of soil particles and the resulting pore space. The nutritional heterogeneity is strongly modulated by the ground-water distribution, which itself depends on the architecture of the pore space. In non-saturated soils, the walls of pores are coated in a film of water, and the larger pores contain pockets of air. This kind of complex environment can be represented by 'removing' some of the hexagonal cells in a tip and bond model, and by assumption these absent hexagons cannot be penetrated by the model hyphal tips [36, 41]. It is also possible to model growth in three dimensions, by representing the location and orientation of hyphae in terms of a face-centred cubic lattice, instead of a two dimensional hexagonal lattice [36].

The movement of hyphal tips in the soil pore space is greatly affected by both the

physical boundaries of the soil particles themselves and also by the surface tension of the water film surrounding these particles. Experimental investigations suggest that mycelial fungi are more commonly found growing on the edges of soil particles than in large air-filled pore spaces [102, 171], and physical constraints also appear to have some impact on the rates of bending and branching [98]. These properties of fungal hyphae can be modelled by biasing the tip movement probabilities so that hyphal tips have a tendency to stay within the water film, without affecting the mean tip speed [41]. Furthermore, fundamental properties of the model pore space, such as its fractal dimension, can be determined enabling qualitative and quantitative comparisons with real soil systems [36, 41].

Lattice free models of growth

For the sake of computational simplicity, our model of a growing fungal network is embedded in a hexagonal lattice. This restriction can be relaxed, as fungal networks can be modelled as a collection of line segments with unrestricted orientation [53, 105]. Calculating when anastomosis occurs is more challenging in that case, but that level of geometric freedom may be necessary for a more detailed model of how environmental factors impact upon the structure and function of a fungal network. This more complex modelling approach may be necessary to accurately model the interaction between the various tropic responses exhibited by fungi, including tropism to toxic metals, liquid flows [144], electric fields and surface contours [98, 105]. It has also been observed that hyphal tips at the edges of a fungal colony tend to display negative autotropic behaviour, which reduces the amount of anastomosis that occurs, while tips behind the leading-edge of the colony do fuse with other hyphae [103]. Automated network extraction may enable experimentalists to measure the scale of various tropic responses, at which time lattice free models may be necessary to assess whether a given set of local, tropic responses can indeed account for the observed, global pattern of fungal growth.

Robustness, grazing and the response of fungal networks

As well as responding to local nutritional stimuli, filamentous fungi effectively respond to damage, predation and attack from other fungi [32, 34], closing septal pores to prevent the loss of cytoplasm, and reconnecting severed regions of the mycelium with a fan of fine, hyphal growth. Further study is required to elucidate the nature of the signal that induces this response, but it is reasonable to claim that in order to function efficiently, mycelial networks must retain their integrity in the face of continuous attack by mycophagous insects and random damage [34]. Grazing typically encourages the proliferation of hyphal growth and the formation of cross-links at the expense of further exploratory growth, effectively re-directing resources to consolidate the existing network [34].

Some network analysis has been carried out to assess the resilience of fungal networks [27, 34, 113], and it is intriguing to note that our model of growth-induced mass flows suggests that the edges which are most critical for maintaining the connectivity between parts of the network are also the edges which are predicted to carry the greatest flux. In other words, it is the edges that carry the greatest flux that most urgently require a protective rind. Moreover, when a cord is severed the flux through the network will be redirected, and cords that previously carried a small current may suddenly carry a much greater flux. Fungi may well be sensitive to this kind of event, and it is plausible that they utilize the patterns of mass flow to make globally efficient decisions on the basis of locally available information. By observing how various species of fungi respond to damage, and by modelling grazing and the ensuing fungal response, it may be possible to draw further conclusions about the efficiency or optimality of fungal responses to grazing, and to assess the extent to which the fungal responses that have been characterized can indeed account for the set of fungal structures that have been observed.

6.3 Modelling Glucose Delivery Through A Vascular Network

In this section we develop a simple model of glucose moving through a vascular network, where the glucose is 'consumed' or transported out of the network by glucose transporters on the surface of the vessels. This model has been presented in a chapter on 'further work' because we have not yet connected our results to any experimental data. Nevertheless. we believe that our results are biologically relevant, and the mathematical methods presented in Chapter 3 should make it computationally feasible to solve our model equations over empirically determined vascular networks (e.g. retinal vascular networks).

For the sake of simplicity we assume that the glucose transporters are uniformly distributed over the interior surface of all of the vessels, so the number of transporters per unit length is proportional to the radius of the vessel, and the number of transporters per unit volume of blood is inversely proportional to the radius of the vessel. The rate of glucose delivery reflects the frequency of interaction between glucose and the glucose transporters. The kinetics of glucose passing through a transporter is rapid [79], so high concentrations of glucose are required to saturate the transporters. Throughout this chapter we assume that the glucose concentration is below the carrying capacity (K_m), and we make the simplifying assumption that the reaction rate is proportional to the concentration of glucose and the concentration of glucose transporters. In other words, we consider the case where the local delivery rate per unit of resource R_{ij} is inversely proportional to the radius of the vessel. By the methods discussed in Chapter 3 we can calculate the concentration throughout any idealized network, but in this chapter we are particularly interested in comparing the total rate of glucose delivery in different networks of cylindrical tubes. This quantity is of particular interest as it corresponds to the total rate at which glucose is transported out of the vasculature and into the surrounding tissue.

Numerical simulations indicate that the distribution of resource reaches a steady state quite rapidly. At steady state, the total rate of resource delivery must equal

the current of resource entering the network minus the current of resource leaving the network. Furthermore, the fundamental advection, diffusion, delivery Equation (3.2) tells us that at steady-state,

$$R_{ij}q_{ij} + u_{ij}\frac{\partial q_{ij}}{\partial x} - D_{ij}\frac{\partial^2 q_{ij}}{\partial x^2} = 0. \tag{6.1}$$

It follows that for each edge there must be a pair of constants A and B such that

$$q_{ij}(x) = Ae^{\frac{u_{ij}+\hat{\alpha}_{ij}}{2D_{ij}}x} + Be^{\frac{u_{ij}-\hat{\alpha}_{ij}}{2D_{ij}}x}, \tag{6.2}$$

$$\text{where} \quad \hat{\alpha}_{ij} = \sqrt{u_{ij}^2 + 4D_{ij}R_{ij}}. \tag{6.3}$$

In the case of a single edge, we could insist that the concentration at node 1 is $c_1(t) = k_1$ and the current of resource entering the network is $I_1(t) = k_2$. We could then determine the constants A and B, which would tell us the steady state distribution of resource, including the critical conditions at node 2, namely $c_2(t)$ and $I_2(t)$ for very large t. However, to satisfy the fundamental Equation (6.1) and the conditions $c_1(t) = k_1$ and $I_1(t) = k_2$, we may require a concentration at node 2 that is much larger than the concentration at node 1, despite the fact that resource is consumed as it flows from node 1 to node 2. A better approach, which we follow, is to assume that the concentration at node 1 is some fixed constant k, and that the current of resource leaving the network at node 2 is proportional to the concentration at node 2. More specifically, we suppose that resource leaves the network by flowing into some dummy edge $2n$, which is assumed to have the same cross-sectional area as the other edges.

Whatever current of resource and medium we introduce and remove from the given network, the steady state distribution of resource must satisfy Equation (6.1). For the sake of simplicity we ignore the process of vascular adaptation whereby vessels dilate, contract or become apoptotic in response to fluid flow and the associated wall shear stress [3, 111, 148, 151], but as our algorithm(s) can be applied to networks with varying cross-sectional areas, we note that such effects could be incorporated into a more complex model.

Calculating Total Rates of Delivery in Idealized Vascular Networks

Our aim is to compare the efficiency of glucose delivery for a range of different networks, and we do this by calculating the total rate of glucose delivery C_{tot} for a particular, representative distribution of glucose. More specifically, we calculate the total rate of glucose delivery in the case where the distribution of glucose is at steady state, the concentration at node 1 is equal to some constant k, the medium-current flowing into node 1 and out of node 2 is proportional to the conductance of the network between nodes 1 and 2 (which is to say that the pressure drop between nodes 1 and 2 is fixed), and finally we assume that resource leaves the network by flowing into a dummy edge. Note that C_{tot} is equal to the total rate at which glucose is transported out of the vasculature and into the surrounding tissue, and at steady state it is also equal to the rate at which glucose flows into the network. To make a fair comparison between different networks, we calculate the total rate of glucose delivery at steady state, under the following assumptions:

1. We assume that the glucose concentration at node 1 is $k = 5$ mmole litre^{-1} (a typical physiological value).

2. All the edges are assumed to be cylindrical, and all the edges (including the dummy edge $2n$) are assumed to have the same cross-sectional area S (see Fig. 6.3).

3. Throughout the network, the local delivery rate $R = \frac{\rho}{\sqrt{S}}$, where value of the parameter ρ reflects the density of transporters on the surface of the edges, and their affinity for glucose.

4. We assume that the flow of fluid is laminar, so the Hagen-Poiseuille equation holds, and the conductance of each edge is proportional to $\frac{S^2}{l_{ij}}$.

5. We assume that the pressure drop across the network is independent of the network structure, and volume is conserved, so when the net medium-current leaving node 1 is F the net medium-current leaving node 2 is $-F$ (see Fig.

6.3). Given the relative conductances of each edge, and given F, we can use basic circuit theory to calculate the mean velocity of fluid flow in each of the edges [96, 100].

6. The molecular diffusion coefficient D_m is a given constant, the cross-sectional areas of the edges are given and we can calculate the mean velocities of fluid flow in each of the edges, so we can find the dispersion coefficients for each edge by plugging these values into Equation (3.1).

7. Resource leaves the network by flowing into a dummy edge $2n$, which has a cross-sectional area S and a mean velocity of flow equal to $\frac{F}{S}$.

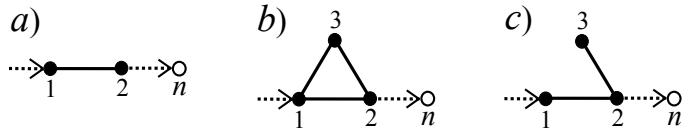

Figure 6.3: **Network structure has a critical influence on the total rate of glucose delivery.** We assume that the pressure drop between nodes 1 and 2 is fixed, as is the concentration at node 1. The rate at which resource leaves node 2 is proportional to the concentration at node 2, and the dummy edge $2n$ is not considered to be part of the network. Crucially, increasing the volume of blood in the network may or may not increase the total rate of glucose delivery, depending on how that change effects the time taken to transit the network. We illustrate this effect by considering the total rate of delivery for a very simple network with edges of variable length, but our mathematical approach can also be applied to any other network.

To calculate the current of glucose leaving the network at node 2, we suppose that at steady state the concentration at node 2 is c_2 while the concentration at node n is 0 (see Fig. 6.3). Equation (6.2) implies that

$$A = \frac{-Sc_2 e^{\frac{-\hat{\alpha}_{2n}}{D_{2n}} l}}{1 - e^{\frac{-\hat{\alpha}_{2n}}{D_{2n}} l}} \quad \text{and} \quad B = \frac{Sc_2}{1 - e^{\frac{-\hat{\alpha}_{2n}}{D_{2n}} l}}, \tag{6.4}$$

where l is the length of the dummy edge $2n$. Letting $l \to \infty$, we have

$$q_{2n}(x) = Sc_2 e^{\frac{u_{2n} - \hat{\alpha}_{2n}}{2D_{2n}} x}. \tag{6.5}$$

Glucose flows out of the network at node 2 at a rate equal to the flux at the beginning of the dummy edge $2n$, and so by Fick's law, the rate at which resource enters the network at node 2 is

$$\hat{I}_2 = -\left[u_{2n}q_{2n}(x) - D_{2n}\frac{d}{dx}q_{2n}(x)\right]_{x=0}. \tag{6.6}$$

This quantity is proportional to the concentration at node 2, and we let $\hat{I}_2 = -F'c_2$. Equations (3.1), (6.3) and (6.5) tell us that

$$\begin{aligned} F' &= S\frac{u_{2n}+\hat{\alpha}_{2n}}{2} \\ &= \frac{F}{2}\left(1+\sqrt{1+\frac{4R_{2n}D_mS^2}{F^2}+\frac{S}{48\pi D_m}}\right). \end{aligned} \tag{6.7}$$

The net current of resource entering the network at node 1 is denoted $\hat{I}_1$, and the net current of resource entering the network at node is $\hat{I}_2 = -F'c_2$. At every other node, the amount of resource entering the node is equal to the amount of resource leaving that node. It follows from Equation (3.23) that we have

$$\mathbf{M}\begin{pmatrix} k \\ c_2 \\ c_3 \end{pmatrix} = \begin{pmatrix} \hat{I}_1 \\ -F'c_2 \\ 0 \end{pmatrix}. \tag{6.8}$$

As we know the values of $\mathbf{M}$ and k, these three equations enable us to calculate the three unknowns $\hat{I}_1$, c_2 and c_3. We could also use this method to calculate the concentrations at the nodes of a network with more than three nodes. Furthermore, at steady state the amount of resource delivered by the network is equal to the net-rate at which resource enters the network, so we have

$$C_{\text{tot}} = \hat{I}_1 + \hat{I}_2 = \hat{I}_1 - F'c_2. \tag{6.9}$$

Analytic Solutions to the Total Rate of Glucose Delivery in Simple Vascular networks

We begin by considering the total rate of resource delivery in a single edge, where we vary the cross-sectional area of the edge, but fix the density of glucose transports on

the surface of the vessel. In other words, we vary S and assume that the local rate of resource delivery $R \propto S^{-\frac{1}{2}}$. To replicate the scales of interest in actual vascular networks, we consider edges of length $l_{12} = 1$mm, and we let $D_m = 6.7 \times 10^{-4}\text{mm}^2\text{s}^{-1}$ (the molecular diffusion coefficient of glucose in water at body temperature). We also let $k = 5$mmole/litre: a typical value for the concentration of glucose in blood. Finally, we assume that there is a fixed number of glucose transporters per unit area, so the local delivery rate $R = \frac{\rho}{\sqrt{S}}$. The numerical value of the parameter ρ reflects the density of transporters, and their affinity for glucose. In the first instance we have let $\rho = 0.03$ mm s^{-1}, so when $S = 0.001$ mm^2, $R = 1$ s^{-1}. We also consider a range of other values for ρ and R, but this figure is reasonable in that it produces a modest but significant drop in the concentration of glucose along the length of the vessel.

To produce the continuous curve shown in Fig. 6.4 we suppose that the pressure drop between nodes 1 and 2 is held constant. The Hagen-Poiseuille equation states that in the case of laminar flow, conductance should scale with the square of a vessel's cross-sectional area. In other words, in the case of a single edge, maintaining a constant pressure drop is equivalent to setting $u_{12} \propto S$. We have also plotted the case where the medium-current $F = 0.01\text{mm}^3\text{s}^{-1}$ regardless of the cross-sectional area S.

We now consider the total rate of glucose delivery by a pair of vessels where we vary the lengths of one or both of the vessels (see Fig. 6.3b). To replicate the scales of interest in actual vascular networks, we let the cross-sectional area $S_{ij} = 0.001\text{mm}^2$ for each edge, we let $D_m = 6.7 \times 10^{-4}\text{mm}^2\text{s}^{-1}$ (the molecular diffusion coefficient of glucose in water at body temperature) and we let the pressure drop be such that when both routes are of length 1mm, the net medium-current entering the network at node 1 is $F = 0.002\text{mm}^3\text{s}^{-1}$. We also suppose that the local delivery rate is constant throughout the network, and compare the results for various values of R.

Note that the medium-current passing through each route will be proportional to its conductance (see Fig. 6.3). If the alternate route between nodes 1 and 2 is very short, its conductance will be very large, the mean transit time will be very

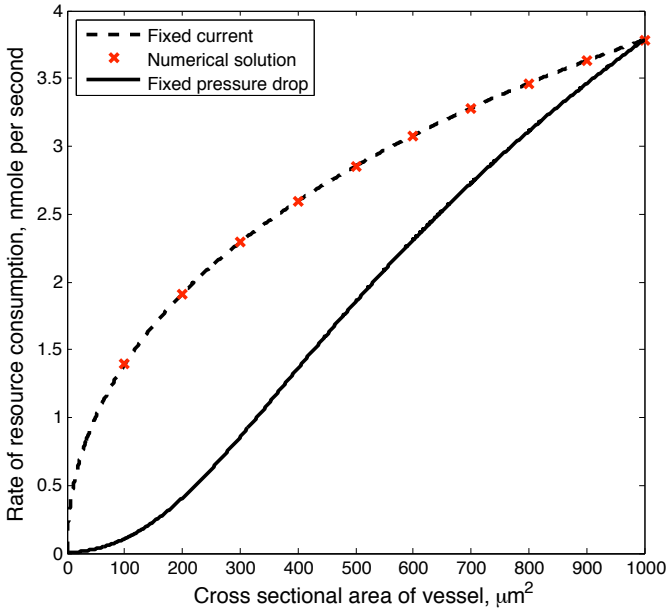

Figure 6.4: In the case where the pressure drop is fixed, the velocity of flow is proportional to S. Where the medium-current is fixed, the velocity of flow is inversely proportional to the vessel's cross-sectional area S. In both cases the volume of blood is proportional to S, the consumption rate per unit of resource $R \propto S^{\frac{-1}{2}}$ and faster flowing fluid results in a smaller drop in concentration over the length of the vessel. Our parameters are such that the medium-current is lower in the case where the pressure drop is fixed, apart from the case where S is the maximum considered, at which point the medium-current $F = 0.01\text{mm}^3\text{s}^{-1}$ in both cases. Since our parameters imply that the medium current is smaller in the case of a fixed pressure drop, we also have a lower mean velocity, a lower mean concentration and a lower total rate of resource consumption.

small, and so the total rate of glucose delivery will also be small. If the alternate route between nodes 1 and 2 is sufficiently long, most of the glucose entering that edge will be consumed. Further increases in the length of that edge will decrease the total rate of glucose delivery, as increasing the length of that edge will increase its resistance, so a larger proportion of the medium and glucose will flow into edge 13 instead, where it is less likely to be consumed. It follows that the total rate of glucose delivery is at a maximum when the alternate route between nodes 1 and 2 is of some intermediate length (see Figs. 6.5 and 6.6).

As a final example we consider the case where our network contains a dead-end (see Fig. 6.3c). We let $S_{12} = 0.001\text{mm}^2$, $l_{12} = 2\text{mm}$, $u_{12} = 1\ \text{mms}^{-1}$ and $u_{23} = 0\ \text{mms}^{-1}$, while D_{ij} is determined by Equation (3.1). In this case we vary the length

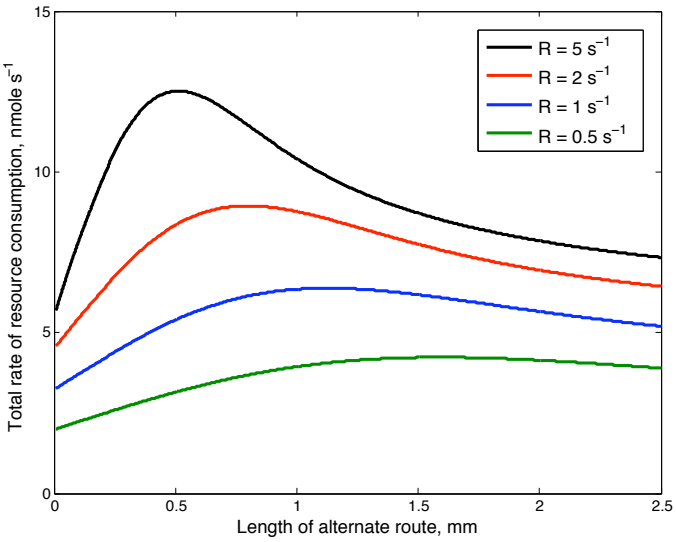

Figure 6.5: **Total rate of glucose delivery in a network with one fixed route and an alternate route of variable length.** In this case we let $l_{13} = l_{32} = 0.5$mm, and vary the length l_{12} between 0 and 3mm. As l_{12} increases, the conductance and medium-current in edge 12 becomes smaller, but a greater proportion of the resource that enters the edge is consumed. Note that C_{tot} is at a maximum for some intermediate value of l_{12}, and that when $l_{12} = 1$mm, the two routes between nodes 1 and 2 are identical and have a mean transit time of 1s.

of the dead-end to see how it effects C_{tot} (see Fig. 6.7).

Biomedical Implications of Altering Vascular Geometry

Despite their simple nature we now suggest that the results of Section 6.3 could have biomedical implications. Tumours require access to blood vessels for growth and metastasis. Consequently anti-angiogenic drugs, which disrupt and inhibit the formation of new blood vessels, are a promising avenue for the treatment of cancer. As single agents, anti-angiogenic drugs have only produced modest clinical improvements [120], but in combination with chemotherapy, the drug bevacizuab (a monoclonal antibody against vascular endothelial growth factor) has produced an unprecedented increase in survival (by 5 months) in colorectal cancer patients [109]. This is somewhat paradoxical, as previous studies have indicated that destroying the vasculature severely compromises the delivery of oxygen and therapeutics, produc-

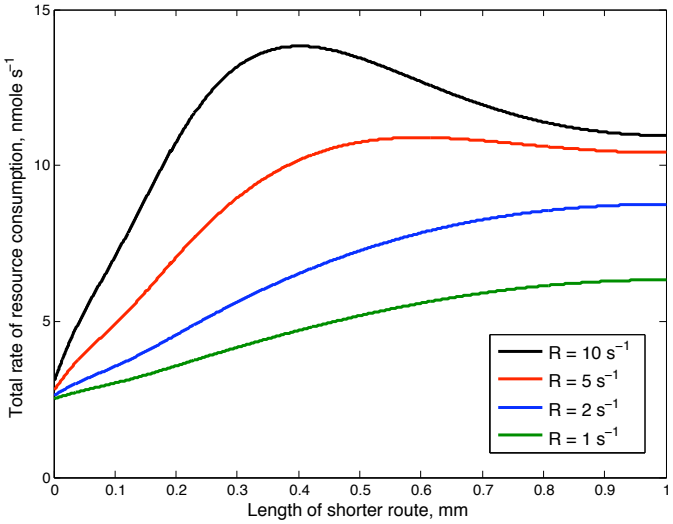

Figure 6.6: **Total rate of glucose delivery in a network with two alternate routes of fixed total length.** In this case we let $l_{13} = l_{32}$, and we vary the length of edge 12 between 0 and 1mm while ensuring that $l_{12} + l_{13} + l_{32} = 2$mm. Note that the total medium-current entering the network is proportional to $1/l_{12} + 1/(2 - l_{12})$, which is at a minimum when $l_{12} = 1$. Also note that when $1/R$ is much greater than the mean time taken to transit the network, almost all the glucose entering the network will be consumed. In that case the total rate of delivery is at a maximum when one edge is shorter than the other, as although this asymmetry means that a smaller fraction of the resource entering the network is consumed, this effect is outweighed by the relatively large current entering the network. In the biologically relevant case where $1/R$ is smaller than the mean time taken to transit the network, C_{tot} is at a maximum when both routes through the network are of the same length. Furthermore, when $1/R$ is very small the concentration throughout the network is very close to k, so in that case varying l_{12} will not have a significant effect on C_{tot}.

ing hypoxia that renders chemotherapy and radiotherapy less effective [112].

Tumours are subject to an unusually high interstitial fluid pressure, which may collapse blood and lymph vessels, and inhibits the interstitial transport of drugs [194]. Furthermore, the blood vessels within tumours are relatively leaky, tortuous, and arranged in a haphazard, irregular pattern of interconnection, which results in velocities of fluid flow that vary spatially and temporally in a random manner [10, 44, 112, 151, 194]. In healthy tissue the endothelial cells of the vasculature are supported by cells known as pericytes, but in tumours the pericytes are loosely attached or absent [51, 112, 209]. Anti-angiogenic drugs may impact on drug delivery in several ways: they can induce the regression of the particularly leaky vessels

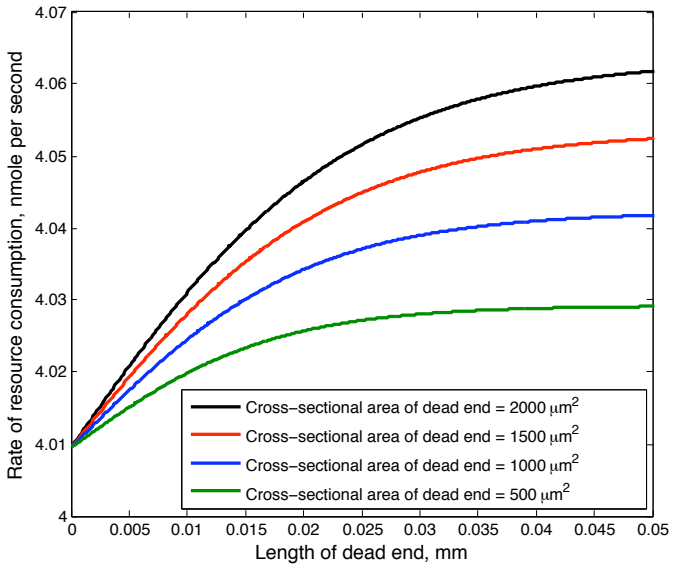

Figure 6.7: If the dead end region is short (see Fig. 6.3c), its presence increases the total rate of resource consumption by an amount that is proportional to both the volume of the dead end region and the consumption rate per unit of resource R_{23}. As we assume that $R_{23} \propto S_{23}^{-\frac{1}{2}}$, it follows that for sufficiently short dead end regions the increase in the total rate of resource consumption is proportional to $l_{23}\sqrt{S_{23}}$. Furthermore, the total rate of resource consumption reaches a maximum when the time taken to diffuse the length of the dead end region is much greater than the time scale of consumption.

that lack pericytes [112], they can encourage the maturation of the remaining vessels into less leaky, less dilated, less tortuous vessels with a greater coverage of pericytes [51, 112, 209], they can alter the pattern of vascular adaptation [3, 111, 148] and they can reduce the interstitial fluid pressure [111, 175, 194]. Finally, by reducing the number of vessels, anti-angiogenic drugs alter the topology of the vasculature. These effects have been described as 'vascular normalization' [10, 112], and they help to explain why the use of anti-angiogenic drugs can actually increase the delivery capacity of the vasculature in tumours, increasing the chemo-sensitivity of the tumour itself.

Our approach helps to illuminate the impact of changes in vascular structure, as we can use our algorithm to compare the delivery rates of various substances for a pair of networks (before and after vascular pruning, say). If the delivery rate per unit of resource R is small enough, almost every particle that enters the network will

exit the network over a time-scale smaller than $1/R$. In that case the concentration of resource will be approximately constant throughout both networks. This implies that any reduction in the total volume of blood vessels will reduce the delivery capacity of the network for the substance in question, as the total rate of resource delivery is equal to the total volume of blood times the mean concentration of resource times R. On the other hand, if R is sufficiently large, almost all the resource that enters the network will be consumed. Again we find that any reduction in the volume of blood vessels will reduce the total rate of resource delivery C_{tot}, but in this case it is because C_{tot} is approximately equal to the current of resource entering the network, and reducing the number of blood vessels will increase the hydraulic resistance of the network, thereby reducing both the medium-current and the current of resource flowing into the network.

The interesting case is also the most biologically relevant one: where R is such that a significant amount of resource is present in the blood that is leaving the network, but the concentration of resource entering the network is significantly greater than the concentration of resource leaving the network. In this intermediate case, reducing the total volume of blood vessels may increase or decrease the delivery capacity of the network (that is, the total rate of resource delivery). If we ignore the impact of vascular pruning on interstitial pressure, Fig. 6.7 indicates that removing dead-ends can only reduce the delivery capacity of the vascular network. Essentially, removing such dead-end regions does not affect the amount of resource entering the network, but it does decrease the mean transit time. It follows that the resource flowing through the network is more likely to exit the network before it is consumed, which is to say that removing dead-end regions will decrease the delivery capacity of any given network.

The effect of removing vessels that are an integral part of the network is more complex. In general, removing the shorter routes between the arteries and veins will increase the delivery capacity of the network, as, in the absence of short cuts, any resource that enters the network will be forced to spend longer within it, increasing the probability that any given particle will be consumed. As an extreme example, when

an arteriovenous malformation is formed (that is, an abnormal connection between arteries and veins) the total volume of blood vessels increases, but such a malformation will effectively short-circuit the capillaries in the region, so the current in the capillaries and the rate of glucose and oxygen delivery drops dramatically [80].

As Figs. 6.5 and 6.6 indicate, delivery is optimal when the various routes through the vasculature are of similar length, which indicates the importance of mechanisms that regulate the demarcation of artery-vein boundaries. This helps to explain the importance of Eph/ephrin signals, and other molecular cues that effectively identify endothelial cells as arterial or venous even before they are fused into a functioning circuit [9, 52]. Indeed, the imperative of avoiding arterio-venous shunts is one of the observations that makes it evident that vascular adaptation must involve more than just a cellular response to wall shear stress [152, 164].

In conclusion, the effect of vascular pruning on glucose delivery will depend on the network structure, and the topological location of the vessels that are pruned. If anti-angiogenic drugs eliminate dead-end vessels, the treatment will decrease the mean transit time of blood flowing through the tumour. This will tend to reduce the total rate of glucose delivery and the chemo-sensitivity of the tumour (though this effect may be swamped by other effects of anti-angiogenic drugs, such as a reduction in interstitial pressure). On the other hand, if anti-angiogenic treatment eliminates the shorter routes by which blood transits through the tumour, our model suggests that the effect will be an increase in the total delivery rate of glucose, and an increase in the chemo-sensitivity of the tumour. This observation suggests that researchers may gain some valuable insights into the process of chemosensitization by measuring the time it takes a tracer to transit a tumour before and after anti-angiogenic treatment.

6.4 Concluding Remarks

In conclusion, we note that the effective incompressibility of the fluids within fungi ensures that there is a rapid global response to local fluid movements. Furthermore,

velocity of fluid flow is a local signal that can convey quasi-global information about the role of a cord within the mycelium. We have found a correlation between the thickening of cords and the speeds or flux densities predicted by our model (Fig. 2.9a and 2.10a). Similarly, there was a positive correlation between predicted current and the thickening of cords (Fig. 2.9b and 2.10b). The speeds predicted by our model of growth-induced mass flows are consistent with experimental data and, contrary to previous analyses [115, 128, 155], we suggest that intrahyphal concentration gradients are not strictly necessary for the production of mass flows.

In Chapter 3 we presented a method for calculating how resource will become dispersed over a network, given the mean velocity of flow and the dispersion coefficient for each edge, and given that the resource in question is consumed at a given rate. This enabled us to investigate the claim that growth-induced mass flows account for a significant proportion of the long range transport in fungal networks. In Chapter 4 we describe the ADD model, in which we assume that resource enters the network at the inoculum at a constant rate, diffuses, and is carried by the currents produced by growth-induced mass flows. While advective mass flows carry resource over long distances from the inoculum out towards the growing tips [49, 115, 147], diffusion and active transport mechanisms may be essential near the sites where the cell wall is expanding. This follows because the cytosol within the apical hyphae moves forward at the same rate as the growing tips [126], but to transport resource from the base of the hyphae to the growing tips, the resource has to move faster than the rate of growth. Complex cellular machinery regulates the addition of material to the cell walls, ensuring that the growing hyphae exhibit polar growth, and only expand at the hyphal tips [20, 127, 135, 180, 181]. The presence of motor proteins and the cytoskeleton will affect the distribution of materials within fungal networks [110, 150, 183, 210], and the possibility of sequestering resources in organelles or the vacuole system will also influence the distribution of materials [62, 66]. Nevertheless, our model suggests that the minimum currents consistent with the observed growth would effectively transport resource from the inoculum to the growing tips over the time-scale of growth. This suggests that the active transport mechanisms

observed in the growing tips of fungal networks may not be required for long range transport.

It is well known that the rate of hyphal branching increases when tips encounter resource rich environments [38, 41, 77, 93, 145, 196]. Turgor pressure and the build up of vesicles have both been implicated, but whatever the mechanism behind this response, differential branching rates may constitute a unique kind of foraging strategy. We have developed a model for growing *in silico* fungal networks which can be used to investigate the complex relationship between local nutrient concentration, growth rates, the transport of resources and the network structures that emerge as a result of those interactions. Such models require a large number of parameters, many of which are phenomenological in character, and cannot be measured directly. Nevertheless, the modelling framework that we have presented can be used to describe fungal growth at a range of scales, and many of the parameters can be calibrated using empirical fungal networks. Our model may therefore be useful in assessing the extent to which global network characteristics can be explained by the local growth behaviours that experimentalists have described.

In Sections 6.1 and 6.2 we have presented a number of experiments and variations on our models that could be used to further the lines of research presented in this thesis. Finally, we note that our method for solving advection, diffusion and delivery equations over a network can also be applied to other biological, geological or technological systems, and in Section 6.3 we used the mathematical machinery described in Chapter 3 to analyze simple models of glucose delivery through a vascular network. These simple models illustrate that the delivery process has a critical impact on the dynamics of the system. In particular, our model illustrates the fact that in certain circumstances, increasing the volume of blood and the number of glucose transporters can actually decrease the total rate of glucose delivery.

In the past, models of transport networks and definitions of transport efficiency have tended to hinge around highly simplified representations of the kind of network in question. As imaging techniques improve, and it becomes increasingly possible to extract digitized descriptions of empirical transport networks, we believe that there

is a compelling need for computationally feasible modelling techniques that utilize this wealth of detailed information. As well as providing insights into the structure and function of fungal networks, we believe that this thesis constitutes a significant contribution to the broader study of biological transport networks.

Bibliography

[1] J. Abate and P. P. Valkó. Multi-precision Laplace transform inversion. *Int. J. Numer. Meth. Engng*, 60:979–993, 2004.

[2] J. Abate and W. Whitt. A unified framework for numerically inverting Laplace transforms. *INFORMS JOC*, 18:408–421, 2006.

[3] T. Alarcon, H. Byrne, and P. K. Maini. A multiple scale model for tumor growth. *Multiscale Model Sim*, 3:440–475, 2005.

[4] R. Amir, D. Levanon, Y. Hadar, and I. Chet. Factors affecting traslocation and sclerotial formation in Morchella esculenta. *Exp. Mycol*, 19:61–70, 1995.

[5] R. Amir, E. Steudle, D. Levanon, Y. Hadar, and I. Chet. Turgor changes in Morchella esculenta during translocation and sclerotial formation. *Exp. Mycol*, 19:129–136, 1995.

[6] R. Aris. On the dispersion of a solute in a fluid flowing through a tube. *Proc. Roy. Soc. A*, 235:67–77, 1956.

[7] D. J. Ashton, J. C. Jarrett, and N. Johnson. Effects of congestion costs on shortest paths through complex networks. *Phys. Rev. Lett*, 94:058701, 2005.

[8] D. Attwell, A. M. Buchan, S. Charpak, M. Lauritzen, B. A. MacVicar, and E. A. Newman. Glial and neuronal control of brain blood flow. *Nature*, 468:232–243, 2010.

[9] H. G. Augustin and Y. Reiss. EphB receptors and ephrinB ligands: Regulators of vascular assembly and homeostasis. *Cell Tissue Res*, 314:25–31, 2003.

[10] J. W. Baish, T. Stylianopoulos, R. M. Lanning, W. S. Kamoun, D. Fukumura, L. L. Munn, and R. K. Jain. Scaling rules for diffusive drug delivery in tumor and normal tissues. *P. Natl. Acad. Sci. USA*, 108:1799–1803, 2011.

[11] J. Banavar, F. Colaiori, A. Flammini, A. Maritan, and A. Rinaldo. Topology of the fittest transportation network. *Phys. Rev. Lett*, 84:4745–4748, 2000.

[12] J. Banavar, J. Damuth, A. Maritan, and A. Rinaldo. Supply-demand balance and metabolic scaling. *P. Natl. Acad. Sci. USA*, 99:10506–10509, 2002.

[13] J. Banavar, A. Maritan, and A. Rinaldo. Size and form in efficient transportation networks. *Nature*, 399:130–132, 1999.

[14] J. Banavar, A. Maritan, and A. Rinaldo. Rivers, blood and transportation networks. *Nature*, 408:159–160, 2000.

[15] J. R. Banavar, M. E. Moses, J. H. Brown, J. Damuth, A. Rinaldo, R. M. Sibly, and A. Maritan. A general basis for quarter-power scaling in animals. *P. Natl. Acad. Sci. USA*, 107:15816–15820, 2010.

[16] P. Bancal and F. Soltani. Source-sink partitioning. Do we need Munch? *J. Exp. Bot*, 53:1919–1928, 2002.

[17] A. Barrat, M. Barthélemy, and A. Vespignani. The effects of spatial constraints on the evolution of weighted complex networks. *J. Stat. Mech*, 2005:P05003, 2005.

[18] M. Barthelemy. Spatial networks. *Physics Reports*, 499, 2010.

[19] M. Barthélemy and A. Flammini. Modeling urban street patterns. *Phys. Rev. Lett*, 100:138702, 2008.

[20] S. Bartnicki-Garcia, D. D. Bartnicki, and G. Gierz. Determinants of fungal cell wall morphology: The vesicle supply center. *Can. J. Bot*, 73:372–378, 1995.

[21] S. Bartnicki-Garcia, D. D. Bartnicki, G. Gierz, R. Lopez-Franco, and C. E. Baracker. Evidence that Spitzenkörper behavior determines the shape of a fungal hypha: A test of the hyphoid model. *Exp. Mycol*, 19:153–159, 1995.

[22] S. Bartnicki-Garcia, C. E. Bracker, G. Gierz, R. López-Franco, and H. Lu. Mapping the growth of fungal hyphae: Orthogonal cell wall expansion during tip growth and the role of turgor. *Biophys. J*, 79:2382–2390, 2008.

[23] S. Bartnicki-Garcia, F. Hergert, and G. Gierz. Computer simulation of morphogenesis: Mathematical basis for the hyphal tip growth. *Protoplasma*, 153, 1989.

[24] J. B. Bassingthwaighte, L. S. Liebovitch, and B. J. West, editors. *Fractal Physiology*. Oxford University Press, 1994.

[25] D. A. Beard and J. B. Bassingthwaighte. Advection and diffusion of substances in biological tissues with complex vascular networks. *Ann. Biomed. Eng*, 28:253–268, 2000.

[26] D. A. Beard and J. B. Bassingthwaighte. Modeling advection and diffusion of oxygen in complex vascular networks. *Ann. Biomed. Eng*, 29:298–310, 2001.

[27] D. P. Bebber, J. Hynes, P. R. Darrah, L. Boddy, and M. D. Fricker. Biological solutions to transport network design. *Proc. Roy. Soc. B*, 274:2307–2315, 2007.

[28] D. P. Bebber, S. C. Watkinson, L. Boddy, and P. R. Darrah. Simulated nitrogen deposition affects wood decomposition by cord-forming fungi. *Oecologia*, 167:1177–1184, 2011.

[29] D. Ben-Avraham and S. Havlin. Diffusion on percolation clusters at criticality. *J. Phys. A*, 15:691–697, 1982.

[30] M. Bernot, V. Caselles, and J. M. Morel. *Optimal transportation networks: Models and theory (Lecture notes in Mathematics)*. Springer, 2008.

[31] P. Blinder, A. Y. Shih, C. Rafie, and D. Kleinfeld. Topological basis for the robust distribution of blood to rodent neocortex. *P. Natl. Acad. Sci. USA*, 107:12670–12675, 2010.

[32] L. Boddy. Saprotrophic cord-forming fungi: Meeting the challenge of heterogeneous environments. *Mycologia*, 91:13–32, 1999.

[33] L. Boddy, J. Hynes, D. Bebber, and M. D. Fricker. Saprotrophic cord systems: Dispersal mechanisms in space and time. *Mycoscience*, 50:9–19, 2009.

[34] L. Boddy, J. Wood, E. Redman, J. Hynes, and M. D. Fricker. Fungal network responses to grazing. *Fungal Genet. Biol*, 47:522–530, 2010.

[35] S. Bohn and M. O. Magnasco. Structure, scaling, and phase transition in the optimal transport network. *Phys. Rev. Lett*, 98:088702, 2007.

[36] G. P. Boswell. Modelling mycelial networks in structured environments. *Mycol. Res*, 112:1015–1025, 2008.

[37] G. P. Boswell, H. Jacobs, F. Davidson, G. Gadd, K. Ritz, and F. A. Davidson. A mathematical approach to studying fungal mycelia. *Mycologist*, 17:165–171, 2003.

[38] G. P. Boswell, H. Jacobs, F. A. Davidson, G. Gadd, and K. Ritz. Functional consequences of nutrient translocation in mycelial fungi. *J. Theor. Biol*, 217:459–477, 2002.

[39] G. P. Boswell, H. Jacobs, F. A. Davidson, G. Gadd, and K. Ritz. Growth and function of fungal mycelia in heterogeneous environments. *Bull. Math. Biol*, 65:447–477, 2003.

[40] G. P. Boswell, H. Jacobs, F. A. Davidson, G. M. Gadd, and K. Ritz. A positive numerical scheme for a mixed-type partial differential equation model for fungal growth. *Appl. Math. Comput*, 138:321–340, 2003.

[41] G. P. Boswell, H. Jacobs, G. Gadd, K. Ritz, and F. A. Davidson. The development of fungal networks in complex environments. *Bull. Math. Biol*, 69:605–634, 2007.

[42] C. Brownlee and D. H. Jennings. Long distance translocation in Serpula lacrimans: Velocity estimates and the continuous monitoring of induced perturbations. *Trans. Br. Mycol. Soc*, 79:43–48, 1982.

[43] C. Brownlee and D. H. Jennings. Pathway of translocation in Serpula lacrimans. *Trans. Br. Mycol. Soc*, 77:401–407, 1982.

[44] E. Bullitt, K. Muller, I. Jung, W. Lin, and S. Aylward. Analyzing attributes of vessel populations. *Med. Image Anal*, 9:39–49, 2005.

[45] A. Bunde and S. Havlin. *Fractals and disordered systems*. Springer-Verlag, 1991.

[46] P. Butti, M. Intaglietta, H. Reimann, C. Holliger, A. Bollinger, and M. Anliker. Capillary red blood cell velocity measurements in human nailfold by videodensitometric method. *Microvasc. Res*, 10:220–227, 1975.

[47] M. X. Caddick. What's for dinner, what shall l choose? *Microbiology Today*, 29:132–134, 2002.

[48] J. W. G. Cairney. Rhizomorphs: Organs of exploration or exploitation? *The Mycologist*, 5:5–10, 1991.

[49] J. W. G. Cairney. Translocation of solutes in ectomycorrhizal and saprotrophic rhizomorphs. *Mycol. Res.*, 96:135–141, 1992.

[50] J. W. G. Cairney. Basidiomycete mycelia in forest soils: Dimensions, dynamics and roles in nutrient distribution. *Mycol. Res.*, 109:7–20, 2005.

[51] P. Carmeliet. Angiogenesis in life, disease and medicine. *Nature*, 438:932–936, 2005.

[52] P. Carmeliet and M. Tessier-Lavigne. Common mechanisms of nerve and blood vessel wiring. *Nature*, 436:193–200, 2005.

[53] I. Carver and G. P. Boswell. A lattice-free model of translocation-induced outgrowth in fungal mycelia. *AENG Int. J. App. Math.*, 38, 2008.

[54] M. Chaplain, S. McDougall, and A. Anderson. Mathematical modeling of tumor-induced angiogenesis. *Annu. Rev. Biomed. Eng.*, 8:233–257, 2006.

[55] S. Chien, S. Li, and J. Y.-J. Shyy. Effects of mechanical forces on signal transduction and gene expression in endothelial cells. *Hypertension*, 31:162–169, 1998.

[56] N. Clipson, J. Cairney, and D. Jennings. Phosphate uptake by cords and mycelium in the laboratory and the field. *New Phytol.*, 105:449–457, 1987.

[57] J. Connolly and J. Jellison. Two-way translocation of cations by the brown rot fungus Gloeophyllum trabeum. *Int. Biodeterior.*, 39:181–188, 1997.

[58] F. Corson. Fluctuations and redundancy in optimal transport networks. *Phys. Rev. Lett.*, 104:048703, 2010.

[59] F. Corson, M. Adda-Bedia, and A. Boudaoud. In silico leaf venation networks: Growth and reorganization driven by mechanical forces. *J. Theor. Biol.*, 259:440–448, 2009.

[60] R. Courant, K. Friedrichs, and H. Lewy. On the partial difference equations of mathematical physics. *Math. Ann.*, 100:215–234, 1928.

[61] P. J. Daley, K. B. Sagar, and L. S. Wann. Doppler echocardiographic measurement of flow velocity in the ascending aorta during supine and upright exercise. *Brit. Heart J.*, 54:562–567, 1985.

[62] P. Darrah, M. Tlalka, A. Ashford, and S. Watkinson. The vacuole system is a significant intracellular pathway for longitudinal solute transport in basidiomycete fungi. *Eukaryotic Cell*, 5:1111–1125, 2006.

[63] F. A. Davidson and S. Olsson. Translocation induced outgrowth of fungi in nutrient-free environments. *J. Theor. Biol.*, 205:73–84, 2000.

[64] B. Davies and B. Martin. Numerical inversion of the Laplace transform: A survey and comparison of methods. *J. Comput. Phys.*, 33:1–32, 1979.

[65] L. de Arcangelis, J. Koplik, S. Redner, and D. Wilkinson. Hydrodynamic dispersion in network models of porous media. *Phys. Rev. Lett*, 57:996–999, 1986.

[66] J. Deacon. *Fungal Biology, 2nd edition*. Blackwell, 2005.

[67] H. A. V. der Vorst. Bi-CGSTAB: A fast and smoothly converging variant of Bi-CG for the solution of nonsymmetric linear systems. *SIAM J. Sci. Stat. Comput.*, 13:631–644, 1992.

[68] P. S. Dodds. Optimal form of branching supply and collection networks. *Phys. Rev. Lett.*, 104:048702, 2010.

[69] A. d'Onofrio and A. Gandolfi. Chemotherapy of vascularised tumours: Role of vessel density and the effect of vascular 'pruning'. *J. Theor. Biol.*, 264:253–265, 2010.

[70] P. G. Doyle and J. L. Snell. *Random walk and electric networks*. American Mathematical Society, 1989.

[71] O. Dreyer. Allometric scaling and central source systems. *Phys. Rev. Lett.*, 87:038101, 2001.

[72] O. Dreyer and R. Puzio. Allometric scaling in animals and plants. *J. Math. Biol.*, 43:144–156, 2001.

[73] M. Durand. Architecture of optimal transport networks. *Phys. Rev. E*, 73:016116, 2006.

[74] M. Durand. Structure of optimal transport networks subject to a global constraint. *Phys. Rev. Lett.*, 98:088701, 2007.

[75] D. Eamus, W. Thompson, J. Cairney, and D. Jennings. Internal structure and hydraulic conductivity of basidiomycete translocating organs. *J. Exp. Bot.*, 36:1110–1116, 1985.

[76] W. Eschrich, R. Evert, and J. Young. Solution flow in tubular semipermeable membranes. *Planta*, 107:279–300, 1972.

[77] R. E. Falconer, J. L. Bown, and J. W. Crawford. Biomass recycling and the origin of phenotype in fungal mycelia. *Proc. Roy. Soc. B*, 272:1727–1734, 2005.

[78] R. E. Falconer, J. L. Brown, N. A. White, and J. W. Crawford. Biomass recycling: A key to efficient foraging by fungal colonies. *Oikos*, 116:1558–1568, 2007.

[79] C. P. Fall, E. S. Marland, J. Wagner, and J. J. Tyson, editors. *Computational cell biology*. Springer-Verlag, 2002.

[80] I. G. Fleetwood and G. K. Steinberg. Arteriovenous malformations. *Lancet*, 359:863–873, 2002.

[81] M. D. Fricker, L. Boddy, and D. P. Bebber. Network organisation of mycelial fungi. *In: R. J. Howard, N. A. R. Gow (Eds.)*, Biology of the fungal cell, Springer-Verlag, Berlin:309–330, 2007.

[82] M. D. Fricker, L. Boddy, T. Nakagaki, and D. P. Bebber. *Adaptive networks: Theory, models and applications*. Springer, 2009.

[83] M. D. Fricker, J. Lee, D. P. Bebber, M. Tlalka, and J. Hynes. Imaging complex nutrient dynamics in mycelial networks. *J. Microsc.*, 231:317–331, 2008.

[84] M. A. Fruttiger. Development of the mouse retinal vasculature: Angiogenesis versus vasculogenesis. *Invest. Ophthalmol. Vis. Sci.*, 43:522–527, 2002.

[85] K. Fushimi and A. S. Verkman. Low viscosity in the aqueous domain of cell cytoplasm measured by picosecond polarization microfluorimetry. *J. Cell Biol.*, 112:719–725, 1991.

[86] G. M. Gadd, editor. *Fungi in biogeochemical cycles*. Cambridge University Press, 2006.

[87] V. V. Gafiychuk and I. A. Lubashevsky. On the principles of the vascular network branching. *J. Theor. Biol.*, 212:1–9, 2001.

[88] M. T. Gastner and M. E. J. Newman. Shape and efficiency in spatial distribution networks. *J. Stat. Mech.*, 2006(1):P01015, 2006.

[89] D. P. Gaver. Observing stochastic processes and approximate transform inversion. *Oper. Res*, 14(3):444–459, 1966.

[90] D. Goldman. Theoretical models of microvascular oxygen transport to tissue. *Microcirculation*, 15:795–811, 2008.

[91] D. Goldman and A. S. Popel. A computational study of the effect of capillary network anastomoses and tortuosity on oxygen transport. *J. Theor. Biol.*, 206:181–194, 2000.

[92] G. W. Gooday. The dynamics of hyphal growth. *Mycol. Res*, 99:385–394, 1995.

[93] N. A. R. Gow and G. M. Gadd, editors. *The growing fungus*. Chapman and Hall, London, 1995.

[94] H. I. Granlund and D. H. Jennings. Scanning electron microscope studies of rhizomorphs of armillaria mellea. *Nova Hedwigia*, 39:85–100, 1984.

[95] H. I. Granlund, D. H. Jennings, and W. Thompson. Translocation of solutes along rhizomorphs of Armillaria mellea. *Trans. Br. Mycol. Soc.*, 84:111–119, 1985.

[96] G. R. Grimmett and H. Kesten. Random electrical networks on complete graphs. *J. Lond. Math. Soc.*, 30:171–192, 1984.

[97] K. Groebe. An easy-to-use model for o2 supply to red muscle. Validity of assumptions, sensitivity to errors in data. *Biophys. J.*, 68:1246–1269, 1995.

[98] K. L. Hanson, D. V. Nicolau, L. Filipponi, L. Wang, A. P. Lee, and D. V. Nicolau. Fungi use efficient algorithms for the exploration of microfluidic networks. *Space-searching algorithms*, 2:1212 – 1220, 2010.

[99] F. Harold. Force and compliance: Rethinking morphogenesis in walled cells. *Fung. Genet. Biol.*, 37:271–282, 2002.

[100] L. L. M. Heaton, E. López, P. K. Maini, M. D. Fricker, and N. S. Jones. Growth-induced mass flows in fungal networks. *Proc. Roy. Soc. B*, 277:3265–3274, 2010.

[101] D. Helbing, D. Armbruster, A. S. Mikhailov, and E. Lefeber. Information and material flows in complex networks. *Physica A*, 363:11–16, 2006.

[102] M. Held, A. P. Lee, C. Edwards, and D. Nicolau. Microfluidics structures for probing the dynamic behaviour of filamentous fungi. *Microelectron. Eng.*, 87:786–789, 2009.

[103] P. C. Hickey, D. J. Jacobson, N. D. Read, and N. L. Glass. Live-cell imaging of vegetative hyphal fusion in Neurospora crassa. *Fung. Genet. Biol.*, 37:109–119, 2002.

[104] A. Hindmarsh, P. Gresho, and D. Griffiths. The stability of explicit Euler time-integration for certain finite difference approximations of the multidimensional advection-diffusion equation. *Int. J. Numer. Methods Fluids*, 4:853–897, 1984.

[105] S. Hopkins and G. P. Boswell. Mycelial response to spatiotemporal nutrient heterogeneity: A velocity-jump mathematical model. *Fungal Ecol.*, 5:124–136, 2011.

[106] R. Howard. Ultrastructural analysis of hyphal tip cell growth in fungi: Spitzenkörper, cytoskeleton and endomembranes after freeze-substitution. *J. Cell Sci.*, 48:89–103, 1981.

[107] Y. Huo and G. S. Kassab. A scaling law of vascular volume. *Biophysical Journal*, 96:347–353, 2009.

[108] Y. Huo and G. S. Kassab. The scaling of blood flow resistance: From a single vessel to the entire distal tree. *Biophys. J.*, 96:339–346, 2009.

[109] H. Hurwitz, L. Fehrenbacher, W. Novotny, T. Cartwright, J. Hainsworth, W. Heim, J. Berlin, A. Baron, S. Griffing, E. Holmgren, N. Ferrara, G. Fyfe, B. Rogers, R. Ross, and F. Kabbinavar. Bevacizumab plus irinotecan, fluorouracil, and leucovorin for metastatic colorectal cancer. *N. Engl. J. Med.*, 350:2335–2342, 2004.

[110] S. Inoue, B. G. Turgeon, O. C. Yoder, and J. R. Aist. Role of fungal dynein in hyphal growth, microtubule organization, spindle pole body motility and nuclear migration. *J. Cell Sci.*, 111:1555–1566, 1998.

[111] R. K. Jain. Molecular regulation of vessel maturation. *Nat. Med.*, 9:685–693, 2003.

[112] R. K. Jain. Normalization of tumor vasculature: An emerging concept in antiangiogenic therapy. *Science*, 307:58–62, 2005.

[113] T. Jarrett, D. Ashton, M. D. Fricker, and N. Johnson. Abrupt structural transitions involving functionally optimal networks. *Phys. Rev. Lett.*, 74, 2005.

[114] G. Jedd. Fungal evo-devo: Organelles and multicellular complexity. *Trends Cell Biol.*, 21:12–19, 2011.

[115] D. H. Jennings. Translocation of solutes in fungi. *Biol. Rev.*, 62:215–243, 1987.

[116] D. H. Jennings and A. D. M. Rayner. *The ecology and physiology of the fungal mycelium*. Cambridge University Press, 1984.

[117] A. Kamiya, R. Bukhari, and T. Togawa. Adaptive regulation of wall shear stress optimizing vascular tree function. *B. Math. Biol.*, 46:127–137, 1984.

[118] G. S. Kassab. Scaling laws of vascular trees: of form and function. *Am. J. Physiol. Heart*, 290:894–903, 2006.

[119] E. Katifori, G. J. Szollosi, and M. O. Magnasco. Damage and fluctuations induce loops in optimal transport networks. *Phys. Rev. Lett*, 104:048704, 2010.

[120] R. Kerbel and J. Folkman. Clinincal translation of angiogenesis inhibitors. *Nature*, 2:727–739, 2002.

[121] J. P. Kirkpatrick, D. M. Brizel, and M. W. Dewhirst. A mathematical model of tumor oxygen and glucose mass transport and metabolism with complex reaction kinetics. *Radiat. Res.*, 159:336–344, 2003.

[122] J. Koplik, S. Redner, and D. Wilkinson. Transport and dispersion in random networks with percolation disorder. *Phys. Rev. A*, 37:2619–2636, 1988.

[123] F. Kreuzer. Oxygen supply to tissues: The Krogh model and its assumptions. *Experimentia*, 38:1415–1426, 1982.

[124] E. Kreyszig. *Advanced engineering mathematics, 9th Edition*. Wiley, 2006.

[125] M. LaBarbera. Principles of design of fluid transport systems in zoology. *Science*, 249:992–1000, 1990.

[126] R. R. Lew. Mass flow and pressure-driven hyphal extension in Neurospora crassa. *Microbiology*, 151:2685–2692, 2005.

[127] R. R. Lew. How does a hypha grow? the biophysics of pressurized growth in fungi. *Nature Rev. Microbiol.*, 9:509–518, 2011.

[128] R. R. Lew, N. Levina, S. Walker, and A. Garrill. Turgor regulation in hyphal organisms. *Fung. Genet. Biol.*, 41:1530–1537, 2004.

[129] W. W. Lilly, G. J. Wallweber, and S. M. Higgins. Proteolysis and amino acid recycling during nitrogen deprivation in Schizophyllum commune. *Curr. Microbiol.*, 23:27–32, 1991.

[130] B. Lindahl, R. Finlay, and S. Olsson. Simultaneous, bidirectional translocation of ^{32}P and ^{33}P between wood blocks connected by mycelial cords of Hypholoma fasciculare. *New Phytol.*, 150:189–194, 2001.

[131] H. A. Makse, J. S. Andrade, and H. E. Stanley. Tracer dispersion in a percolation network with spatial correlations. *Phys. Rev. E*, 61:583–586, 2000.

[132] A. Maritan, F. Colaiori, A. Flammini, M. Cieplak, and J. Banavar. Universality classes of optimal channel networks. *Science*, 272:984–986, 1996.

[133] K. A. McCulloh, J. S. Sperry, and F. R. Adler. Water transport in plants obeys Murray's law. *Nature*, 421:939–942, 2003.

[134] N. Money. Wishful thinking of turgor revisited: The mechanics of fungal growth. *Fungal Genet. Biol.*, 21:173–187, 1997.

[135] N. Money. Insights on the mechanics of hyphal growth. *Fungal Biol. Rev.*, 22:71–76, 2008.

[136] C. D. Murray. The physiological principle of minimum work applied to the angle of branching of arteries. *J. Gen. Physiol.*, 9:835–841, 1926.

[137] C. D. Murray. The physiological principle of minimum work. I. The vascular system and the cost of blood volume. *Proc. Natl. Acad. Sci. USA*, 12:207–214, 1926.

[138] C. D. Murray. The physiological principle of minimum work. II. Oxygen exchange in capillaries. *Proc. Natl. Acad. Sci. USA*, 12:299–304, 1926.

[139] C. D. Murray. A relationship between circumference and weight in trees and its bearing on branching angles. *J. Gen. Physiol.*, 10:725–729, 1927.

[140] P. Nelson. *Biological physics: Energy, information, life.* W.H. Freeman and Company., 2003.

[141] P. S. Nobel. *Physicochemical and environmental plant physiology*. San Diego: Academic Press, 1991.

[142] B. Obara, M. D. Fricker, D. Gavaghan, and V. Grau. Contrast-independent curvilinear structure detection in biomedical images. *IEEE Trans. Image. Process.*, 99, 2012.

[143] B. Obara, M. D. Fricker, D. Gavaghan, and V. Grau. Contrast-independent junction detection in biological images. *Botanical Microscopy*, 2012.

[144] K. Oh, T. Nishiyama, E. Sakai, H. Matsuoka, and H. Kurata. Flow sensing in mycelial fungi. *J. Biotechnology*, 58:197–204, 1997.

[145] S. Olsson. Mycelial density profiles of fungi on heterogeneous media and their interpretation in terms of nutrient reallocation patterns. *Mycol. Res.*, 99:143–153, 1995.

[146] S. Olsson. Colonial growth of fungi. *In: R. J. Howard, N. A. R. Gow (Eds.)*, The Mycota, Springer-Verlag:125–141, 2001.

[147] S. Olsson and S. N. Gray. Patterns and dynamics of ^{32}P-phosphate and labelled 2-aminoisobutyric acid (14C-AIB) translocation in intact basidiomycete mycelia. *FEMS Microbiol. Ecol.*, 26:109–120, 1998.

[148] M. R. Owen, T. Alarcón, P. K. Maini, and H. M. Byrne. Angiogenesis and vascular remodelling in normal and cancerous tissues. *J. Math. Biol.*, 58:689–721, 2009.

[149] E. C. Peterson, Z. Wang, and G. Britz. Regulation of cerebral blood flow. *Int. J. Vasc. Med.*, 2011:823525, 2011.

[150] M. Plamann, P. Minke, J. H. Tinsley, and K. S. Bruno. Cytoplasmic dynein and actin-related protein Arp1 are required for normal nuclear distribution in filamentous fungi. *J. Cell Biol.*, 127:139–149, 1994.

[151] A. R. Pries, A. J. M. Cornelissen, A. A. Sloot, M. Hinkeldey, M. R. Dreher, M. Höpfner, M. W. Dewhirst, T. W. Secomb, and J. A. Papin. Structural adaptation and heterogeneity of normal and tumor microvascular networks. *PLoS Comput. Biol.*, 5:10000394, 2009.

[152] A. R. Pries, M. Höpfner, F. le Noble, M. W. Dewhirst, and T. W. Secomb. The shunt problem: Control of functional shunting in normal and tumour vasculature. *Nature*, 10:587–593, 2010.

[153] A. R. Pries, B. Reglin, and T. W. Secomb. Structural adaptation of vascular networks: Role of the pressure response. *Hypertension*, 38:1476–1479, 2001.

[154] S. L. Ramos-García, R. W. Roberson, M. Freitag, S. Bartnicki-García, and R. R. Mouriño-Pérez. Cytoplasmic bulk flow propels nuclei in mature hyphae of Neurospora crassa. *Eukaryot. Cell*, 8:1880–1890, 2009.

[155] A. Rayner. The challenge of the individualistic mycelium. *Mycologia*, 83:48–71, 1991.

[156] A. Rayner, Z. R. Watkins, and J. R. Beeching. Self-integration - an emerging concept from the fungal mycelium. *N. A. R. Gow, G. D. Robson, G. M. Gadd (Eds.)*, The Fungal Colony, Cambridge University Press, Cambridge:1–24, 1991.

[157] A. D. M. Rayner, K. A. Powell, W. Thompson, and D. H. Jennings. *Developmental Biology of Higher Fungi*. Cambridge University Press, 1985.

[158] S. Redner. *A Guide to First-Passage Processes*. Cambridge University Press, 2001.

[159] M. Reinhardt. Das wachsthum der pilzhyphen. *Jahrb. Wissenschaft. Bot.*, 23:479–566, 1892.

[160] A. Rinaldo, J. Banavar, V. Colizza, and A. Maritan. On network form and function. *Physica A*, 340:749–755, 2004.

[161] A. Rinaldo, J. Banavar, and A. Maritan. Trees, networks, and hydrology. *Water Resour. Res.*, 42:10.1029, 2006.

[162] M. Riquelme, C. G. Reynaga-Pena, G. Gierz, and S. Bartnicki-Garcia. What determines growth direction in fungal hyphae? *Fung. Genet. Biol.*, 24:101–109, 1998.

[163] N. F. Robertson. Observations on the effect of water on the hyphal apices of Fusarium oxysporum. *Ann. Bot.*, 22:159–173, 1958.

[164] S. Rodbard. Vascular caliber. *Cardiology*, 60:4–49, 1975.

[165] A. Roth-Nebelsick, D. Uhl, V. Mosbrugger, and H. Kerp. Evolution and function of leaf venation architecture: A review. *Ann. Bot.*, 87:553–566, 2001.

[166] L. Sack and N. M. Holbrook. Leaf hydraulics. *Ann. Rev. Plant Biol.*, 57:361–381, 2006.

[167] M. Sahimi. Hydrodynamic dispersion near the percolation threshold: Scaling and probability densities. *J. Phys. A: Math. Gen.*, 20:1293–1298, 1987.

[168] M. Sahimi, H. T. Davis, and L. E. Scriven. Dispersion in disordered porous media. *Chem. Eng. Commun.*, 23:329–341, 1983.

[169] K. Sampson, R. Lew, and I. B. Heath. Time series analysis demonstrates the absence of pulsatile hyphal growth. *Microbiology*, 149:3111–3119, 2003.

[170] V. M. Savage, E. J. Deeds, and W. Fontana. Sizing up allometric scaling theory. *PLoS Comput. Biol.*, 4:1000171, 2008.

[171] H. Schack-Kirchner, K. V. Wilpert, and E. E. Hildebrand. The spatial distribution of soil hyphae in structured spruce-forest soils. *Plant Soil*, 224:195–205, 2000.

[172] T. W. Secomb. Theoretical models for regulation of blood flow. *Microcirculation*, 15:765–775, 2008.

[173] T. F. Sherman. On connecting large vessels to small: The meaning of Murray's law. *J. Gen. Physiol.*, 78:431–453, 1981.

[174] T. F. Sherman, A. S. Popel, A. Koller, and P. C. Johnson. The cost of departure from optimal radii in microvascular networks. *J. Theor. Biol.*, 136:245–265, 1989.

[175] R. J. Shipley and S. J. Chapman. Multiscale modelling of fluid and drug transport in vascular tumours. *B. Math. Biol*, 72:1464–1491, 2010.

[176] G. D. Smith. *Numerical Solution of Partial Differential Equations: Finite Difference Methods*. Oxford University Press, 1985.

[177] M. Smith, J. Bruhn, and J. Anderson. The fungus Armillaria bulbosa is among the largest and oldest living organisms. *Nature*, 356:428–431, 1992.

[178] E. Sousa. The controversial stability analysis. *Appl. Math. Comput.*, 145:777–794, 2003.

[179] H. Stehfest. Numerical inversion of Laplace transforms. *Comm. ACM*, 13:47–49, 1970.

[180] G. Steinberg. Organelle transport and molecular motors in fungi. *Fungal Genet. Biol.*, 24:161–177, 1998.

[181] G. Steinberg. Hyphal growth: a tale of motors, lipids, and the Spitzenkörper. *Eukaryotic Cell*, 6:351–360, 2006.

[182] P. S. Stevens. *Patterns in Nature*. Little, Brown and Company, 1974.

[183] R. Suelmann, N. Sievers, and R. Fischer. Nuclear traffic in fungal hyphae: In vivo study of nuclear migration and positioning in Aspergillus nidulans. *Mol. Microbiol.*, 25:757–769, 1997.

[184] D. Szczerba and G. Székely. Computational model of flow-tissue interactions in intussusceptive angiogenesis. *J. Theor. Biol.*, 234:87–97, 2005.

[185] G. Taylor. Dispersion of soluble matter in solvent flowing slowly through a tube. *Proc. Roy. Soc. A*, 219:186–203, 1953.

[186] M. V. Thompson. Phloem: The long and the short of it. *Trends Plant Sci.*, 11:1360–1385, 2005.

[187] W. Thompson, C. Brownlee, D. Jennings, and A. Mortimer. Localized, cold-induced inhibition of translocation in mycelia and strands of Serpula lacrimans. *J. Exp. Botany*, 38:889–899, 1987.

[188] W. Thompson, D. Eamus, and D. H. Jennings. Water flow through the mycelium of Serpula lacrimans. *Trans. Br. Mycol. Soc.*, 84:601–608, 1985.

[189] M. Tlalka, D. P. Bebber, P. R. Darrah, S. C. Watkinson, and M. D. Fricker. Quantifying dynamic resource allocation illuminates foraging strategy in Phanerochaete velutina. *Fung. Genet. Biol.*, 45:1111–1121, 2008.

[190] M. Tlalka, D. Hensman, P. R. Darrah, S. C. Watkinson, and M. D. Fricker. Noncircadian oscillations in amino acid transport have complementary profiles in assimilatory and foraging hyphae of Phanerochaete velutina. *New Phytol.*, 158:325–335, 2003.

[191] M. Tlalka, S. C. Watkinson, P. R. Darrah, and M. D. Fricker. Continuous imaging of amino-acid translocation in intact mycelia of Phanerochaete velutina reveals rapid, pulsatile uxes. *New Phytol.*, 153:173–184, 2002.

[192] T. Toni and M. P. H. Stumpf. Simulation-based model selection for dynamical systems in systems and population biology. *Bioinformatics*, 26:104–110, 2010.

[193] J. N. Topper and M. A. Gimbrone. Blood flow and vascular gene expression: Fluid shear stress as a modulator of endothelial phenotype. *Mol. Med. Today*, 5:40–46, 1999.

[194] G. A. Truskey, F. Yuan, and D. F. Katz. *Transport Phenomena in Biological Systems*. Pearson, 2010.

[195] A. Wagner. *Robustness and Evolvability in Living Systems*. Princeton University Press, 2005.

[196] S. C. Watkinson, L. Boddy, K. Burton, P. R. Darrah, D. Eastwood, M. D. Fricker, and M. Tlalka. New approaches to investigating the function of mycelial networks. *Mycologist*, 19:11–17, 2005.

[197] J. Wells and L. Boddy. Effect of temperature on wood decay and translocation of soil-derived phosphorus in mycelial cord systems. *New Phytol.*, 129:289–297, 1995.

[198] J. Wells, L. Boddy, and R. Evans. Carbon translocation in mycelial cord systems of Phanerochaete velutina. *New Phytol.*, 129:467–476, 1995.

[199] J. Wells, M. Harris, and L. Boddy. Encounter with new resources causes polarized growth of the cord-forming basidiomycete Phanerochaete velutina on soil. *Microb. Ecol.*, 36:372–382, 1998.

[200] J. M. Wells, L. Boddy, and D. P. Donnelly. Wood decay and phosphorus translocation by the cord-forming basidiomycete Phanerochaete velutina: The significance of local nutrient supply. *New Phytol.*, 138:607–617, 1998.

[201] M. Welter, K. Bartha, and H. Rieger. Emergent vascular inhomogeneities and resulting blood flow patterns in a growing tumor. *J. Theor. Biol.*, 250:257–280, 2008.

[202] J. G. H. Wessels. Wall growth, protein excretion and morphogenesis in fungi. *New Phytol.*, 123:397–413, 1993.

[203] G. West, J. Brown, and B. Enquist. A general model for the origin of allometric scaling laws in biology. *Science*, 276:122–126, 1997.

[204] G. West, J. Brown, and B. Enquist. The fourth dimension of life: Fractal geometry and allometric scaling of organisms. *Science*, 284:1677–1679, 1999.

[205] G. B. West and J. H. Brown. Life's universal scaling laws. *Physics Today*, 57:36–42, 2004.

[206] G. B. West, W. H. Woodruff, and J. H. Brown. Allometric scaling of metabolic rate from molecules and mitochondria to cells and mammals. *Proc. Natl. Acad. Sci. USA*, 99:2473–2478, 2002.

[207] J. P. Whiteley, D. J. Gavaghan, and C. E. W. Hahn. Mathematical modelling of oxygen transport to tissue. *J. Math. Biol.*, 44:503–522, 2002.

[208] M. D. Whiteside, K. Treseder, and P. Atsatt. The brighter side of soils: Quantum dots track organic nitrogen through fungi and plants. *Ecology*, 90:100–108, 2009.

[209] F. Winkler, S. V. Kozin, R. T. Tong, S.-S. Chae, M. F. Booth, I. Garkavtsev, L. Xu, D. J. Hicklin, D. Fukumura, E. di Tomaso, L. L. Munn, and R. K. Jain. Kinetics of vascular normalization by VEGFR2 blockade governs brain tumor response to radiation: Role of oxygenation, angiopoietin-1, and matrix metalloproteinases. *Cancer Cell*, 6:553–563, 2004.

[210] A. Yamamoto. Cytoplasmic dynein in fungi: insights from nuclear migration. *J. Cell Sci.*, 116:4501–4512, 2003.

[211] J. H. Young, R. F. Evert, and W. Eschrich. On the volume-flow mechanism of phloem transport. *Planta*, 113:355–366, 1973.

[212] V. Zakian. Numerical inversion of Laplace transform. *Electron. Lett.*, 5:120–121, 1969.

[213] V. Zakian. Optimisation of numerical inversion of Laplace transforms. *Electron. Lett.*, 6:677–679, 1970.

[214] M. Zamir. Cost analysis of arterial branching in the cardiovascular systems of man and animals. *J. Theor. Biol.*, 120:111–123, 1986.